High-throughput screening of multifunctional magnetic materials

Gao, Qiang

(2020)

DOI (TUprints): https://doi.org/10.25534/tuprints-00014194

High-throughput screening of multifunctional magnetic materials

Hochdurchsatz-Screening multifunktionaler magnetischer Materialien
Zur Erlangung des Grades eines Doktors der Naturwissenschaften (Dr. rer. nat.)
genehmigte Dissertation von Qiang Gao aus Liaoning, China
Tag der Einreichung: March 2, 2020, Tag der Prüfung: June 2, 2020
Darmstadt — D 17

1. Gutachten: Hongbin Zhang
2. Gutachten: Yuriy Mokrousov

TECHNISCHE
UNIVERSITÄT
DARMSTADT

Fachbereich 11-Material-und Geowissenschaften
TMM-Theorie magnetischer Materialien

High-throughput screening of multifunctional magnetic materials
Hochdurchsatz-Screening multifunktionaler magnetischer Materialien

Genehmigte Dissertation von Qiang Gao aus Liaoning, China

1. Gutachten: Hongbin Zhang
2. Gutachten: Yuriy Mokrousov

Tag der Einreichung: March 2, 2020
Tag der Prüfung: June 2, 2020

Darmstadt — D 17

Bitte zitieren Sie dieses Dokument als:
URN: urn:nbn:de:tuda-tuprints-141943
URL: https://tuprints.ulb.tu-darmstadt.de/id/eprint/14194

Erklärung zur Dissertation

Hiermit versichere ich, die vorliegende Dissertation ohne Hilfe Dritter nur mit den angegebenen Quellen und Hilfsmitteln angefertigt zu haben. Alle Stellen, die aus Quellen entnommen wurden, sind als solche kenntlich gemacht. Diese Arbeit hat in gleicher oder ähnlicher Form noch keiner Prüfungsbehörde vorgelegen.

Darmstadt, den November 15, 2020

(Q. Gao)

There are no thousand miles to go without cumulative steps.

Xun Kuang

Contents

Acknowledgements

I would like to express my deep gratitude to Prof. Hongbin Zhang for giving me the possibility to work within the group Theory of Magnetic Materials. I would like to offer my special thanks to Prof. Yuriy Mokrousov for the spontaneous willingness to serve as Co-referee and for the insightful suggestions. I would also like to extend my thank Prof. Karsten Albe and Prof. Lambert Alff to be my auditors. I would also thanks to Prof. Karsten Albe for the revision of my research proposal which was used for the application of the scholarship from Chinese Scholarship Council (CSC). I like to thank Prof. Karsten Albe and Prof. Lambert Alff for their nice lectures which give me much help in material science. I would also like to thank Prof. Oliver Gutfleisch for insightful discussions. Special thanks to Dr. Ingo Opahle for his kind help to me in both science and life.

Special thanks to Ms. Maria Walker, the administrator of our group, for her kind help in everyday. I would also thank the meaningful discussions and support from colleagues during my PhD study. They are Dr. Jürgen Weischenberg, Dr. Zeying Zhang, Prof. Xinru Li, Dr. Tingting Lin, Prof. Lei Xu, Nuno Miguel Fortunato dos Santos, Ilias Samathrakis, Harish Kumar Singh, Niloofar Hadaeghi, Teng Long, Chen Shen, Yi Xiao, Yixuan Zhang, Mian Dai, Yaqian Guo, Ling Fan. I would also thank many friends, such as Shuangcheng Li, Prof. Lei Li, Xiaoxiong Liu, Prof. Min Yi, Dr. Yanyan Shao, Dr. Yangbin Ma, Dr. Shuai Wang, Dr. Ying Zhao, Qihua Gong, Yao Liu, Yang Bai, Ziqi Zhou, Yangyiwei Yang, Dr. Zhen Sun and so on.

I would like to acknowledge the financial support from Chinese Scholarship Council (CSC) and the LOEWE project FLAME funded by the Ministry of Higher Education, Research, and the Arts (HMWK) of the Hessen state. I gratefully acknowledge computational time on the Lichtenberg High Performance Supercomputer.

Finally, I would thank the support from my parents.

Abstract

Magnetic materials are of great importance for energy harvesting and conversion and information technologies, as exemplified by permanent magnets and spintronic applications, respectively. There is a strong impetus to develop new high performance magnets to satisfy the increasing requirements of such technologies. On the other hand, high-throughput (HTP) screening based on density functional theory calculations provides an efficiency way to predict novel materials with target properties. Therefore, it is meaningful to accelerate the development of functional magnetic materials by using the high-throughput screening method. In this thesis, we endeavored to perform HTP engineering of both 3D and 2D magnetic materials, focusing on spintronic and permanent magnet applications.

For the spintronic applications, based on HTP density functional theory calculations, we performed a systematic screening by examining peculiar electronic structure. For instance, we have done HTP screening for spin-gapless semiconductors (SGSs) in quaternary Heusler alloys XX′YZ. Following an empirical rule, we focused on compounds with 21, 26, or 28 valence electrons, resulting in 12000 possible chemical compositions. After systematically evaluating the thermodynamic, mechanical, and dynamical stabilities, we have identified 70 so far unreported SGSs, confirmed by explicit electronic structure calculations with proper magnetic ground states, of which 17 candidates have a distance to the convex hull smaller than 0.10 eV/atom. It is demonstrated that all four types of SGSs can be realized, defined based on the spin characters of the touching bands around the Fermi energy. Particularly, it is found that the type-II SGSs exhibit promising transport properties for spintronic applications, such as large anisotropic magnetoresistance and anomalous Nernst effects driven by spin-orbit coupling.

On the other hand, as to 2D materials, we carried out a systematic HTP screening for in-plane ordered MXene (i-MXene), which can be obtained by etching the main group element (A) away from the recently synthesized in-plane ordered MAX (i-MAX) phase. Such 2D i-MXenes provide us a new playground for 2D magnetic materials. It is observed that the spin configurations, hence the magnetic anisotropy, can be tuned by strain. We found that five i-MXenes have a significantly large out-of-plane magnetic anisotropy energy (>0.5 meV/f.u.), and the four ferromagnetic candidates have high Curie temperature based on the 2D Ising model. Additionally, we found i-MXene can realize large Seebeck effect, antiferromagnetic topological insulator, and spin-gapless semiconductors, making them interesting for future studies.

In terms of designing permanent magnets, we carried out a systematic HTP screening for rare-earth free permanent magnets by incorporating light interstitials (H, B, C, N) into magnetic full Heusler alloys. We successfully identified 32 candidates with an out-of-plane magnetic anisotropy larger than 0.4 MJ/m^3 as well as 10 cases with large in-plane anisotropy. Detailed analysis reveals that the interstitials are very efficient in inducing global tetragonal distortions, whereas the local chemical bonding and changes in the crystalline environment result in significant enhancement of MAE. We strongly believe this provides an efficient way to tailor MAE, and such newly predicted permanent magnet candidates are promising gap magnets between rare earth based Sm-Co and Nd-Fe-B and the transition metal based AlNiCo and ferrite.

To summarise, in addition to screening over various types of functional magnetic materials, my work provides valuable solutions to the pending challenges of HTP design of magnetic materials. We have established automated workflows, which can be easily applied on the other magnetic

materials. This paves the way for further design of advanced magnetic materials with optimal performance.

Zusammenfassung

Magnetische Materialien sind von großer Bedeutung für Technologien zur Gewinnung und Umwandlung von Energie und Informationen. Es ist sehr dringlich, neue Hochleistungsmagneten zu entdecken, um die wachsenden Ansprüche neuer Technologien zu befriedigen. Andererseits ist Hochdurchsatz-Screening (High-Throughput-Screening, HT-Screening) ein hocheffizienter Weg, um neue Materialien mit besonderen Eigenschaften zu entwickeln. Unter diesem Gesichtspunkt ist es sinnvoll, den Prozess der Entdeckung neuer Materialien durch den Einsatz von High-Throughput-Screening Methoden zu beschleunigen. In dieser Doktorarbeit wurde ein High-Throughput-Screening für zwei- und dreidimensionale magnetische Materialien durchgeführt mit einem Fokus auf Spintronik- und Permanentmagnetanwendungen.

Für Spintronikanwendungen wurde ein systematisches Screening auf der Basis von Hochdurchsatz-Dichtefunktionaltheorieberechnungen in 2D und 3D Materialien durchgeführt. Erstens wurde ein HT Screening für Halbleiter mit verschwindender Bandlücke in einem Spinkanal (spin-gapless semiconductors, SGSs) in quaternären Heusler Verbindungen $X\,X'\,Y\,Z$ durchgeführt (X, X', und Y sind Übergangsmetallelemente außer Tc, und Z ist eines der Elemente B, Al, Ga, In, Si, Ge, Sn, Pb, P, As, Sb, and Bi). Einer empirischen Regel folgend, haben wir uns auf Verbindungen mit 21, 26, oder 28 Valenzelektronen konzentriert, mit 12.000 chemischen Zusammensetzungen. Nach systematischer Auswertung der thermodynamischen, mechanischen und dynamischen Stabilität haben wir 70 vorher nicht veröffentlichte SGSs identifiziert, bestätigt durch explizite Elektronenstrukturberechnungen mit dem richtigen magnetischen Grundzustand, von denen 17 Kandidaten einen Abstand zur konvexen Hülle von weniger als 0,10 eV/Atom haben. Es konnte gezeigt werden, dass alle vier SGSs-Typen realisiert werden können, definiert anhand des Spincharakters der sich berührenden Bänder an der Fermienergie. Typ-II SGSs zeigen vielversprechende Transporteigenschaften für Spintronikanwendungen. Der Einfluss von Spin-Bahn-Kopplung wurde untersucht, mit dem Ergebnis von großen anisotropen Magnetwiderständen und anormalen Nernst-Effekten.

Für 2D Materialien, im Geiste der aus der MAX Phase gewonnenen 2D MXene, haben wir eine systematische Hochdurchsatzuntersuchung von in der Ebene geordneten MXenen (i-MXene) durchgeführt, die leicht durch Wegätzen des Hauptgruppenelements A von den kürzlich synthesierten in der Ebene geordneten MAX (i-MAX) Phasen gewonnen werden können. Diese 2D i-MXene versorgen uns mit einer Spielwiese für 2D Materialien jenseits von Graphen, insbesondere für 2D Magnetenanwenwendungen. Es wurde beobachtet, dass die Spinkonfiguration und damit die magnetische Anisotropie durch Verzerrung verändert werden kann. Für fünf i-MXene haben wir eine beobachtbare (>0.5 meV/f.u.) uniaxiale magnetische Anisotropieenergie gefunden, und die vier ferromagnetischen Kandidaten haben eine signifikant hohe Curie-Temperatur basierend auf dem 2D Ising-Modell. Im Hinblick auf die Elektronenstruktur haben wir gefunden, dass in i-MXenen ein großer Seebeckeffekt, antiferromagnetische topologische Isolatoren und SGSs realisiert werden können.

Für Permanentmagnetanwendungen haben wir ein systematisches High-Throughput-Screening für seltenerdfreie Permanentmagneten durch Einbindung von leichten interstitiellen Atomen (H, B, C, N) in magnetische vollständige Heuslerverbindungen durchgeführt. Wir haben erfolgreich 32 Kandidaten mit uniaxialier magnetischer Anisotropie größer als 0.4 MJ/m^3 sowie 10 Fälle mit großer Anisotropie und in der Ebene-Magnetisierung gefunden. Detaillierte Analyse zeigt dass die interstitiellen Atome sehr effizient sind um tetragonale Verzerrungen zu bewirken, wohingegen

die lokale chemische Bindungund und änderungen in der kristallinen Umgebung eine deutliche Verbesserung der MAE bewirken. Wir sind überzeugt davon, dass dies ein effizienter und generischer Weg ist um die MAE maßzuschneidern, und dass solche neuen Permanentmagnetkandidaten die Lücke im Anwendungsspektrum zwischen den seltenerdbasierten Permanentmagneten Sm-Co und Nd-Fe-B und den übergangsmetallbasierten leistungsschwächeren AlNiCo- und Ferritmagneten füllen können.

Zusammenfassend lässt sich sagen, dass meine Arbeit neben dem Screening verschiedener Arten von funktionellen magnetischen Materialien hilfreiche Lösungen für die anstehenden Herausforderungen des HTP-Designs von magnetischen Materialien bietet. Wir haben automatisierte Arbeitsabläufe etabliert, die sich leicht auf die anderen magnetischen Materialien anwenden lassen. Dies ebnet den Weg für das weitere Design von fortschrittlichen Magnetmaterialien mit optimaler Leistung.

1 Introduction

Advanced materials play a vital role in the development and welfare of the human society [1]. Magnetic materials have been applied in the last thousands of years, and are essential for nowadays energy and information technologies. For instance, permanent magnets can be used to convert between mechanical and electrical energies, leading to applications in wind turbines and electric vehicles [2, 3]. Another subject of great interest is spintronics, where the spin degree of freedom of electrons is applied to store and transfer information, with many different types of magnetic materials engaged [2, 4, 5]. An emergent research field is two-dimensional (2D) magnetism, motivated by the discovery of 2D graphene [6], which exhibits many intriguing fundamental problems and is very promising to engineer miniaturised devices. Thus, it is of great impetus to develop mechanistic understanding of the existing magnetic materials and to design novel systems with optimal performance.

Particularly, spin-orbit coupling (SOC) couples the spin and orbital degrees of freedom of the electrons, which is a relativistic effect [4, 7], giving rise to many interesting magnetic properties for practical applications. For instance, when combined with time-reversal symmetry breaking (*i.e.*, magnetic ordering), SOC lowers the crystalline symmetry of the magnetic materials, resulting in anisotropic physical properties. A well known example is the magnetocrystalline anisotropy energy (MAE), which determines the spontaneous magnetization direction and is a critical factor for permanent magnets, magnetic storage, and 2D magnets [2, 3, 4, 8, 9]. Moreover, in terms of nonequilibirum properties, SOC acts as an artificial magnetic field in the reciprocal space, which sets the foundation for the second generation of spintronics, dubbed as spin-orbitronics. In contrast to the spin-dependent electric current studied in the first generation of spintronics, spin-orbitronics deals with the generation, manipulation, and detection of pure spin current to operate information [2, 5]. **Therefore, our goals in this thesis are to elucidate the role of SOC in various types of magnetic materials and to design functional magnetic materials via accurate density functional theory (DFT) calculations.**

On the other hand, previous materials design paradigms are mostly carried out based on the empirical understanding of the structural-property relationships and the try-and-error experiments. Such methods are resource and time costly. To accelerate the development and exploitation of novel materials, the US government launched the Materials Genome Initiative (MGI) in 2011, where integrated theoretical and experimental methodologies are proposed to engineer the materials properties. DFT calculations play an essential role in MGI, due to the predictive power enabled by the accurate evaluation of the electronic structure. Facilitated by the abundant computational resources available, high-throughput (HTP) DFT calculations become the working horse of materials design, where automated workflows are carried out on thousands of compounds in contrast to the traditional way of performing calculations on a few compounds. Nevertheless, due to the peculiarities of magnetic materials, there are many challenges to perform systematic HTP calculations to screen for magnetic materials with optimal performance. **We endeavor to explore several aspects of constructing HTP workflows applicable for designing magnetic materials, as discussed in detail later.**

In the follow-up sections of this chapter, we will review briefly the fundamental theory of permanent magnets, spintronics, and 2D magnets, aiming at elucidating the current challenges and justifying our theoretical and numerical solutions.

Permanent magnets are widely applied in modern advanced technologies, *e.g.*, electric vehicles, wind turbines, automatization, and robotics [3]. At present, the rare-earth based magnets Sm-Co and Nd-Fe-B are prototypical of high performance permanent magnets, with a substantial cost and performance gap to other classes of commercially available permanent magnets such as AlNiCo and ferrites [10]. In terms of the intrinsic properties of permanent magnets, the key quantities are Curie temperature ($\mathrm{T_C}$), saturation magnetization ($\mathrm{M_S}$), and MAE. The MAE (represented by the lowest-order uniaxial anisotropy K) sets an upper limit for the intrinsic coercivity $\frac{2K}{\mu_0 M_s}$, where the coercivity is given by

$$H_\alpha = \frac{\alpha 2K}{\mu_0 M_s} - \beta M_s. \tag{1.1}$$

Here, α and β are phenomenological parameters, corresponding to extrinsic mechanisms and the local demagnetization effect. The uniaxial anisotropy K reflects the crystal symmetry. Based on thermodynamics law, we use the Callen-Callen model [11] to get the anisotropy K behaviour at low temperature ($\mathrm{T}<<\mathrm{T_C}$)

$$\frac{K(T)}{K(0)} = [\frac{M_S(T)}{M_S(0)}]^n \tag{1.2}$$

where $n = (l+1)l/2$ is the exponent related to the crystal symmetry and l is the order of the spherical harmonic describing the angular dependence of the anisotropy.

It is noted that MAE originates from the relativistic effects, *i.e.*, the intrinsic MAE related to the crystal structure and chemical bonding environment resulting from the SOC, the shape anisotropy associated with the macroscopic shape caused by the dipole-dipole interaction. The SOC of a local atom breaks the continuous symmetry of the magnetization by developing anisotropic energy surface [11], making local contribution to the intrinsic MAE. The SOC term in the Hamiltonian is written as

$$H_{SOC} = -\frac{\boldsymbol{\nabla} V}{2m^2c^2}\mathbf{s}\cdot\mathbf{l} = \xi\mathbf{s}\cdot\mathbf{l}, \tag{1.3}$$

where $\boldsymbol{\nabla} V$, m and c denote the derivative of a scalar electrostatic potential, the mass of the electron and the speed of light, respectively, while $\mathbf{s}$ ($\mathbf{l}$) is the spin (orbital) angular momentum operator. ξ is the SOC strength, which can be estimated by $\xi = 0.4(\epsilon_{d_{5/2}} - \epsilon_{d_{3/2}})$ for the d orbitals and $\xi = 0.4(\epsilon_{f_{7/2}} - \epsilon_{f_{5/2}})$ for the f orbitals [12], respectively. The SOC strength is proportional to the derivative of the scalar potential. Therefore, the larger the atomic number is, the larger the magnitude of the SOC strength. Furthermore, the MAE can be understood in a way that SOC tries to recover the orbital moment which is quenched in solids, *i.e.*, it can be attributed to the interplay of exchange splitting, crystal fields, and SOC. Using the second order perturbation theory, a model was put forward by Bruno [13] that the intrinsic MAE is associated with the orbital moment as

$$MAE = -\sum_i \frac{\xi_i}{4\mu_B}\Delta l_i^{\downarrow} \tag{1.4}$$

where $\Delta l_i^{\downarrow}$ is the orbital moment difference between the hard and easy axes for atom i, and ξ_i is the SOC strength for atom i. The Bruno model is best applicable when the spin up channel is nearly fully occupied. A more general model is shown by van der Laan [14] by considering the spin-flip effect.

At present the mostly available high-performance permanents are the rare earth element based $4f$-$3d$ alloys Sm-Co and Nd-Fe-B [3]. Thus it is important to understand the magnetism of $4f$-$3d$ alloys for better applications. It is noted that the SOC strength and exchange splitting are atomic properties determined by the relativistic effects and the screened Coulomb interaction, whereas the crystal field depends on the hybridization of the d-orbitals of the magnetic transition metal (TM) atoms or the rare earth (RE) f-orbitals with the surrounding atoms, providing an effective way to tailor the MCA by engineering local crystalline environments. The most salient feature behind the $4f$-$3d$ magnetic compounds is the energy hierarchy, driven by the coupling between RE-$4f$ and TM-$3d$ sublattices [15], namely, the high T_C ensured by the strong TM-TM exchange coupling and MCA originated from the interplay of RE and TM sublattices. For instance, the Y-based compounds usually exhibit significant MCA, such as YCo_5 [16], whereas for the RE atoms with nonzero $4f$ moments, the MCA is significantly enhanced due to non-spherical nature of the RE-$4f$ charges caused by the crystal fields [17]. Moreover, the exchange coupling between RE-$4f$ and TM-$3d$ moments is activated via the RE-$5d$ orbitals, which enhances the MCA by entangling the RE and TM sublattices. On the other hand, the intra-atomic $4f$-$5d$ coupling on the RE sites is strongly ferromagnetic, while the interatomic $3d$-$5d$ between TM and RE atoms is antiferromagnetic (AFM). This leads to the AFM coupling between the spin moments of the TM-$3d$ and RE-$4f$ moments, as observed in most $4f$-$3d$ magnets. Such multiple sublattice couplings for TM-Re materials give rise to two challenges for the understanding of the magnetism in theory, *i.e.* it is hard to treat the strongly correlated $4f$-electrons and the multiple sublattice couplings have been utilized to construct atomistic spin models to understand the finite temperature magnetism of $4f$-$3d$ materials. Therefore, to understand the $4f$-$3d$ magnetic materials, it is necessary to treat the correlated $4f$-electrons with SOC and spin fluctuations consistently, where the most accurate method probably is DFT+DMFT with the continuous time quantum Monte Carlo based impurity solver [18]. For instance, based on the implemented method to evaluate the free energy at a finite temperature [19], both the transversal and longitudinal magnetic fluctuations are accounted for in the DFT+DMFT methods [20], leading to a good estimation of the Curie temperature of Fe.

Turning towards applications, it is of great importance to develop novel permanent magnets to fill in the gap of MAE and magnetization between the high performance magnets (Sm-Co and Nd-Fe-B) and the widely used magnets (ferrite and alnico), ideally without critical elements such as rare-earth elements. Such permanents are classified as gap magnets [21]. In the past decades, several typical gap magnets have been designed. For instance, by alloying technology, we can achieve the Mn based gap magnets Mn-Al and Mn-Bi alloys [2, 22, 23, 24]. For τ-MnAl, it took about 20 years (from 1960 to 1980) to realize half value of the theoretical energy density due to the difficulty to achieve both the high purity and the high ordered micro magnetic structures [25]. At room temperature, the coercivity of α-MnBi is as high as 2 kOe [26, 27], but with low purity due to phase competition [23]. On the other hand, the most efficient way to achieve high performance α-MnBi with high purity is to fabricate thin films [28, 29]. Another gap magnet is the $L1_0$ FeNi alloys, of which the MAE is as large as 1.3 MJ/m^3, arising from the tetragonal distortion and chemical bonding [30]. However, it is difficult to synthesize highly ordered $L1_0$ FeNi. Several techniques have been developed to obtain pure ordered $L1_0$ FeNi, *e.g.* cyclicoxi-reduction process at low temperature, inducing nitride interstitials into $A1$-FeNi, and inducing tetragonal distortion by interface associated strain [31, 32]. FeCo, FeMn and MnNi magnets can also be grown by interface engineering with comparable performance as $L1_0$ FeNi [33, 34, 31]. Lastly, the Co-rich intermetallic compounds, *e.g.* $HfCo_7$ and Zr_2Co_{11}, are also high performance permanent magnets with large magneto-crystalline anisotropy constant K_1, large saturation magnetization M_s, and high Curie temperature T_C [35, 36, 37, 38, 39, 40].

In practice, substitution doping, imposed strain and interstitial doping are used to design new gap magnets. For instance, with proper substitution doping of Co, the MAE of tetragonally distoted Fe can be enhanced with a magnitude of meV [33] However, such a tetragonal distortion is not stable if the film is thicker than 2 nm [41, 42, 43]. Further theoretical and experimental studies demonstrate C and B interstitial doping can stabilize the tetragonal distortion of α-Fe with Co substitution doping [44, 45]. Similarly, the MAE of Heusler alloys (Ni-Mn-Sn, Ni-Mn-Sb and Ni-Mn-In) can be enhanced by incorporating with interstitial C and B [46, 47, 48, 49].

In our work, we have done a systematic high-throughput screening on the effect of light interstitial C, N, B, and H in the cubic magnetic full Heusler alloys aiming at designing new gap magnets [50]. We found the enhanced MAE of Heuslers with interstitial originates from not only the induced tetragonal distortion but also the chemical environment surrounding the interstitial atoms. Our research demonstrates that Heusler alloys with interstitial atoms can fill in the gap between the present high and low performance permanent magnets, awaiting for further experimental study.

1.2 Spintronics

In the last century, one of the most important technology achievements is the semiconductor silicon chip based electronics. The operation for computation in electronics is realized by using the complementary metal-oxide semiconductor (CMOS) logic, where binary data is stored as charge switching of "on" and "off" in the field-effect transistors (FETs). In traditional electronics, the freedom of charge is applied to manipulate, store and transfer information. However, the size of the electronic transistors cannot be reduced illimitably because the scorching heat of current will decrease the efficiency of the device and the quantum effects play a critical role at nanoscale size. On the other hand, the electron has the degree of freedom of not only charge but also spin. Thus, scientists are trying to take advantage of the spin degree of freedom of electrons to realize devices with high efficiency, small size and low (or zero) current, leading to spintronics based information technology [2].

The first generation spintronics is based on ferromagnetic materials, beginning with the discovery of giant magnetoresistance (GMR) effect [51]. In 1986, Peter Grünberg [51] observed the switching between antiferromagnetic and ferromagnetic coupling in multilayer Fe/Cr by applying an external magnetic field, leading to further discoveries of GMR in multilayers Fe/Cr [52] and Fe/Cr/Fe [53]. Later on, such GMR effect is explained by the scattering between layers, the scattering originated from the roughness of layers and the orientation of the magnetization of the magnetic layers [54, 55]. Immediately after the discovery of GMR, Parkin *et al.* found the oscillatory behaviour of the GMR by manipulating the thickness of the nonmagnetic layers [56]. Furthermore, the GMR effect was also discovered in multi-layers composed of magnetic layers with different coercivities [57]. Following the discovery of GMR, researchers also developed the tunnel magnetoresistance (TMR) and spin-transfer torque (STT) technologies. In TMR, the resistance of the magnetic tunnel junction (MTJ) is manipulated by tilting the spin configuration of the electrode. The Fe/MgO/Fe based MTJ can even realize the TMR ratio as large as 600% [58]. The GMR and TMR now are applied mostly as read heads for the hard disk drives,

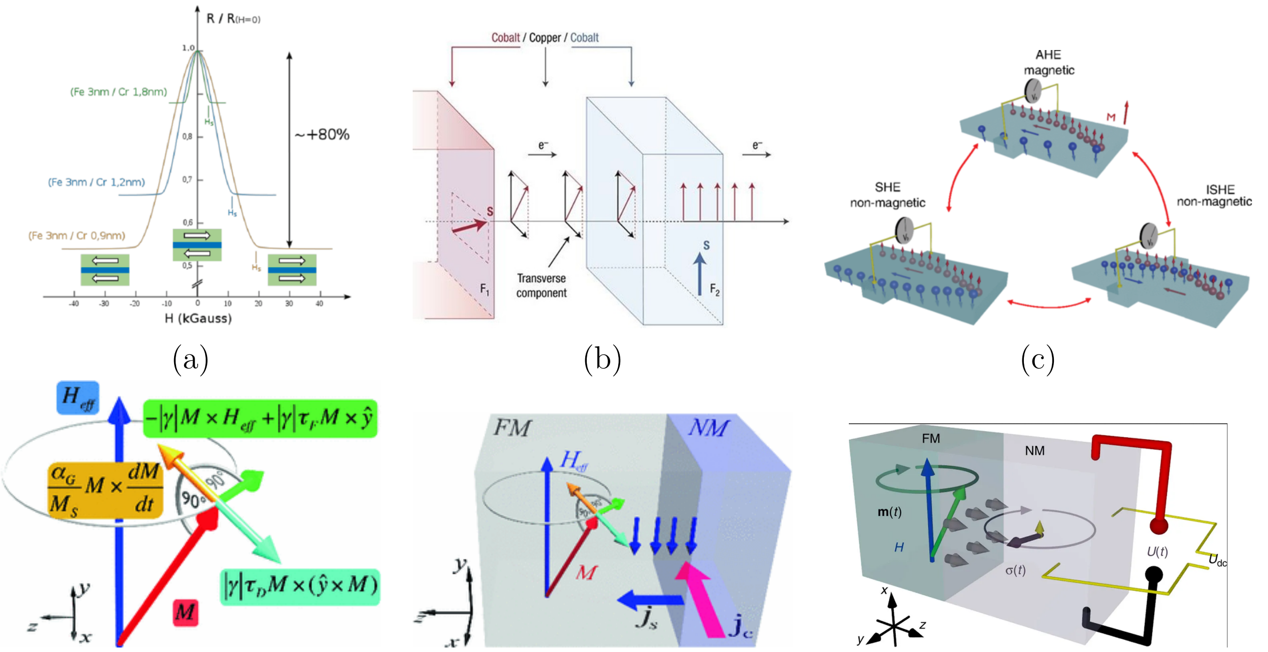

(a) (b) (c)

(d) (e) (f)

Figure 1: (a)GMR effect at 4.2 K in FeCr(001) multi-layers. In the parallel spin configuration, the electrons can go easily through both magnetic layers, leading to small resistance. In the anti-parallel spin configuration, the electrons of each channel are slowed down, leading to high resistance. (b) Sketch of the spin transfer torque. (c) The illustration of the spin-dependent Hall effects, *i.e.* anomalous Hall effect (AHE), spin Hall effect (SHE) and inverse spin Hall effect (ISHE). (d) Schematic of the torques acting on the magnetization. (e) Sketch of SOT in ferromagnetic (FM)/normal metal (NM) bilayer. (f) Sketch for the spin pumping and ISHE voltage signal.

improving the information storage performance dramatically. TMR is also applied in the magnetic random-access memories (MRAM) [2]. However such TMR-based MRAM is expensive in power consumption. This leads to the new concept of STT, lowering the energy consumption by transferring the spin angular momentum of the magnetic materials through a spin polarized current [59, 60]. Injecting into a ferromagnet, the spin polarized current will transfer its transverse component, creating a torque on the magnetization or a steady-state gyration regimethe, leading to spin-transfer oscillator [61]. STT can also realize racetrack memory [62] and nonvolatile random-access memory [63].

In spintronics, the essential target is to make use of the spin degree of freedom of electrons. In the above, the ferromagnetic materials are applied to achieve that purpose. However, the stray field caused by the domain ferromagnetism will impede the applications. To solve this problem, in the second generation spintronics, SOC plays an essential role, leading to spin-orbitronics [64]. In spin-orbitronics, we work with the spin current instead of spin-polarized current. Correspondingly, the conversion and store of information are realized by the generation, manipulation and detection of the spin current (the flow of spin angular momentum). Spin Hall effect (SHE) and spin-orbit torque (SOT) are two major subjects for spin-orbitronics.

The heavy metals have strong SOC thus large SHE, which is an efficient method to convert charge current into spin current and vice-versa. SHE has been observed in paramagnetic Ta and Pt, ferromagnetic metal FePt, antiferromagnetic MnPt, $Mn_{80}Ir_{20}$ and Mn_3Sn, semiconductor GaAs, and topological materials Bi_2Se_3 and TaAs [65, 66, 67, 68, 69, 70, 71, 72, 73]. In the opposite process, namely inverse spin Hall effect (ISHE), a pure spin current gets through the materials generating the pure charge current, which can be used for the detection of spin current. It is noted that both SHE and ISHE are characterised by the spin Hall angle θ, defined by the ratio between the transverse spin current component density and the longitudinal charge current density.

SOT is another popular spin-orbitronic technology, dealing with the interaction of the magnetization and spin current. Such SOT can be applied in magnetization switching and spin-orbit pumping. The theory begins with the Landau-Lifshitz-Gilbert (LLG) equation [74]

$$\frac{d\mathbf{m}}{dt} = \underbrace{-\gamma \mathbf{m} \times \mathbf{B}}_{\text{precession}} \quad + \quad \underbrace{\alpha \mathbf{m} \times \frac{d\mathbf{m}}{dt}}_{\text{relaxation}} \quad + \quad \underbrace{\frac{\gamma}{M_s}\mathbf{T}}_{\text{torque}}, \tag{1.5}$$

where γ, α, and M_S denote the gyromagnetic ratio, the Gilbert damping parameter, and the saturation magnetization, respectively, while $\mathbf{m}$, $\mathbf{B}$ and $\mathbf{T}$ mark the magnetization unit vector, the effective field and the total torque, respectively. Perpendicular to $\mathbf{m}$, the torque is expressed by [75]

$$\mathbf{T} = \underbrace{\tau_{FL} \mathbf{m} \times \epsilon}_{\text{FL: field-like}} \quad + \quad \underbrace{\tau_{DL} \mathbf{m} \times (\mathbf{m} \times \epsilon)}_{\text{DL: damping-like}} \tag{1.6}$$

where ϵ is the unit torque vector. The field- and damping-like terms act on the magnetization like the precession and relaxation terms in the LLG equation (1.5). To generate finite SOT, we can use either SHE or Edelstein effect to create an effective non-equilibrium spin polarization [76]. In view of symmetry, for SOT non-centrosymmetric symmetry is a necessary condition, which can be realized in NM/FM hetrostructures, *e.g.* Ta/CoFeB and Pt/Co [77, 78, 79]. On the other hand, Edelstein effect requires Rashba splitting, which can also be applied for spin-charge conversion hence SOT, as has been observed in $LaAlO_3/SrTiO_3$, Ag/Bi, and $Cu/Bi_2O_3/NiFe$ [80, 81, 82]. As SOT can be summarized as torque induced by spin current, the Onsager reciprocal effect is spin pumping. Usually we can realize spin pumping through pure spin current by means of generating non-equilibrium magnetization dynamics using the ferromagnetic resonance (FMR). Then the pure spin current can be injected into the conducted NM layers with zero charge under zero bias voltage, as has been observed in bilayers NiFe/Pt and Au (or Mo)/GaAs [83, 84]. Furthermore, the spin pumping can generate a time dependent spin polarized current including both *dc*- and *ac*-components. It is found that the *ac*-component is at least one order of magnitude than the *dc*-component ()NiFe|Pt [85, 86], leading to *ac* spintronics applications.

Recent studies [87, 75, 88] have shown antiferromagnets (AFM) can also be applied in spin-orbitronics. For instance, both theoretical and experimental studies have shown that AFM MnX (X= Fe, Pd, Ir, and Pt) also have large SHE, even stronger than nonmagnetic heavy metals [89, 90]. Further, SOT switching has been observed in the FM/AFM junctions, *e.g.*, IrMn|CoFeB [91], IrMn|NiFe [92], MnPt|Coe [93], and Mn_3Ir|NiFe [94]. Such SOT switching has the potential for future neuromorphic computing.

Lastly, the skyrmion, which is a topological swirling configuration of spins, is also a way to create spin polarized current by SOC, of which the magnetization rotates continuously without changing the chirality at the edge. Here the chirality is given by the Dzyaloshinskii-Moriya interaction (DMI) [95, 96]

$$H_{DMI} = (\mathbf{S}_1 \times \mathbf{S}_2) \cdot \mathbf{d}_{12} \tag{1.7}$$

where $\mathbf{S}_1$ and $\mathbf{S}_2$ are the neighbor spins and $\mathbf{d}_{12}$ is the DMI vector, where DMI is a chirality interaction lowering or increasing the energy for the spin rotation. Such DMI is induced by SOC in materials without inversion symmetry, where the crystal is non-centrosymmetric when the inversion symmetry is broken by disorder or interface of materials. The skyrmion can be applied in information storage and processing due to their ultra-small and nonvolatile quasi-particle features [97, 98].

Overall, spintronics is attracting more and more interest due to the potential for future high-performance information technologies. In our work, we focus on ferromagnetic materials. In ferromagnetic spintronics, the injection of spin polarized electrons from a ferromagnetic electrode into a semiconductor will realize devices with non-volatile, reconfigurable logic functions and ultralow power consumption, which is called spin field effect transistors (spin-FETs). Such spin-FET devices are required in future quantum computing [99]. One intuitive idea to manipulate the injected spin polarized current is to obtain additional functionality in a semiconductor, which has been realized in the diluted magnetic semiconductor (DMS), *e.g.*, the magnetic transition metal (Fe, Cr, Mn, Ni, Co, and Gd) doped III-V semiconductor [100]. Moreover, the spin polarized current source can be generated by the half metallic materials with 100% spin polarized current, of which the electronic structures have a finite gap around Fermi level in one spin channel and finite states around Fermi level in the opposite spin channel [99].

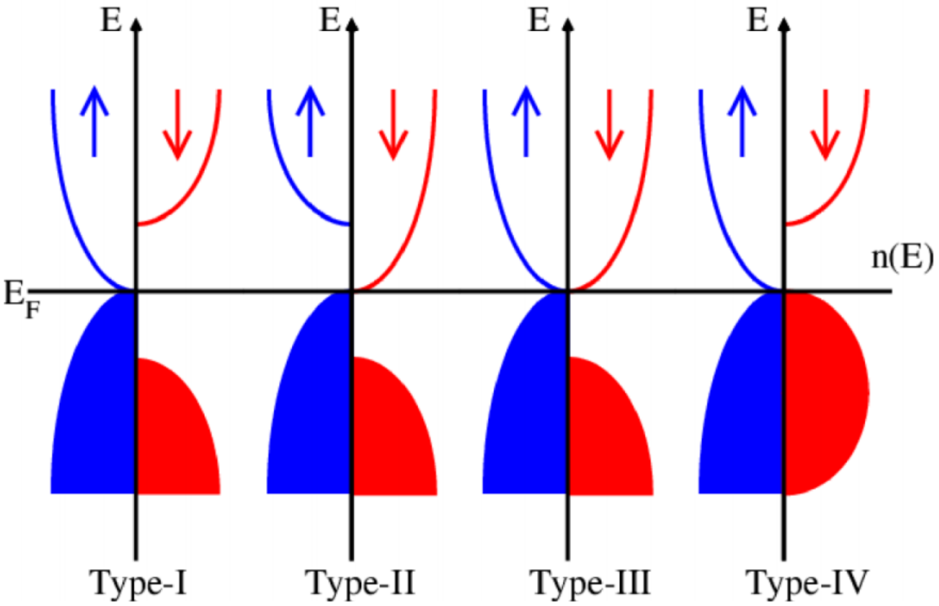

Figure 2: Sketches of the density of states for the four types of SGSs, defined based on the touching schemes of the majority (marked in blue) and minority (marked in red) bands.

One interesting question is whether we can combine the features of both the diluted magnetic semiconductor and half-metal, where the so-called spin-gapless semiconductors (SGSs) concept was introduced in Co-doped $PbPdO_2$ in 2008 [101]. In a half-metal, if in the majority spin channel the density of states is nearly zero forming the gapless state, while there is still a finite gap in the minority spin channel, then such materials can be classified as SGSs. In general, the main characteristic feature of SGSs is that the valence band maximum (VBM) and conduction band minimum (CBM) touch each other directly or indirectly in the spin polarized systems, corresponding to the direct and indirect SGSs. Following Ref. [101], four types of SGSs can be defined based on the spin characters of the touching bands around the Fermi level as sketched in Fig. 2. In type-I SGSs, the VBM and CBM are in the same spin channel while there is a gap in the opposite spin channel, which is the conventional SGS. Contrary to type-I, the VBM and CBM can hold the opposite spin characters, hereafter dubbed type-II SGSs. Moreover, if the VBM (CBM) is of one spin character while the CBMs (VBMs) originate from both spin channels, type-III (type-IV) SGSs will be defined. Due to the special electronic structures, the superior performance of SGSs in comparison to the usual half-metals is that 100% spin polarized carriers can be excited from the valence to conduction bands with no energy cost, leading to new functionalities of spintronics devices and potential applications in logic gates. For instance, the spin-polarized transport properties of SGSs can be tuned by shifting the Fermi energy with finite gate voltages [101, 102], which is promising for future spintronic applications. Heusler alloys have been regarded as the most promising playground for SGGs research since the first above room temperature SGS is realized in the inverse Heusler Mn_2CoAl [102]. During the exploration of SGSs in Heusler alloys, an empirical rule is discovered, that is, only in cases of the valence electrons with a number of 18, 21, 24 or 28 the Heusler alloys are more likely to realize SGS phase [103, 104, 105]. Furthermore, for direct gapped SGSs, it is of great interest to study spin-orbit coupling effect. If the direct gap is opened, then such SGS is a promising candidate for quantum anomalous Hall effect, while there should be some underlying symmetries protected by the degeneracy if the gap is not opened. So, based on the empirical valence electron number rule, we have done a systematic screening for SGSs in Heusler alloys, especially focusing on the mechanism behind forming a SGS and SOC effect on the transport properties [106]. We found the transport properties of type-II SGS are particularly interesting as the sign of anomalous Hall conductivity (AHC) can be tuned by just applying a slight chemical potential though the AHC is zero at Fermi level, thus leading to a large anomalous Nernst effect near Fermi level. Such results reveal that type-II SGSs are likely promising candidates for engineering spintronic field-effect transistors.

1.3 2D magnets

Table 1: Summary of experimental realized 2D magnets. M_{ord}, T_C, T_N, and P.N. denote the magnetic order, Curie temperature, Néel temperature, and physical nature, respectively. J_{inter} J_{intra} are the interlayer and intralayer exchange parameters. $|M_{at}|$ stands for the magnetic moment per magnetic atom.

Compound	M_{ord}	T_C/ T_N (K)	J_{inter} J_{intra} (meV/at.)	MAE (meV)	$\lvert M_{at}\rvert$ (μB/at.)	P.N.
CrI_3 [107]	FM	61	11.64 2.37	0.85	3.0	Insulating
$Cr_2Ge_2Te_6$ [108]	FM	68	6.70 0.47	0.66	3.4	Insulating
$Fe_3Ge_2Te_2$ [107]	FM	205	23.40 3.71	2.00	1.4	Metallic
$MnPS_3$ [109]	Néel-AFM	78	-0.77 -0.07	–	2.4	Insulating
$FePS_3$ [110]	Néel-AFM	104	- -	–	2.4	Insulating
$NiPS_3$ [111]	Néel-AFM	155	- -	–	2.4	Insulating

Pioneered by the discovery of graphene [112, 113, 114, 115], two dimensional (2D) materials have been attracting intensive interest to researchers, due to a vast spectrum of functionalities such as in mechanical, electrical, optoelectronic, superconducting, and topological [113, 114] applications and thus immense potential in engineering miniaturized devices. Particularly, 2D materials can realize van der Waals (vdW) heterostructures without enforcing the lattice matching [116, 117, 118], leading to a various combinations of materials and thus further opportunities to tailor properties [118]. However, 2D magnets remain to be a challenge in experiments. Until very recently, the long range magnetic orderings have been observed in monolayers $\mathrm{CrI_3}$ [119], $\mathrm{Cr_2Ge_2Te_6}$ [108] and $\mathrm{Fe_3GeTe_2}$ [120, 121]. Furthermore, 2D magnets can form van der Waals (vdW) heterostructures with the recent synthesized 2D ferroelectric $\mathrm{In_2Se_3}$ [122], to realize multiferroics and hence to pave the way to engineer novel spintronic devices. Overall, 2D magnetism is a challenging field, awaiting for extensive research.

From the theoretical perspective, 2D magnetism can be explained by a generalized Heisenberg spin Hamiltonian [123]:

$$H = -\frac{1}{2}\sum_{i,j}(J_{ij}\mathbf{S}_i \cdot \mathbf{S}_j + \xi \mathbf{S}_i^z \cdot \mathbf{S}_j^z) - \sum_i \Lambda(\mathbf{S}_i^z)^2, \tag{1.8}$$

where J_{ij} denotes the exchange coupling between spin site i (with spin operator $\mathbf{S}_i$) and j (with spin operator $\mathbf{S}_j$), while Λ and ξ are the “onsite” and “intersite” magnetic anisotropies. Here, the isotropic Heisenberg model corresponds to the weak magnetic anisotropy case ($\Lambda \approx 0$ and $\xi \approx 0$), while Ising model and XY model are valid for the strong magnetic anisotropy case. In fact, the 2D magnetism is significantly different from 3D magnetism due to the dimension crossover. According to the Mermin-Wagner theorem [8], the long-range ordering is strongly suppressed at finite temperature for systems with short-range interactions of continuous symmetry in reduced dimensions, due to the divergent thermal fluctuations. Nevertheless, Onsager proved that the 2D magnets can be protected by a gap in the spin-wave spectra originated from a strong magnetic anisotropy [9]. Moreover, if the rotational invariance of spins is broken by a dipolar interaction, single-ion anisotropy, anisotropic exchange interactions, or external magnetic fields, the 2D magnetism can be retained at finite temperature.

Coming to materials, perhaps the family of transition metal thiophosphates $\mathrm{MPS_3}$ (M = Mn, Fe, and Ni) is the best representative for magnetic phases in 2D magnets, *i.e.* the natures for few layer form $\mathrm{MPS_3}$ (M = Mn, Fe, and Ni) are 2D-Heisenberg, 2D-Ising and 2D XXZ models [124, 125]. For few layer systems $\mathrm{FePS_3}$ and $\mathrm{MnPS_3}$, the magnetic phase transition temperatures remain almost the same as the corresponding bulk compounds [111]. On the other hand, for $\mathrm{NiPS_3}$, the monolayer system is nonmagnetic while few-layer slab has a slightly reduced Néel temperature comparing to the bulk form [126]. Such special magnetic ordering behaviour can be attributed to the 2D-XXZ nature of the effective Hamiltonian [111]. A more interesting and complex ordering 2D monolayer magnet is the $\mathrm{CrI_3}$ with FM interlayer coupling [119], while the corresponding bulk form is AFM [127]. The $\mathrm{Cr^{3+}}$ ions in the octahedral environment have t_{2g} orbitals occupied by the $3\mathrm{d}^3$ electron configuration, leading to quenched SOC effect and hence making negligible contribution to the MAE [109]. Moreover, the large out-of-plane MAE originates from the strong intersite SOC of I atoms [109]. Perhaps the most surprising observation is the bilayer of $\mathrm{CrI_3}$ becomes interlayer AFM coupling again [128] with a reduced Néel temperature of 46 K comparing to the bulk value of 61 K. Such magnetic order transition FM→AFM between monolayer and bilayer can be explained by the stacking fault of bilayer based on DFT calculations, namely the rhombohedral (monoclinic) stacking favors FM (AFM) interlayer exchange [129, 130]. Thus, in 2D magnets, an intriguing question to explore is the dimensional crossover, *i.e.*, how the magnetic ordering changes few-layer and monolayer cases in comparison to the bulk phases.

Interestingly, the magnetism of 2D magnets can be manipulated by various methods, such as electric control, vdW hetrostructures with 2D ferroelectric materials and mechanical forces (strain or pressure). The electric control, through either an electric field or electrostatic doping, changes the electron population, orbital occupation, and electrochemical reaction, leading to tunability of the exchange coupling and magnetic anisotropy and thus the magnetism. Under a bias electric field, the spin configuration for the bilayer CrI_3 can be switched between the FM and AFM interlayer coupling [128, 131], where the gating effect can be further enhanced by the sandwich of dielectric BN layers/electrode/CrI_3 layers [132]. Surprisingly, ionic gating on monolayer Fe_3GeTe_2 can even enhance the Curie temperature to the room temperature due to that the MAE is sensitive to the bias voltage [133]. The electrostatic field via electron-and hole-doping can switch the spin-configuration of $MnPSe_3$ between AFM and FM [134], providing a new technology for magnetization switching for logics and memories. Magnetic materials critically hinge on the material structure where the magnetism can be controlled by pressure or strain, leading to spin-lattice coupling and magnetostriction effect. Under pressure of 1 GPa, the magnetization of $Cr_3Ge_2Te_6$ can be switched from out-of-plane to in-plane [135]. Due to lattice mismatch, the strain has been applied to tailor the properties of vdW materials. For instance, it is demonstrated that 2% biaxial compressive strain leads to a magnetic state transition from AFM to FM for $FePS_3$ monolayers [134], and 1.8% tensile strain changes the FM ground state into AFM for CrI_3 monolayers [136]. Moreover, strain can also induce significant modification of the MAE, *e.g.*, 4% tensile strain results in a 73% increase of MAE for Fe_3GeTe_2 with a monotonous dependence in ±4% range [121]. On the other hand, the ferroelectric vdW materials are sensitive to strain as well [137]. Therefore, it is fascinating to investigate the multiferroic vdW heterostructures compositing of 2D magnetic and ferro-/piezo-electric materials, where the effective interlayer coupling originated from charge, lattice, and magnetic degrees of freedom can be tailored by strain and external electric fields. For instance, theoretical research found that the vdW heterostructure $Cr_2Ge_2Te_6/In_2Se_3$ can realize mutiferroic duality, namely switching between FM and magnetic semiconductor states [116]. More interestingly, DFT calculations reveal that the valence state of Fe and the spin configurations can be tuned by switching the polarisation direction in vdW hetrostructure FeI_2/In_2Se_3 [138].

Overall, 2D magnet is an interesting field with rich physics and interesting applications, waiting for further exploration. In the past decade, the MAX phases with a chemical formula of $M_{n+1}AX_n$ (M: early transition metal; A: main group element; X: C or N; n: integer up to 6), provide a good playground for 2D materials beyond graphene since the corresponding 2D nanosheets $M_{n+1}X_n$ can be obtained by etching the A elements away from the parent MAX compounds [139]. Quite a few 2D MXenes, *e.g.*, Sc_2C, V_2C, Mo_2C, Nb_2C, Ta_2C, Ti_2C, Zr_2C, Hf_2C, Ti_2N, Zr_2N, and Hf_2N, have been experimentally synthesized [140]. Gao *et al.* predicted that the MXenes Ti_2C and Ti_2N are nearly half metals (the magnetism is not very stable as the exchange splitting is rather weak), which can be further tuned into SGSs under biaxial strain [141]. It is also found that Mn_2N with functional groups O, OH and F can also be half-metals [142]. It is a pity there is still no magnetic MXene reported in experiments due to the fact that it is difficult to obtain the MAX compound with Fe, Co and Ni [143, 144]. Furthermore, the in-plane ordered MAX (i-MAX) compounds with a formula of $(M_{2/3}M'_{1/3})_2AX$ have been synthesized by substituting 1/3 transition metal or rare earth element M' for M in M_2AX compounds [145, 146], which may provide us new opportunities for realizing intrinsic 2D magnetic in-plane ordered MXene (i-MXene) $(\mathrm{M}_{2/3}\mathrm{M}'_{1/3})_2\mathrm{X}$ as there is the possibility to etch the A element away from the i-MAX $(\mathrm{M}_{2/3}\mathrm{M}'_{1/3})_2\mathrm{AX}$ compounds with magnetic doped M' atoms. Based on this, we have done a systematic high-throughput screening for i-MXene $(\mathrm{M}_{2/3}\mathrm{M}'_{1/3})_2\mathrm{X}$, especially focusing on the case where M' is magnetic [147]. We found the intrinsic spontaneous magnetism can be induced in i-MXenes with remarkably high Curie temperature evaluated using 2D Ising model. In terms of electronic structure, the magnetic i-MXenes can host fascinating transport properties, *e.g.*, antiferromagnetic topological insulators and spin-gapless semiconductors.

In the last century, one of the greatest scientific milestones is the development and application of quantum mechanics, which opens the door for fundamental understanding on the atomic and subatomic physics. Correspondingly, in order to perform effective calculations on the solid state properties, density functional theory (DFT) has been formulated, where the many-body interacting systems are mapped onto noninteracting homogeneous systems via the electron density, leading to an accurate description of the electronic structure of the ground state. This offers a significant reduction of the numerical efforts to solve the many-body problem in comparison with the wave-function based methods. DFT is constructed based on two fundamental theorems, *i.e.*, the Hohenberg-Kohn [148] and Kohn-Sham [149] theorems, resulting in an effective single particle approximation where the exchange-correlation functional is subject to constant development up to today. From the applications point of view, DFT has been used to evaluate various physical properties of different classes of materials, providing a starting point for more accurate descriptions [150, 151]. In this chapter, we go through the fundamental aspects of DFT and briefly the construction of high-throughput (HTP) workflows.

2.1 Quantum Many Body Problem

The physical properties of a solid are directly determined by its electronic structure. The solid systems include quite a large amount of particles (in the order of magnitude of 10^{23}). In order to understand the solid systems, we have to solve the quantum many body problems. However, it is impossible to get the analytical solutions. So we have to make some proper approximations. Ignoring the relativistic effects, the Hamiltonian of a solid with N electrons and M nuclei is written as

$$\begin{aligned}\hat{H} &= \hat{T}_e + \hat{V}_{e-e} + \hat{V}_{ext} + \hat{T}_n + \hat{V}_{n-n} \\ &= -\sum_{i=1}^{N} \frac{\hbar^2}{2m_e}\boldsymbol{\nabla}_i^2 + \frac{1}{2}\sum_{i\neq j}\frac{Z_i Z_j e^2}{4\pi\epsilon_0|\boldsymbol{r_i}-\boldsymbol{r_j}|} - \sum_{i}^{N}\sum_{I}^{M}\frac{Z_n e^2}{4\pi\epsilon_0|\boldsymbol{r_i}-\boldsymbol{R_I}|} - \sum_{I=1}^{M}\frac{\hbar^2}{2m_n}\boldsymbol{\nabla}_I^2 \\ &\quad + \frac{1}{2}\sum_{I\neq J}\frac{Z_I Z_J e^2}{4\pi\epsilon_0|\boldsymbol{R_i}-\boldsymbol{R_j}|}.\end{aligned} \tag{2.1}$$

where $\boldsymbol{r_i}$ and $\boldsymbol{R_I}$ denote the position for i-th electron and I-th nucleus. $\hat{T}_e$ and $\hat{T}_N$ denote the kinetic energies of electrons and nuclei. $\hat{V}_{e-e}$ ($\hat{V}_{n-n}$) denotes the Coulomb interaction potential of electrons (nuclei). $\hat{V}_{ext}$ is the potential acting on the electrons. The mass of a nucleus is much heavier (in the magnitude of 10^3) than that of an electron. Therefore an electron moves much faster than a nucleus. In this regard, Born-Oppenheimer (BO) approximation [152] points out that in a solid system the motion of the nuclei and electrons can be separated from each other. Based on BO approximation, the nuclei can be seen as fixed while the electrons are just moving in a static external potential V_{ext} formed by the nuclei. For the electrons, the Hamiltonian is

$$\hat{H} = \hat{T}_e + \hat{V}_{e-e} + \hat{V}_{ext} + \hat{V}_{n-n}. \tag{2.2}$$

The Schrödinger equation for electrons is expressed by

$$i\hbar\frac{\partial}{\partial t}\psi(\{\boldsymbol{r_i}\},t) = \hat{H}\psi(\{\boldsymbol{r_i}\},t) = E\psi(\{\boldsymbol{r_i}\},t). \tag{2.3}$$

where $\psi(\{\boldsymbol{r_i}\},t)$ is wavefunction for time independent potentials, factorized as

$$\psi(\{\boldsymbol{r_i}\},t) = \psi(\{\boldsymbol{r_i}\})e^{-i\frac{E}{\hbar}t}. \tag{2.4}$$

In principle, all physical properties of a solid system can be derived from wavefunctions. Especially, the total energy is written as the expectation value of the Hamiltonian

$$E = \langle H\rangle = \langle\psi|\,\hat{H}\,|\psi\rangle = T_e + V_{e-e} + V_{n-n} + V_{e-n} + \int d^3rV_{ext}(\boldsymbol{r})\rho(\boldsymbol{r}), \tag{2.5}$$

where the electron density $\rho(\boldsymbol{r})$ is expressed by the expectation value of the wavefunction

$$\rho(\boldsymbol{r}) = \langle\psi|\,\hat{\rho}(\boldsymbol{r})\,|\psi\rangle = N\int d^3r_1d^3r_2...d^3r_N|\psi(\boldsymbol{r}_1,\boldsymbol{r}_2,...,\boldsymbol{r}_N)|^2. \tag{2.6}$$

However, the Schrödinger equation Eq. (2.3) cannot be solved exactly since it is still a many body problem. So further approximations are still needed.

2.2 Density Functional Theory

DFT is a powerful method to solve the electronic structures of solid systems. It is a mean field theory for many body systems, leading to an effective single particle Schrödinger equation based on the variational principle. DFT has been successfully applied in the fields of condensed-matter physics, computational physics, and computational chemistry. The results have been proven to be well compared with that of experiments. Showing in Fig. (3) [151], the number of publications on the topic of DFT has been dramatically increased in the past 40 years.

Before the birth of DFT, dating back to 1920s, the Thomas-Fermi model has been proposed to solve the electronic structures of many body systems by using the density of electrons instead of wave function [153]. Based on the Thomas-Fermi model, the electrons are assumed to exist in the ideal homogeneous gas environment and the interactions of electrons are not considered. Then the quantum many body problem is simplified to the single particle problem, of which the solution can be obtained by solving Schrödinger equation. Furthermore, motivated by the spirit of Thomas-Fermi model, W. Kohn and P. Hohenberg constructed the basic theories of density functional theory [149, 148].

2.2.1 Hohenberg-Kohn Theorems

In the trailblazing paper [148], P. Hohenberg and W. Kohn pointed out that the total energy of the ground state for an inhomogeneous electron gas system could be obtained by introducing a universal functional of the electron density independent of the external potential. Such arguments are named as Hohenberg-Kohn (H-K) theorems:

1. The external potential $\nu(\boldsymbol{r})$ (hence the total energy) is uniquely determined by the functional of the charge density $\rho(\boldsymbol{r})$ at the ground state.

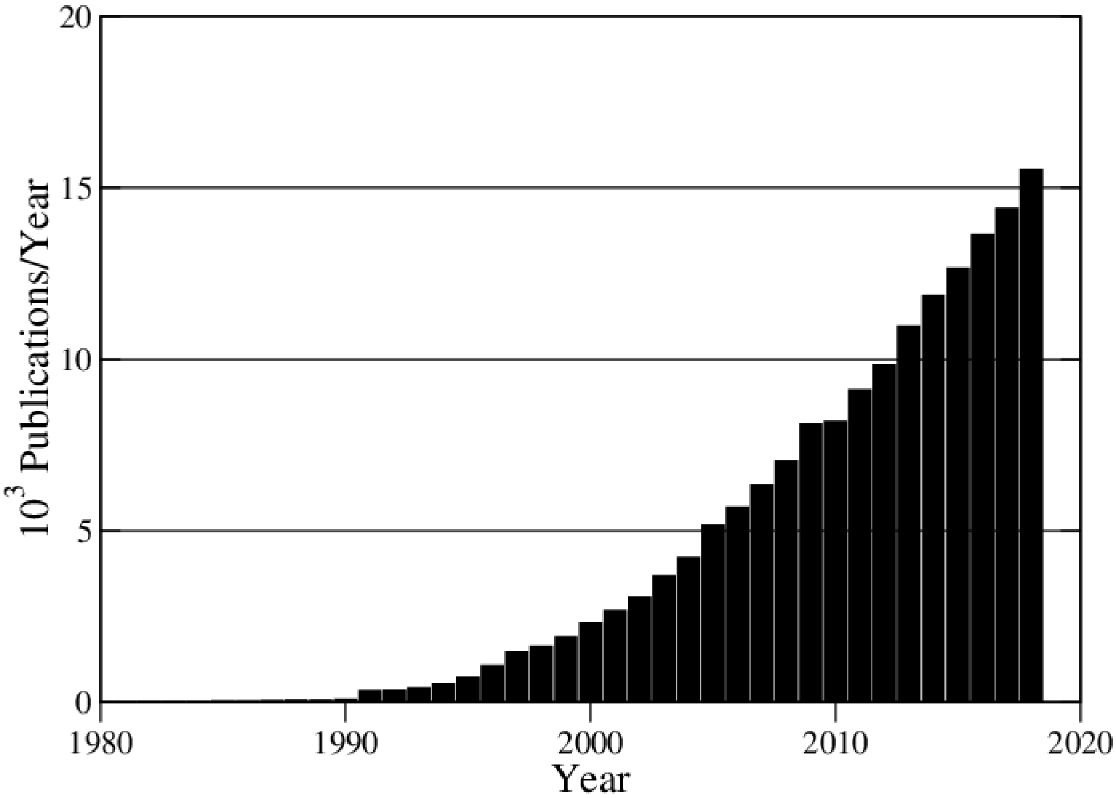

Figure 3: The number of publications per year (1980-2019) on topic of DFT. Data is from ISI web of science with the key word of "density functionary theory".

2. A universal functional for the total energy (E[$\rho(\boldsymbol{r})$]) of the ground state can be defined in terms of the charge density $\rho(\boldsymbol{r})$. The ground state is the global minimum of such functional.

The above theorems are the essential theories for DFT. In the following we will show the proof of both theorems.

Proof of the first H-K theorem: We are going to prove that the external potential $\nu(\boldsymbol{r})$ is the only functional of the electron density $\rho(\boldsymbol{r})$ by contradiction. We assume there is another external potential function $\nu'(\boldsymbol{r})$ (different more than a constant from $\nu(\boldsymbol{r})$) which gives rise to the same electron density state $\rho(\boldsymbol{r})$. In the following, the quantity corresponding to external potential function $\nu'(\boldsymbol{r})$ is labeled with a prime symbol. Obviously, $\nu'(\boldsymbol{r})$ and $\nu(\boldsymbol{r})$ belong to distinct Hamiltonians H$'$ and H, hence give rise to distinct wavefunctions ψ' and ψ. Based on the variational principle, there is no wavefunction to give an energy that is less than the energy of ψ state to the Hamiltonian H,

$$E = \langle\psi| H |\psi\rangle < \langle\psi'| H |\psi'\rangle \tag{2.7}$$

Assuming the ground state is not degenerated, we can rewrite the exception value in Eq. (2.7) by the following expression

$$\langle\psi'| H |\psi'\rangle = \langle\psi'| H' |\psi'\rangle + \int d^3r[\nu(\boldsymbol{r}) - \nu'(\boldsymbol{r})]\rho(\boldsymbol{r}) \tag{2.8}$$

Exchanging labels in Eq. (2.8), we obtain

$$\langle\psi| H' |\psi\rangle = \langle\psi| H |\psi\rangle + \int d^3r[\nu'(\boldsymbol{r}) - \nu(\boldsymbol{r})]\rho(\boldsymbol{r}) \tag{2.9}$$

Combining Eqs. (2.8), (2.9) and (2.7), we can obtain:

$$E + E' < E' + E \tag{2.10}$$

which is totally a contradiction. Therefore this theorem has been proven.

Proof of the second H-K theorem: The second H-K theorem demonstrates that the ground state energy of any solid system can be expressed by a universal functional of electron density $\rho(\boldsymbol{r})$. The ground state energy and electron density can be obtained by minimizing such functional with respect to the electron density. Considering the kinetic energy and the electron-electron interactions, P. Hohenberg and W. Kohn defined a universal functional $F_{HK}[\rho(\boldsymbol{r})]$

$$F_{HK}[\rho(\boldsymbol{r})] = T[\rho(\boldsymbol{r})] + V_{e-e}[\rho(\boldsymbol{r})] \tag{2.11}$$

The total energy functional can be expressed by functional $F_{HK}[n(\boldsymbol{r})]$ as

$$\begin{aligned} E_{HK}[\rho(\boldsymbol{r})] &= F_{HK}[\rho(\boldsymbol{r})] + \int d^3r V_{ext}\rho(\boldsymbol{r}) + V_{n-n} \\ &= T[\rho(\boldsymbol{r})] + U_{e-e}[\rho(\boldsymbol{r})] + \int d^3r V_{ext}\rho(\boldsymbol{r}) + U_{n-n}. \end{aligned} \tag{2.12}$$

The potential $\nu(\boldsymbol{r})$ is uniquely determined by the electron density and the potential in turn uniquely (apart from degenerated state) determines the wavefunction of ground state. So, all the other observables of the system are also uniquely determined. Then we can rewrite the energy as a function of wavefunction as

$$E[\rho(\boldsymbol{r})] = E[\rho(\boldsymbol{r})] = \langle\psi|\,\hat{H}\,|\psi\rangle \tag{2.13}$$

On the other hand, the ground state energy (E_0) can be expressed by the unique electron density $\rho_0(\boldsymbol{r})$

$$E_0 = E[\rho_0(\boldsymbol{r})] = \langle\psi_0|\,\hat{H}\,|\psi_0\rangle \tag{2.14}$$

Considering the variational principle, a different electron density state $\rho'(\boldsymbol{r})$ will give rise a higher energy

$$E' = E[\rho'(\boldsymbol{r})] = \langle\psi'|\,\hat{H}\,|\psi'\rangle > \langle\psi_0|\,\hat{H}\,|\psi_0\rangle = E_0 \tag{2.15}$$

Therefore the ground state really has the lowest energy functional. Moreover, the charge density and energy at the ground state can be obtained by minimizing the energy functional with respect to the variations in the charge density $\rho_0(\boldsymbol{r})$.

In summary, the charge density $\rho(\boldsymbol{r})$ is considered as the basic variable in HK theorems. However, the problem is still unsolved because the universal functional $F_{HK}[n(\boldsymbol{r})]$ is unknown. W. Kohn and L.J. Sham [149] derived the explicit universal functional $F_{HK}[n(\boldsymbol{r})]$ by inducing the Kohn-Sham ansatz as following.

2.2.2 Kohn-Sham Equations

After the birth of Schrödinger equation, quantum mechanics was immediately applied in analytically solving the Hydrogen or hydrogen-like atom system. Thereafter, Hartree introduced the self-consistent field method to approach the wave functions and energies for many-body time-independent Schrödinger equation [154]. Unfortunately, the method did not respect to the anti-symmetry principle for wave function. Fock modified Hartree's method by considering exchange coupling and the principle of antisymmetry of the wave function in the self-consistent field method. This leads to the famous Hartree-Fock method [155], which is a variational, wavefunction-based approximation, where the solution for the many body system is approached by a single-particle picture. The electrons are treated as single particle orbitals, where the interactions of the other electrons are approximated in an effective potential. The Hartree-Fock method is the basic theory for energy band theory. However, the electron correlation is not considered in such a method.

Motivated by the Hartree-Fock method, Kohn and Sham [149] proposed a way to determine the explicit functional of electron density and kinetic energy for the Hohenberg-Kohn theorems. Here, the many body system is mapped onto a fictitious noninteracting system with the same electron density as the many body system, such that we can solve the many body problem in a single-particle-like Schrödinger equation way while the electron interaction part is summarized in an exchange-correlation term. The mapping is performed for the purpose to minimize the energy functional of the fictitious noninteracting system by using the variational principle.

In the non-interacting system, only the kinetic energy $T[\rho(\boldsymbol{r})]$ makes a contribution to the universal functional F: $F^0[\rho(\boldsymbol{r})] = T[\rho(\boldsymbol{r})]$ (the superscript "0" represents the non-interaction system). Moreover, the universal functional of the interacting system is logically written by

$$F[\rho(\boldsymbol{r})] = T_s[\rho(\boldsymbol{r})] + U_H[\rho(\boldsymbol{r})] + E_{XC}[\rho(\boldsymbol{r})], \tag{2.16}$$

where $U_H[\rho(\boldsymbol{r})]$ denotes the electrostatic interaction which is expressed by

$$U_H[\rho(\boldsymbol{r})] = \frac{1}{2}\int\int \frac{\rho(\boldsymbol{r})\rho(\boldsymbol{r}')}{|\boldsymbol{r}-\boldsymbol{r}'|} d\boldsymbol{r}\, d\boldsymbol{r}'. \tag{2.17}$$

In Eq. (2.16), we use the kinetic energy of the non-interacting system, where the kinetic energy difference between interacting and non-interacting systems is counted in the term $E_{XC}[\rho(\boldsymbol{r})]$. In the fictitious non-interacting system, the following constrained conditions should be satisfied

$$\rho(\boldsymbol{r}) = \sum_i \rho_i(\boldsymbol{r})|\phi_i(\boldsymbol{r})|^2, \tag{2.18}$$

$$\langle\phi_i|\phi_j\rangle = \delta_{ij}. \tag{2.19}$$

The kinetic energy is obtained by the constrained condition functional

$$T[\rho] = \min_{\rho_i,\phi_i}\left\{\sum_i \langle\phi_i|\boldsymbol{\nabla}^2|\phi_i\rangle\right\}, \rho(\boldsymbol{r}) = \sum_i \rho_i(\boldsymbol{r})|\phi_i(\boldsymbol{r})|^2, \langle\phi_i|\phi_j\rangle = \delta_{ij} \tag{2.20}$$

Then the ground state energy is evaluated by

$$\begin{aligned} E[\nu_{ext},\rho] = &\min_{\rho_i,\phi_i}\left\{T[\sum_i \rho_i|\phi_i|^2] + U_H[\sum_i \rho_i|\phi_i|^2] + E_{XC}[\sum_i \rho_i|\phi_i|^2] - \langle\rho|\nu_{ext}\rangle\right\}, \\ &\rho(\boldsymbol{r}) = \sum_i \rho_i(\boldsymbol{r})|\phi_i(\boldsymbol{r})|^2, \langle\phi_i|\phi_j\rangle = \delta_{ij}. \end{aligned} \tag{2.21}$$

The exchange correlation term ($E_{XC}[\rho(\boldsymbol{r})]$) is the contribution from all errors derived by the treatment of noninteracting system apart from the classical Coulomb self-interaction term $V_H[\rho(\boldsymbol{r})]$. Based on variation principle, we can obtain the single-particle-like Schrödinger equation

$$[-\frac{1}{2}\boldsymbol{\nabla}^2 + V_{KS}(\boldsymbol{r})]\phi_j(\boldsymbol{r}) = \epsilon_j\phi_j(\boldsymbol{r}), \tag{2.22}$$

where $\phi_j(\boldsymbol{r})$ and ϵ_j denote the one-electron wave function (called Kohn-Sham orbital) of the fictitious noninteracting system and the corresponding Kohn-Sham eigenvalue. The electron moves in the effective Kohn-Sham potential

$$V_{KS}(\boldsymbol{r}) = \nu_{ext}(\boldsymbol{r}) + V_H(\boldsymbol{r}) + V_{XC}(\boldsymbol{r}), \tag{2.23}$$

where the external potential $\nu_{ext}(\boldsymbol{r})$ is also included, while the Hartree energy related potential is called as Hartree potential

$$V_H(\boldsymbol{r}) = \frac{\delta U[\rho]}{\delta\rho(\boldsymbol{r})} = \int \frac{\rho(\boldsymbol{r}')}{|\boldsymbol{r} - \boldsymbol{r}'|}d\boldsymbol{r}'. \tag{2.24}$$

And the exchange-correlation contribution is

$$V_{XC}(\boldsymbol{r}) = \frac{\delta E_{XC}[\rho]}{\delta\rho(\boldsymbol{r})}. \tag{2.25}$$

The fine exchange-correlation V_{XC} for the fictitious noninteracting system should result in the right ground electron density $\rho(\boldsymbol{r})$ for the original interacting many body system, which is expressed by the state ϕ_j of noninteracting system. The Kohn-Sham potential Eq. (2.23) depends on the accuracy of the electron density functional $\rho(\boldsymbol{r})$ in Eq. (2.18) obtained from an iterative solution of Eqs. (2.22), (2.23), (2.20), (2.21) and are dubbed as Kohn-Sham equations. Kohn-Sham equations are now widely applied in modern DFT codes. As shown in Fig. (4), the procedure is that we set an initial guessed starting electron density. Finally, we can solve the equations iteratively to reach self-consistency.

2.2.3 Exchange Correlation Functional

Until now, the Kohn-Sham equations are strictly clear and exact, except for the unknown exchange correlation term. In principle, we can get the strictly exact solution for such Kohn-Sham equations if the exchange correlation functional is chosen properly. However, in practice, the exchange correlation functional cannot be exactly determined. Firstly, it is conceptually impossible: We can never obtain the wavefunction for any many-body system. Secondly, the inaccuracy originates from the numerical nature. So the wave functions can only be numerically expressed using a certain basis. An exact solution requires a complete basis set. However, the problems cannot be solved analytically. This means we have to use the infinite expansion expression to approach the real wavefunction, which can never be realized in a numerical way. We have to set a suitable expansion cut-off. In conclusion, some further approximations have to be considered to approach the exchange correlation functional.

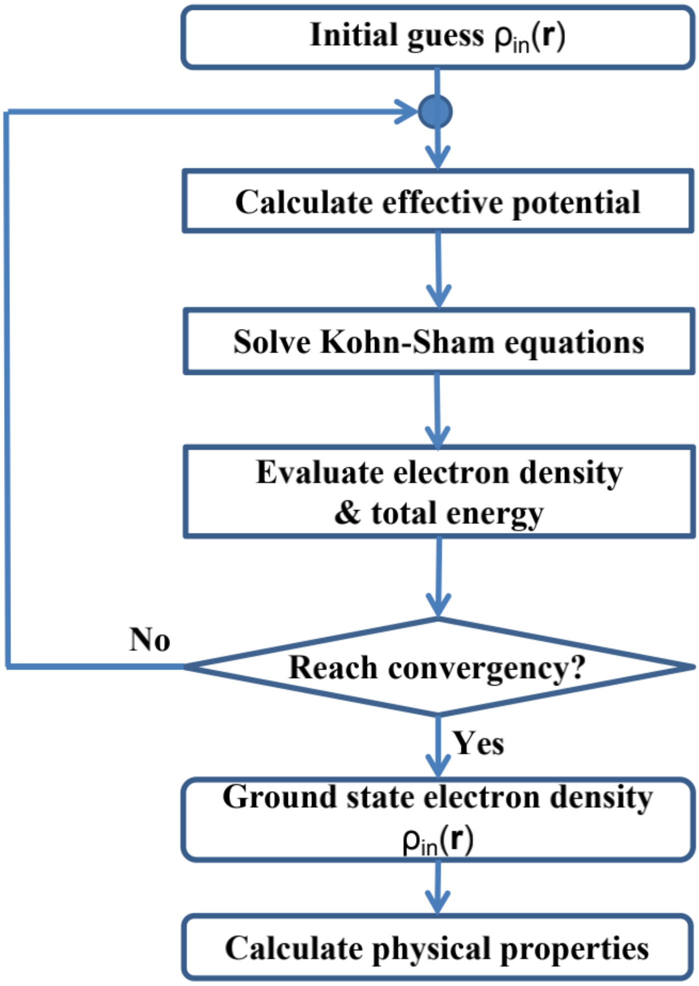

Figure 4: Scheme of the iterative numerical way to procedure Kohn-Sham equations in a self-consistency way for normal DFT calculations.

2.2.4 Local Density Approximation

One simple idea to construct Exchange Correlation Functional is based on the homogeneous electron gas (HEG) model, where the electrons are treated as localized on a positive charge background of nuclei [148]. The exchange contribution in the HEG can be analytically known. On the other hand, the electron density can be split into exchange (e_X^{HEG}) and correlation (e_C^{HEG}) parts:

$$e_{XC}^{HEG}[\rho(\boldsymbol{r})] = e_X^{HEG}[\rho(\boldsymbol{r})] + e_C^{HEG}[\rho(\boldsymbol{r})]. \tag{2.26}$$

For the nonspinpolarized system, the exchange correlation functional is expressed as

$$\begin{aligned} E_{XC}^{LDA}[\rho(\boldsymbol{r})] &= \int \rho(\boldsymbol{r}) e_{XC}^{HEG}[\rho(\boldsymbol{r})] d\boldsymbol{r} \\ &= \int (e_X^{HEG}[\rho(\boldsymbol{r})] + e_C^{HEG}[\rho(\boldsymbol{r})]) d\boldsymbol{r} \\ &= E_X^{LDA}[\rho(\boldsymbol{r})] + E_C^{LDA}[\rho(\boldsymbol{r})]. \end{aligned} \tag{2.27}$$

Obviously, the exchange correlation E_{XC}^{LDA} only depends on the local density. So such functional is named as local density approximation (LDA) [156]. The expression of exchange energy functional e_X^{LDA} is analytically written as [156]

$$\begin{aligned} E_X^{LDA}[\rho(\boldsymbol{r})] &= \int \rho(\boldsymbol{r}) e_X^{HEG}[\rho(\boldsymbol{r})] d\boldsymbol{r} \\ &= -\frac{3}{4}(\frac{3}{\pi})^{1/3} \int \rho(\boldsymbol{r})^{4/3} d\boldsymbol{r} \end{aligned} \tag{2.28}$$

where

$$e_X^{HEG}[\rho(\boldsymbol{r})] = -\frac{3}{4}(\frac{3}{\pi})^{1/3} \rho(\boldsymbol{r})^{1/3}. \tag{2.29}$$

On the other hand, the correlation part cannot be explicitly expressed, implying further approximation is still needed. One simple approximation is based on the perturbation theory. In current DFT codes, the expressions are parameterized based on the data of quantum Monte Carlo simulations of the HEG [157]. The HEG somehow behaves like a metallic system. So LDA functional is well suited for metallic solids. Surprisingly, LDA also can give rise to fine results for a molecule system due to system-error cancellation [151]. However, LDA tends to overestimate the binding energies, resulting in too short bond lengths. Several LDA xc functionals have already been widely applied in modern DFT codes, *e.g.*, Vosko-Wilk-Nusair (VWN), Perdew-Zunger (PZ81), Cole-Perdew (CP), and Perdew-Wang (PW92) [156, 158, 159, 160].

2.2.5 Generalized Gradient Approximation

More physically, the electron density should have a gradient, where the homogeneous gas model is not strictly exact. So, a more accurate approximation is to consider the electron density distribution has a gradient, meaning the exchange-correlation functional is affected by both the electron density and the corresponding gradient. A so-called gradient expansion approximations (GEA) tried to include higher-order corrections in terms of $|\boldsymbol{\nabla}\rho(\boldsymbol{r})|$, $|\boldsymbol{\nabla}^2\rho(\boldsymbol{r})|$ *etc.* [161]. However, such approximation always gives rise to even worse results than LDA. A modified approximation of GEA was made by a more general functional of both the electron density $\rho(\boldsymbol{r})$ and the corresponding gradient $\boldsymbol{\nabla}\rho(\boldsymbol{r})$ instead of a power series like expansion [162], which is expressed as

$$E_{XC}^{GGA}[\rho(\boldsymbol{r})] = \int f(\rho(\boldsymbol{r}), \boldsymbol{\nabla}\rho(\boldsymbol{r})) d\boldsymbol{r}. \tag{2.30}$$

Such approximation is called generalized gradient approximation (GGA), which is especially accurate for systems with a significant inhomogeneous electron density. At present, there are two concepts for GGA. Becke argued that the GGA functional should be fitted by the experimental and computational data and whether a functional good or not is determined by the computational results. An important functional based on such a concept is the B88 functional proposed by Becke [163]. On the other hand, Perdew held the point that the functional should be determined by the physical nature of a solid system. Based on such a concept, Perdew, Burke and Ernzerhof developed the so-called PBE functional [162], without any empirical parameters.

2.2.6 Spin-polarized calculations in DFT

Up to now, we have focused on the nonmagnetic system. In order to understand magnetic materials, it is necessary to expand DFT to spin-polarized systems. For the collinear magnetism, one simple treatment is to deal with the electron density in each spin orientation, that is to decompose electron density $\rho(\boldsymbol{r})$ into spin up $\rho_\uparrow(\boldsymbol{r})$ and spin down $\rho_\downarrow(\boldsymbol{r})$ channels. Then the total electron density $\rho(\boldsymbol{r})$, spin density $s(\boldsymbol{r})$ and spin polarization $(P(\boldsymbol{r}))$ can be written as

$$\rho(\boldsymbol{r}) = \rho_\uparrow(\boldsymbol{r}) + \rho_\downarrow(\boldsymbol{r}) \tag{2.31}$$

$$s(\boldsymbol{r}) = \rho_\uparrow(\boldsymbol{r}) - \rho_\downarrow(\boldsymbol{r}) \tag{2.32}$$

$$P(\boldsymbol{r}) = \frac{\rho_\uparrow(\boldsymbol{r}) - \rho_\downarrow(\boldsymbol{r})}{\rho_\uparrow(\boldsymbol{r}) + \rho_\downarrow(\boldsymbol{r})} \tag{2.33}$$

The Kohn-Sham equations are then decomposed into spin-up and -down channels with a spin dependent equations indexed by σ:

$$[-\frac{1}{2}\boldsymbol{\nabla}^2 + V_{KS}^\sigma(\boldsymbol{r})]\phi_j^\sigma(\boldsymbol{r}) = \epsilon_j^\sigma \phi_j^\sigma(\boldsymbol{r}). \tag{2.34}$$

$$V_{KS}^\sigma(\boldsymbol{r}) = \nu^\sigma(\boldsymbol{r}) + \frac{\delta U[\rho_\uparrow(\boldsymbol{r}), \rho_\downarrow(\boldsymbol{r})]}{\delta \rho^\sigma} + \frac{\delta E_{XC}[\rho_\uparrow(\boldsymbol{r}), \rho_\downarrow(\boldsymbol{r})]}{\delta \rho^\sigma} \tag{2.35}$$

$$\rho(\boldsymbol{r}) = \sum_\sigma \sum_{j=1}^{N_\sigma} |\phi_j^\sigma(\boldsymbol{r})|^2 \tag{2.36}$$

where N_α is the number of electrons for spin α (up or down) channel. Then the exchange correlation functional is changed accordingly into local spin density approximation (LSDA). Logically, we can write the LDA and GGA functionals in the form of

$$E_{XC}^{LSDA}[\rho_\uparrow(\boldsymbol{r}), \rho_\downarrow(\boldsymbol{r})] = \int \rho(\boldsymbol{r}) e_{XC}^{HEG}[\rho_\uparrow(\boldsymbol{r}), \rho_\downarrow(\boldsymbol{r})] d\boldsymbol{r} \tag{2.37}$$

$$E_{XC}^{GGA}[\rho_\uparrow(\boldsymbol{r}), \rho_\downarrow(\boldsymbol{r})] = \int f(\rho_\uparrow(\boldsymbol{r}), \rho_\downarrow(\boldsymbol{r}), \boldsymbol{\nabla}\rho_\uparrow(\boldsymbol{r}), \boldsymbol{\nabla}\rho_\downarrow(\boldsymbol{r})) d\boldsymbol{r}. \tag{2.38}$$

Based on functional deviation, the effective exchange-correlation potential is logically written as:

$$\nu_{XC\text{-}\sigma}^{LSDA/GGA} = \frac{\delta E_{XC}^{LSDA/GGA}}{\delta \rho_\sigma} \tag{2.39}$$

where σ denotes the spin polarization direction of spin up or spin down channel.

Further, the non-collinear magnetic DFT calculations can be realized by substituting a 3D spin density $s(\boldsymbol{r})$ matrix into the spin-polarized calculations scheme.

It is well known that spin is of the relativistic origin [7]. The relativistic effects on a solid system can be divided into the kinematical and spin-orbit coupling (SOC) parts [7]. The kinematical effects originate from "contracted" orbitals due to the high speed electron moving around a heavy nucleus, which are more probably in s and p shells. However, orbitals with larger angular momentum are affected by core orbitals in an expansion of the valence state (d and f orbitals). On the other hand, the spin-orbit coupling, namely the coupling between orbital and spin degrees of freedom, will give rise to subshell splitting [7]. In the following, we will focus on the spin-orbit coupling effect, which is described by a four component formulated Dirac equation [164]. The single particle Dirac equation is written as

$$H^D\psi = E\psi, \tag{2.40}$$

where ψ denotes the four component single particle wavefunction and H^D is the single particle Dirac Hamiltonian

$$H^D = c\boldsymbol{\alpha}\cdot\boldsymbol{p} + \beta mc^2 + V. \tag{2.41}$$

Here, $\boldsymbol{\alpha}_i$ (i=1,2,3) and β are defined to satisfy the energy-momentum relation

$$\alpha_i = \begin{bmatrix} 0 & \sigma_i \\ \sigma_i & 0 \end{bmatrix}, \beta = \begin{bmatrix} I_2 & 0 \\ 0 & -I_2 \end{bmatrix}, \tag{2.42}$$

where σ_i denotes the Pauli matrix [164, 165], $\boldsymbol{p}$ is the momentum operator $\boldsymbol{p} = -i\hbar\boldsymbol{\nabla}$ and I_2 is a 2×2 unit matrix

$$I_2 = \begin{bmatrix} 1 & 0 \\ 0 & 1 \end{bmatrix}. \tag{2.43}$$

The magnetism or spin can be physically explained by the Dirac theory for the electrons [166]. Firstly, the magnetization connects spin with Maxwell equation. Secondly, the spin-orbit interaction is the origin for the magneto-crystalline anisotropy. The first aspect will help us to construct the modern spin-density-functional theory. Assuming the electronmagnetimetic field is described by the scalar potential φ and the vector potential $\boldsymbol{A}$, the momentum can be obtained by minimal substitution $p^\mu \to \boldsymbol{p} - q\boldsymbol{A}$.

At the beginning, we consider only the effect of time-independent vector potential $q\boldsymbol{A}$. The stationary Dirac equation for an electron is expressed by

$$H\Psi = E\Psi = [c\boldsymbol{\alpha}\cdot(\boldsymbol{p} - e\boldsymbol{A}) + \beta mc^2]\Psi. \tag{2.44}$$

The solution for the above equation is a four component spinor function in terms of two-component function ϕ and χ, which is expressed by

$$\Psi = \begin{bmatrix} \phi \\ \chi \end{bmatrix}. \tag{2.45}$$

Here ϕ and χ are dubbed as the "large" and "small" components, respectively. Then we can rewrite the Dirac equation as

$$\begin{bmatrix} mc^2 & c\boldsymbol{\sigma}\cdot(\boldsymbol{p} - e\boldsymbol{A}) \\ c\boldsymbol{\sigma}\cdot(\boldsymbol{p} - e\boldsymbol{A}) & -mc^2 \end{bmatrix} \begin{bmatrix} \phi \\ \chi \end{bmatrix} = E \begin{bmatrix} \phi \\ \chi \end{bmatrix}. \tag{2.46}$$

Based on the above, we can obtain two coupled equations as

$$mc^2\phi + c\boldsymbol{\sigma}\cdot(\boldsymbol{p} - e\boldsymbol{A})\chi = E\phi, \tag{2.47}$$

$$c\boldsymbol{\sigma}\cdot(\boldsymbol{p} - e\boldsymbol{A})\phi - mc^2\chi = E\chi. \tag{2.48}$$

Define $W = E - mc^2$, which is the energy shift over the rest mass energy. In the non-relativistic limit, $W \ll mC^2$. Then we obtain $\chi = \frac{c\boldsymbol{\sigma}\cdot(\boldsymbol{p}-e\boldsymbol{A})}{2mc^2+W}\phi \approx \frac{c\boldsymbol{\sigma}\cdot(\boldsymbol{p}-e\boldsymbol{A})}{2mc^2}\phi$. Thus, we can obtain

$$[\frac{1}{2m}(\boldsymbol{p} - e\boldsymbol{A})^2 - \frac{e\hbar}{2m}\boldsymbol{\sigma}\cdot(\boldsymbol{\nabla}\times\boldsymbol{A})]\phi = W\phi. \tag{2.49}$$

As is known $\boldsymbol{\nabla}\times\boldsymbol{A} = \boldsymbol{B}$. The $\frac{e\hbar}{2m}\boldsymbol{\sigma}\cdot(\boldsymbol{\nabla}\times\boldsymbol{A})$ term is just the Zeeman splitting induced by the magnetic field: $\mu_S\cdot\boldsymbol{B}$, which is just the concept of spin.

Next, we consider the time-independent scalar potential $V = -e\varphi$. The stationary Dirac equation will be $H\Psi = E\Psi = [c\boldsymbol{\alpha}\cdot\boldsymbol{p} + \beta mc^2 + V]\Psi$. Here the wavefunction can still be expressed by the "large" and "small" components. Similarly, we can obtain

$$\begin{bmatrix} V + mc^2 & c\boldsymbol{\sigma}\cdot\boldsymbol{p} \\ c\boldsymbol{\sigma}\cdot\boldsymbol{p} & V - mc^2 \end{bmatrix}\begin{bmatrix}\phi \\ \chi\end{bmatrix} = E\begin{bmatrix}\phi \\ \chi\end{bmatrix}. \tag{2.50}$$

Then two coupled equations can be obtained

$$(V + mc^2)\phi + c\boldsymbol{\sigma}\cdot\boldsymbol{p}\chi = E\phi, \tag{2.51}$$

$$c\boldsymbol{\sigma}\cdot\boldsymbol{p}\phi + (V - mc^2)\chi = E\chi \tag{2.52}$$

Easily, we can get

$$\chi = \frac{c\boldsymbol{\sigma}\cdot\boldsymbol{p}}{(E - V + mc^2)}\phi. \tag{2.53}$$

Similar to vector potential case, we can still use the relation $W = E - mc^2$:

$$\frac{1}{E - V + mc^2} = \frac{1}{W - V + 2mc^2} = \frac{1}{2mc^2}(1 + \frac{W - V}{2mc^2})^{-1} \approx \frac{1}{2mc^2}(1 - \frac{W - V}{2mc^2}). \tag{2.54}$$

Substituting the above to Eq. (2.53), we can obtain:

$$\chi = c\boldsymbol{\sigma}\cdot\boldsymbol{p}\frac{1}{2mc^2}(1 - \frac{W - V}{2mc^2})\phi. \tag{2.55}$$

Moreover, we can get:

$$(\frac{\boldsymbol{p}^2}{2m} + V - \frac{\boldsymbol{p}^4}{8m^3c^2} - \frac{i\boldsymbol{\sigma}\cdot\boldsymbol{p}\times[\boldsymbol{p}, V]}{4m^2c^2} - \frac{\boldsymbol{p}\cdot[\boldsymbol{p}, V]}{4m^2c^2})\phi = W\phi, \tag{2.56}$$

where,

$$[\boldsymbol{p}, V(\boldsymbol{r})]\phi = -i\hbar(\boldsymbol{\nabla}V(\boldsymbol{r}))\phi. \tag{2.57}$$

If we consider the relativistic effect as perturbation, we can decompose the Dirac Hamiltonian into two independent parts as

$$H^D\Psi = W\Psi + H_{SOC}\Psi = E\Psi, \tag{2.58}$$

where W is nonrelativistic contribution and H_{SOC} is the relativistic or spin-orbit coupling effect part. We call the third term in the left hand of Eq. (2.56) as the spin-orbit coupling term which is expressed as [166]

$$\begin{aligned} H_{SOC} &= -\frac{i\boldsymbol{\sigma} \cdot \boldsymbol{p} \times [\boldsymbol{p}, V]}{4m^2c^2} \\ &= -\frac{\hbar \boldsymbol{\nabla} V}{4M^2c^2}\boldsymbol{\sigma} \cdot \boldsymbol{p} \times \boldsymbol{r} \\ &\approx \xi(r)\boldsymbol{\sigma} \cdot \boldsymbol{l} \end{aligned} \tag{2.59}$$

where $\boldsymbol{\nabla} V(\boldsymbol{r}) = -e\phi(\boldsymbol{r})$ is the electrostatic potential felt by the electron. The electrostatic potential always has strong effect in the core regions. Thus SOC term can be regarded as the summation of the local contribution $\xi\boldsymbol{\sigma} \cdot \boldsymbol{l}$. The SOC constant ξ is a radial function as:

$$\xi(r) = \frac{-Ze\hbar^2}{2m^2c^2}\frac{1}{r}\frac{d\phi}{dr}. \tag{2.60}$$

In general, SOC is the interaction between spin and orbit motion around the nucleus. When an electron is moving around the electric field originated from the nucleus, the atomic energy level will be shifted due to SOC interaction. Such energy level shifting will be reflected in the electronic structures, leading to various interesting physics in solid systems. For instance, in a semiconductor without inversion symmetry, SOC interaction will cause a spin splitting of electron (or hole) at non-zero K point in absence of magnetic field, which is called Dresselhaus effect [167]. Another example is the Rushba effect [168], of which the spin splitting happens in the 2D plane where the inversion symmetry is broken by a gradient potential ($\boldsymbol{\nabla} V$) along the perpendicular direction. The corresponding Rushba spin-orbit coupling is given by

$$H_R = \alpha(\boldsymbol{\nabla} V \times \mathbf{p}) \cdot \sigma \tag{2.61}$$

where $\alpha = \frac{g\mu_B E_0}{2mc^2}$ (E_0 is the eigenvalue). Furthermore, SOC interaction is the essential physics of spintronics and magnetic anisotropy, as has been discussed in Chapter of Introduction.

Moreover the Kohn-Sham-Dirac equation is written as [7, 166]

$$\begin{aligned} &[-i\hbar c\alpha \cdot \boldsymbol{\nabla} + \beta mc^2 + \nu(\boldsymbol{r}) + \nu^h(\boldsymbol{r}) + \boldsymbol{v}^{xc}(\boldsymbol{r})]\psi_{\boldsymbol{k}}(\boldsymbol{r}) \\ &-\mu_0\beta\int d\boldsymbol{r}'[\boldsymbol{h}(\boldsymbol{r}') + \boldsymbol{h}^h(\boldsymbol{r}') + \boldsymbol{h}^{xc}(\boldsymbol{r}')] \cdot \frac{\delta\mathcal{M}(\boldsymbol{r}')}{\delta\psi_{\boldsymbol{k}}(\boldsymbol{r})} = E_k\psi_{\boldsymbol{k}}(\boldsymbol{r}). \end{aligned} \tag{2.62}$$

where $\nu(\boldsymbol{r})$, $\nu^h(\boldsymbol{r})$ and $\boldsymbol{v}^{xc}(\boldsymbol{r})$ denote the mechanical, Hartree and exchange correlation potentials, while $\boldsymbol{h}(\boldsymbol{r}')$, $\boldsymbol{h}^h(\boldsymbol{r}')$, and $\boldsymbol{h}^{xc}(\boldsymbol{r}')$ denote the magnetic, Hartree, and exchange correlation fields. In general, the order of magnitude for $\boldsymbol{h}^h(\boldsymbol{r}')$ is 2 to 3 times lower than that for $\boldsymbol{h}^{xc}(\boldsymbol{r}')$. The nonlocal term in $E_{XC}[J]$ is near to the exchange correlation for LSDA:

$$E_{XC}[J] \approx E_{XC}^{LSDA} \tag{2.63}$$

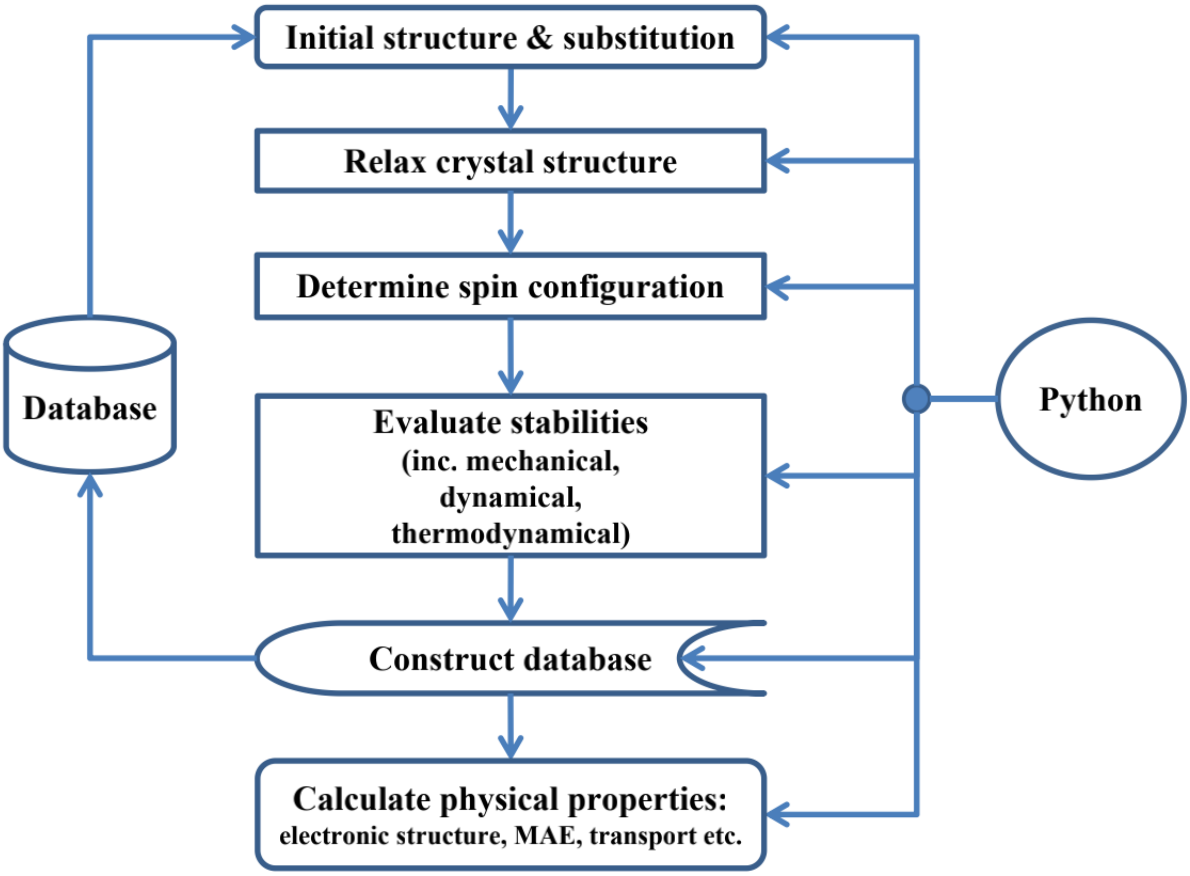

Figure 5: Workflow for a typical HTP computational research.

2.4 DFT codes and HTP

In our research, all calculations are carried out in an automatic way within our in-house-developed high-throughput environment (HTE) [169, 170]. The structure relaxation is performed by using the Vienna *ab initio* Simulation Package (VASP) [171, 172] in a two-step manner to save computational time. Firstly, ultrasoft pseudopotentials [172] are used in combination with the PW91 [173] exchange correlation functional, where the cutoff energy for the plane wave basis is set to 250 eV and a k-space density of 30 Å^{-1}. The follow-up finer relaxation is done using the projector augmented plane wave (PAW) method with the exchange-correlation functional under the generalized gradient approximation (GGA) parametrized by Perdew, Burke, and Ernzerhof (PBE) [162]. The cutoff energy for the plane wave expansion is increased to 350 eV and the k-mesh density is increased to 40 Å^{-1} to achieve a good convergence. The electronic structure together with the magnetic moments of the candidates are calculated with a k-mesh density of 120 Å^{-1} using the full-potential local-orbital minimum-basis band structure scheme (FPLO) [174, 175]. Based on the force theorem [176], the MAE value is calculated by using FPLO in a two-step way. Firstly, the self-consist DFT calculation is performed using FPLO code with the the exchange-correlation functional of PBE-GGA approximation in a k-mesh density of 50 Å^{-1}. Then a one-step DFT calculation is performed based on the converged charge density within the magnetization parallel to different directions. Thus the MAE value is obtained by considering the Bloch band energy difference between different magnetization directions. The semi-classical Boltzmann transport calculations are calculated based on the first-principles electronic structures obtained from the full-potential (linearized) augmented plane wave and local orbitals (FP(L)APW+lo) method, as implemented in the WIEN2K package [177]. The value of $R_{MT}K_{max}$ is set to be 8 for good convergence, where R_{MT} is the minimum of the muffin-tin radii of the atoms and K_{max} is the cutoff vector for the interstitial plane waves. The default values of the muffin-tin radii have been chosen so there is no charge leakage out of the muffin-tin spheres. The self-consistent calculations are performed using the PBE-GGA approximation for the exchange-correlation functional with a total Monkhorst-Pack k-points of 8000 in the whole Brillouin zone. Then the semi-classical transport properties are calculated by using the BoltzTrap code [178] based on the electronic structures obtained from a one-step calculation with a denser k-points of 64,000 in the whole Brillouin zone.

To satisfy the requirement of new technologies, it is becoming more and more urgent to design materials with desired properties, leading to the concept of Materials Genome Initiative (MGI) [179]. Particularly, DFT is a powerful method for material design in MGI due to its high accuracy. Furthermore, high-throughput (HTP) screening method based on DFT can realize automation for computational material science [170, 180], where thousands of compounds can be calculated following the workflows. Using HTP, a large amount of calculations have been done recently, where the data are also stored for further reutilization (such as machine learning). For instance, the Automatic Flow (AFLOW) HTP environment is used in screening of super alloys, high entropy alloys and metallic glasses [181], while Open Quantum Materials Database (OQMD) HTP is widely applied in the energy materials, such as Li battery electrodes and anodes, Li battery cathode coatings with HF, inorganic perovskites for solar cell [182]. The automated interactive infrastructure and database (AiiDA) is a user-friendly environment for HTP computational studies with the features of open source, plugin framework, high performance computer Interface, workflows, data provenance, and open science [183]. In 2D field, the Computational 2D Materials Database (C2DB) is a systematic HTP environment, which has been used to study the stabilities and magnetic properties of 2D materials [184]. It should be noticed that the HTP calculations for magnetic materials is still a challenging field. For instance, it is even hard to do calculations in a HTP manner for the key intrinsic magnetic properties, *i.e.* M_S, MAE and T_C. Moreover, it is a tricky problem to determine the magnetic ground state as the magnetic subspacegroup method will give rise to too many magnetic structures [185] and the prototype substitution method is not systematic. In this point of view, we still need to develop a more systematic and reasonable method to do HTP screening for magnetic materials.

The essential spirit of HTP is to manage the tedious DFT calculations automatically as shown in Fig. 5. Firstly, the elements are substituted into the initial structure. Then the crystal structures together with the magnetic spin configurations are relaxed. Based on the relaxed structures, the database is constructed to determine the thermodynamical stability according to the formation energy (ΔH) and the convex hull (E_{con}). The follow-up step is to check the mechanical stability (which is determined by the elastic constant) and the dynamical stability (which is determined by the Phonon dispersion obtained from Phonopy code [186]). Finally, the physical properties of the stable candidates are calculated.

Transport phenomena refer to the transformation of any physical quantity [187], *e.g.* mass, energy, momentum, particle, charge, angular momentum *etc.* All physical changes in the universe are associated with transport. Regarding this, transport is the fundamental mechanics behind the evolution of the universe.

Table 2: Comparison between diffusion of momentum, energy and mass.

Transported quantity	Physical phenomenon	Physical law	Equation
Momentum	Viscosity	Newton fluid	$\tau = -\nu \frac{\partial \rho \nu}{\partial x}$
Energy	Heat conduction	Fourier′s law	$\frac{q}{A} = -k \frac{dT}{dx}$
Mass	Molecular diffusion	Fick′s law	$J = -D \frac{\partial C}{\partial x}$

In general, there are two commonalities in transport phenomena as shown below.

1. **Diffusion**: Diffusion is the movement of anything (*e.g.*, particles, momentum, and energy) from the high to low density region when there is a gradient source. There are some obvious similarities in form for the transport equations of diffusion as shown in Table (2) [187]. More generally, we use the diffusion flux ($\boldsymbol{J}$) to describe the transfer of a physical quantity (n) through the local gradient source with the intensity (W)

$$\frac{\partial n}{\partial t} = -\boldsymbol{\nabla} \cdot \boldsymbol{J} + W. \tag{3.1}$$

   Analogous to Newton's second law, the dynamics for a diffusion process can be expressed by

$$m\frac{d^2x}{dt^2} = \frac{1}{\mu}\frac{dx}{dt} + F(t), \tag{3.2}$$

   where μ and F denote the mobility of particle and the external force.

2. **Onsager reciprocal relation**: In the first principle, ($\boldsymbol{J}$) is the flux of transported physical quantity as a result of the gradient distribution of some physical source ($\boldsymbol{X}$). In the homogenous system, the flux should be proportional to the intensity of the physical force

$$\boldsymbol{J} = L\boldsymbol{X}, \tag{3.3}$$

   where L is the Onsager transport coefficients. In practice, a few kinds of physical sources and fluxes can coexist. Thus, we should rewrite Eq. (3.3) in a generalized way as

$$J_k = \sum_l L_{kl} X_l, \tag{3.4}$$

   which reflects the effect of the local source on the local flux. Combining the above equation with statistical physics, we can obtain the flux of local entropy as

$$(\frac{\partial S}{\partial t})_k = \sum_l L_{kl} X_l. \tag{3.5}$$

According to the second thermodynamics law, the phenomenological coefficients L_{kl} should be positive. Furthermore, Onsager stated that the phenomenological coefficients L_{kl} is symmetric except for the case when time-reversal symmetry is broken [188]. In math, such Onsager reciprocal relation is expressed as

$$L_{kl} = L_{lk}. \tag{3.6}$$

In our research, we focus on the electron transport of solid systems based on the above fundamental principles.

3.1 Semi-classical Boltzmann Transport

3.1.1 Boltzmann equation

In general, the transport properties of a solid system are affected by the external fields and (or) temperature gradients as well as scattering derived by impurities, lattice waves, *etc.* In the weak field environment, the dynamical behavior for a wavepacket can be expressed by semi-classical dynamical equations as

$$\frac{d\boldsymbol{r}}{dt} = \boldsymbol{v}_n(\boldsymbol{k}) = \frac{1}{\hbar}\frac{\partial E_n(\boldsymbol{k})}{\partial \boldsymbol{k}} \tag{3.7}$$

and

$$\frac{d\boldsymbol{k}}{dt} = -\frac{e}{\hbar}\boldsymbol{\varepsilon}(\boldsymbol{r},t) - \frac{e}{\hbar c}\boldsymbol{v_n}(\boldsymbol{k}) \times \boldsymbol{B}(\boldsymbol{r},t), \tag{3.8}$$

where n is the index for the n-th band, while $E_n(\boldsymbol{k})$ is the corresponding eigenvalue. $\boldsymbol{\varepsilon}$ and B denote the external electric and magnetic fields.

For a solid state system, there are many electrons. So we use the distribution function to describe the collective behavior of the electrons:

$$f_{n\sigma}(\boldsymbol{r},\boldsymbol{k},t)\frac{d\boldsymbol{r}\,d\boldsymbol{k}}{(2\pi)^3}. \tag{3.9}$$

The above equation describes the electron distribution for the spin σ of band n in the interval phase space within the position $d\boldsymbol{r}$ of $\boldsymbol{r}$ and wavevectors $d\boldsymbol{k}$ of $\boldsymbol{k}$. The transport properties of a solid system are determined by the distribution function $f(\boldsymbol{r},\boldsymbol{k},t)$. The current density is eventually written by the integrals of the distribution function for the velocity over the whole Brillouin zone (Ω)

$$\boldsymbol{j}(\boldsymbol{r},t) = -\frac{e}{(2\pi)^3}\sum_{n,\sigma}\int_{\Omega} f_{n,\sigma}(\boldsymbol{r},\boldsymbol{k},t)\boldsymbol{v}_n(\boldsymbol{k})d\boldsymbol{k}. \tag{3.10}$$

Based on Fermi-Dirac statistics, we know the static equilibrium electron distribution function is easily written as

$$f^0 = \frac{1}{e^{(E_n-\mu)/k_BT}+1}. \tag{3.11}$$

where n is the index for the n-th band, while E_n is the corresponding eigenvalue. We always deal with the case where the non-equilibrium state does not depart very much from the equilibrium state. In such a situation, the local interval phase arrivals the local equilibrium, while the whole system is under nonequilibrium state. Assume τ is the average relaxation time for an interval phase and T is the relaxation time of the whole system, then the dynamical (δt) process time should satisfy the condition

$$\tau << \delta t << T. \tag{3.12}$$

Considering the electron number conservation rule, without collisions, the electron distribution function of the solid system must obey the continuity equation such that

$$\frac{\partial f}{\partial t} + \boldsymbol{\nabla} \cdot (\boldsymbol{u} f) = 0, \tag{3.13}$$

where $\boldsymbol{u}$ is in the six-dimensional phase space as $\boldsymbol{u} = (\dot{x}, \dot{y}, \dot{z}, \dot{k_x}, \dot{k_y}, \dot{k_z})$. Considering the incompressible flow condition, $\boldsymbol{\nabla} \cdot \boldsymbol{u} = 0$ should be satisfied [189]. Then we can rewrite Eq. (3.13) as

$$\frac{\partial f}{\partial t} + \boldsymbol{u} \cdot \boldsymbol{\nabla} f = 0. \tag{3.14}$$

The above equation describes the dynamical behaviour of the electrons by the external force, which is a reversible process. Such an external force will change the positions and velocities of the original equilibrium state. Thus the solid system reaches in a nonequilibrium state, which is assumed to be a nearly equilibrium state. Furthermore, the collisions will force the system to recover to the equilibrium state. So the collision should be balanced with the impact induced by the external force. The collisions will change the momentum of the electrons. Arising from the defects, phonons, or other electrons, the collisions do not allow the discontinuous change for the number of electrons and their momenta. All collision effects are summarized as a collision term. Then we can write

$$\frac{\partial f}{\partial t} + \dot{r} \cdot \boldsymbol{\nabla}_{\boldsymbol{r}} f + \dot{k} \cdot \boldsymbol{\nabla}_{\boldsymbol{k}} f = I_{\boldsymbol{k}}\{f\}, \tag{3.15}$$

where $I_{\boldsymbol{k}}\{f\}$ is the collision integral. The above equation is the so called Boltzmann equation. In general, $I_{\boldsymbol{k}}\{f\}$ is a function of $\boldsymbol{r}$, $\boldsymbol{k}$ and t, and a functional of the distribution function f. The probability $\theta(\boldsymbol{k}, \boldsymbol{k}')$ is the collision process for carriers from state $\boldsymbol{k}$ to $\boldsymbol{k}'$. The opposite process has the probability of $\theta(\boldsymbol{k}', \boldsymbol{k})$. Based on the detailed balance principle, the probability matrix should satisfy the following condition $\theta(\boldsymbol{k}, \boldsymbol{k}') = \theta(\boldsymbol{k}', \boldsymbol{k})$. The decrease of distribution at phase space $(\boldsymbol{r}, \boldsymbol{k})$ by scattering from $\boldsymbol{k}$ to $\boldsymbol{k}'$ is written as

$$\int f(\boldsymbol{r}, \boldsymbol{k}, t)[1 - f(\boldsymbol{r}, \boldsymbol{k}', t)]\theta(\boldsymbol{k}, \boldsymbol{k}')d\boldsymbol{k} = a. \tag{3.16}$$

Similarly, the increase of distribution at phase space $(\boldsymbol{r}, \boldsymbol{k})$ is caused by the scattering process from $\boldsymbol{k}'$ to $\boldsymbol{k}$ as

$$\int f(\boldsymbol{r}, \boldsymbol{k}', t)[1 - f(\boldsymbol{r}, \boldsymbol{k}, t)]\theta(\boldsymbol{k}', \boldsymbol{k})d\boldsymbol{k}' = b. \tag{3.17}$$

Eventually, we can write the collision integral as

$$I_{\boldsymbol{k}}\{f\} = b - a. \tag{3.18}$$

Collision acts locally in space, establishing a local equilibrium in a short time scale. Such a process is described by

$$f^0(\boldsymbol{r},\boldsymbol{k},t) = \frac{1}{exp(\frac{E(\boldsymbol{k}-\mu(\boldsymbol{(}r),t))}{k_B T(\boldsymbol{(}r,t)}) + 1}. \tag{3.19}$$

To obtain the solution of Boltzmann equation (3.15), we rewrite the distribution function as

$$f(\boldsymbol{r},\boldsymbol{k},t) = f^0(\boldsymbol{r},\boldsymbol{k},t) + \delta f(\boldsymbol{r},\boldsymbol{k},t). \tag{3.20}$$

In order to solve the deviation $\delta f(\boldsymbol{r},\boldsymbol{k},t)$, we assume $\mu = \mu(\boldsymbol{r})$ and $T = T(\boldsymbol{r})$ are time independent. Then the differential of f^0 is written as

$$\begin{aligned} df^0 &= k_B T \frac{\partial f^0}{\partial E} d(\frac{E-\mu}{k_B T}) \\ &= k_B T \frac{\partial f^0}{\partial E}(-\frac{d\mu}{k_B T} - \frac{(E-\mu)dT}{k_B T^2} + -\frac{dE}{k_B T}) \\ &= -\frac{\partial f^0}{\partial E}(\frac{\partial \mu}{\partial \boldsymbol{r}} \cdot d\boldsymbol{r} + \frac{E-\mu}{T}\frac{\partial T}{\partial \boldsymbol{r}} \cdot d\boldsymbol{r} - \frac{\partial E}{\partial \boldsymbol{k}} \cdot d\boldsymbol{k}). \end{aligned} \tag{3.21}$$

Then

$$\frac{\partial f^0}{\partial \boldsymbol{r}} = (\frac{\partial \mu}{\partial \boldsymbol{r}} + \frac{E-\mu}{T}\frac{T}{\partial \boldsymbol{r}})(-\frac{\partial f^0}{\partial E}) \tag{3.22}$$

$$\frac{\partial f^0}{\partial \boldsymbol{k}} = \hbar \nu \frac{\partial f^0}{\partial E}. \tag{3.23}$$

Therefore the Boltzmann equation is obtained as

$$\frac{\partial \delta f}{\partial t} + \boldsymbol{\nu} \cdot \boldsymbol{\nabla}_{\boldsymbol{r}} \delta f - \frac{e}{\hbar}[\boldsymbol{\varepsilon} + \frac{1}{c}\nu \times \boldsymbol{B}] \cdot \frac{\partial \delta f}{\partial \boldsymbol{k}} + \boldsymbol{\nu} \cdot [\boldsymbol{\nabla}_{\boldsymbol{r}} \mu + \frac{E-\mu}{T} \boldsymbol{\nabla}_{\boldsymbol{r}} T](-\frac{\partial f^0}{\partial E}) = I_{\boldsymbol{k}}(f^0 + \delta f). \tag{3.24}$$

The above is a nonlinear integrodifferential equation in δf. It is noticed that δf is first order small of f^0. So the gradient term $\boldsymbol{\nabla}_{\boldsymbol{r}} \delta f$ is second order smallness. Then we drop the second order small item, obtaining the linearized Boltzmann equation:

$$\frac{\partial \delta f}{\partial t} - \frac{e}{\hbar}[\boldsymbol{\varepsilon} + \frac{1}{c}\nu \times \boldsymbol{B}] \cdot \frac{\partial \delta f}{\partial \boldsymbol{k}} + \boldsymbol{\nu} \cdot [\boldsymbol{\nabla}_{\boldsymbol{r}} \mu + \frac{E-\mu}{T} \boldsymbol{\nabla}_{\boldsymbol{r}} T](-\frac{\partial f^0}{\partial E}) = L\delta f, \tag{3.25}$$

where $L\delta f$ is the linearized collision integral. L is a linear operator acting on δf.

3.1.2 Relaxation time approximation and metal conductivity

In principle, the nonequilibrium distribution function can be obtained by solving the Boltzmann equation (3.24). However this equation is a too complex partial differential equation to be easily solved. If an external field (gradient external magnetic and electrical field, or gradient temperature) is applied, the system will go beyond the equilibrium. Removing external force, the scattering term will recover the system to equilibrium. Let us consider the uniform field, where $\boldsymbol{\nabla}_{\boldsymbol{r}} f = 0$. For convenience, we always use the first order linear to approach the scattering item as

$$\frac{\partial f(\boldsymbol{k},t)}{\partial t}|_{collion} = b - a = -\frac{f(\boldsymbol{k},t) - f^0(\boldsymbol{k},t)}{\tau(\boldsymbol{k})} = -\frac{\delta f}{\tau(\boldsymbol{k})}, \tag{3.26}$$

where $f^0(\boldsymbol{k},t)$ is the equilibrium Fermi-Dirac distribution function $f^0(\boldsymbol{k}) = \frac{1}{1+exp(\frac{E(\boldsymbol{k})-\mu}{k_B T})}$. Here we use a phenomenological model to describe the Boltzmann partial differential equation by inducing the difference of the distribution function between nonequilibrium and equilibrium states, and the relaxation time $\tau(\boldsymbol{k})$. Such method is based on the spirit that the scattering relaxes the system to the equilibrium state, where the relaxation time is proportional to the difference between nonequilibrium and equilibrium distribution functions in the linear approach. In general, the relaxation will be as a function of momentum $\boldsymbol{k}$. The solution of equation (3.26) is rewritten as

$$f(\boldsymbol{k},t) = f^0(\boldsymbol{k}) + [f(\boldsymbol{k},t=0) - f^0(\boldsymbol{k})]exp[-t/\tau[\boldsymbol{k})]. \tag{3.27}$$

In the above equation, the initial nonequilibrium distribution function $f(\boldsymbol{k},t=0)$ will recover to the equilibrium distribution function using time $\tau(\boldsymbol{k})$. So, this method is called relaxation time approximation.

Consider a normal metal under a uniform stationary electric field $\boldsymbol{\varepsilon}$ while $\boldsymbol{B} = 0$ and $\boldsymbol{\nabla}_T = 0$. The external force is expressed as

$$\frac{d\boldsymbol{k}}{dt} = -\frac{e}{\hbar}\boldsymbol{\varepsilon}. \tag{3.28}$$

Under such a condition, the distribution function in Boltzmann equation is independent of the position $\boldsymbol{r}$. Considering the relaxation time approximation, the Boltzmann equation in Eq. (3.15) is reduced to

$$-\frac{e}{\hbar}\boldsymbol{\varepsilon}\cdot\boldsymbol{\nabla}_{\boldsymbol{k}} f(\boldsymbol{k}) = -\frac{f(\boldsymbol{k}) - f^0(\boldsymbol{k})}{\tau(\boldsymbol{k})}. \tag{3.29}$$

Obviously, the nonequilibrium distribution function f should depend on the external field $\boldsymbol{\varepsilon}$. Then f can be expressed by the Taylor expansion series in term of $\boldsymbol{\varepsilon}$ as

$$f = f^0 + f^1 + f^2 + ... \tag{3.30}$$

Then Eq. (3.29) is changed into

$$\frac{e}{\hbar}\boldsymbol{\varepsilon}\cdot\boldsymbol{\nabla}_{\boldsymbol{k}} f^0 + \frac{e}{\hbar}\boldsymbol{\varepsilon}\cdot\boldsymbol{\nabla}_{\boldsymbol{k}} f^1 + ... = \frac{f^1}{\tau(\boldsymbol{k})} + \frac{f^2}{\tau(\boldsymbol{k})} + ... \tag{3.31}$$

The terms with the same order should have the same parameter in the right and left in the above equation. Then we can obtain:

$$\frac{e}{\hbar}\boldsymbol{\varepsilon}\cdot\boldsymbol{\nabla}_{\boldsymbol{k}} f^0 = \frac{f^1}{\tau(\boldsymbol{k})} \tag{3.32}$$

and

$$\frac{e}{\hbar}\boldsymbol{\varepsilon}\cdot\boldsymbol{\nabla}_{\boldsymbol{k}} f^1 = \frac{f^2}{\tau(\boldsymbol{k})}. \tag{3.33}$$

Based on Eq. (3.32), we can rewrite the first item as

$$\begin{aligned} f^1 &= \frac{e\tau(k)}{\hbar}\boldsymbol{\varepsilon}\cdot\boldsymbol{\nabla}_{\boldsymbol{k}} f^0 \\ &= \frac{e\tau(k)}{\hbar}\boldsymbol{\varepsilon}\cdot[\boldsymbol{\nabla}_{\boldsymbol{k}} E(\boldsymbol{k})(\frac{\partial f^0}{\partial E})] \\ &= e\tau(\boldsymbol{k})\boldsymbol{\varepsilon}\cdot\nu(\boldsymbol{k})(\frac{\partial f^0}{\partial E}). \end{aligned} \tag{3.34}$$

Here we have used the relationship of $\frac{1}{\hbar}\boldsymbol{\nabla}_{\boldsymbol{k}} E(\boldsymbol{k}) = \nu(\boldsymbol{k})$, which can be obtained from electronic structures by using DFT calculations. In the weak field condition, the nonequilibrium distribution function f is close to the equilibrium distribution function f^0. Then we can just consider the zero and first order terms for the nonequilibrium distribution function, *i.e.*, $f = f^0 + f^1$. Then the current density is expressed as

$$\begin{aligned} \boldsymbol{j}^\alpha &= -\frac{2e}{(2\pi)^3}\int\limits_\Omega f\,\boldsymbol{\nu}^\alpha(\boldsymbol{k})d\boldsymbol{k} \\ &= \frac{2e}{(2\pi)^3}\int\limits_\Omega (f^0+f^1)\,\boldsymbol{\nu}^\alpha(\boldsymbol{k})d\boldsymbol{k} \\ &= -\frac{2e}{(2\pi)^3}\int\limits_\Omega f^0\,\boldsymbol{\nu}^\alpha(\boldsymbol{k})d\boldsymbol{k} - \frac{2e^2}{(2\pi)^3}\int\limits_\Omega \tau(\boldsymbol{k})\nu^\beta(\boldsymbol{k})[\nu^\alpha(\boldsymbol{k})](\frac{\partial f^0}{\partial E})d\boldsymbol{k}. \end{aligned} \tag{3.35}$$

The equilibrium distribution f^0 makes no contribution to the current density due to the anti-symmetry relationship $f^0(-\boldsymbol{k}) = -f^0(\boldsymbol{k})$. Then

$$\boldsymbol{j}^\alpha = -\frac{2e^2}{(2\pi)^3}\int\limits_\Omega \tau(\boldsymbol{k})\nu^\beta(\boldsymbol{k})\nu^\alpha(\boldsymbol{k})(\frac{\partial f^0}{\partial E})d\boldsymbol{k}. \tag{3.36}$$

Based on Ohm's law, the conductivity tensor has a linear relationship with the current density as $j^\alpha = \sigma_{\alpha\beta}\boldsymbol{\varepsilon}^\beta$. So the conductivity tensor thereby can be expressed by

$$\sigma^{\alpha\beta} = -\frac{2e^2}{(2\pi)^3}\int\limits_\Omega \tau(\boldsymbol{k})\nu^\beta(\boldsymbol{k})\nu^\alpha(\boldsymbol{k})(\frac{\partial f^0}{\partial E})d\boldsymbol{k}. \tag{3.37}$$

The partial derivative function for equilibrium distribution function f^0 is expressed as

$$\frac{\partial f^0}{\partial E} = -\frac{\partial f^0}{\partial \mu} = -\frac{T}{E(\boldsymbol{k}) - \mu}\frac{\partial f^0}{\partial T} = -\frac{exp(\frac{E(\boldsymbol{k})-\mu}{k_B T})}{k_B T(exp(\frac{E(\boldsymbol{k})-\mu}{k_B T}) + 1)^2}. \tag{3.38}$$

We should notice that the partial functions $\frac{\partial f^0}{\partial \mu}$, $\frac{\partial f^0}{\partial E}$ and $\frac{\partial f^0}{\partial T}$ decrease sharply when the eigensvalue $E(\boldsymbol{k})$ is away from the chemical potential μ, reaching 0.1% of the peak at just about $5k_B T \approx 0.1$ eV (T is room temperature) as showing in Fig. (6). Therefore only the states around Fermi level make a contribution to the conductivity hence the transport properties.

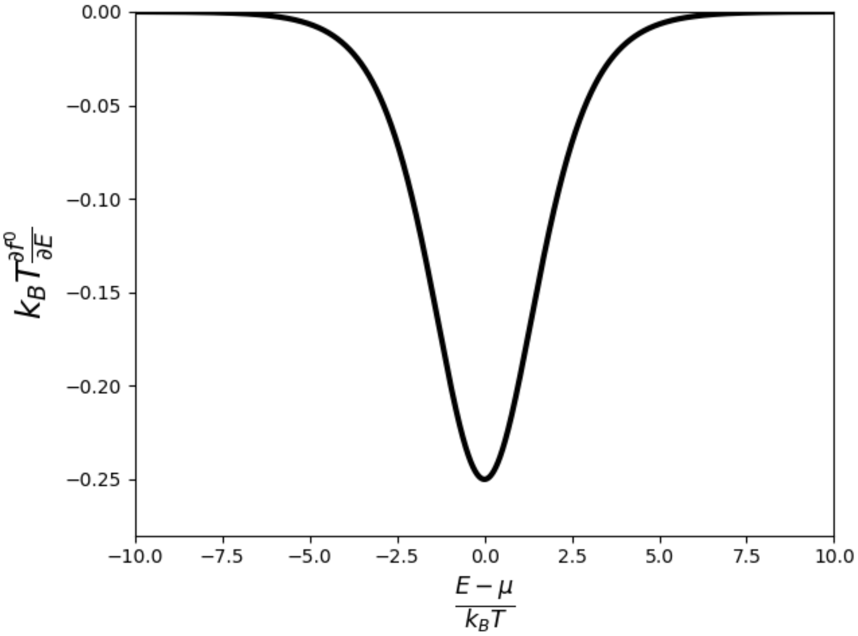

Figure 6: The distribution $\frac{\partial f^0}{\partial E}$ as a function of eigen value $E - \mu$.

3.2 Topological transport

3.2.1 Bloch theorem

In a crystal with the periodic potential, the Hamiltonian of an electron should naturally satisfy the following condition:

$$H(\boldsymbol{r}) = H(\boldsymbol{r} + \boldsymbol{R}), \tag{3.39}$$

where $\boldsymbol{r}$ and $\boldsymbol{R}$ denote the position of the electron and the translation vector of the lattice, respectively. Moreover, F. Bloch derived the so-called Bloch theorem [190]. Such theorem states that the solution eigenfunction of the Schrödinger equation for an electron in a periodic potential condition should satisfy

$$|\psi_{n,\boldsymbol{k}}(\boldsymbol{r} + \boldsymbol{R})\rangle = e^{i\boldsymbol{k}\cdot\boldsymbol{R}} |\psi_{n,\boldsymbol{k}}(\boldsymbol{r})\rangle . \tag{3.40}$$

On the other hand, Bloch theorem also indicates that the wavefunction of an electron in a periodic potential must be in the form of

$$\left|\psi_{n,\boldsymbol{k}}(\boldsymbol{r})\right\rangle = e^{i\boldsymbol{k}\cdot\boldsymbol{r}} \left|u_{n,\boldsymbol{k}}(\boldsymbol{r})\right\rangle, \tag{3.41}$$

where $u_{n,\boldsymbol{k}}$ has the same periodicity as crystal lattice

$$\left|u_{n,\boldsymbol{k}}(\boldsymbol{r}+T)\right\rangle = \left|u_{n,\boldsymbol{k}}(\boldsymbol{r})\right\rangle. \tag{3.42}$$

The wavefunction of Eq. (3.41) is named as "Bloch wavefunction". We will give a restricted proof of the Bloch theorem in the following. Firstly, we define a translation operator $\mathrm{T_R}$ to describe the period boundary condition, where any function should obey

$$T_{\boldsymbol{R}} f(\boldsymbol{r}) = f(\boldsymbol{r}+\boldsymbol{R}). \tag{3.43}$$

Considering the periodicity of Hamiltonian in Eq. (3.39), we can obtain:

$$T_{\boldsymbol{R}} H(\boldsymbol{r}) \left|\psi_{n,\boldsymbol{k}}(\boldsymbol{r})\right\rangle = H(\boldsymbol{r}+\boldsymbol{R}) \left|\psi_{n,\boldsymbol{k}}(\boldsymbol{r}+\boldsymbol{R})\right\rangle = H(\boldsymbol{r}) \left|\psi_{n,\boldsymbol{k}}(\boldsymbol{r}+\boldsymbol{R})\right\rangle = H(\boldsymbol{r}) T_{\boldsymbol{R}} \left|\psi_{n,\boldsymbol{k}}(\boldsymbol{r})\right\rangle. \tag{3.44}$$

So,

$$T_{\boldsymbol{R}} H = H T_{\boldsymbol{R}}. \tag{3.45}$$

This means H and $T_{\boldsymbol{R}}$ commute with each other. On the other hand, a translation operator that acts on the lattice just plays a role to shift the lattice. In this point of view, we can easily know

$$T_{\boldsymbol{R}} T_{\boldsymbol{R'}} = T_{\boldsymbol{R'}} T_{\boldsymbol{R}} = T_{\boldsymbol{R}+\boldsymbol{R'}}. \tag{3.46}$$

Therefore any translation operator is associated with a good quantum number, of which the solution can be simultaneously solved by:

$$H(\boldsymbol{r}) \left|\psi_{n,\boldsymbol{k}}(\boldsymbol{r})\right\rangle = \varepsilon_{n,\boldsymbol{k}} \left|\psi_{n,\boldsymbol{k}}(\boldsymbol{r})\right\rangle \tag{3.47}$$

$$T_{\boldsymbol{R}} \left|\psi_{n,\boldsymbol{k}}(\boldsymbol{r})\right\rangle = C(\boldsymbol{R}) \left|\psi_{n,\boldsymbol{k}}(\boldsymbol{r})\right\rangle. \tag{3.48}$$

Based on Eq. (3.46), we can easily obtain:

$$T_{\boldsymbol{R}} T_{\boldsymbol{R'}} \left|\psi_{n,\boldsymbol{k}}(\boldsymbol{r})\right\rangle = C(\boldsymbol{R'}) T_{\boldsymbol{R}} \left|\psi_{n,\boldsymbol{k}}(\boldsymbol{r})\right\rangle = C(\boldsymbol{R'}) C(\boldsymbol{R}) \left|\psi_{n,\boldsymbol{k}}(\boldsymbol{r})\right\rangle. \tag{3.49}$$

$$T_{\boldsymbol{R}} T_{\boldsymbol{R'}} \left|\psi_{n,\boldsymbol{k}}(\boldsymbol{r})\right\rangle = T_{\boldsymbol{R}+\boldsymbol{R'}} \left|\psi_{n,\boldsymbol{k}}(\boldsymbol{r})\right\rangle = C(\boldsymbol{R}+\boldsymbol{R'}) \left|\psi_{n,\boldsymbol{k}}(\boldsymbol{r})\right\rangle. \tag{3.50}$$

So,

$$C(\boldsymbol{R'}) C(\boldsymbol{R}) = C(\boldsymbol{R}+\boldsymbol{R'}). \tag{3.51}$$

The translation vector can be expressed by the primitive Bravais lattice

$$\boldsymbol{R} = n_1 \boldsymbol{a}_1 + n_2 \boldsymbol{a}_2 + n_3 \boldsymbol{a}_3. \tag{3.52}$$

Based on Eq. (3.51), we can get:

$$C(\boldsymbol{R}) = C(\boldsymbol{a}_1)^{n_1} C(\boldsymbol{a}_2)^{n_2} C(\boldsymbol{a}_3)^{n_3}. \tag{3.53}$$

According to the form of Eq. (3.51), the format solution of C($\boldsymbol{a}_i$) should be

$$C(\boldsymbol{a}_i) = e^{i2\pi x_i}. \tag{3.54}$$

Here, we use the Born-von Karman boundary condition [188] to describe $\boldsymbol{k} = x_1\boldsymbol{b}_1 + x_2\boldsymbol{b}_2 + x_3\boldsymbol{b}_3$, where $\boldsymbol{b}_i$ is the basis vector for the reciprocal lattice satisfying $\boldsymbol{b}_i \cdot \boldsymbol{a}_j = 2\pi\delta_{ij}$. Then, we obtain

$$C(\boldsymbol{R}) = C(\boldsymbol{a}_1)^{n_1} C(\boldsymbol{a}_2)^{n_2} C(\boldsymbol{a}_3)^{n_3} = e^{i2\pi \sum_i x_i n_i} = e^{i2\pi \sum_i \boldsymbol{a}_i \cdot \boldsymbol{b}_i} = e^{i\boldsymbol{k}\cdot\boldsymbol{R}}. \tag{3.55}$$

Substituting Eq. (3.55) into Eq. (3.48), we can get the conclusion

$$\left|\psi_{n,\boldsymbol{k}}(\boldsymbol{r}+\boldsymbol{R})\right\rangle = e^{i\boldsymbol{k}\cdot\boldsymbol{R}} \left|\psi_{n,\boldsymbol{k}}(\boldsymbol{r})\right\rangle. \tag{3.56}$$

Finally, the Bloch theorem is proven.

3.2.2 Adiabatic theorem

The adiabatic theorem was originally pointed out by M. Born and V. Fock [191]. In such a theorem, a physical system remains in the instantaneous eigenstate if a given perturbation is acting on it slowly enough to recover to the equilibrium and if there is a gap between the eigenvalue and the rest of the Hamiltonian's spectrum. M. Born and V. Fock also firstly proved such theorem [191] as follows. The concept is in the situation to deal with the time-dependent Hamiltonian.

The solution of the Schrödinger equation for the time-dependent Hamiltonian is written as

$$i\hbar\frac{\partial}{\partial t}\Psi(x,t) = \hat{H}\Psi(x,t), \tag{3.57}$$

which can be obtained from the time-independent Schrödinger equation $\hat{H}\psi_n(x) = E_n\psi_n(x)$ as

$$\Psi(x,t) = \sum_n c_n\Psi_n(x,t) = \sum_n c_n\psi_n(x)e^{-iE_nt/\hbar}. \tag{3.58}$$

The n-th eigenstate $\Psi_n(x,t)$ of time-dependent Hamiltonian is formed just by picking up a phase factor $-iE_nt/\hbar$ from the eigenstate $\psi_n(x)$ in the time-independent Hamiltonian. In the adiabatic process, both the eigenvalues and eigenfunctions are time-dependent as the Hamiltonian will change with-respect to time.

$$\hat{H}(t)\psi_n(x,t) = E_n(t)\psi_n(x,t). \tag{3.59}$$

At any instant time point, the eigenstate should form a complete orthogonal basis as

$$\langle\psi_n(t)|\psi_m(t)\rangle = \delta_{nm}. \tag{3.60}$$

Based on the Eqs. (3.59), (3.58), and (3.60), we can write the general solution for the time-dependent Schrödinger equation as

$$\Psi(t) = \sum_n c_n(t)\psi_n(t)e^{i\theta_n(t)}, \tag{3.61}$$

where the phase factor is expressed as the integral of energy

$$\theta_n(t) = -\frac{1}{\hbar}\int_0^t E_n(t')dt'. \tag{3.62}$$

Here $\theta_n(t)$ is defined as the dynamic phase factor. Substituting such term, the Schrödinger equation is then rewritten as

$$i\hbar\sum_n(\dot{c_n}\psi_n + c_n\dot{\psi_n} + ic_n\psi_n\dot{\theta_n})e^{i\theta_n} = \sum_n c_n\hat{H}\psi_n e^{i\theta_n}. \tag{3.63}$$

Considering $\dot{\theta_n} = -\frac{d}{dt}\frac{1}{\hbar}\int_0^t E_n(t')dt' = -\frac{E_n(t)}{\hbar}$, the third term of the left side will be $i\hbar\sum_n ic_n\psi_n\dot{\theta_n}e^{i\theta_n} = \sum_n c_nE_n\psi_ne^{i\theta_n}$. Based on the time-independent Schrödinger equation, the third term of the left side is then canceled with the right side for Eq. (3.63). So, we can obtain

$$\sum_n \dot{c_n}\psi_n e^{i\theta_n(t)} = -\sum_n c_n\dot{\psi_n}e^{i\theta_n(t)}. \tag{3.64}$$

Adding an arbitrary eigenstate $\langle\psi_m|$ to give an inner product, we obtain the following expression from Eq. (3.64) based on the complete orthogonal basis.

$$\dot{c_m} = -\sum_n c_n \left\langle \psi_m \middle| \dot{\psi_n} \right\rangle e^{i(\theta_n - \theta_m)}. \tag{3.65}$$

In Schrödinger equation, the the time derivative is written as

$$\dot{H}\left|\psi_n\right\rangle + H\left|\dot{\psi_n}\right\rangle = \dot{E}_n\left|\psi_n\right\rangle + E_n\left|\dot{\psi_n}\right\rangle. \tag{3.66}$$

Again, we take the inner product by inducing $\langle\psi_m|$

$$\left\langle\psi_m\right|\dot{H}\left|\psi_n\right\rangle + \left\langle\psi_m\right|H\left|\dot{\psi_n}\right\rangle = \left\langle\psi_m\right|\dot{E}_n\left|\psi_n\right\rangle + \left\langle\psi_m\right|E_n\left|\dot{\psi_n}\right\rangle. \tag{3.67}$$

Considering the hermiticity of Hamiltonian, $\left\langle\psi_m\right|\hat{H}\left|\dot{\psi_n}\right\rangle = E_m\left\langle\psi_m\middle|\dot{\psi_n}\right\rangle$. Then, we can obtain

$$\left\langle\psi_m\right|\dot{H}\left|\psi_n\right\rangle + E_m\left\langle\psi_m\middle|\dot{\psi_n}\right\rangle = \dot{E}_n\delta_{mn} + E_n\left\langle\psi_m\middle|\dot{\psi_n}\right\rangle. \tag{3.68}$$

So,

$$\dot{c_m}(t) = -c_m\left\langle\psi_m\middle|\dot{\psi_m}\right\rangle - \sum_{n,n\neq m} c_n \frac{\left\langle\psi_m\right|\dot{H}\left|\psi_n\right\rangle}{E_n - E_m} e^{i(\theta_n-\theta_m)}. \tag{3.69}$$

In the adiabatic approximation, the evolution time for the system is slowly enough that we can assume $\dot{H} \approx 0$. Thus the second term of the above equation can be ignored. Therefore, the solution is written as

$$c_m(t) = c_m(0)e^{i\gamma_m(t)} = c_m(0)e^{-\int_0^t \left\langle\psi_m(t')\middle|\dot{\psi}_m(t')\right\rangle dt'}, \tag{3.70}$$

where

$$\gamma_m(t) = i\int_0^t \left\langle\psi_m(t')\middle|\dot{\psi}_m(t')\right\rangle dt'. \tag{3.71}$$

The above is the so-called geometric phase, of which the value must be a real number. Assuming $c_n(0) = 1$ and $c_m(0) = 0$, the particle remains in the n-th eigenstate of the time-evolving Hamiltonian, only picking up the phase factor during the evolution process. Then Eq. (3.61) is rewritten as

$$\Psi_n(t) = e^{i\theta_n(t)}e^{i\gamma_n(t)}\psi_n(t). \tag{3.72}$$

3.2.3 Berry phase approach

In the adiabatic approximation, the geometric phase factor $\gamma_n(t)$ in principle can be canceled out by an appropriate choice of the gauge for the eigenfunctions. Further, if the adiabatic process is cyclic, the geometric phase becomes a gauge-invariant physical quantity, dubbed as Berry phase. In the following, we will discuss Berry phase.

Based on Bloch theorem, the choice of $u_{n,\boldsymbol{k}}$ is not unique as there is a phase uncertainty. On the other hand, any physically observed quantity should be independent of gauge choice. Here we discuss the system with a Hamiltonian varying through a parameter $\boldsymbol{R} \rightarrow \boldsymbol{R}(t)$. Moreover, a cyclic process happens in such a system from t=0 to T, where $\boldsymbol{R}(t=0) \to \boldsymbol{R}(t=T)$. In the system, the state changes so slowly that it will recover to an instantaneous equilibrium along a closed path C in the parameter space. For the purpose of understanding the evolution of the phase factor, we use an instantaneous orthogonal basis $u_n(\boldsymbol{R}(t))$ from the instantaneous eigenstates $E_n(\boldsymbol{t})$ with an instantaneous Hamiltonian $H(\boldsymbol{R}(t))$ with parameter $\boldsymbol{R}(t)$ at time t:

$$H(\boldsymbol{R}(t)) \left| u_n(\boldsymbol{R}(t)) \right\rangle = E_n(t) \left| u_n(\boldsymbol{R}(t)) \right\rangle . \tag{3.73}$$

Due to phase uncertainty, the above equation does not completely determine the eigenstate. On the other hand, the eigenstate can change smoothly with a single value along the closed path as the system changes slowly enough. Furthermore, the time resolved evolution of the eigenstate should be expressed by the time-dependent Schrödinger equation as

$$i\hbar \frac{\partial}{\partial t} \left| \Phi(t) \right\rangle = H(\boldsymbol{R}(t)) \left| \Phi(t) \right\rangle . \tag{3.74}$$

According to adiabatic theorem, the system will always stay in the instantaneous state (ground state), just picking up a phase factor during the evolution process. Based on Eq (3.70), the time dependent eigenstate can be expressed by

$$\left| \Phi(t) \right\rangle = e^{i\gamma_n(t)} e^{i\theta(t)} \left| u_n(\boldsymbol{R}(t)) \right\rangle \tag{3.75}$$

and

$$\frac{\partial}{\partial t} \gamma_n(t) = i \left\langle u_n(\boldsymbol{R}(t)) \right| \frac{\partial}{\partial t} \left| u_n(\boldsymbol{R}(t)) \right\rangle . \tag{3.76}$$

As the eigenstate is time-dependent to parameter $\boldsymbol{R}(t)$. We can obtain: $\frac{\partial u_n}{\partial t} = \frac{\partial u_n}{\partial \boldsymbol{R}} \frac{d\boldsymbol{R}}{dt}$. Then based on Eq. (3.71) the geometric phase is expressed by an integral over an arbitrary path in the parameter phase as

$$\gamma_n(t) = i \int \left\langle u_n \right| \frac{d}{dt} \left| u_n \right\rangle dt = i \int \left\langle u_n \right| \frac{\partial}{\partial \boldsymbol{R}} \left| u_n \right\rangle \cdot d\boldsymbol{R} = i \int \left\langle u_n \right| \boldsymbol{\nabla}_{\boldsymbol{R}} \left| u_n \right\rangle \cdot d\boldsymbol{R} = i \int d\boldsymbol{R} \cdot \boldsymbol{A}_n(\boldsymbol{R}). \tag{3.77}$$

That is the geometric phase

$$\gamma_n(t) = \int d\boldsymbol{R} \cdot \boldsymbol{A}_n(\boldsymbol{R}), \tag{3.78}$$

where $\boldsymbol{A}_n(\boldsymbol{R})$ is a vector expressed by:

$$\boldsymbol{A}_n(\boldsymbol{R}) = i \left\langle u_n(\boldsymbol{R}(t)) \right| \boldsymbol{\nabla}_{\boldsymbol{R}} \left| u_n(\boldsymbol{R}(t)) \right\rangle . \tag{3.79}$$

Such a vector is called “Berry connection” or “Berry vector potential”, originally introduced by M. Berry [192]. Obviously, the dynamic phase depends on the integrated path of the parameter phase $\boldsymbol{A}_n(\boldsymbol{R})$. The eigenstate will pick up the phase factor $\gamma_n(t)$. The vector potential $\boldsymbol{A}_n(\boldsymbol{R})$ is a gauge dependent quantity. After gauge transformation, we can therefore obtain the following

$$\boldsymbol{A}_n(\boldsymbol{R}) \to \boldsymbol{A}_n(\boldsymbol{R}) - \boldsymbol{\nabla}_{\boldsymbol{R}} \chi \tag{3.80}$$

and

$$\left| u_n(\boldsymbol{R}(t)) \right\rangle \to e^{i\chi(\boldsymbol{R}(t))} \left| u_n(\boldsymbol{R}(t)) \right\rangle . \tag{3.81}$$

Thus, the phase factor will be determined by the difference of χ between the initial and final points: $\chi(\boldsymbol{R}(t=T))-\chi(\boldsymbol{R}(t=0))$. For a cyclic process through a closed path C, the single value condition of the wavefunction requires the phase term to be one. Obviously, we can obtain:

$$\chi(\boldsymbol{R}(t=T))-\chi(\boldsymbol{R}(t=0))=2m\pi, \tag{3.82}$$

where m is an integer. Thus, we can conclude that along a closed path the geometric phase is gauge independent, which is called the "Berry phase" [192]:

$$\gamma_C=\oint_C d\boldsymbol{R}\cdot\boldsymbol{A}_n(\boldsymbol{R}). \tag{3.83}$$

Based on Stokes$'$ theorem, the Berry phase can also be expressed by the integration of the area formed by the closed path

$$\gamma_C=\oint_S d\boldsymbol{S}\cdot\Omega_n(\boldsymbol{R}). \tag{3.84}$$

The curvature of the Berry connection is expressed by

$$\Omega^n(\boldsymbol{R})=\boldsymbol{\nabla}_{\boldsymbol{R}}\times\boldsymbol{A}_n(\boldsymbol{R}). \tag{3.85}$$

The $\alpha\beta$ component of Berry curvature tensor is obtained by

$$\begin{aligned}\Omega^n_{\alpha\beta}(\boldsymbol{R})&=\frac{\partial}{\partial R_\alpha}(\boldsymbol{A})_\beta-\frac{\partial}{\partial R_\beta}(\boldsymbol{A})_\alpha\\&=i\left\langle\frac{\partial}{\partial R_\alpha}u_n(\boldsymbol{R})\middle|\frac{\partial}{\partial R_\beta}u_n(\boldsymbol{R})\right\rangle-i\left\langle\frac{\partial}{\partial R_\beta}u_n(\boldsymbol{R})\middle|\frac{\partial}{\partial R_\alpha}u_n(\boldsymbol{R})\right\rangle.\end{aligned} \tag{3.86}$$

The berry curvature plays a role just like the magnetic field in electrodynamics. In the following, we will show the derivation of the Berry curvature in another expression. We begin with Schrödinger equation

$$H\left|u_n(\boldsymbol{R})\right\rangle=E_n\left|u_n(\boldsymbol{R})\right\rangle. \tag{3.87}$$

Inducing the spatial gradient, we can obtain

$$\boldsymbol{\nabla}_{\boldsymbol{R}}(H\left|u_n(\boldsymbol{R})\right\rangle)=\boldsymbol{\nabla}_{\boldsymbol{R}}(E_n\left|u_n(\boldsymbol{R})\right\rangle). \tag{3.88}$$

The above can be converted into

$$\boldsymbol{\nabla}_{\boldsymbol{R}}H\left|u_n(\boldsymbol{R})\right\rangle+H\left|\boldsymbol{\nabla}_{\boldsymbol{R}}u_n(\boldsymbol{R})\right\rangle=\boldsymbol{\nabla}_{\boldsymbol{R}}E_n\left|u_n(\boldsymbol{R})\right\rangle+E_n\left|\boldsymbol{\nabla}_{\boldsymbol{R}}u_n(\boldsymbol{R})\right\rangle. \tag{3.89}$$

By taking an arbitrary state $\langle u_m(\boldsymbol{R})|$ in the above equation, we obtain the following expression

$$\langle u_m(\boldsymbol{R})|\,\boldsymbol{\nabla}_{\boldsymbol{R}}H\left|u_n(\boldsymbol{R})\right\rangle+\langle u_m(\boldsymbol{R})|\,H\left|\boldsymbol{\nabla}_{\boldsymbol{R}}u_n(\boldsymbol{R})\right\rangle=\langle u_m(\boldsymbol{R})|\,\boldsymbol{\nabla}_{\boldsymbol{R}}E_n\left|u_n(\boldsymbol{R})\right\rangle+\langle u_m(\boldsymbol{R})|\,E_n\left|\boldsymbol{\nabla}_{\boldsymbol{R}}u_n(\boldsymbol{R})\right\rangle. \tag{3.90}$$

That is

$$\langle u_m(\boldsymbol{R})|\,\boldsymbol{\nabla}_{\boldsymbol{R}}H\left|u_n(\boldsymbol{R})\right\rangle+\langle u_m(\boldsymbol{R})|\,H\left|\boldsymbol{\nabla}_{\boldsymbol{R}}u_n(\boldsymbol{R})\right\rangle=\boldsymbol{\nabla}_{\boldsymbol{R}}E_n\delta_{mn}+E_n\left\langle u_m(\boldsymbol{R})|\boldsymbol{\nabla}_{\boldsymbol{R}}u_n(\boldsymbol{R})\right\rangle. \tag{3.91}$$

We can also make use of the hermiticity relationship of Hamiltonian: $\langle u_m(\boldsymbol{R})| H |\boldsymbol{\nabla_R} u_n(\boldsymbol{R})\rangle = E_m \langle u_m(\boldsymbol{R})|\boldsymbol{\nabla_R} u_n(\boldsymbol{R})\rangle$. Then we can obtain:

$$\langle u_m(\boldsymbol{R})| \boldsymbol{\nabla_R} H |u_n(\boldsymbol{R})\rangle + E_m \langle u_m(\boldsymbol{R})|\boldsymbol{\nabla_R} u_n(\boldsymbol{R})\rangle = \boldsymbol{\nabla_R} E_n \delta_{mn} + E_n \langle u_m(\boldsymbol{R})|\boldsymbol{\nabla_R} u_n(\boldsymbol{R})\rangle . \tag{3.92}$$

So, for $n \neq m$, we can conclude the identity as

$$\langle u_m(\boldsymbol{R})|\boldsymbol{\nabla_R} u_n(\boldsymbol{R})\rangle = \frac{\langle u_m(\boldsymbol{R})| \boldsymbol{\nabla_R} H |u_n(\boldsymbol{R})\rangle}{E_n - E_m}. \tag{3.93}$$

We should notice the completeness relation for the basis

$$\sum_m |u_m\rangle \langle u_m| = 1. \tag{3.94}$$

The Berry phase can be expressed by substituting Eq. (3.79) into Eq. (3.90)

$$\begin{aligned}
\gamma_C &= i \int_{\boldsymbol{S}} d\boldsymbol{S} \cdot \Omega(\boldsymbol{R}) \\
&= i \int_{\boldsymbol{S}} d\boldsymbol{S} \cdot \boldsymbol{\nabla} \times \langle u_n| \boldsymbol{\nabla} |u_n\rangle \\
&= i \int_{\boldsymbol{S}} d\boldsymbol{S} \cdot [\langle \boldsymbol{\nabla} u_n| \times |\boldsymbol{\nabla} u_n\rangle + \langle u_n| \boldsymbol{\nabla} \times |\boldsymbol{\nabla} u_n\rangle] \\
&= i \int_{\boldsymbol{S}} d\boldsymbol{S} \cdot \langle \boldsymbol{\nabla} u_n| \times |\boldsymbol{\nabla} u_n\rangle \\
&= i \int_{\boldsymbol{S}} d\boldsymbol{S} \cdot \sum_{m, m\neq n} \langle \boldsymbol{\nabla} u_n | u_m\rangle \times \langle u_m|\boldsymbol{\nabla} u_n\rangle .
\end{aligned} \tag{3.95}$$

The phase factor should be a real number. So the above equation suggests the Berry phase is the negative value of the imaginary part

$$\gamma_C = -Im \int_{\boldsymbol{S}} d\boldsymbol{S} \cdot \sum_{m, m\neq n} \langle \boldsymbol{\nabla} u_n | u_m\rangle \times \langle u_m|\boldsymbol{\nabla} u_n\rangle . \tag{3.96}$$

By substituting Eq (3.93) into Eq (3.96) and considering the commutative of the index m and n, we can finally obtain the perturbation theory expression of Berry curvature as

$$\Omega^n = Im \sum_{m\neq n} \frac{\langle u_n(\boldsymbol{R})| \boldsymbol{\nabla_R} H |u_m(\boldsymbol{R})\rangle \times \langle u_m(\boldsymbol{R})| \boldsymbol{\nabla_R} H |u_n(\boldsymbol{R})\rangle}{(E_n - E_m)^2}. \tag{3.97}$$

3.2.4 Magnetic monopole

In this part, we will discuss two simple examples of Berry phase applications. The Hamiltonian for a two level system is generally written as

$$H = \frac{1}{2}\begin{bmatrix} Z & X - iY \\ X + iY & -Z \end{bmatrix} = \frac{1}{2}(\boldsymbol{R} \cdot \boldsymbol{\sigma}). \tag{3.98}$$

The two states have the eigenvalues of $E_\pm = \pm R = \pm\sqrt{X^2 + Y^2 + Z^2}$, crossing with each other at the original point ($\boldsymbol{R} = 0$). This result demonstrates that the degeneracy occurs when all three parameters vanish, which has been originally discovered by V Neumann and Wigner [193]: it is necessary to vary three parameters in order to obtain an accident degeneracy for a Hermit Hamiltonian. The gradient of the Hamiltonian is $\boldsymbol{\nabla}_{\boldsymbol{R}} H = \frac{1}{2}\boldsymbol{\sigma}$. Therefore the Berry curvature is

$$\Omega = \frac{1}{2}\frac{\boldsymbol{R}}{R^2}, \tag{3.99}$$

which can be considered as a magnetic field originated from a monopole at the original point. In the monopole, the integration of the Berry curvature over a sphere on the surface can be calculated as

$$\frac{1}{2\pi}\int_{\boldsymbol{S}} d\boldsymbol{S}\cdot\Omega = 1. \tag{3.100}$$

The divergence of the curvature is

$$\boldsymbol{\nabla}_{\boldsymbol{R}}\cdot\Omega = 2\pi\delta(\boldsymbol{R}). \tag{3.101}$$

Obviously, the magnetic field behaves like a point resource field at $\boldsymbol{R} = 0$, leading to Berry curvature. Such special field is called as “magnetic monopole” [193].

3.2.5 Berry phase for Bloch bands

In a solid system with crystal periodicity, the eigenstate $\psi_{n\boldsymbol{k}}$ in the Hamiltonian is expressed by the quantum number of ($\boldsymbol{k}$, n). Based on Bloch theory, the eigenstate is expressed by

$$\psi_{n\boldsymbol{k}}(\boldsymbol{r}) = e^{i\boldsymbol{k}\cdot\boldsymbol{r}}u_{n\boldsymbol{k}}(\boldsymbol{r}) \tag{3.102}$$

and

$$H\psi_{n\boldsymbol{k}}(\boldsymbol{r}) = E_{n\boldsymbol{k}}\psi_{n\boldsymbol{k}}(\boldsymbol{r}). \tag{3.103}$$

In the momentum representation, we can rewrite

$$H_{\boldsymbol{k}}\psi_{n\boldsymbol{k}}(\boldsymbol{r}) = E_{n\boldsymbol{k}}\psi_{n\boldsymbol{k}}(\boldsymbol{r}), \tag{3.104}$$

where $H(\boldsymbol{k})$ is generated by Fourier transformation

$$H_{\boldsymbol{k}}\psi_{n\boldsymbol{k}(\boldsymbol{r})} = e^{-i\boldsymbol{k}\cdot\boldsymbol{r}}He^{i\boldsymbol{k}\cdot\boldsymbol{r}}. \tag{3.105}$$

If we select k as the parameter $\boldsymbol{R}$ in the Berry phase, we can construct Berry connection as

$$A^n(\boldsymbol{k}) = i\left\langle u_{n\boldsymbol{k}}\right|\frac{\partial}{\partial\boldsymbol{k}}\left|u_{n\boldsymbol{k}}\right\rangle. \tag{3.106}$$

For the Bloch bands, we select the closed path over the whole Brillouin zone (BZ). Based on Eqs. (3.83) and (3.79), the Berry phase is written as

$$\gamma_C = i\int_{BZ} d\boldsymbol{k}\cdot\left\langle u_n(\boldsymbol{k})\right|\boldsymbol{\nabla}_{\boldsymbol{k}}\left|u_n(\boldsymbol{k})\right\rangle. \tag{3.107}$$

Similar to Eq. (3.85), the Berry curvature of the Bloch bands is expressed by

$$\boldsymbol{\Omega}^n(\boldsymbol{k}) = \boldsymbol{\nabla_k} \times \langle u_n(\boldsymbol{k})| i\boldsymbol{\nabla_k} |u_n(\boldsymbol{k})\rangle . \tag{3.108}$$

In a solid system, the driving force of the electron dynamics could be either an external electric or magnetic field. In the weak field condition, we can use the perturbation theory to express the Berry curvature as

$$\Omega^n_{ij} = Im \sum_{m\neq n} \frac{\langle u_{n\boldsymbol{k}}(\boldsymbol{k})| \boldsymbol{\nabla}_{\boldsymbol{k}i} H_{\boldsymbol{k}} |u_{m\boldsymbol{k}}(\boldsymbol{k})\rangle \times \langle u_{m\boldsymbol{k}}(\boldsymbol{k})| \boldsymbol{\nabla}_{\boldsymbol{k}j} H_{\boldsymbol{k}} |u_{n\boldsymbol{k}}(\boldsymbol{k})\rangle}{(E_{n\boldsymbol{k}} - E_{m\boldsymbol{k}})^2}. \tag{3.109}$$

In general, we are interested in Hamiltonian which dependents not only on the $\boldsymbol{k}$ but also another parameter λ, meaning $H = H(\lambda, \boldsymbol{k})$. In general, the Berry phase should be in phase $(\lambda, \boldsymbol{k})$ space with components: $\boldsymbol{\Omega}^n_{\boldsymbol{kk}} \equiv \boldsymbol{\Omega}^n_{\boldsymbol{k}}$ and $\Omega^n_{\lambda\lambda} \equiv \Omega^n_\lambda$, which can be easily obtained from Eq. (3.109). Merging k_i and k_j in $\boldsymbol{k}$, we can write a Berry curvature involving λ- and $\boldsymbol{k}$-derivatives:

$$\boldsymbol{\Omega}^n_{\lambda\boldsymbol{k}} = Im \sum_{m\neq n} \frac{\langle u_{n\boldsymbol{k}}| \boldsymbol{\nabla_k} H(\boldsymbol{k}, \lambda) |u_{m\boldsymbol{k}}\rangle \times \langle u_{m\boldsymbol{k}}| \boldsymbol{\nabla}_\lambda H(\boldsymbol{k}, \lambda) |u_{n\boldsymbol{k}}\rangle}{(E_{n\boldsymbol{k}} - E_{m\boldsymbol{k}})^2}, \tag{3.110}$$

which is called the mixed Berry curvature. Obviously, in the $\boldsymbol{k}$ space, the Berry curvature should obey the following symmetric constraints [194]: (i) having time-reversal symmetry, $\Omega^n(\text{-}\boldsymbol{k}) = \text{-}\Omega(\boldsymbol{k})$; (ii) having space-inversion $\Omega^n(\text{-}\boldsymbol{k}) = \Omega(\boldsymbol{k})$. Therefore, with both space and time inversion symmetries, the solid system will have exactly zero Berry curvature at each $\boldsymbol{k}$ point. In order to achieve non-trivial Berry curvature, the material can have (i) either non-zero electric polarization, breaking the space-inversion symmetry, (ii) or spontaneous magnetization (such as ferromagnetic or anti-ferromagnetic), which breaks the time inversion symmetry [194]. From now on, we will focus on the spontaneous magnetization situation.

3.2.6 Anomalous Hall conductivity

In this part, we will demonstrate the method to calculate the intrinsic anomalous Hall conductivity (AHC) in solids based on Berry phase approach. Let us begin with the unperturbed Hamiltonian

$$H = \frac{\boldsymbol{p}^2}{2m} + V(\boldsymbol{r}). \tag{3.111}$$

The evolution of velocity for electrons is beyond adiabatic approximation. On the other hand, under a weak electric field $\boldsymbol{\varepsilon}$, the Bloch theorem is invalid because the wave vector is not a good quantum number any more. Luckily, the time dependent electric field can be canceled out by introducing a uniform vector potential:

$$\frac{\partial}{\partial t}\boldsymbol{A}(t) = -\boldsymbol{\varepsilon}. \tag{3.112}$$

Then the Hamiltonian will be time dependent:

$$H(t) = \frac{1}{2m}(\boldsymbol{p} + e\boldsymbol{A}(t))^2 + V(\boldsymbol{r}). \tag{3.113}$$

After gauge transformation, the lattice translation symmetry is retained, implying momentum $\boldsymbol{p}$ becomes a good quantum number again. Taking the relationship of $\boldsymbol{p} = \hbar\boldsymbol{q}$, we can rewrite the Hamiltonian as:

$$H(\boldsymbol{q}, t) = H(\boldsymbol{q} + \frac{e}{\hbar}\boldsymbol{A}(t)). \tag{3.114}$$

The gauge-invariant crystal momentum is

$$\boldsymbol{k} = \boldsymbol{q} + \frac{e}{\hbar}\boldsymbol{A}(t). \tag{3.115}$$

Considering $\frac{d\boldsymbol{q}}{dt} = 0$, we can get

$$\frac{d\boldsymbol{k}}{dt} = -\frac{e}{\hbar}\boldsymbol{\varepsilon}. \tag{3.116}$$

The velocity operator is defined as

$$\boldsymbol{v} = \frac{d\boldsymbol{r}}{dt} = \frac{i}{\hbar}[H, \boldsymbol{r}]. \tag{3.117}$$

In momentum space, the velocity operator is then expressed as

$$\boldsymbol{v}(\boldsymbol{q}) = \frac{d\boldsymbol{r}}{dt} = e^{-i\boldsymbol{q}\cdot\boldsymbol{r}}\frac{i}{\hbar}[H, \boldsymbol{r}]e^{i\boldsymbol{q}\cdot\boldsymbol{r}} = \frac{1}{\hbar}\boldsymbol{\nabla}_{\boldsymbol{q}}H(\boldsymbol{q}, t). \tag{3.118}$$

Due to the time dependent term $\boldsymbol{A}(t)$, the wavefunction should be obtained by solving the time-dependent Schrödinger equation

$$i\hbar\frac{\partial}{\partial t}\left|\psi(t)\right\rangle = H(t)\left|\psi(t)\right\rangle. \tag{3.119}$$

We can express $\psi(t)$ in basis of the instantaneous eigenstates $u_n(t)$ as

$$\left|\psi(t)\right\rangle = \sum_n e^{-\frac{i}{\hbar}\int_0^t dt' E_n(t')} a_n(t)\left|u_n(\boldsymbol{q}, t)\right\rangle. \tag{3.120}$$

Based on time-dependent perturbation theory, we can rewrite the $\psi(t)$ by using the first order perturbation correction as [194]

$$\left|\psi(t)\right\rangle = e^{-\frac{i}{\hbar}\int_0^t dt' E_n(t')}[\left|u_n(\boldsymbol{q}, t)\right\rangle - i\hbar\sum_{m, m\neq n}\frac{\left\langle u_m(\boldsymbol{q}, t)\right|\frac{\partial}{\partial t}\left|u_n(\boldsymbol{q}, t)\right\rangle}{E_n - E_m}\left|u_m(\boldsymbol{q}, t)\right\rangle]. \tag{3.121}$$

Based on the velocity operator in Eq. (3.118), we can calculate the velocity with perturbated correction as

$$\boldsymbol{v}_n(\boldsymbol{q}) = -i\sum_{m, m\neq n}(\frac{\left\langle u_n(\boldsymbol{q}, t)\right|\boldsymbol{\nabla}_{\boldsymbol{q}}H\left|u_m(\boldsymbol{q}, t)\right\rangle \times \left\langle u_m(\boldsymbol{q}, t)\right|\frac{\partial}{\partial t}H(\boldsymbol{q}, t)\left|u_n(\boldsymbol{q}, t)\right\rangle}{(E_n - E_m)^2} - h.c.) + \frac{1}{\hbar}\boldsymbol{\nabla}_{\boldsymbol{q}}E_n(\boldsymbol{q}). \tag{3.122}$$

Furthermore, based on the mixed Berry phase in Eq. (3.110), we can write the Berry curvature in the ($\boldsymbol{q}$, t) space as

$$\Omega^n_{t\boldsymbol{q}} = -2Im \sum_{m\neq n} \frac{\langle u_{n\boldsymbol{q}}(\boldsymbol{q},t)| \boldsymbol{\nabla}_{\boldsymbol{k}} H(\boldsymbol{k},t) |u_{m\boldsymbol{q}}(\boldsymbol{q},t)\rangle \times \langle u_{m\boldsymbol{q}}(\boldsymbol{q},t)| \frac{\partial}{\partial t} H(\boldsymbol{q},t) |u_{n\boldsymbol{q}}(\boldsymbol{q},t)\rangle}{(E_{n\boldsymbol{q}} - E_{m\boldsymbol{q}})^2}, \tag{3.123}$$

So, the velocity is written as

$$v_n(\boldsymbol{q}) = \frac{1}{\hbar} - \Omega^n_{t\boldsymbol{q}}. \tag{3.124}$$

Using the identity relationship

$$\langle u_{n\boldsymbol{q}}(\boldsymbol{q},t)| \boldsymbol{\nabla}_{\boldsymbol{q}} H |u_{m\boldsymbol{q}}(\boldsymbol{q},t)\rangle = (E_n - E_m) \langle \boldsymbol{\nabla}_{\boldsymbol{q}} u_{n\boldsymbol{q}}(\boldsymbol{q},t)|u_{m\boldsymbol{q}}(\boldsymbol{q},t)\rangle, \tag{3.125}$$

we can also write the above Berry curvature as

$$\Omega^n_{t\boldsymbol{q}} = i(\left\langle \boldsymbol{\nabla}_{\boldsymbol{q}} u_{n\boldsymbol{q}}(\boldsymbol{q},t) \middle| \frac{\partial}{\partial t} u_{n\boldsymbol{q}}(\boldsymbol{q},t) \right\rangle - \left\langle \frac{\partial}{\partial t} u_{n\boldsymbol{q}}(\boldsymbol{q},t) \middle| \boldsymbol{\nabla}_{\boldsymbol{q}} u_{n\boldsymbol{q}}(\boldsymbol{q},t) \right\rangle). \tag{3.126}$$

In summary, in the weak electric field condition, the perturbation will create an anomalous transverse velocity which is proportional to the Berry curvature of the Bloch band [195]. From Eqs. (3.115) and (3.116), we can get:

$$\boldsymbol{\nabla}_{\boldsymbol{q}} = \boldsymbol{\nabla}_{\boldsymbol{k}} \tag{3.127}$$

$$\frac{\partial}{\partial t} = \frac{\partial}{\partial t}\boldsymbol{k} \cdot \boldsymbol{\nabla}_{\boldsymbol{k}} = -\frac{e}{\hbar}\boldsymbol{\varepsilon} \cdot \boldsymbol{\nabla}_{\boldsymbol{k}}. \tag{3.128}$$

Then the velocity is expressed by

$$v_n(\boldsymbol{k}) = \frac{1}{\hbar}\boldsymbol{\nabla}_{\boldsymbol{q}} E_n(\boldsymbol{k}) - \frac{e}{\hbar}\boldsymbol{\varepsilon} \times \Omega^n_{\boldsymbol{k}}, \tag{3.129}$$

where

$$\Omega^n(\boldsymbol{k}) = i \langle \boldsymbol{\nabla}_{\boldsymbol{k}} u_{n\boldsymbol{k}}| \times |\boldsymbol{\nabla}_{\boldsymbol{k}} u_{n\boldsymbol{k}}\rangle. \tag{3.130}$$

In format, the Berry curvature component is written as

$$\Omega^n_{ij}(\boldsymbol{k}) = Im \sum_{m,m\neq n} \frac{\langle u_{n\boldsymbol{k}}| \boldsymbol{\nabla}_{\boldsymbol{k}_i} H |u_{m\boldsymbol{k}}\rangle \times \langle u_{m\boldsymbol{k}}| \boldsymbol{\nabla}_{\boldsymbol{k}_j} H |u_{n\boldsymbol{k}}\rangle}{(E_n - E_m)^2} \tag{3.131}$$

Overall, the external field creates an adiabatic process, where the non-zero Berry curvature will produce a transverse velocity. Based on the previous semiclassical Boltzmann transport theory, the electric current density is expressed by the Fermi-Dirac distribution function ($f(\boldsymbol{k})$)

$$\boldsymbol{j}^\alpha = -\frac{2e}{(2\pi)^2} \int d\boldsymbol{k} f(\boldsymbol{k}) \boldsymbol{v}^\alpha(\boldsymbol{k}) \cdot \boldsymbol{\varepsilon}. \tag{3.132}$$

The first term in Eq. (3.129) makes no contribution to the current density due to anti-symmetry of Bloch bands. Considering $j_\alpha = \sigma_{\alpha\beta}\epsilon_{\alpha\beta}\varepsilon_\beta$, we can finally conclude the expression of anomalous Hall conductivity as:

$$\sigma_{\alpha\beta} = \frac{e^2}{\hbar} \sum_n \int_{BZ} d\boldsymbol{k} \Omega^n_{\alpha\beta}. \tag{3.133}$$

It should be noticed that the anomalous Hall conductivity expression can also be derived by the Kubo formula [196].

1. Qiang Gao, Ingo Opahle, and Hongbin Zhang. High-throughput screening for spin-gapless semiconductors in quaternary Heusler compounds. Physical Review Materials **3**, 024410 (2019).
2. Qiang Gao, Ingo Opahle, Oliver Gutfleisch, and Hongbin Zhang. Designing rare-earth free permanent magnets in heusler alloys via interstitial doping. Acta Materialia **186**, 355 (2020).
3. Qiang Gao and Hongbin Zhang. Magnetic i-MXene: a new class of multifunctional two-dimensional materials. Nanoscale **12**, 5995 (2020).
4. Dominik Ohmer, Qiang Gao, Ingo Opahle, Harish K. Singh, and Hongbin Zhang. High-throughput design of 211-M_2AX compounds. Physical Review Materials **3**, 053803 (2019).
5. Zeying Zhang, Qiang Gao, Cheng-Cheng Liu, Hongbin Zhang, and Yugui Yao. Physical Review B **98**, 121103(R) (2018).
6. Tingting Lin, Qiang Gao, Guodong Liu, Xuefang Dai, Xiaoming Zhang, and Hongbin Zhang. Current Applied Physics **19**, 721 (2019).

In this work, we have carried out a systematic high throughput screening for SGSs out of 12, 000 Heusler with different chemical compositions based on the empirical rule, and we successfully identified 70 SGSs which are thermodynamically, mechanically, and dynamically stable. It is demonstrated that the magnetization of such compounds can be understood following the Slater-Pauling rule but a new scheme of crystal field splitting of the D_{4h}-type is required, originated from the anisotropic chemical bonding. Furthermore, all four types of SGSs can be realized, where the conductivities show interesting behavior.

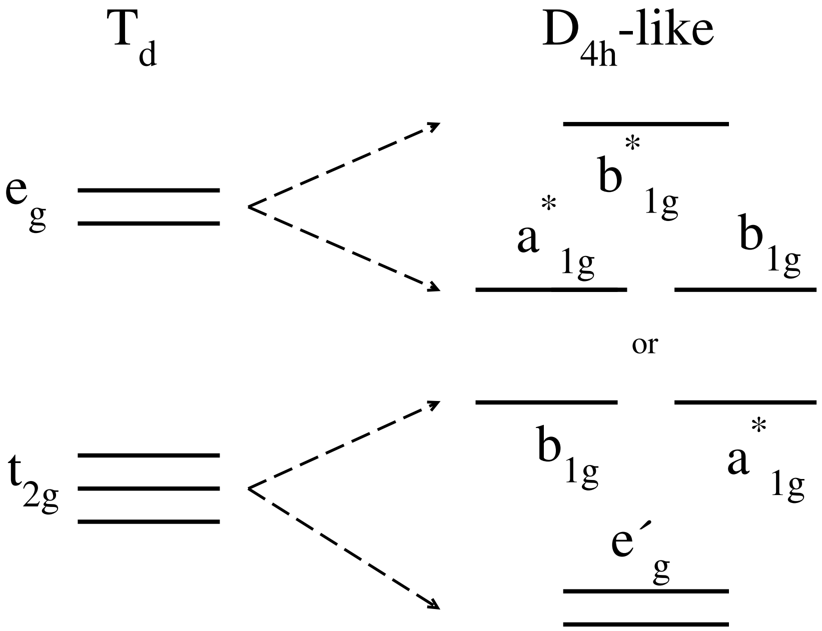

PHYSICAL REVIEW MATERIALS **3**, 024410 (2019)

High-throughput screening for spin-gapless semiconductors in quaternary Heusler compounds

Qiang Gao, Ingo Opahle, and Hongbin Zhang[*]
Institute of Materials Science, Technische Universität Darmstadt, 64287 Darmstadt, Germany

(Received 1 August 2018; revised manuscript received 14 December 2018; published 27 February 2019)

Based on high-throughput density functional theory calculations, we performed a systematic screening for spin-gapless semiconductors (SGSs) in quaternary Heusler alloys $XX'YZ$ (X, X', and Y are transition metal elements except Tc, and Z is one of B, Al, Ga, In, Si, Ge, Sn, Pb, P, As, Sb, and Bi). Following an empirical rule, we focused on compounds with 21, 26, or 28 valence electrons, resulting in 12 000 possible chemical compositions. After systematically evaluating the thermodynamic, mechanical, and dynamical stabilities, we have identified 70 so far unreported SGSs, confirmed by explicit electronic structure calculations with proper magnetic ground states, of which 17 candidates have a distance to the convex hull smaller than 0.10 eV/atom. It is demonstrated that all four types of SGSs can be realized, defined based on the spin characters of the bands around the Fermi energy. Type-II SGSs show promising transport properties for spintronic applications. The effect of spin-orbit coupling is investigated, resulting in large anisotropic magnetoresistance and anomalous Nernst effects.

DOI: 10.1103/PhysRevMaterials.3.024410

I. INTRODUCTION

In recent years, spin-gapless semiconductors (SGSs) have drawn intensive attention to the spintronics community. Conventional SGSs are half metals with the majority-spin channel being semimetallic, i.e., the gap is zero, while there is a finite band gap in the minority-spin channel. Following Ref. [1], four types of SGSs can be defined based on the spin character of the bands around the Fermi energy as sketched in Fig. 1(a). In the type-I SGSs, the valence band maximum (VBM) and conduction band minimum (CBM) are in the same spin channel while there is a gap in the opposite spin channel. This is the conventional SGS mentioned above. Moreover, the CBM and VBM can hold opposite spin characters, hereafter dubbed type-II SGSs. Additionally, if the VBM (CBM) is of one spin character while the CBMs (VBMs) originate from both spin channels, type-III (type-IV) SGSs will be defined. In principle, the VBM and CBM can touch each other at the same or different k points, corresponding to the direct or indirect zero band gap. In comparison to the usual half metals, the 100% spin-polarized carriers can be excited from the valence to conduction bands with no energy cost, leading to new functionalities and potential applications in logic gates. For instance, the spin-polarized transport properties of SGSs can be tuned by shifting the Fermi energy with finite gate voltages [1,2], which is promising for future spintronic applications.

Based on first-principles calculations, it was originally proposed that Co-doped $PbPdO_2$ can host the SGS state [1]. However, its Curie temperature (T_C) is just about 180 K [3], well below room temperature. The first above-room-temperature SGS was experimentally observed in the inverse Heusler Mn_2CoAl ($T_C = 720$ K) [2]. Later on, the Heusler compounds were considered outstanding candidates for SGSs. For example, ternary Heusler Ti_2MnAl, quaternary Heusler CoFeMnSi, and DO_3-type Heusler V_3Al were predicted theoretically to be SGSs [4–6] and also confirmed by experimental measurements [7–9]. Interestingly, during the explorations of SGSs in the Heusler compounds, an empirical rule was discovered. That is, the Heusler compounds with 18, 21, 26, or 28 valence electrons are more likely to realize the SGS phase [4,10,11]. However, there has been no systematic study to design novel SGS Heusler systems. Particularly, there are still a few questions about SGSs to be understood. For instance, all four types of SGSs should in principle exist but most experimentally studied systems are of type I and type II [4,5,10]. A particularly intriguing question is the effect of spin-orbit coupling (SOC) on the transport properties of SGSs, i.e., whether a band gap can be opened with nontrivial topological properties. Wang has proposed recently that SGSs are promising for massless and dissipationless spintronics and quantum anomalous Hall effects [12]. In this regard, SGSs with direct band touching will be very interesting, since they may host nontrivial topological properties after considering SOC.

On the other hand, high-throughput (HTP) screening based on density functional theory (DFT) calculations has been proven to be an efficient way to search for materials with desired properties [13,14]. Using the AFLOWLIB database, Carrete *et al.* have done HTP calculations on approximately 79 000 half-Heusler compounds and found 75 systems which are thermodynamically stable, where the thermal conductivities and thermoelectric performance have also been evaluated [15]. The Heusler compounds with ten valence electrons (X_2YZ, X = Ca, Sr, and Ba; Y= Au; Z = Sn, Pb, As, Sb, and Bi) are demonstrated to have ultralow lattice thermal conductivities according to He's HTP calculations [16]. In a more recent HTP study, He *et al.* have identified 99 new nonmagnetic semiconductors following the 18 valence electron rule with promising thermoelectric properties [17]. Furthermore, for spintronic applications, Ma *et al.* have performed a

---

[*] Corresponding author: hzhang@tmm.tu-darmstadt.de

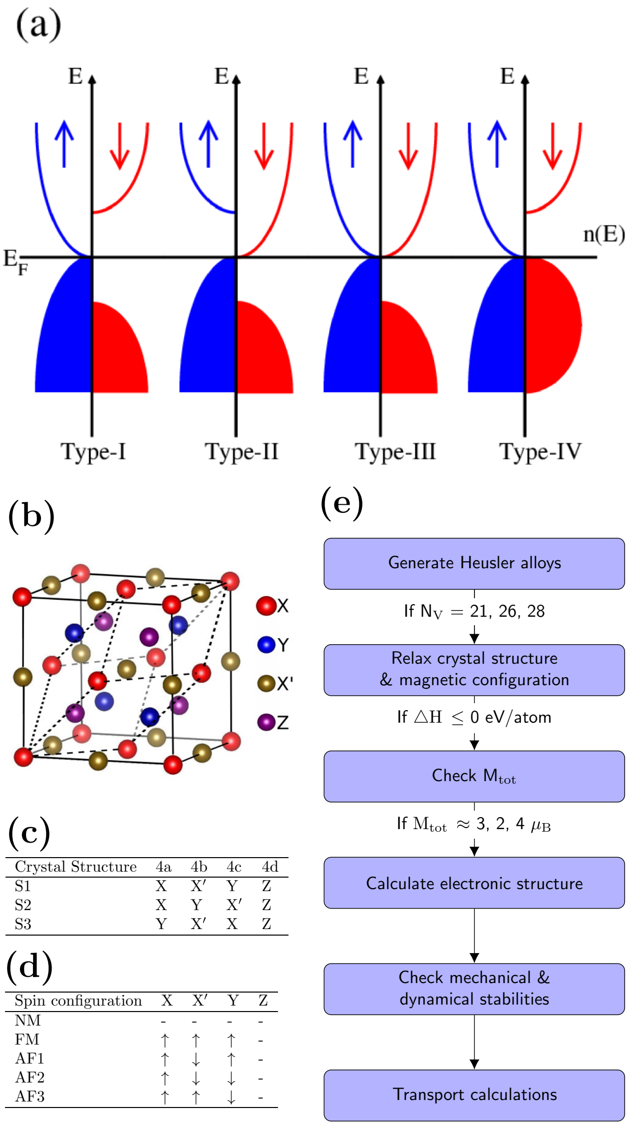

Crystal Structure	4a	4b	4c	4d
S1	X	X′	Y	Z
S2	X	Y	X′	Z
S3	Y	X′	X	Z

Spin configuration	X	X′	Y	Z
NM	-	-	-	-
FM	↑	↑	↑	-
AF1	↑	↓	↑	-
AF2	↑	↓	↓	-
AF3	↑	↑	↓	-

FIG. 1. (a) Sketches of the density of states for the four types of SGSs, defined based on the touching schemes of the majority (marked in blue) and minority (marked in red) bands. (b) The crystal structure of quaternary Heusler $XX'YZ$, where the solid (dashed) lines indicate the conventional cubic (primitive rhombohedral) cell. (c) The three possible site occupations for a quaternary Heusler alloy with a specific chemical composition. (d) The possible spin configurations within the primitive cell. (e) The work flow for the present HTP screening.

systemic HTP study on 405 inverse Heusler alloys resulting in 14 stable semiconductors and 10 half metals [18]. Focusing on the magnetic properties, Sanvito *et al.* did HTP calculations on 36 540 Heusler alloys, leading to 248 thermodynamically stable compounds with 20 magnetic cases [19]. Moreover, 21 antiferromagnetic Heusler compounds with high Néel temperature have been proposed for spintronic applications [20]. Last but not least, among 286 Heusler compounds, HTP screening calculations suggest 62% have a tetragonal structure due to the peak-and-valley character in the density of states [21].

In this work, we have carried out a systematic HTP screening for SGSs in Heusler compounds (including DO_3 binary, ternary, and quaternary Heusler systems). Based on the empirical rule, we considered 12 000 systems with 21, 26, or 28 valence electrons and identified 80 novel SGSs, which are thermodynamically stable based on the formation energies. Among them, 70 are both mechanically and dynamically stable. It is noted that the Heusler alloys with 18 valence electrons are also promising for realizing SGSs [4,7,22], which will be investigated in the future. We have identified all four types of SGSs in the quaternary Heusler compounds, together with one case showing direct band touching at the Fermi energy. The longitudinal and transversal transport properties were also evaluated based on the semiclassical transport theory, revealing that SGSs are promising materials for spintronic applications. It is demonstrated that the magnetization direction can be used to tailor the electronic structure and hence the physical properties for SGSs with heavy elements, due to the anisotropy caused by SOC.

II. COMPUTATIONAL DETAILS

We considered quaternary Heusler compounds with a general chemical formula $XX'YZ$, where X, X', and Y are transition metal elements except for the radioactive Tc, and Z is one of the main group elements among B, Al, Ga, In, Si, Ge, Sn, Pb, P, As, Sb, and Bi. For convenience, the ternary and binary (DO_3-type) Heusler systems are considered as quaternary Heusler by allowing X, X', or Y to be the same element. As shown in Fig. 1(b), quaternary Heusler $XX'YZ$ has the so-called LiMgPdSn-type structure with space group $F\bar{4}3m$ (space group 216), consisting of 4 Wyckoff positions 4a(0,0,0), 4c($\frac{1}{4}$, $\frac{1}{4}$, $\frac{1}{4}$), 4b($\frac{1}{2}$, $\frac{1}{2}$, $\frac{1}{2}$), and 4d($\frac{3}{4}$, $\frac{3}{4}$, $\frac{3}{4}$) [23,24]. According to the empirical rule for the number of valence electrons (N_V), all the possible chemical composition with 21, 26, and 28 valence electrons are generated, leading to about 12 000 possible compounds. Moreover, three site occupations are considered for each chemical composition, as shown in Fig. 1(c) [25]. Lastly, we consider that all the transition metal elements (X, X', and Y) are magnetic while the main group element (Z) is nonmagnetic (NM). For each chemical composition in each site occupation, we consider five spin configurations, namely, the NM, FM, AF1, AF2, and AF3 phases [Fig. 1(d)].

The HTP screening has been carried out in an automated way following the work flow shown in Fig. 1(e), managed with our in-house-developed high-throughput environment (HTE) [14,26]. The DFT calculations are performed using the Vienna *ab initio* Simulation Package (VASP) [27,28]. For each composition-occupation case, the structural relaxation is done in a two-step manner to save computational time. In the first step, ultrasoft pseudopotentials [29] are used in combination with the PW91 [30] exchange correlation functional, where the cutoff energy for the plane wave basis is set to 250 eV and a k-space density of 30 Å^{-1}. The follow-up finer relaxation is done using the projector augmented plane wave (PAW) method with the exchange-correlation functional under the generalized gradient approximation (GGA) parametrized by Perdew, Burke, and Ernzerhof (PBE) [31]. The cutoff energy for the plane wave expansion is increased to 350 eV and the k-mesh density is increased to 40 Å^{-1} to achieve good convergence. The structural relaxations are done for each magnetic configuration mentioned above.

After obtaining the magnetic ground state together with the optimized crystalline structures, the formation energy (ΔH) is evaluated to verify the thermodynamic stability, i.e., the stability with respect to decomposing into constituting elements. For a general quaternary Heusler $XX'YZ$, the formation energy is expressed as

$$\Delta H^{XX'YZ} = \tfrac{1}{4}[E^{XX'YZ} - (E^{X} + E^{X'} + E^{Y} + E^{Z})], \tag{1}$$

where E^X, $E^{X'}$, E^Y, and E^Z are the energies of elements X, X', Y, and Z in their bulk forms, while $E^{XX'YZ}$ is the ground state energy of $XX'YZ$. In addition, we also evaluated the distances to the convex hull based on the Open Quantum Materials Database (OQMD) [32].

The electronic structure together with the magnetic moments of the compounds with negative formation energies are calculated with a denser k mesh of $21 \times 21 \times 21$ using the full-potential local-orbital minimum-basis band structure scheme (FPLO) [33,34]. The SGS phase can be identified by examining the value of magnetic moments (i.e., being an integer following the Slater-Pauling rule as discussed below) and the band structure directly.

For the candidate SGSs, we further checked the mechanical and dynamical stability. The mechanical stability describes the stability of the crystal against deformations or distortions in terms of strain, which can be obtained based on the elastic constants (C_{ij}). The elastic constants are associated with the second-order change of the internal energy for a crystal under an arbitrary deformation of strain as

$$C_{ij} = \frac{1}{V_0}\left(\frac{\partial^2 E}{\partial\varepsilon_i \partial\varepsilon_j}\right), \tag{2}$$

where E is the internal energy, V_0 is the equilibrium volume of the crystal, and ε_i or ε_j denote applied strains. For a cubic crystal system (such as Heusler compounds in this work), the elastic constant matrix has only three independent elements as

$$C_{\text{cubic}} = \begin{bmatrix} C_{11} & C_{12} & C_{12} & 0 & 0 & 0 \\ C_{12} & C_{11} & C_{12} & 0 & 0 & 0 \\ C_{12} & C_{12} & C_{11} & 0 & 0 & 0 \\ 0 & 0 & 0 & C_{44} & 0 & 0 \\ 0 & 0 & 0 & 0 & C_{44} & 0 \\ 0 & 0 & 0 & 0 & 0 & C_{44} \end{bmatrix}. \tag{3}$$

Correspondingly, the Born stability conditions [35] suggest

$$C_{11} + 2C_{12} > 0, \quad C_{11} - C_{12} > 0, \quad C_{44} > 0, \tag{4}$$

which are related to the bulk, tetragonal, and shear moduli, respectively.

On the other hand, the dynamical stability describes the change of the total energy with respect to the internal degrees of freedom, i.e., the atomic displacements. In the harmonic approximation, the total energy of a crystal can be expressed as in terms of displacements $D_{\mathbf{R}\sigma}$,

$$E = E_0 + \frac{1}{2}\sum_{\mathbf{R},\sigma}\sum_{\mathbf{R}',\sigma'} D_{\mathbf{R}\sigma}\Phi^{\sigma\sigma'}_{\mathbf{R}\mathbf{R}'}D_{\mathbf{R}'\sigma'}, \tag{5}$$

where $\mathbf{R}$ is the position, σ is the Cartesian index, and $\Phi^{\sigma\sigma'}_{\mathbf{R}\mathbf{R}'}$ is the interatomic force constant matrix. The dynamical stability is determined by the dynamical matrix $D(\mathbf{q})$, which can be obtained from Fourier transformation of $\Phi(\mathbf{R})$ as follows:

$$D(\mathbf{q}) = \frac{1}{M}\sum_{R}\Phi(\mathbf{R})e^{-i\mathbf{q}\mathbf{R}}, \tag{6}$$

where $\mathbf{q}$ is the wave vector of phonon. Dynamical stability indicates that $D(\mathbf{q})$ is positive-definite, meaning all the phonons have real and positive frequencies $\omega(\mathbf{q})$. The phonon dispersion calculations are carried out using the Phonopy [36] package with force constants obtained from VASP.

Finally, the transport properties are studied for a few representative SGS candidates, including the anomalous Hall conductivity (AHC) and the longitudinal conductivity. The AHC is calculated by integrating the Berry curvature [$\Omega(\mathbf{k})$] over the whole Brillouin zone (BZ) as $\sigma_{xy} = \frac{e^2}{\hbar}\int_{BZ}\Omega(\mathbf{k})d^3\mathbf{k}$, with the Berry curvature given by

$$\Omega_{xy}(\mathbf{k}) = 2\mathrm{Im}\sum_{\epsilon_{n\mathbf{k}},\epsilon_{m\mathbf{k}}\leqslant E_F}\sum_{m\neq n}\frac{\langle\psi_{n\mathbf{k}}|v_x|\psi_{m\mathbf{k}}\rangle\langle\psi_{m\mathbf{k}}|v_y|\psi_{n\mathbf{k}}\rangle}{(\epsilon_{m\mathbf{k}}-\epsilon_{n\mathbf{k}})^2}, \tag{7}$$

where $\psi_{\alpha\mathbf{k}}$ is the spinor Bloch wave function corresponding to the eigenenergy $\epsilon_{\alpha\mathbf{k}}$, and v_i is the ith Cartesian component of the velocity operator. In our calculations, in order to achieve numerical convergence, the AHC is obtained using the Wannier interpolation technique based on the maximally localized Wannier functions [37]. Furthermore, the longitudinal conductivities at finite temperature (300 K) for SGSs are calculated based on the semiclassical theory with the BoltzTrap [38] code. Here the energy-independent relaxation time (τ) is used to approximate the distribution function as

$$\left(\frac{\partial f}{\partial t}\right)_s = -\frac{f - f_0}{\tau}, \tag{8}$$

where f_0 and f are the equilibrium and nonequilibrium distribution functions, respectively. The conductivity is expressed by

$$\sigma_{\alpha\beta}(T,\mu) = \frac{1}{V}\int\bar{\sigma}_{\alpha\beta}(\epsilon)\left[-\frac{\partial f_0(T,\epsilon,\mu)}{\partial\epsilon}\right]d\epsilon, \tag{9}$$

where α and β are the Cartesian indices, and V and μ indicate the unit cell volume and the chemical potential, respectively. The transport distribution function $\bar{\sigma}_{\alpha\beta}(\epsilon)$ can be evaluated by

$$\bar{\sigma}_{\alpha\beta}(\epsilon) = \frac{e^2}{N}\sum_{i,\mathbf{k}}\tau\cdot v_\alpha(i,\mathbf{k})\cdot v_\beta(i,\mathbf{k})\cdot\frac{\delta(\epsilon-\epsilon_{i,\mathbf{k}})}{d\epsilon}, \tag{10}$$

$$v_\alpha(i,\mathbf{k}) = \frac{1}{\hbar}\nabla_k\epsilon_{i,\mathbf{k}}, \tag{11}$$

where $\mathbf{k}$, i, and N are the wave vector, band index, and the number of the sampled $\mathbf{k}$ points. For bonding analysis, the crystal orbital Hamilton population (COHP) was evaluated using the LOBSTER code [39].

III. RESULTS AND DISCUSSION

A. HTP search validation

To validate our HTP scheme, we collected previously reported Heusler SGSs, and compared with our DFT results (Table I). The lattice constants, total magnetic moments

TABLE I. Comparisons between our HTP calculations and previous reported SGSs. For the mechanical and dynamical stabilities, “1” (“0”) indicates the system is stable (unstable). “Ref. Exp.” and “Ref. Cal.” denote experimental and computational references. The latt., ΔH, and ΔE_{con} are the lattice constant, formation energy, and distance to the convex hull per atom. “Dyn. sta.” and “Mec. sta.” mean dynamical and mechanical stabilities.

Compound	latt. (Å)	M_{tot} (μ_B)	ΔH (eV/at.)	Mec. sta.	Dyn. sta.	ΔE_{con} (eV/at.)
			$N_V = 21$			
Ti_2CoSi	5.081	3.00	−0.3718	0	1	0.3222
Ref. Cal. [4]	6.030	3.03				
MnCrTiSi	5.855	3.02	−0.4103	1	1	0.1237
Ref. Cal. [40]	5.860	2.98				
MnCrVAl	5.897	3.00	−0.2110	1	1	0.0023
Ref. Cal. [40]	5.900	2.99				
MnVTiAs	5.978	2.90	−0.2353	1	1	0.3807
Ref. Cal. [40]	5.990	2.87				
CoVTiAl	5.978	3.00	−0.3248	1	1	0.1032
Ref. Cal. [40]	6.040	3.00				
FeVTiSi	5.978	3.02	−0.4351	1	1	0.1899
Ref. Cal. [40]	5.910	2.99				
FeCrTiAl	5.964	3.02	−0.2920	1	1	0.0720
Ref. Cal. [40]	5.970	3.00				
CoVHfGa	6.193	2.95	−0.2434	1	1	0.1916
Ref. Cal. [41]	6.260	3.00				
CrFeHfGa	6.127	3.00	−0.1858	1	1	0.1252
Ref. Cal. [41]	6.261	3.02				
ZrCoVIn	6.445	2.97	−0.0632	0	1	0.2468
Ref. Cal. [10]	6.468	3.00	−0.3500			
ZrFeCrIn	6.408	3.02	0.0279	1	0	0.2419
Ref. Cal. [10]	6.419	3.00	−0.0325			
ZrFeCrGa	6.177	3.00	−0.1690	1	1	0.1580
Ref. Cal. [10]	6.184	3.00	−0.2400			
ZrFeVGe	6.199	3.06	−0.2069	1	0	0.2691
Ref. Cal. [10]	6.210	3.00	−0.2500			
			$N_V = 26$			
Mn_2CoAl	5.729	2.01	−0.2666	1	1	0.0404
Ref. Exp. [2]	5.798	2.00				
Ref. Cal. [42]	5.760	2.00				
CoFeCrAl	5.692	2.00	−0.1931	1	1	0.1139
Ref. Exp. [43]	5.736	2.00				
Ref. Cal. [44]	5.710	2.00	−0.2500			
CoFeCrGa	5.717	2.00	−0.0686	1	1	0.0984
Ref. Exp. [45]	5.736	2.00				
Ref. Cal. [44]	5.730	2.00				
CoFeTiAs	5.835	2.00	−0.3615	1	1	0.2895
Ref. Cal. [40]	5.850	1.99				
CoMnCrSi	5.669	2.00	−0.3280	1	1	0.0710
Ref. Cal. [5]	5.630	2.00	−0.3750			
FeMnCrSb	6.059	2.00	0.0996	1	1	0.2896
Ref. Cal. [5]	5.980	2.00				
ZrCoFeP	5.941	2.00	−0.3491	0	0	0.5949
Ref. Cal. [10]	5.944	2.00	−0.6500			
			$N_V = 28$			
CoFeMnSi	5.597	4.00	−0.3833	1	1	0.0137
Ref. Exp. [8]	5.658	4.00				
Ref. Cal. [46]	5.609	4.00				
Mn_2CuAl	5.710	0.00	−0.1066	0	0	0.0454
Ref. Cal. [47]	5.650	0.00				
Cr_2ZnSi	5.972	0.00	0.08745	1	0	0.3500
Ref. Cal. [48]	5.850	0.00				
Cr_2ZnGe	6.123	0.00	0.1898	1	1	0.2750
Ref. Cal. [48]	6.140	0.22				
Cr_2ZnSn	6.413	0.00	0.3079	1	0	0.3079
Ref. Cal. [48]	6.530	0.14				

(Table I), and the electronic structure (not shown) are in good agreement with the literature. However, even though the formation energies for most of the reported Heusler SGSs are negative, ZrFeCrIn and Cr_2ZnX ($X =$ Si, Ge, and Sn) turn out to be thermodynamically unstable in our HTP calculations. For ZrFeCrIn, in the previous calculations [10], the energies of composite elements with the fcc structure are considered, which leads to an underestimation of the formation energy. This explains also the big difference for the formation energy of ZrCoVIn. For the Cr_2ZnX ($X =$ Si, Ge, and Sn) compounds, only the inverse Heusler structure is considered in Ref. [48]. According to our calculations, for all three compounds, an antiferromagnetic metallic configuration in the full Heusler structure is energetically preferable, but the formation energies are still positive. Clearly, even though the electronic structure might be interesting with the hypothetical crystal structures, the stability should be checked before making valid predictions.

For quaternary compounds, the thermodynamical stability with respect to other competing binary, ternary, and quaternary phases, i.e., the distance to the convex hull, should also be evaluated. We note that 55 previously unknown, thermodynamically stable (low convex hull) quaternary Heusler compounds are discovered among 2 000 000 compounds by using a machine-learning method [49]. Moreover we evaluate the distances to the convex hull. As shown in Table I, for the experimentally synthesized cases, CoFeCrAl and CoFeCrGa have distances to the convex hull of 0.1139 and 0.0984 eV/atom, respectively. As reported, CoFeCrAl and CoFeCrGa are stable in partially disordered and ordered phases [43,45,50], respectively. This suggests that quaternary Heusler compounds with a distance to the convex hull of 0.10 eV/atom can still be synthesized. On the other hand, Mn_2CoAl has a small convex hull of 0.0404 eV/atom, and CoFeMnSi is the most stable one with respect to the competing phases as its distance to the convex hull is just 0.0137 eV/atom. In this regard, we suspect that MnCrVAl, CoVTiAl, FeCrTiAl, CoMnCrSi, and Mn_2CuAl from previous theoretical calculations are more likely to be synthesized.

Furthermore, it is observed that the mechanical stability or the dynamical stability criteria are also critical for some previously predicted compounds. For instance, according to our calculations, Ti_2CoSi and ZrCoVIn are mechanically unstable, ZrFeVGe is dynamically unstable, and ZrCoFeP and Mn_2CuAl are both mechanically and dynamically unstable. We note that such compounds may still be synthesized experimentally using molecular beam epitaxy, which is known

TABLE II. Basic information on the newly predicted SGS candidates with negative formation energies (ΔH). Candidates with a distance to the convex hull (ΔE_{con}) less than 0.10 eV/atom are highlighted in bold. The compounds with symbol † are either dynamically or mechanically unstable.

$XX'YZ$ (4a,4b,4c,4d)	latt. (Å)	M_{tot} (μ_B)	ΔH (eV/atom)	ΔE_{con} (eV/atom)	SGS type	$XX'YZ$ (4a,4b,4c,4d)	latt. (Å)	M_{tot} (μ_B)	ΔH (eV/atom)	ΔE_{con} (eV/atom)	SGS type
$N_V = 21$						$N_V = 26$					
IrVYSn	6.720	3.00	-0.0942	0.5628	SOC-I	CoOsTiSb	6.255	2.00	-0.1635	0.3515	I
CoVYSn	6.620	3.00	-0.0862	0.3848	II	CoFeHfSb	6.232	2.00	-0.2847	0.2523	I
CoVScSn	6.402	3.00	-0.2049	0.2221	III	CoOsZrSb	6.453	2.00	-0.1075	0.4645	I
IrVScSn	6.518	3.00	-0.2488	0.4052	SOC-II	RhFeTiSb	6.259	1.95	-0.3896	0.1104	I
RhVScSn	6.518	3.00	-0.2773	0.3527	I	CoFeTiSb	6.074	2.00	-0.2948	0.2202	I
CoVYGe	6.377	3.00	-0.0763	0.4697	II	IrFeTiSb	6.287	1.99	-0.2932	0.3108	III
CoVScGe	6.145	3.00	-0.2749	0.2931	II	CoRuTiSb	6.228	2.00	-0.3261	0.1889	I
IrVScGe	6.300	3.00	-0.3025	0.4045	II	CoFeNbGe	5.961	2.00	-0.2374	0.1506	I
RhVScGe	6.290	3.00	-0.3318	0.4502	II	CoOsNbSn†	6.352	2.00	-0.0609	0.2091	I
RhVYGe	6.512	3.00	-0.1377	0.5663	III	CoRuTaSn†	6.303	2.00	-0.1268	0.1852	I
CoVYSi	6.297	3.00	-0.1077	0.4701	II	IrFeTaSn	6.354	1.98	-0.1782	0.2328	I
CoVScSi	6.058	3.00	-0.3550	0.2990	II	CoOsTaGe	6.143	2.00	-0.0702	0.3048	I
IrVScSi	6.215	3.00	-0.4254	0.4096	SOC-II	CoOsTaSi†	6.064	1.99	-0.2546	0.2234	I
RhVScSi	6.210	3.00	-0.4242	0.4628	II	CoOsTaSn	6.332	2.00	-0.007	0.2413	I
RhVYSi	6.438	3.00	-0.1862	0.6398	III	CoFeTaGe	5.938	2.00	-0.2475	0.1275	I
PtVScAl	6.369	3.00	-0.4431	0.2869	SOC-I	CoFeTaSi	5.856	2.00	-0.4222	0.1275	I
PtVYAl	6.608	3.00	-0.2477	0.5013	I	**CoFeTaSn**	6.154	2.00	-0.1522	0.0898	I
PtVYGa	6.600	3.00	-0.1867	0.5733	I	**IrCoNbAl**	6.162	1.99	-0.5563	0.0277	I
FeCrHfAl	6.142	3.00	-0.2456	0.0504	II	**IrCoNbGa**	6.173	2.00	-0.4043	0.0097	I
OsCrHfAl	6.299	3.00	-0.403	0.0530	II	IrCoNbIn	6.360	2.00	-0.1326	0.1544	I
RuCrHfAl	6.284	3.00	-0.4544	0.0666	II	**IrCoTaAl**	6.140	2.00	-0.5579	0.0631	I
FeCrTiAl	5.964	3.00	-0.292	0.0504	II	IrCoTaGa†	6.150	2.00	-0.4200	0.0370	I
FeCrZrAl	6.194	3.00	-0.2156	0.0914	III	IrCoTaIn†	6.336	2.00	-0.1622	0.1768	I
OsCrZrAl	6.347	3.00	-0.3543	0.0617	SOC-II	CoCoNbAl†	5.970	2.00	-0.4312	0.0082	I
RuCrZrAl	6.335	3.00	-0.4154	0.0626	III	CoCoNbGa†	5.968	2.00	-0.3299	0.0001	I
FeCrScSi	5.992	3.00	-0.279	0.2400	II	CoCoNbIn†	6.179	2.00	-0.0869	0.0331	I
FeCrScSn	6.364	3.00	-0.0891	0.2309	II	IrCoTiPb	6.380	2.00	-0.0571	0.3829	I
FeCrYSi	6.236	3.00	-0.0081	0.4739	III	IrCoTiSn	6.276	2.00	-0.3789	0.1461	I
OsCrYSi	6.386	3.00	-0.0246	0.4860	SOC-III	**IrCoTiSi**	5.965	2.00	-0.6805	0.0785	I
CoVHfAl	6.211	3.00	-0.2896	0.1134	I	CoRuCrAl†	5.848	2.01	-0.2802	0.0558	II
IrVHfAl	6.346	3.00	-0.4634	0.1596	II	NiCrMnAl	5.809	2.00	-0.2127	0.1173	III
RhVHfAl	6.342	3.00	-0.3855	0.2355	II	NiReCrAl	5.920	1.97	-0.1633	0.2177	II
CoVZrAl	6.258	3.00	-0.2662	0.1408	I	**CoOsCrAl**	5.866	2.00	-0.2412	0.0688	II
CoVZrGa	6.238	3.00	-0.2317	0.2233	I	$N_V = 28$					
IrTiZrSn†	6.651	2.98	-0.3335	0.3965	II	**NiFeMnAl**	5.731	4.00	-0.2773	0.0577	IV
IrTiZrSi	6.385	2.96	-0.4232	0.4778	II	Continue with $N_V = 21$					
FeVNbAl	6.117	2.99	-0.2012	0.1238	II	**MnCrNbAl**	6.077	3.00	-0.1912	0.0228	II
FeVTaAl	6.097	2.99	-0.2202	0.0958	II	**MnCrTaAl**	6.053	2.99	-0.2124	0.0256	II
MnCrZrGe	6.157	2.99	-0.1473	0.2687	II	FeVHfGe	6.158	3.00	-0.2094	0.2646	II
MnCrZrSi	6.076	3.00	-0.2569	0.2621	II	FeVHfSi	6.079	3.00	-0.3187	0.2753	II
MnCrZrSn	6.393	3.00	-0.0593	0.2317	II	FeVHfSn	6.386	3.00	-0.129	0.1580	II

to be efficient in obtaining metastable crystalline phases. For all the systems which have been experimentally synthesized, such as CoFeCrAl, CoFeCrGa, CoFeMnSi, and Mn_2CoAl, we observed that they fulfill all three stability criteria based on our calculations. This confirms the reliability of our theoretical framework to do HTP screening for novel SGSs.

B. New SGS candidates

In the previous section we have shown that our high-throughput approach is suitable to identify realistic SGS candidates reported in the literature. We now proceed with HTP calculations for potential new SGS candidates following the work flow shown in Fig. 1(e). In total, we have identified 80 new SGS candidates with negative formation energies. These compounds are listed in Table II along with their calculated lattice parameters, total magnetic moment, formation energy, and the distance to the convex hull data as well as the type of SGS. More detailed information can be found in the Supplemental Material [51], including elastic constants, local magnetic moments, dynamical and mechanical stability (Sec. S1), as well as band structures (Secs. S3 and S4).

Among the SGS candidates listed in Table II, 70 compounds are also mechanically and dynamically stable. Consideration of the distance to the convex hull reduces the number of stable SGS candidates significantly. The results obtained in the previous section indicate that quaternary Heusler compounds with a distance to the convex hull ΔE_{con} of about 0.1 eV/atom can still be synthesized. This relatively large ΔE_{con} may be partially due to disorder effects. Among our newly predicted SGS candidates, 17 compounds have a distance to the convex hull below 0.1 eV/atom. These alloys are thus most likely to be synthesized and highlighted in Table II. CoRuCrAl, IrCoTaGa, and $\mathrm{Co_2Nb}X$ (X = Al, Ga, and In) also have very small distances (<0.03 eV/atom) to the convex hull, but are either dynamical or mechanical unstable. Such candidates may be synthesized by special experimental techniques such as the molecular beam epitaxy method.

Recent studies have shown that configuration-disorder-driven entropy can stabilize some oxides and alloys [52,53]. Similarly, CoFeCrAl with a distance to the convex hull as high as 0.1139 eV/atom can be synthesized due to Cr-Al antisite disorder [43,50]. Furthermore, disorder will also have an impact on the electronic structure. To explore this further, we performed a case study on NiFeMnAl. The total magnetic moment will be reduced by 8% for $\mathrm{Ni(Fe_{0.7}Mn_{0.3})(Mn_{0.7}Fe_{0.3})Al}$ with Fe-Mn antisite disorder. The energy bands are smeared out due to the disorder effect, but the main features of the electronic structures are still preserved. Detailed discussion of disorder effect can be found in Sec. S5 of the Supplemental Material [51].

Most of the newly predicted SGSs in Table II are quaternary Heusler compounds. We have only found three new ternary SGSs (e.g., $\mathrm{Co_2Nb}X$, X = Al, Ga, and In), but they are either dynamically or mechanically unstable. Among the previous predicted six ternary Heusler SGSs, only $\mathrm{Mn_2CoAl}$ is a stable candidate. In this regard, $\mathrm{Mn_2CoAl}$ is a special case. Our analysis on systems with the same number of valence electrons as $\mathrm{Mn_2CoAl}$, such as $\mathrm{Mn_2FeSi}$, reveals that the CBM and VBM have very strong overlap, destroying the SGS behavior. In general, the occurrence of the SGS phase depends significantly on detailed hybridization of the atomic orbitals, as discussed below. Therefore, the empirical rule on the number of electrons serves only as a qualitative guide, and explicit DFT calculations on the electronic structure are required to identify such phases. It is noteworthy that all four types of SGSs as sketched in Fig. 1(a) are represented in Table II. There are 28 (32, 9, and 1) type-I (type II, type-III, and type-IV) SGSs, respectively. In the following, we will discuss the electronic and magnetic properties for some representative cases among the 70 both mechanically and dynamically stable candidates, focusing on developing better understanding of the physical properties.

1. Magnetization

Essentially, SGSs are half metals; thus the total magnetic moments are expected to be integers, and they should obey the Slater-Pauling rule [10,40]. According to Table II, it is obvious that when N_V is 26 and 28, the resulting magnetic moments are 2.0 μ_{B} and 4.0 μ_{B} following $M_{\mathrm{tot}} = (N_V - 24)\ \mu_{\mathrm{B}}$, where M_{tot} and N_V are the total magnetic moment and number of valence electrons per unit cell, respectively. For the cases with N_V being 21, the total magnetic moments are 3.0 μ_{B} following $M_{\mathrm{tot}} = (N_V - 18)\ \mu_{\mathrm{B}}$. This is consistent with the expected values based on the Slater-Pauling rule.

Such behaviors of the magnetization for Heusler compounds can be understood based on the atomic models, as demonstrated in previous studies [10,40]. Generally, the magnitude of the magnetic moments is caused by the competition between the crystal field splitting (between t_{2g} and e_g states) and the exchange splitting (between the majority and minority spin channels) [54–56]. In Ref. [40], a picture with bonding and antibonding t_{2g} and e_g bands is applied to interpret the quaternary Heusler compounds with one magnetic ion, due to significant hybridization between the d orbitals. Such a picture has to be generalized in order to understand the magnetization of the quaternary Heusler SGSs, especially for cases with more than one type of magnetic atom.

The t_{2g}-e_g picture is valid for compounds with one magnetic ion. For instance, as shown by the density of states for PtVYAl (Fig. S1(a) in the Supplemental Material [51]), the t_{2g} states in the majority-spin channels are occupied, resulting in a total magnetization of 3.0 μ_{B} per formula unit. This is generally true for other cases with $N_V = 21$, such as XVScSn (X = Co, Ir, and Rh), PtVYAl, and FeCrScSi. For the $N_V = 26$ cases, the t_{2g} shells in both spin channels are filled, while the e_g state is only occupied in the majority-spin channel, leading to a total magnetization of 2.0 μ_{B} per formula unit, as demonstrated by IrFeTiSb Fig. S1(b) in the Supplemental Material.

The crystal field splitting changes greatly for systems with two or more magnetic ions. It is well known that for full Heusler with chemical formula X_2YZ, the site symmetry for both Y and Z is $m\bar{3}m$ (O_h), while that for X is $\bar{4}3m$ (T_d). The d shell will split into t_{2g} and e_g subshells in both O_h and T_d crystallographic symmetries [57]. For quaternary Heuslers, the site symmetry for X, X', Y, and Z sites is the same, i.e., of the T_d type. However, it is observed that the t_{2g}-e_g picture is not applicable in quaternary Heusler alloys with two magnetic ions, as detailed below.

In the tetrahedral crystal field (T_d symmetry), the doubly degenerated state e_g is lower in energy than the triply degenerated t_{2g} state [58]. It is noted that the relative energy level between the t_{2g} and e_g states depends on the bonding to the neighboring atoms [56]. Furthermore, we found that the t_{2g} and e_g shells will "split" into subshells, namely, $t_{2g} \rightarrow e'_g + b_{1g}$ and $e_g \rightarrow a^*_{1g} + b^*_{1g}$, as sketched in Fig. 2(a) (cf. Sec. S2.1 in the Supplemental Material [51] for a detailed discussion on the effect of chemical environment on the crystal field splitting). Taking FeVNbAl as an example, for both Fe and V atoms, as indicated by the partial density of states shown in Fig. 2(b), there are two peaks (marked as e'_g and b_{1g}) originating from the t_{2g} orbitals, which can accommodate two and one electrons, respectively. For the e_g orbitals, the two resulting peaks are denoted as a^*_{1g} and b^*_{1g}; each can host one electron. We want to emphasize that the $t_{2g} \rightarrow e'_g + b_{1g}$ and $e_g \rightarrow a^*_{1g} + b^*_{1g}$ "splitting" are not due to the lowering of the symmetry from T_d to D_{4h} but due to the strong d-d hybridization as detailed below. Thus we dub it the *D_{4h}-like picture*. As shown in Fig. S7 in the Supplemental Material [51], the resulting e'_g and b_{1g} subshells have equal contributions from the d_{xy}, d_{yz}, and d_{zx} orbitals, which is also the same for the

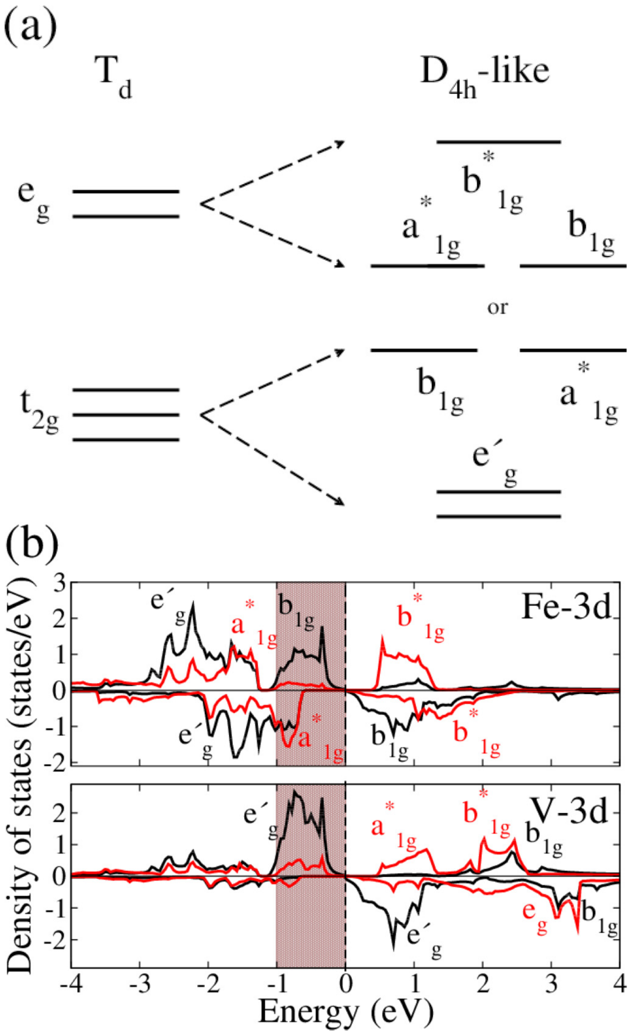

FIG. 2. (a) Sketch of crystal field splitting for magnetic atoms in typical quaternary Heusler compounds (see main text for detailed discussion). (b) Local density of states (LDOS) for Fe (upper panel) and V (lower panel) atoms in FeVNbAl. The dashed line denotes the Fermi level. The black and red curves denote the t_{2g} and e_g orbitals, respectively. The shaded region highlights the strong hybridization between the Fe-b_{1g} subshell and V-e'_g subshell in the majority spin channel, of which the energy range is from about -1 to 0 eV.

a^*_{1g} and b^*_{1g} subshells with equal contributions from the $d_{x^2-y^2}$ and $d_{3z^2-r^2}$ orbitals. In general, for the quaternary Heusler compounds, it is observed that the b_{1g} subshell originating from the t_{2g} shell can be either higher or lower in energy than the e_g-derived a^*_{1g} subshells [Figs. 2(a) and 2(b)].

Such a D_{4h}-*like picture* of crystal field splitting can be attributed to the bonding strength of different atomic pairs associated with the magnetic ions. For FeVNbAl, although the nearest-neighbor V-Nb bond length (2.64 Å) is the same as that of the nearest-neighbor V-Al bond, the integrated COHP for the V-Nb bonds is about −4.04 eV, which is much stronger than the V-Al bonding with an integrated COHP of −1.33 eV. The nearest-neighbor Fe-Nb and Fe-Al bond lengths are the same (2.64 Å), and also the integrated-COHP values are comparable (−2.33 eV and −2.07 eV). Moreover, the next-nearest-neighbor V-Fe bond length is about 3.05 Å, but the integrated COHP is about −1.62 eV, which is comparable to that of the nearest-neighbor V-Al, Fe-Nb, and Fe-Al bonds, indicating strong bonding between next-nearest-neighbor V-Fe bonds. Such features can be clearly observed from the DOS [Fig. 2(b)], where the hybridization between the d orbitals of V and Fe is obviously strong. Such splittings of the original t_{2g} and e_g shells do not result in the separation of the $\{d_{xy}, d_{yz}, d_{zx}\}$ (due to local tetragonal crystal fields) or $\{d_{x^2-y^2}, d_{3z^2-r^2}\}$ (due to Jahn-Teller like distortions) orbitals (cf. Fig. S7 in the Supplemental Material [51]), like the local tetragonal distortions on the d orbitals in the octahedral environment. In contrast, the $\{d_{xy}, d_{yz}, d_{zx}\}$ orbitals are still triply degenerated in the e'_g and b_{1g} subshells, while the $\{d_{x^2-y^2}, d_{3z^2-r^2}\}$ orbitals are still doubly degenerated in both a^*_{1g} and b^*_{1g} subshells (cf. Fig. S7 in the Supplemental Material [51]).

Following such a splitting scheme, the resulting magnetic moments for compounds with two magnetic elements can be easily understood. For the $N_V = 21$ cases such as FeVNbAl (cf. Fig. 2(b) and Fig. S5 in the Supplemental Material [51]), the magnetic moment of 2.0 μ_B on the V atoms is due to the e'_g subshell (which originates from t_{2g} shell) in the majority-spin channel [Fig. 2(b)]. Moreover, for the Fe atoms, the e'_g, b_{1g}, and a^*_{1g} subshells in the majority-spin channel are occupied, while only the e'_g and a^*_{1g} subshells in the minority-spin channel are occupied, resulting in a magnetic moment of 1.0 μ_B. It is noted that in this case the b_{1g} subshells can be higher in energy than the a^*_{1g} subshells. The magnetization of other two magnetic ion compounds with $N_V = 21$ can also be understood in a similar way (not shown).

A similar picture can also be applied to the $N_V = 26$ cases with two magnetic ions, where the total magnetic moments of 2.0 μ_B can be attributed to 1.0 μ_B atomic moments from two atoms. Here we take CoFeTaGe (cf. Fig. S2(b) and Fig. S6 in the Supplemental Material [51]) as an example. The bond lengths of nearest-neighbor Co-Ge and Fe-Ge almost have the same value as 2.57 Å. However the integrated COHP of Co-Ge is −1.62 eV, which is larger than that of Fe-Ge (−1.03 eV). Moreover, the next-nearest-neighbor Co-Fe bonds have a comparable bond length to the Co-Ge and Fe-Ge bonds (about 2.96 Å), but a much weaker bonding with integrated COHP as −0.50 eV. The resulting crystal field splittings are very comparable to those in the cases with $N_V = 21$ (cf. Fig. S6 in the Supplemental Material [51]). For the Co atoms, the only unoccupied state is the b^*_{1g} subshell in the minority-spin channel, whereas the majority-spin channel is fully occupied, resulting in a 1.0 μ_B magnetic moment. For the Fe atoms, the t_{2g} is not split in either spin channel and lies below the Fermi level. The e_g state is weakly split into a^*_{1g} and b^*_{1g} subshells below the Fermi level in the majority-spin channel. On the other hand, in the minority-spin channel the e_g state is split into a widespread a^*_{1g} subshell below the Fermi level and a localized b^*_{1g} above the Fermi level. So the majority-spin channel also has one more state than the minority-spin channel, resulting in one μ_B magnetic moment (cf. Fig. S6 in the Supplemental Material).

In short, it is observed that the magnetization of quaternary Heusler compounds with two magnetic ions can be understood based on the crystal splittings of the D_{4h}-*like* *picture*. Such splittings originate from the anisotropic bonding between the ions. In this regard, the required band filling to achieve SGSs is more flexible for quaternary Heusler compounds than the ternary cases. This explains also why we found more candidate SGSs in the quaternary Heusler systems, as mentioned above. On the other hand, as to the only new SGS (NiFeMnAl) with 28 electrons (cf. Fig. S3 in the Supplemental Material), the hybridization between *d* orbitals from the Ni, Fe, and Mn atoms is so strong that the atomic picture is not applicable. This is also true for the other cases with three magnetic ions.

2. Properties of four types of SGSs

For all four types of SGSs, the electronic structures for one representative case in each class are shown in Fig. 3, together with the AHCs and spin-resolved longitudinal conductivities. For PtVYAl, which is a type-I SGS, the VBM (at the Γ point) and CBM (at the X point) touch each other indirectly in the majority-spin channel, while there is a gap of about 0.6 eV in the minority-spin channel. Thus, the system is expected to show typical behavior of half metals, i.e., 100% spin-polarized transport properties. For type-II SGSs as exemplified by FeVHfSi, the VBM and CBM have the opposite spin characters and touch each other indirectly at the Fermi level [Fig. 3(b)]. In this case, the spin polarization of the resulting current can be tuned by tailoring the Fermi energy. For RuCrZrAl which represents type-III SGSs, the valence bands near the Fermi energy are mostly of the majority-spin character, while the conduction bands constitute both majority and minority spin character carriers. This is in contrast to the case of NiFeMnAl (a type-IV SGS), where the conduction bands originate from one spin channel while the valence bands have both majority and minority spin characters.

Such specific electronic structures for four types of SGSs can be reflected in the transport properties in terms of the AHC and longitudinal conductivity, shown as well in Fig. 3. Due to vanishing DOS at the Fermi energy, a common phenomenon for the four representative SGSs is that the AHC vanishes at Fermi level. That is, the indirect band gaps for such compounds are topologically trivial, i.e., there exists no quantum anomalous Hall effect. This is comparable with the experimental AHC of $\mathrm{Mn_2CoAl}$ (also a type-II SGS) [2]. Moreover, for type-II SGSs such as HfVFeSi, there is a sign change for the AHC around the Fermi energy, due to the fact that the spin character of the carriers changes when they are excited from VBM to CBM. The resulting derivative of the AHC is as high as 1597 S/(cm eV), corresponding to a large anomalous Nernst effect (ANE). In this sense, such type-II SGSs are likely promising candidates for engineering spintronic field-effect transistors.

The right panels of Fig. 3 display the spin-resolved longitudinal conductivities at 300 K for four types of SGSs. Like the AHC, the longitudinal conductivities of all four SGSs are quite low due to the vanishing DOS at the Fermi energy. For type-I SGSs as exemplified by PtVYAl, the conductivity mostly originates from the majority-spin channel, showing typical behavior of half metals. For type-II SGSs (FeVHfSi), due to the VBM and CBM with opposite spin characters, the spin polarization of the longitudinal conductivity can be conveniently tuned by controlling the chemical potential. Such compounds may be used to fabricate spin valves which are switchable via electrostatic gating. In case of type-III SGSs (RuCrZrAl), above the Fermi energy the conductivity has finite values for both spin channels, while the conductivity is nonzero only for one spin channel below the Fermi energy (Fig. 3). Such transport property is opposite that of the type-IV SGSs [Fig. 3(d)]. It is an interesting question how such two types of SGSs can be utilized for future spintronic devices.

3. Effects of spin-orbit coupling

It is observed that SOC can induce significant changes in the electronic structure of SGSs, since the band gaps of SGSs are on average of small magnitude (cf. Sec. S4 in the Supplemental Material [51]). For instance, for IrVScSn, the indirect band gap is about 58.4 meV without SOC [Fig. 4(a)]. When SOC is turned on with magnetization direction along the [001] direction, the band gap is reduced to only 0.6 meV. Such a large change in the magnitude of the band gap can be attributed to the fact that the CBM is mainly derived from the Ir-*d* orbitals, where the atomic SOC strength is about 0.5 eV. Such SOC effect on electronic structure is particularly associated with compounds constituted of heavy elements such as Os, Ir, and Pt, due to the strong atomic SOC strength. Similarly, it is expected that SOC has significant influence on the electronic structure for compounds with heavy elements such as Os, Ir, and Pt. This is indeed confirmed by our explicit DFT calculations for IrVScSn, IrVScSi, IrVYSn, PtVScAl, and OsCrZrAl (cf. Sec. S4 in the Supplemental Material), where the band gap size can be fine tuned by about 15 meV on average. As to OsCrYSi, the gap is even closed and the CBM and VBM are overlapping. In the following we discuss IrVScSn as an example for SOC effects on SGSs.

As the SGSs are magnetic, the combination of magnetic ordering with SOC lowers the symmetry of the systems, leading to magnetization-direction-dependent physical properties. Figure 4(c) shows the magnetization direction dependence of the band gap for IrVScSn, as the magnetization direction rotates in the (001) plane. Obviously, the magnitude of the band gap shows a continuous behavior of the sinusoidal type as a function of the azimuthal angle φ (the angle between the magnetization direction and the [100] axis). A maximal band gap of 14.8 meV is achieved for $\varphi = \frac{\pi}{4}$. Such changes in the fine structure of electronic structure can be manifested by the anisotropic magnetoresistance (AMR) effect. Using the constant relaxation time (τ) approximation, we estimated the AMR ratio at 300 K following the semiclassical transport theory, given by

$$\frac{\rho(0)-\rho\left(\frac{\pi}{4}\right)}{\rho(0)} = \frac{\frac{1}{\sigma(0)}-\frac{1}{\sigma(\frac{\pi}{4})}}{\frac{1}{\sigma(0)}} = \frac{\frac{1}{\sigma(0)/\tau}-\frac{1}{\sigma(\frac{\pi}{4})/\tau}}{\frac{1}{\sigma(0)/\tau}}, \qquad (12)$$

where $\sigma(\varphi)$ [$\rho(\varphi)$] is the longitudinal conductivity (resistivity) with the azimuthal angle φ for the magnetization direction in the (001) plane. This results in an AMR ratio as large as 33%. On the other hand, the magnetocrystalline anisotropy energy between such two cases with azimuthal angle $\varphi = 0$ and $\frac{\pi}{4}$ is only about 10^{-6} eV per formula unit, due to the underlying cubic symmetry. Therefore, we suspect that such materials with large AMR ratio and easily tunable

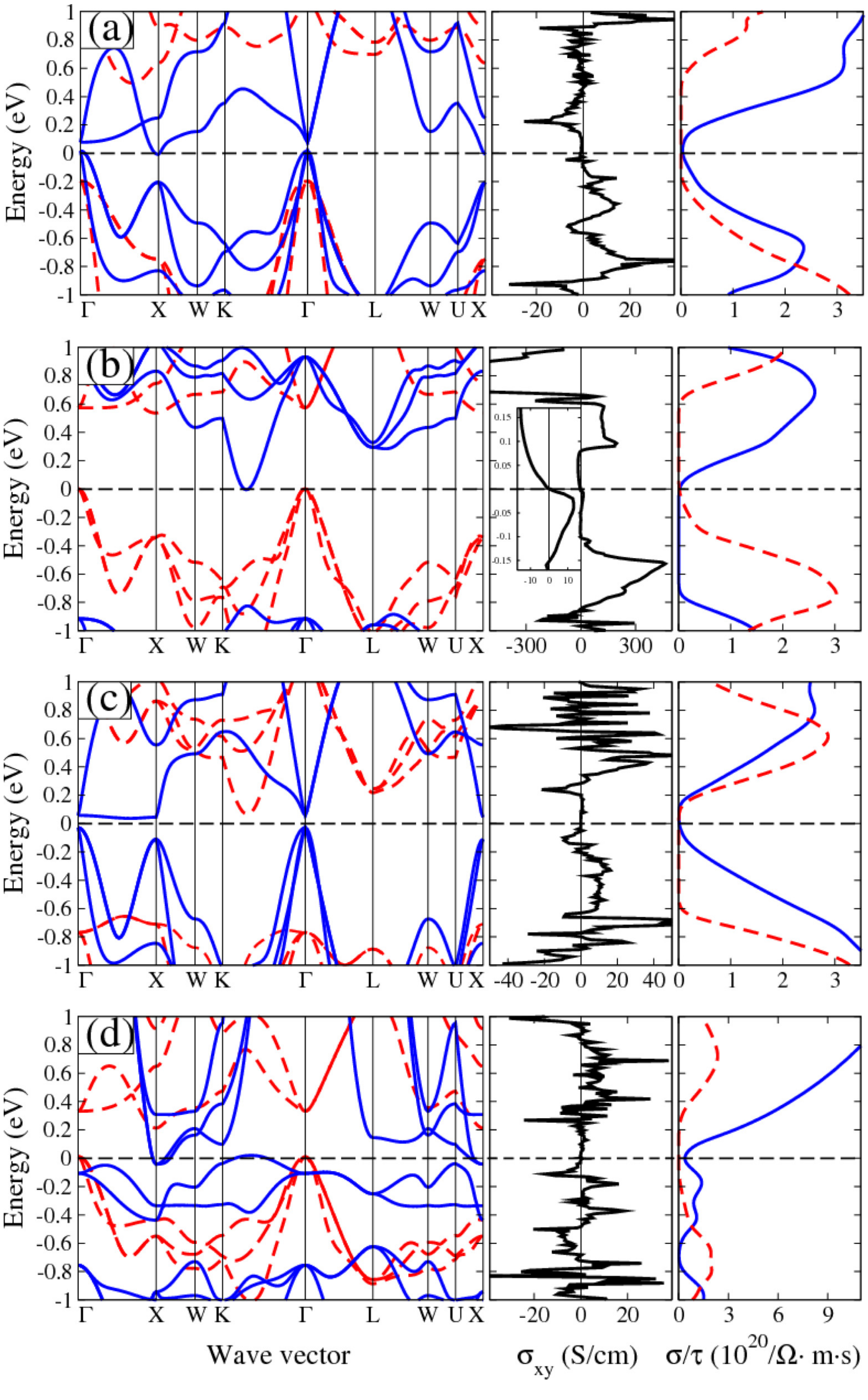

FIG. 3. (a), (b), (c), and (d) are the band structure (left), anomalous Hall conductivity (middle), and spin-resolved longitudinal conductivity (right) of PtVYAl (type I), FeVHfSi (type II), RuCrZrAl (type III), and NiFeMnAl (type IV), respectively. The inset in the middle panel of (b) displays the zoom-in of AHC ±0.17 eV around the Fermi energy. The solid blue and dashed red lines denote the majority and minority spin channels, respectively. The horizontal dashed lines indicate the Fermi energy.

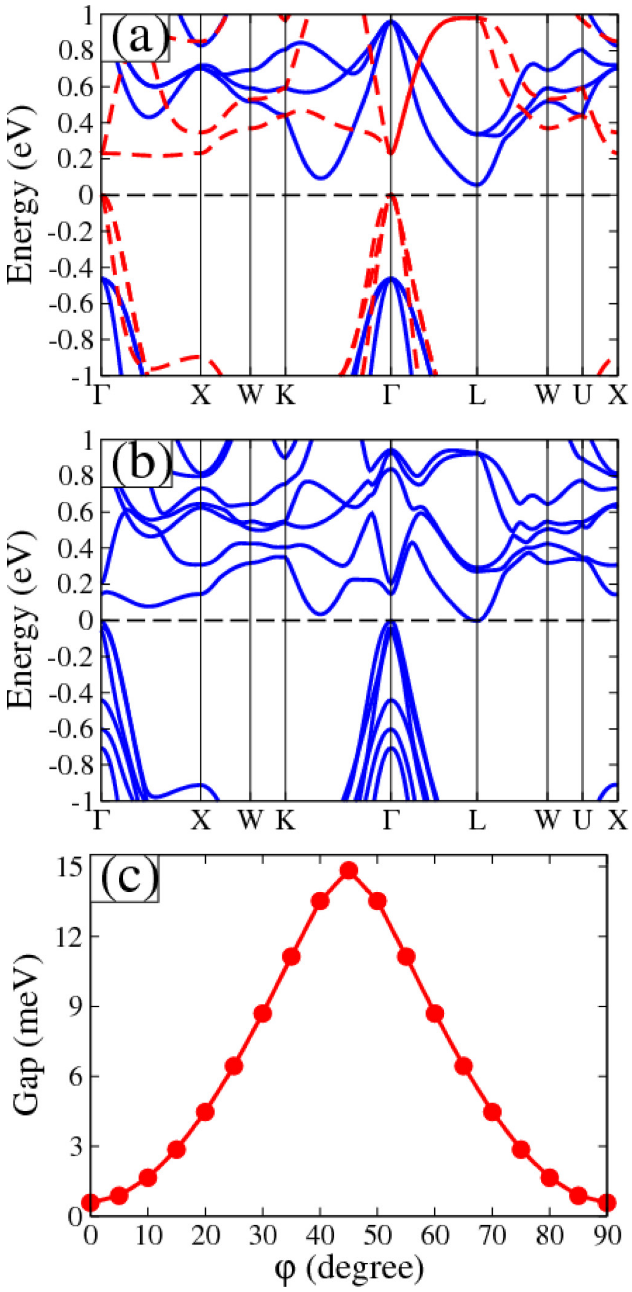

FIG. 4. (a) and (b) are the band structures of IrVScSn without and with SOC. Without SOC, the solid blue and dashed red curves are majority and minority spin channels, respectively. (c) The calculated gap as a function of azimuthal angle φ (the angle between the magnetization direction and the [100] axis) in the (001) plane. The horizontal dashed lines indicate the Fermi energy.

magnetization directions can be applied for future spintronic applications.

4. *SGS with direct band touching*

As shown in Fig. 5, we find NiCrMnAl is a special SGS, where a direct band touching occurs at the Γ point. Without considering SOC, the CBM from the minority-spin channel touches the VBM with the opposite spin character. That is, it is a type-II SGS following the classification discussed above. Unfortunately, due to the presence of a conduction band which goes slightly below the Fermi energy at the X point, the direct touching point is hidden. When SOC is turned on, a band gap of 24 meV is opened locally at the Γ point. However, the resulting band gap is topologically trivial according to the AHC shown in Fig. 5(c), since the AHC changes its sign around the Fermi energy, similarly to what we saw in the above discussions of FeVHfSi. Moreover, the AHC shows a singularity for an energy about 50 meV above the Fermi energy. This indicates there is band anticrossing in the electronic

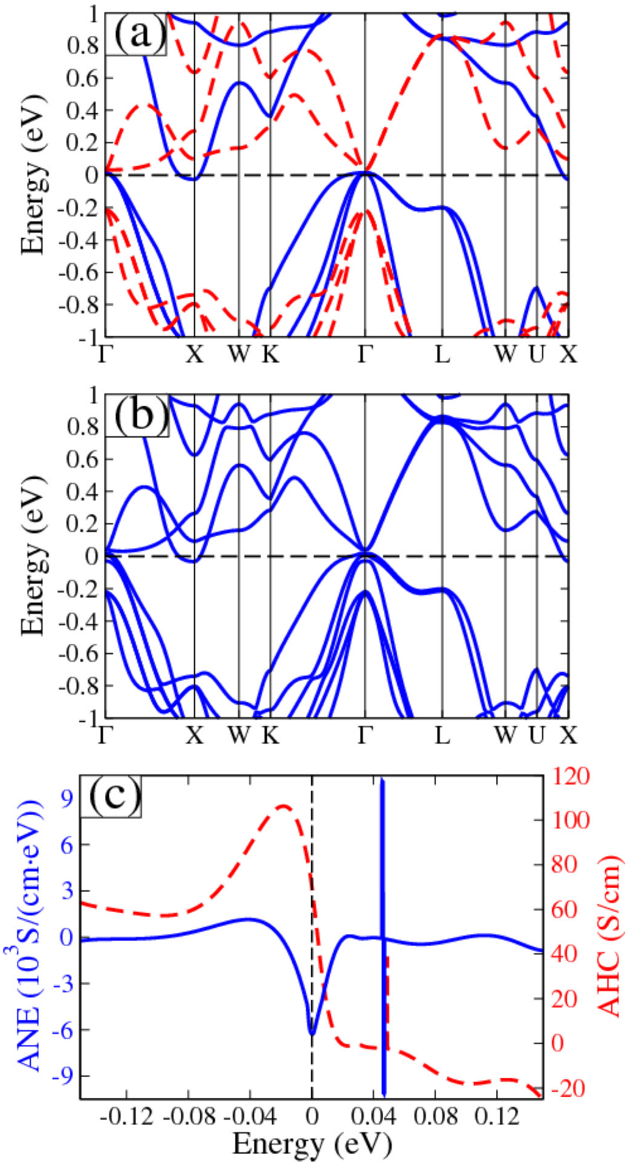

FIG. 5. (a) and (b) are the band structures of NiCrMnAl without and with SOC. Without SOC, the solid blue and dashed red curves are majority and minority spin channels, respectively. (c) The dashed red and solid blue curves are AHC and ANE results ±0.15 eV around Fermi level, respectively. The horizontal [panels (a) and (b)] and vertical [panel (c)] dashed lines indicate the Fermi energy.

structure. Particularly, due to the drastic variation of the AHC with respect to the chemical potential around Fermi level, the resulting derivative of the AHC is as large as -6000 S/(cm eV) at the Fermi level. That is, a gigantic anomalous Nernst effect is expected in NiCrMnAl. Such a derivative of the AHC is much larger than that of the recent experimentally realized large anomalous Nernst effect in Mn_3Sn with a value of -845 S/(cm eV) [59–61]. In this sense, type-II SGSs may be promising materials for anomalous Nernst applications.

IV. CONCLUSIONS

To summarize, we have carried out a systematic high-throughput screening for spin-gapless semiconductors (SGSs) in quaternary Heusler compounds with 21, 26, and 28 valence electrons. After validating our calculations with the previously reported cases, we predicted 80 new stable compounds (based on the formation energy) as promising candidates of spin-gapless semiconductors, where 70 cases are stable based on further evaluation of the mechanical and dynamical stabilities. The magnetization of SGSs obeys the Slater-Pauling rule, which can be interpreted based on a new scheme of crystal field splitting of the D_{4h}*-like picture*. Interestingly, all four types of SGSs have been identified among our candidate systems, where both the longitudinal conductivity and transversal anomalous Hall conductivity are calculated. We find the type-II SGSs are particularly interesting for spintronic applications as the spin polarization of the longitudinal conductivity is very sensitive to the chemical potential, while the anomalous Hall conductivity changes its sign across the Fermi level, leading to a significant anomalous Nernst effect. This is also true for the SGS candidate NiCrMnAl with direct touching. Additionally, it is also demonstrated that spin-orbit coupling can have significant effect on the electronic structure of SGSs with heavy elements, where the band gap can be tuned by the magnetization direction, resulting in a large anisotropic magnetoresistance in cubic crystals. Therefore, we suspect that SGSs are promising materials for future spintronic applications, awaiting further experimental and theoretical explorations.

All the data are freely available in the Novel Materials Discovery (NOMAD) Laboratory [62].

ACKNOWLEDGMENTS

Q.G. acknowledges financial support from the China Scholarship Council. The authors gratefully acknowledge computational time on the Lichtenberg High Performance Supercomputer.

[1] X. L. Wang, Phys. Rev. Lett. **100**, 156404 (2008).
[2] S. Ouardi, G. H. Fecher, C. Felser, and J. Kübler, Phys. Rev. Lett. **110**, 100401 (2013).
[3] M. Wang, R. P. Campion, A. W. Rushforth, K. W. Edmonds, C. T. Foxon, and B. L. Gallagher, Appl. Phys. Lett. **93**, 132103 (2008).
[4] S. Skaftouros, K. Özdoğan, E. Şaşioğlu, and I. Galanakis, Appl. Phys. Lett. **102**, 022402 (2013).
[5] G. Z. Xu, E. K. Liu, Y. Du, G. J. Li, G. D. Liu, W. H. Wang, and G. H. Wu, Europhys. Lett. **102**, 17007 (2013).
[6] G. Y. Gao and K. L. Yao, Appl. Phys. Lett. **103**, 232409 (2013).
[7] W. Feng, X. Fu, C. Wan, Z. Yuan, X. Han, N. V. Quang, and S. Cho, Phys. Status Solidi RRL **9**, 641 (2015).
[8] L. Bainsla, A. I. Mallick, M. M. Raja, A. K. Nigam, B. S. D. C. S. Varaprasad, Y. K. Takahashi, A. Alam, K. G. Suresh, and K. Hono, Phys. Rev. B **91**, 104408 (2015).
[9] M. E. Jamer, B. A. Assaf, G. E. Sterbinsky, D. Arena, L. H. Lewis, A. A. Saul, G. Radtke, and D. Heiman, Phys. Rev. B **91**, 094409 (2015).
[10] Q. Gao, H. H. Xie, L. Li, G. Lei, J. B. Deng, and X. R. Hu, Superlattice Microstruct. **85**, 536 (2015).
[11] X. T. Wang *et al.*, J. Mater. Chem. C **4**, 7176 (2016).
[12] X. L. Wang, Natl. Sci. Rev. **3**, 252 (2016).
[13] S. Curtarolo, G. L. W. Hart, M. Buongiorno Nardelli, N. Mingo, S. Sanvito, and O. Levy, Nat. Mater. **12**, 191 (2013).
[14] I. Opahle, A. Parma, E. J. McEniry, R. Drautz, and G. K. H. Madsen, New J. Phys. **15**, 105010 (2013).
[15] J. Carrete, W. Li, N. Mingo, S. Wang, and S. Curtarolo, Phys. Rev. X **4**, 011019 (2014).
[16] J. G. He, M. Amsler, Y. Xia, S. S. Naghavi, V. I. Hegde, S. Hao, S. Goedecker, V. Ozolins, and C. Wolverton, Phys. Rev. Lett. **117**, 046602 (2016).
[17] J. G. He *et al.*, arXiv:1802.04875.
[18] J. Ma, J. He, D. Mazumdar, K. Munira, S. Keshavarz, T. Lovorn, C. Wolverton, A. W. Ghosh, and W. H. Butler, Phys. Rev. B **98**, 094410 (2018).
[19] S. Sanvito *et al.*, Sci. Adv. **3**, 1602241 (2017).
[20] J. Balluff, K. Diekmann, G. Reiss, and M. Meinert, Phys. Rev. Mater. **1**, 034404 (2017).
[21] S. V. Faleev, Y. Ferrante, J. Jeong, M. G. Samant, B. Jones, and S. S. P. Parkin, Phys. Rev. Appl. **7**, 034022 (2017).
[22] Y. Venkateswara, S. Gupta, S. S. Samatham, M. R. Varma Enamullah, K. G. Suresh, and A. Alam, Phys. Rev. B **97**, 054407 (2018).
[23] P. Klaer, B. Balke, V. Alijani, J. Winterlik, G. H. Fecher, C. Felser, and H. J. Elmers, Phys. Rev. B **84**, 144413 (2011).
[24] X. P. Wei, Y. L. Zhang, Y. D. Chu, X. W. Sun, T. Sun, P. Guo, and J. B. Deng, J. Phys. Chem. Solids **82**, 28 (2015).
[25] V. Alijani *et al.*, Phys. Rev. B **84**, 224416 (2011).
[26] I. Opahle, G. K. H. Madsen, and R. Drautz, Phys. Chem. Chem. Phys. **14**, 16197 (2012).
[27] G. Kresse and J. Furthmuller, Phys. Rev. B **54**, 11169 (1996).
[28] G. Kresse and D. Joubert, Phys. Rev. B **59**, 1758 (1999).
[29] D. Vanderbilt, Phys. Rev. B **41**, 7892(R) (1990).
[30] J. P. Perdew, J. A. Chevary, S. H. Vosko, K. A. Jackson, M. R. Pederson, D. J. Singh, and C. Fiolhais, Phys. Rev. B **46**, 6671 (1992).
[31] J. P. Perdew, K. Burke, and M. Ernzerhof, Phys. Rev. Lett. **77**, 3865 (1996).
[32] J. E. Saal, S. Kirklin, M. Aykol, B. Meredig, and C. Wolverton, JOM **65**, 1501 (2013).
[33] K. Koepernik and H. Eschrig, Phys. Rev. B **59**, 1743 (1999).
[34] I. Opahle, K. Koepernik, and H. Eschrig, Phys. Rev. B **60**, 14035 (1999).
[35] M. Born and K. Huang, *Dynamics Theory of Crystal Lattices* (Oxford University Press, 1954).

[36] A. Togo and I. Tanaka, Scr. Mater. **108**, 1 (2015).

[37] A. A. Mostofi, J. R. Yates, Y. S. Lee, I. Souza, D. Vanderbilt, and N. Marzari, Comput. Phys. Commun. **178**, 685 (2008).

[38] G. K. H. Madsen and D. J. Singh, Comput. Phys. Commun. **175**, 67 (2006).

[39] V. L. Deringer, A. L. Tchougreeff, and R. Dronskowski, J. Phys. Chem. A **116**, 21 (2011).

[40] K. Özdoğan, E. Şaşioğlu, and I. Galanakis, J. Appl. Phys. **113**, 193903 (2013).

[41] X. Yang, X. Wu, B. Wu, Y. Feng, P. Li, and H. Huang, Mater. Sci. Eng. B **209**, 45 (2016).

[42] N. Xing, H. Li, J. Dong, R. Long, and C. Zhang, Comput. Mater. Sci. **42**, 600 (2008).

[43] J. Nehra, V. D. Sudheesh, N. Lakshmi, and K. Venugopalan, Phys. Status Solidi RRL **7**, 289 (2013).

[44] G. Y. Gao, L. Hu, K. L. Yao, B. Luo, and N. Liu, J Alloy. Compd. **551**, 539 (2013).

[45] L. Bainsla, A. I. Mallick, M. M. Raja, A. A. Coelho, A. K. Nigam, D. D. Johnson, A. Alam, and K. G. Suresh, Phys. Rev. B **92**, 045201 (2015).

[46] X. Dai, G. Liu, G. H. Fecher, C. Felser, Y. Li, and H. Liu, J. Appl. Phys. **105**, 07E901 (2009).

[47] H. Z. Luo, Y. P. Xin, B. H. Liu, F. B. Meng, H. Y. Liu, E. K. Liu, and G. H. Wu, J. Alloy. Compd. **665**, 180 (2016).

[48] Y. J. Zhang, Z. H. Liu, E. K. Liu, G. D. Liu, X. Q. Ma, and G. H. Wu, Europhys. Lett. **111**, 37009 (2015).

[49] K. Kim, L. Ward, J. G. He, A. Krishna, A. Agrawal, P. Voorhees, and C. Wolverton, Accelerated discovery of quaternary Heusler with high-throughput density functional theory and machine learning; paper presented at APS March Meeting 2018, March 5-9, 2018, Los Angeles, California.

[50] L. Bainsla, M. M. Raja, A. K. Nigam, B. S. D. C. S. Varaprasad, Y. K. Takahashi, K. G. Suresh, and K. Hono, J. Phys. D: Appl. Phys. **48**, 125002 (2015).

[51] See Supplemental Material at http://link.aps.org/supplemental/10.1103/PhysRevMaterials.3.024410 for the atomic resolved moments, elastic constants, mechanical and dynamical stability, orbital-resolved density of states, and the band structures for the newly predicted SGS candidates, as well as discussions on the effect of disorder for NiFeMnAl.

[52] C. M. Rost, E. Sachet, T. Borman, A. Moballegh, E. C. Dickey, D. Hou, J. L. Jones, S. Curtarolo, and J. P. Maria, Nat. Commun. **6**, 8485 (2015).

[53] Y. Lederer, C. Toher, K. S. Vecchio, and S. Curtarolo, Acta Mater. **159**, 364 (2018).

[54] C. Felser, L. Wollmann, S. Chadov, G. H. Fecher, and S. S. P. Parkin, APL Mater. **3**, 041518 (2015).

[55] L. Wollmann, A. K. Nayak, S. S. Parkin, and C. Felser, Annu. Rev. Mater. Res. **47**, 247 (2017).

[56] T. Graf, C. Felser, and S. S. P. Parkin, Prog. Solid State Chem. **39**, 1 (2011).

[57] I. Galanakis, P. H. Dederichs, and N. Papanikolaou, Phys. Rev. B **66**, 174429 (2002).

[58] G. L. Miessler, P. J. Fischer, and D. A. Tarr, *Inorganic Chemistry*, 5th ed. (Pearson Education Press, 2012), p. 381.

[59] G. Y. Guo and T. C. Wang, Phys. Rev. B **96**, 224415 (2017).

[60] X. K. Li, L. C. Xu, L. C. Ding, J. H. Wang, M. S. Shen, X. F. Lu, Z. W. Zhu, and K. Behnia, Phys. Rev. Lett. **119**, 056601 (2017).

[61] M. Ikhlas, T. Tomita, T. Koretsune, M. T. Suzuki, D. N. Hamane, R. Arita, Y. Otani, and S. Nakatsuji, Nat. Phys. **13**, 1085 (2017).

[62] NOMAD: Novel Materials Discovery, https://repository.nomad-coe.eu (please search for the data using the author name “Qiang Gao”).

Supplemental Material

Qiang Gao, Ingo Opahle, and Hongbin Zhang

Institute of Materials Science, Technische Universität Darmstadt, 64287 Darmstadt, Germany

January 22, 2020

S1 Detailed data

The detailed data is shown in the following table, including lattice constants, total and partial magnetic moments, formation energies, distances to the convex hull, elastic constants, mechanical and dynamical stabilities, magnetic orders, and SGS types. a_{opt}, $\triangle$H, and E_{con} are lattice constant, formation energy, and the distance to the convex hull, respectively. For mechanical and dynamical stabilities, 1 and 0 are stable and unstable. In magnetic order, FM and FIM are ferromagnetic and ferrimagnetic. In SGS type, 'SOC-' means spin-orbit coupling (SOC) has significant influence on such SGS. The compounds are arranged according to similar chemical component. The convex hull is obtained from the Open Quantum Materials Database (OQMD). [1]

XX'YZ (4a,4b,4c,4d)	a_{opt} (Å)	Magnetic moment (μ_B)					△H (eV/atom)	△E_{con} (eV/atom)	Mechanical properties (GPa)				Dynamic stability	Magnetic order	SGS type
		M_{tot}	M_X	$M_{X'}$	M_Y	M_Z			C_{11}	C_{12}	C_{44}	Stability			
N_V=21															
IrVYSn	6.720	3.00	-0.11	3.13	0.13	-0.15	-0.0942	0.5628	1444.44	1111.68	551.67	1	1	FM	SOC-I
CoVYSn	6.620	3.00	-0.37	3.24	0.27	-0.14	-0.0862	0.3848	1267.66	894.53	274.54	1	1	FM	II
CoVScSn	6.402	3.00	-0.23	3.01	0.36	-0.14	-0.2049	0.2221	1299.00	1125.56	562.45	1	1	FM	III
IrVScSn	6.518	3.00	-0.08	2.99	0.24	-0.14	-0.2488	0.4052	1581.98	1336.81	843.97	1	1	FM	SOC-II
RhVScSn	6.518	3.00	-0.10	2.98	0.31	-0.18	-0.2773	0.3527	1477.41	1180.15	713.52	1	1	FM	I
CoVYGe	6.377	3.00	-0.14	3.09	0.24	-0.19	-0.0763	0.4697	1790.24	776.20	401.23	1	1	FM	II
CoVScGe	6.145	3.00	-0.04	2.87	0.35	-0.18	-0.2749	0.2931	1373.08	1229.15	268.70	1	1	FM	II
IrVScGe	6.300	3.00	-0.02	2.92	0.28	-0.18	-0.3025	0.4045	1649.16	1448.43	618.57	1	1	FM	II
RhVScGe	6.290	3.00	-0.04	2.92	0.36	-0.24	-0.3318	0.4502	1571.79	1288.05	545.01	1	1	FM	II
RhVYGe	6.512	3.00	-0.07	3.10	0.22	-0.26	-0.1377	0.5663	1382.2	1040.53	14.82	1	1	FM	III
CoVYSi	6.297	3.00	-0.05	2.97	0.19	-0.11	-0.1077	0.4701	2011.85	797.49	263.92	1	1	FM	II
CoVScSi	6.058	3.00	0.03	2.77	0.30	-0.10	-0.3550	0.2990	1610.23	1273.57	196.07	1	1	FM	II
IrVScSi	6.215	3.00	0.00	2.85	0.25	-0.10	-0.4254	0.4096	1901.04	1469.97	570.36	1	1	FM	SOC-II
RhVScSi	6.210	3.00	-0.02	2.85	0.32	-0.15	-0.4242	0.4628	1763.41	1305.32	487.31	1	1	FM	II
RhVYSi	6.438	3.00	-0.05	3.03	0.20	-0.17	-0.1862	0.6398	2038.11	931.95	445.75	1	1	FM	III
PtVScAl	6.369	3.00	-0.05	2.93	0.27	-0.14	-0.4431	0.2869	1454.09	1230.24	606.16	1	1	FM	SOC-I
PtVYAl	6.608	3.00	-0.07	3.09	0.14	-0.17	-0.2477	0.5013	1255.87	1014.52	119.06	1	1	FM	I
PtVYGa	6.600	3.00	-0.09	3.10	0.16	-0.17	-0.1867	0.5733	1612.47	917.37	568.16	1	1	FM	I
FeCrHfAl	6.142	3.00	0.39	3.02	-0.23	-0.18	-0.2456	0.0504	2162.27	1161.77	792.65	1	1	FM	II
OsCrHfAl	6.299	3.00	0.10	3.24	-0.17	-0.17	-0.403	0.0530	2313.54	1435.06	911.27	1	1	FM	II
RuCrHfAl	6.284	3.00	0.10	3.27	-0.17	-0.19	-0.4544	0.0666	2250.27	1267.65	777.88	1	1	FM	II
FeCrTiAl	5.964	3.00	0.65	2.88	-0.38	-0.15	-0.292	0.0504	2221.68	1299.39	812.77	1	1	FM	II
FeCrZrAl	6.194	3.00	0.38	3.08	-0.28	-0.18	-0.2156	0.0914	2054.02	1094.3	745.66	1	1	FM	III
OsCrZrAl	6.347	3.00	0.11	3.29	-0.22	-0.18	-0.3543	0.0617	2185.12	1375.21	853.99	1	1	FM	SOC-II
RuCrZrAl	6.335	3.00	0.10	3.32	-0.22	-0.20	-0.4154	0.0626	2124.7	1205.88	747.77	1	1	FM	III
FeCrScSi	5.992	3.00	0.15	3.07	-0.06	-0.16	-0.279	0.2400	2032.16	1203.68	619.56	1	1	FM	II
FeCrScSn	6.364	3.00	-0.45	3.61	-0.01	-0.15	-0.0891	0.2309	1555.52	1038.03	700.85	1	1	FIM	II
FeCrYSi	6.236	3.00	-0.05	3.32	-0.09	-0.17	-0.0081	0.4739	1830.6	892.57	133.78	1	1	FM	III
OsCrYSi	6.386	3.00	-0.06	3.38	-0.13	-0.19	-0.0246	0.4860	1890.94	1154.33	70.6	1	1	FM	SOC-III
CoVHfAl	6.211	3.00	0.17	2.76	0.16	-0.09	-0.2896	0.1134	1729.55	1264.07	529.04	1	1	FM	I
IrVHfAl	6.346	3.00	0.05	2.87	0.16	-0.08	-0.4634	0.1596	2093.72	1490.79	865.2	1	1	FM	II
RhVHfAl	6.342	3.00	0.04	2.86	0.21	-0.11	-0.3855	0.2355	1914.62	1325.73	695.68	1	1	FM	II
CoVZrAl	6.258	3.00	0.14	2.78	0.16	-0.09	-0.2662	0.1408	1691.94	1149.2	510.03	1	1	FM	I
CoVZrGa	6.238	3.00	0.15	2.77	0.18	-0.10	-0.2317	0.2233	1701.93	1205.16	489.22	1	1	FM	I
MnCrNbAl	6.077	3.00	1.40	2.42	-0.65	-0.16	-0.1912	0.0228	2462.69	1423.41	1005.01	1	1	FIM	II
MnCrTaAl	6.053	2.99	1.33	2.38	-0.57	-0.15	-0.2124	0.0256	2619.06	1490.77	1088.21	1	1	FIM	II
FeVHfGe	6.158	3.00	0.55	2.57	0.03	-0.15	-0.2094	0.2646	1831.54	1547.04	533.73	1	1	FM	II
FeVHfSi	6.079	3.00	0.57	2.49	0.01	-0.08	-0.3187	0.2753	2023.68	1502.87	520.06	1	1	FM	II
FeVHfSn	6.386	3.00	0.42	2.69	0.01	-0.11	-0.129	0.1580	1525.88	1168.86	687.86	1	1	FM	II
MnCrZrGe	6.157	2.99	1.01	2.61	-0.41	-0.21	-0.1473	0.2687	1941.37	1633.75	780.66	1	1	FIM	II
MnCrZrSi	6.076	3.00	1.06	2.48	-0.38	-0.16	-0.2569	0.2621	2343.88	1348.96	751.11	1	1	FIM	II
MnCrZrSn	6.393	3.00	0.78	2.88	-0.50	-0.16	-0.0593	0.2317	2265.13	995.37	869.8	1	1	FIM	II
IrTiZrSi	6.385	2.96	0.15	2.22	0.54	0.05	-0.4232	0.4778	2323.43	1295.74	377.34	1	1	FM	II
IrTiZrSn	6.651	2.98	0.10	2.31	0.62	-0.04	-0.3335	0.3965	2079.32	1154.1	792.38	1	0	FM	II
FeVNbAl	6.117	2.99	0.92	2.33	-0.17	-0.09	-0.2012	0.1238	2237.73	1424.33	813.39	1	1	FM	II
FeVTaAl	6.097	2.99	0.85	2.32	-0.10	-0.08	-0.2202	0.0958	2336.25	1509.09	870.01	1	1	FM	II
N_V=26															
CoOsTiSb	6.255	2.00	1.44	0.33	0.18	0.05	-0.1635	0.3515	2357.73	1771.08	850.92	1	1	FM	I
CoFeHfSb	6.232	2.00	0.94	1.32	-0.26	0.01	-0.2847	0.2523	1728.05	1704.68	608.8	1	1	FM	I
CoOsZrSb	6.453	2.00	1.48	0.42	0.03	0.07	-0.1075	0.4645	2192.24	1578.65	675.35	1	1	FM	I
RhFeTiSb	6.259	1.95	0.33	1.91	-0.31	0.02	-0.3896	0.1104	1917.69	1541.17	706.26	1	1	FM	I
CoFeTiSb	6.074	2.00	0.99	1.31	-0.31	0.00	-0.2948	0.2202	2359.05	1405.26	879.59	1	1	FM	I
IrFeTiSb	6.287	1.99	0.24	2.04	-0.29	0.00	-0.2932	0.3108	1953.78	1670.36	652.99	1	1	FM	III
CoRuTiSb	6.228	2.00	1.38	0.42	0.14	0.06	-0.3261	0.1889	2268.57	1618.19	817.63	1	1	FM	I
CoFeNbGe	5.961	2.00	1.07	1.11	-0.16	-0.03	-0.2374	0.1506	2587.37	1797.67	865.23	1	1	FM	I
CoOsNbSn	6.352	2.00	1.51	0.26	0.21	0.02	-0.0609	0.2091	2489.47	1840.72	923.98	1	0	FM	I
CoRuTaSn	6.303	2.00	1.42	0.41	0.12	0.05	-0.1268	0.1852	1596.63	2245.27	682.8	0	1	FM	I
IrFeTaSn	6.354	1.98	0.24	1.99	-0.24	-0.01	-0.1782	0.2328	2325.66	1914.48	849.42	1	1	FM	I
CoOsTaGe	6.143	2.00	1.47	0.33	0.14	0.06	-0.0702	0.3048	2644.71	2141.96	679.39	1	1	FM	I
CoOsTaSi	6.064	1.99	1.45	0.30	0.16	0.08	-0.2546	0.2234	2226.66	2589.35	828.63	0	1	FM	I
CoOsTaSn	6.332	2.00	1.48	0.33	0.14	0.04	-0.007	0.2413	2653.79	1937.05	992.24	1	1	FM	I
CoFeTaGe	5.938	2.00	1.02	1.14	-0.17	-0.00	-0.2475	0.1275	2784.17	1876.34	949.15	1	1	FM	I
CoFeTaSi	5.856	2.00	1.05	1.07	-0.13	0.01	-0.4222	0.1098	3096.22	1962.23	993.53	1	1	FM	I
CoFeTaSn	6.154	2.00	0.99	1.26	-0.23	-0.01	-0.1522	0.0898	2737.87	1570.89	980.47	1	1	FM	I
IrCoNbAl	6.162	1.99	0.25	1.53	0.21	0.00	-0.5563	0.0227	2677.65	1816.63	1109.06	1	1	FM	I
IrCoNbGa	6.173	2.00	0.26	1.55	0.18	0.02	-0.4043	0.0097	2448.38	1931.28	1046.66	1	1	FM	I
IrCoNbIn	6.360	2.00	0.24	1.58	0.17	0.01	-0.1326	0.1544	2316.71	1725.38	1007.19	1	1	FM	I
IrCoTaAl	6.140	2.00	0.29	1.51	0.17	0.03	-0.5579	0.0631	1599.75	1348.15	294.18	1	1	FM	I
IrCoTaGa	6.150	2.00	0.30	1.52	0.13	0.05	-0.4200	0.0370	1989.06	2344.12	778.05	0	1	FM	I
IrCoTaIn	6.336	2.00	0.29	1.54	0.14	0.03	-0.1622	0.1768	1909.34	2041.26	43.81	0	1	FM	I
CoCoNbAl	5.970	2.00	1.04	1.04	-0.03	-0.04	-0.4312	0.0082	2847.43	1482.45	1144.34	1	0	FM	I
CoCoNbGa	5.968	2.00	1.03	1.03	-0.05	-0.00	-0.3299	0.0001	2663.63	1615.45	1121.47	1	0	FM	I
CoCoNbIn	6.179	2.00	1.06	1.06	-0.10	-0.02	-0.0869	0.0331	2479.01	1379.61	962.42	1	0	FM	I
IrCoTiPb	6.380	2.00	0.29	1.53	0.15	0.04	-0.0571	0.3829	1874.6	1532.82	640.63	1	1	FM	I
IrCoTiSi	5.965	2.00	0.28	1.47	0.18	0.07	-0.6805	0.0785	2752.08	1909.19	1030.24	1	1	FM	I
IrCoTiSn	6.276	2.00	0.29	1.50	0.18	0.04	-0.3789	0.1461	2236.11	1650.11	937.67	1	1	FM	I
NiCrMnAl	5.809	2.00	0.54	-1.70	3.15	0.01	-0.2127	0.1173	2087.24	1517.73	410.95	1	1	FIM	III
NiReCrAl	5.920	1.97	0.50	-0.52	2.03	-0.05	-0.1633	0.2177	2586.08	1936.29	1087.5	1	1	FIM	II
CoOsCrAl	5.866	2.00	0.83	-0.38	1.67	-0.12	-0.2412	0.0688	2668.91	2127.81	1171.99	1	1	FIM	II
CoRuCrAl	5.848	2.01	0.72	-0.35	1.77	-0.13	-0.2802	0.0558	2082.98	2151.72	964.53	0	1	FIM	II
N_V=28															
NiFeMnAl	5.731	4.00	0.39	0.82	2.96	-0.17	-0.2773	0.0577	2596.28	1440.29	1387.76	1	1	FM	IV

S2 Density of states for magnetism discussions

We have discussed the magnetism of Heusler SGSs in the main text. For the understanding of exchange and crystal field splitting, we have shown the representative total and partial density of sates (DOS) of the considered 1 and 2 main magnetic compounds with N_V=21 or 26. In case of N_V=21, PtVYAl and FeVNbAl are the representatives of 1 and 2 main magnetic ions Heusler SGS. In case of N_V=26, IrFeTiSb and CoFeTaGe are the representatives of 1 and 2 main magnetic ions Heusler SGS.

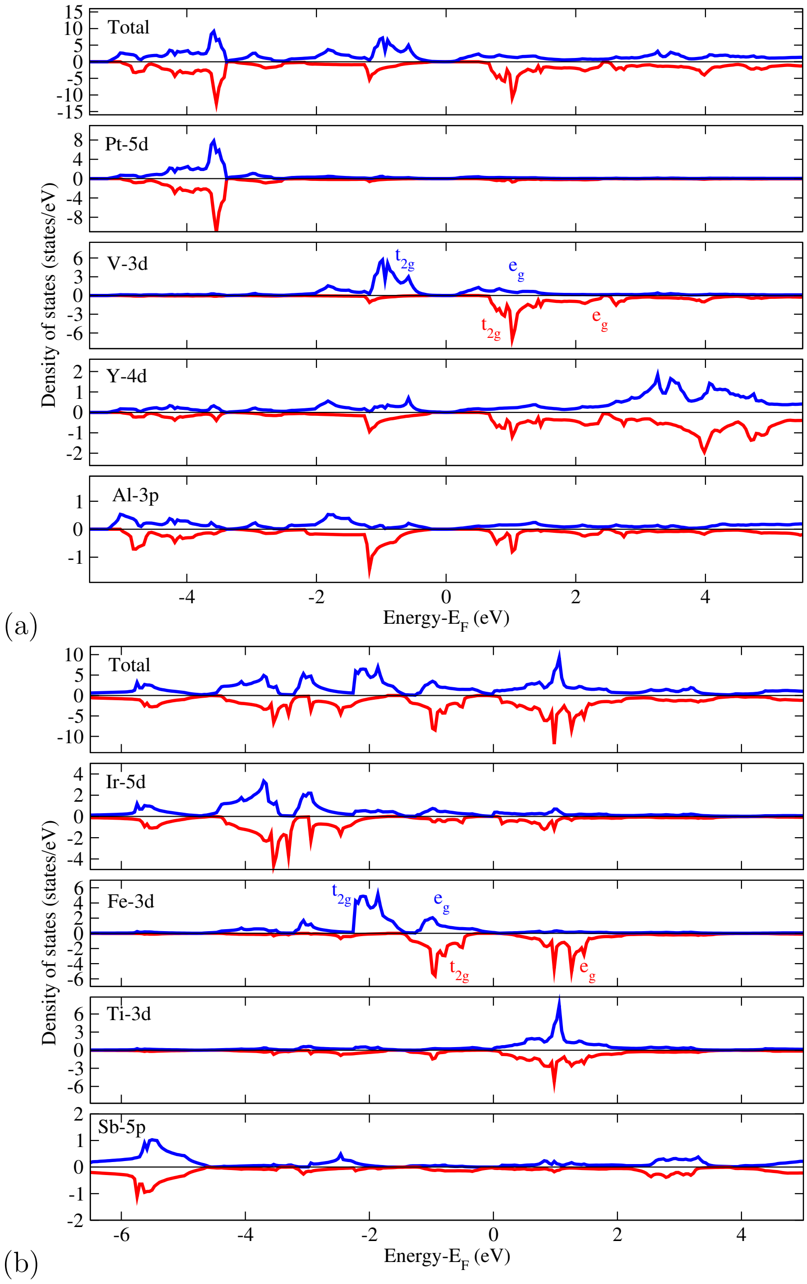

Figure S1: DOS for one magnetic ion Heusler SGS. (a) N_V=21 Heusler SGS PtVYAl. V makes main contribution to the magnetic moment. (b) N_V=26 Heusler SGS IrFeTiSb. Fe makes main contribution to the magnetic moment. Here the blue and red curves are the majority and minority spin channels, respectively. (a) PtVYAl is one main magnetic ion SGS. V makes main contribution to the magnetic moment. (b)

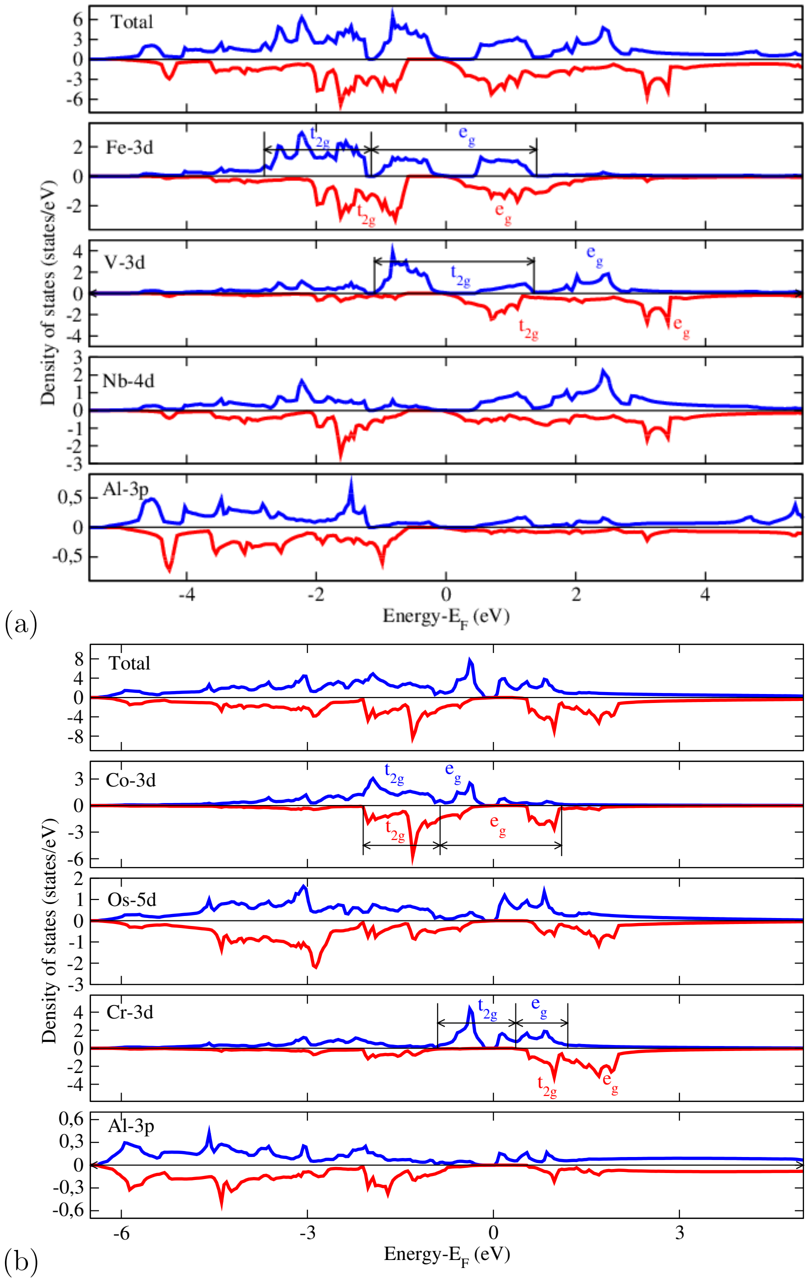

Figure S2: DOS for two magnetic ions Heusler SGS. (a) N_V=21 Heusler SGSs FeVNbAl. It has two main magnetic ions with about 2 μ_B magnetic moment in V and 1 μ_B in Fe. (b) N_V=26 Heusler SGSs CoFeTaGe. It has two main magnetic ions with about 1 μ_B magnetic moment in both Co and Fe. Here the blue and red curves are the majority and minority spin channels, respectively. Here we do not show the simple atom model for the two magnetic ions SGSs.

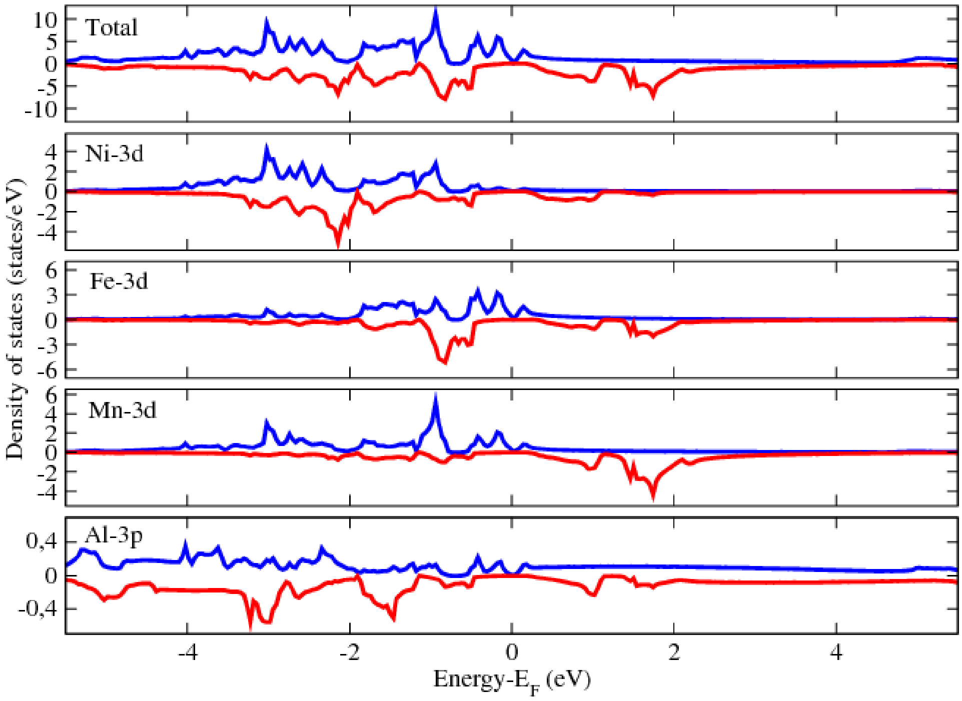

Figure S3: DOS for 28 valence Heusler SGS NiFeMnAl. It can be seen that there is strong hybridization between Ni, Fe, and Mn.

S2.1 Crystal field splitting

In order to understand the spin splitting clearly for the two magnetic ion SGS clearly, we show the local density of states (LDOS) of the magnetic ions for FeVNbAl and CoFeTaGe in the following.

Here we want to demonstrate that chemical environment can change crystal field splitting. For instance, following wikipedia on crystal field theory, for the O_h point group, the t_{2g} shell should be lower in energy than the e_g shell; whereas for the T_d point group, the t_{2g} shell is higher than the e_g shell. To clarify the situation, we have performed calculations on the local density of states for the hypothetical V_2NbFe and Al_2NbFe compounds, as shown in Fig. S4 in comparison with that of NbFeVAl. For V_2NbFe and Al_2NbFe, the local group of Fe is O_h, resulting in a splitting of t_{2g} and e_g shells from the Fe-3d states. However, for V_2NbFe, the t_{2g} shell is lower in energy than the e_g shell, while the main peaks for the t_{2g} and e_g shells are located at the same energy for Al_2NbFe. In this sense, depending on the chemical environment, the crystal field splitting can be changed significantly. We believe this is what happens in NbFeVAl, where the t_{2g} shell is lower in energy than the e_g shell due to the anisotropic bonding environment.

As shown in Fig. S5, in comparison to the Fe-3d shell in V_2NbFe, the Fe-3d shell in FeVNbAl will split into four peaks, marked as e'_g, b_{1g}, a^*_{1g}, and b^*_{1g} subshells. Such a picture is not driven by lowering of the local symmetry. For instance, both the e'_g and b_{1g} subshells originated from the t_{2g} shell have equal contributions from the d_{xy}, d_{yz}, and d_{zx} orbitals (Fig. S5(c)), and the a^*_{1g} and b^*_{1g} subshells originated from the e_g shell have equal contributions from the $d_{x^2-y^2}$ and $d_{3z^2-r^2}$ orbitals (Fig. S5(c)). That is, the three-fold (two-fold) degeneracy for the t_{2g} (e_g) shell is kept, as required by the T_d point group. In FeVNbAl (Fig. S5), the triply degenerated Fe-t_{2g} and V-t_{2g} states split into e'_g and b_{1g} subshells in both spin channels. On the other hand, the e_g states of Fe in both spin channels and V in the majority spin channel split into two subshells a^*_{1g} and b^*_{1g}. We suspect that such pseudo splitting ($t_{2g} \rightarrow e'_g + b_{1g}$ and $e_g \rightarrow a^*_{1g} + b^*_{1g}$) is caused by the strong hybridization between the Fe-3d and V-3d electrons, as highlighted in Fig. **??** (b)&(c) for the t_{2g} shell. Such a "splitting" picture of the "2-1-1-1" type can be applied for many other quaternary Heusler compounds as discussed in the main text. It is very comparable to the splitting scheme for the D_{4h} symmetry, thus we call it "D_{4h}-like picture".

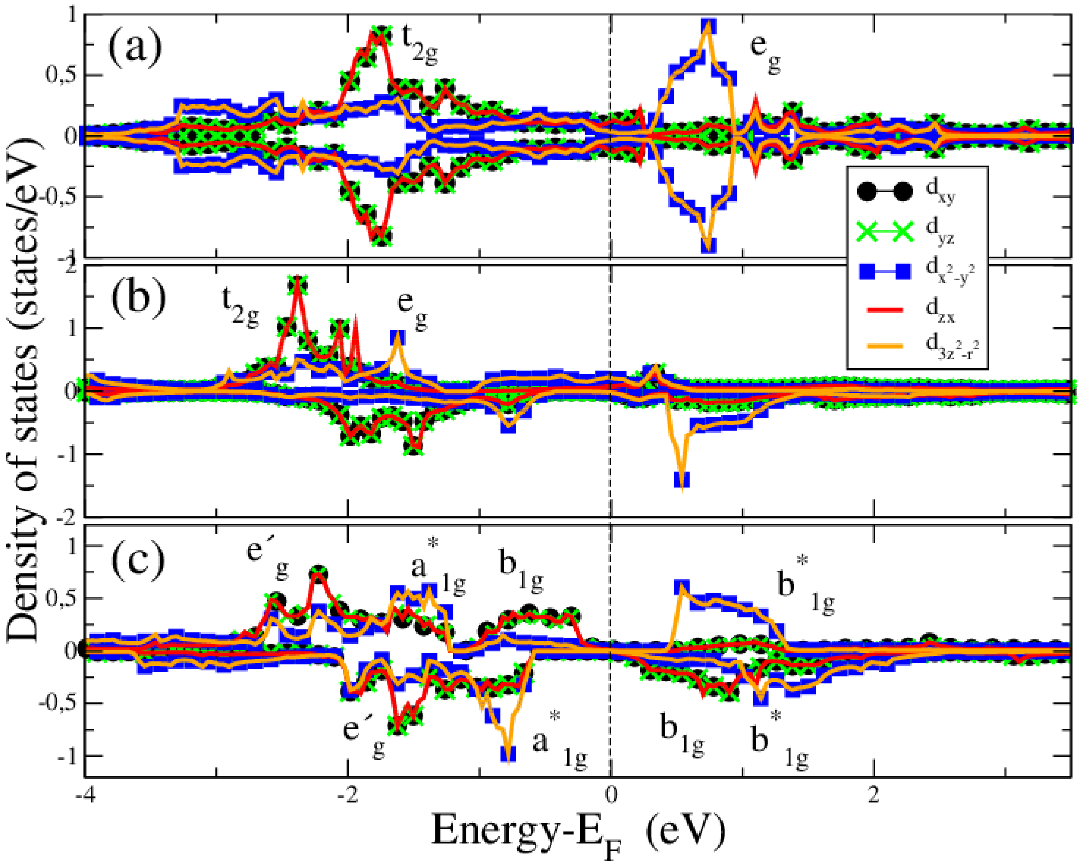

Figure S4: Local density of states (LDOS) of Fe atoms in V_2NbFe [a], Al_2NbFe [b], and NbFeVAl [c].

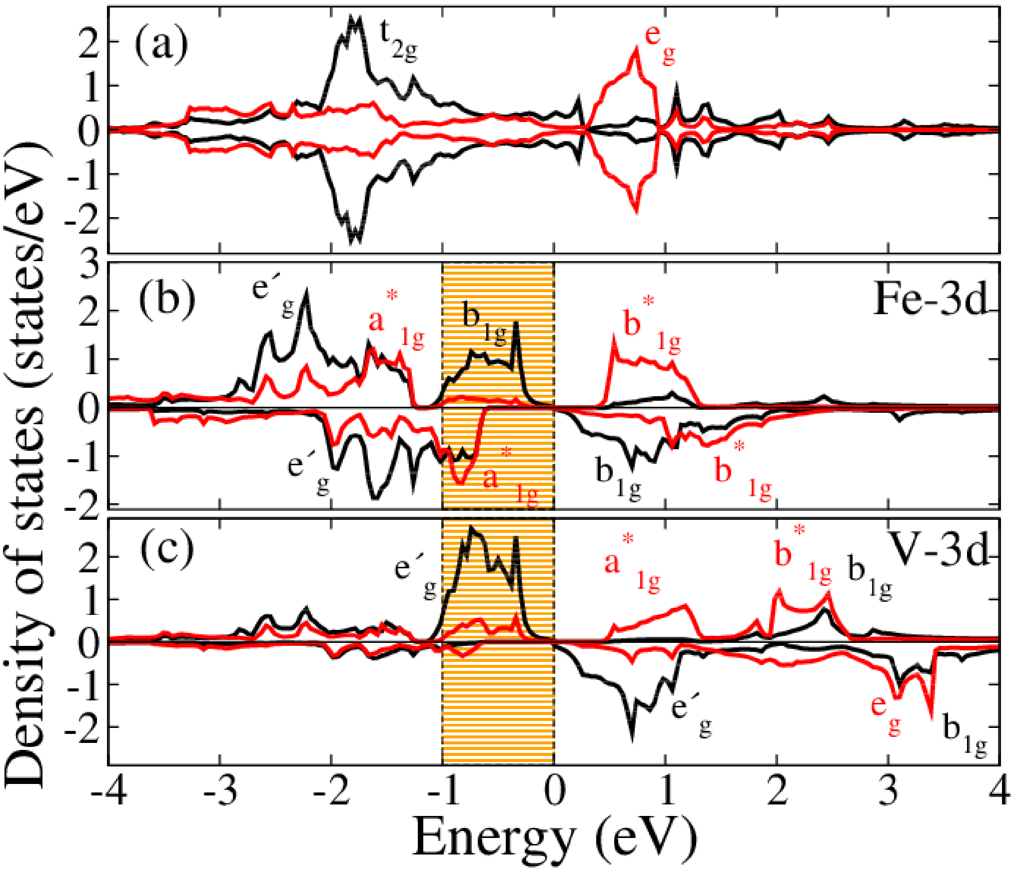

Figure S5: [a] The LDOS of Fe-3d in the arbitrary calculation V$_2$NbFe, which is the pure octahedral crystal field. [b] The LDOS of Fe-3d in FeVNbAl. [c] The LDOS of V-3d in FeVNbAl. In[b] and [c], the shaded region highlights strong hybridization between the Fe-b_{1g} and V-e'_g subshells in the majority spin channel, of which the energy range is from about -1 to 0 eV.

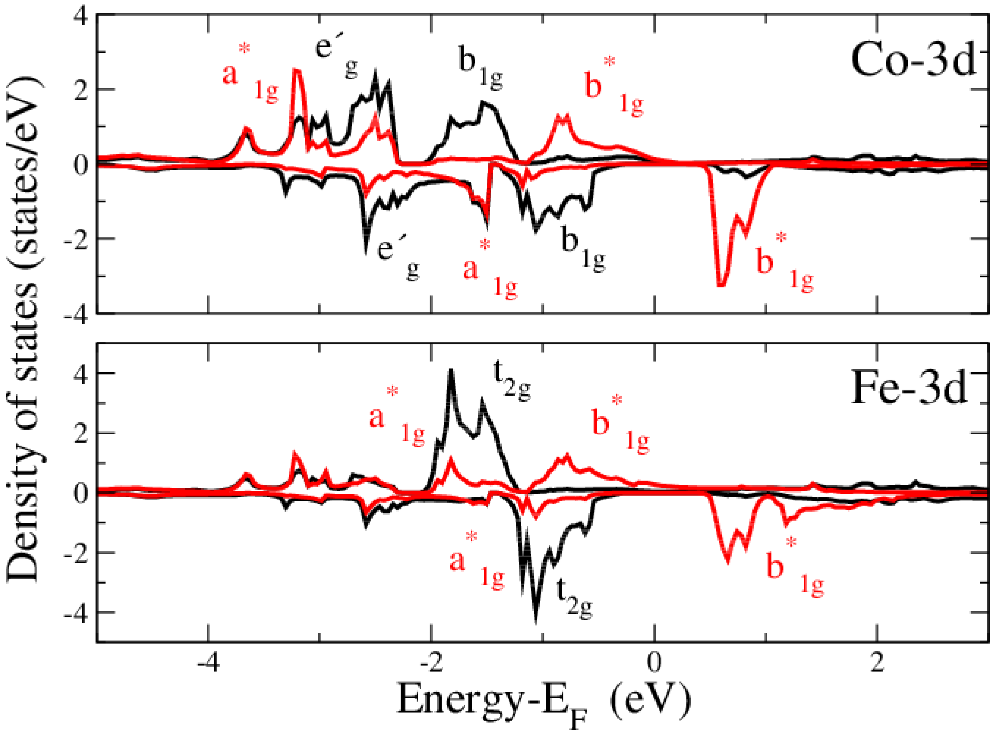

Figure S6: LDOS for magnetic ions in CoFeTaGe. Up: Co with 1 μ_B magnetic moments. Down: Fe with 1 μ_B magnetic moments. The black and red curves are the original t$_{2g}$ and e$_g$ states, respectively.

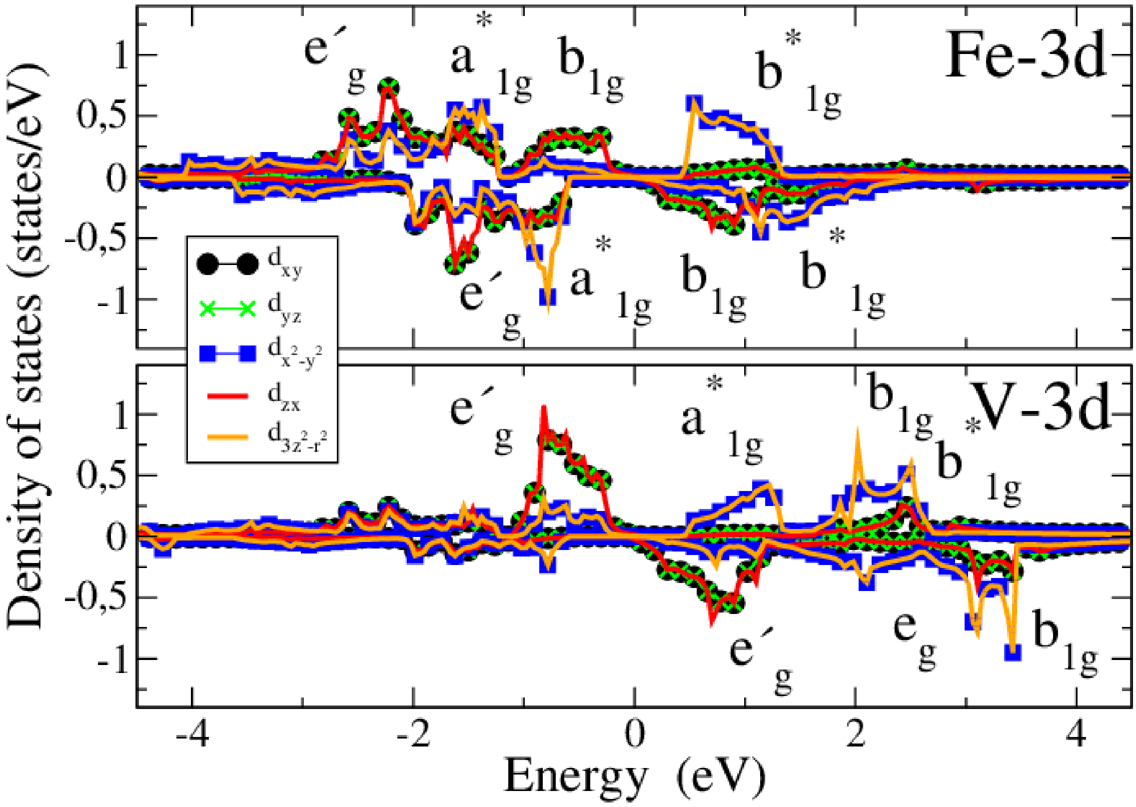

Figure S7: LDOS for decomposed orbitals of the two magnetic ions in FeVNbAl. Up and down are Fe and V. We can see that the orbitals d_{xy}, d_{yz}, and d_{zx} are always degenerated in the e_g and b_{1g} subshells originated from the t_{2g} shell, which is the same for the $d_{x^2-y^2}$, $d_{3z^2-r^2}$ orbitals in the a^*_{1g} and b^*_{1g} subshells originated from e_g shell.

S5 Disorder effect

Taking NiFeMnAl (with formation energy of -0.28 eV/atom and distance to the convex Hull being 0.05 eV/atom) as an example, we discuss the effect of the anti-site induced disorder on the magnetic properties and electronic structures of the SGS NiFeMnAl by using the the AKAI-KKR-CPA code (cpa2002v010). [2, 3]

The Fe-Mn anti-site disorder is applied in this case study. For a specific anti-site concentration x, the chemical formula is $\mathrm{Ni(Fe_{1-x}Mn_x)(Mn_{1-x}Fe_x)Al}$. The magnetic moment as a function of anti-site concentration plot is shown in Fig. S8. When the disorder degree is increased, the total magnetic moment is decreased.

As to disorder effect on the electronic structures, we calculated the Bloch spectral function for NiMnFeAl with 10% Fe-Mn anti-side disorder as shown in Fig. S9. After inducing anti-site disorder, in the majority spin channel, the once separated conduction and valence bands are overlapping. On the other hand, the main features of the electronic structures are still kept.

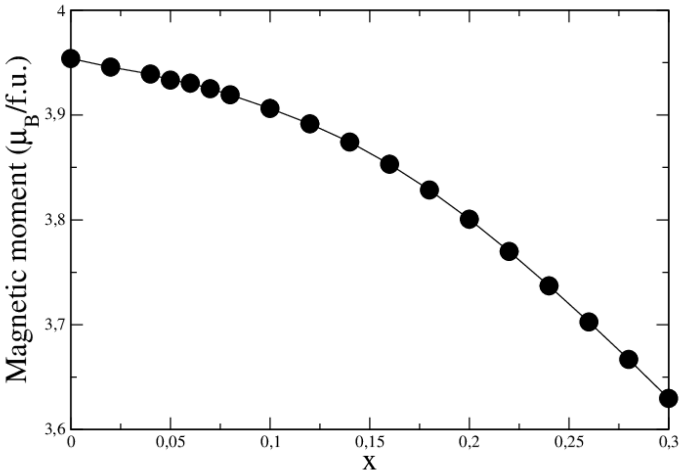

Figure S8: The total magnetic moment as a function of anti-site degree.

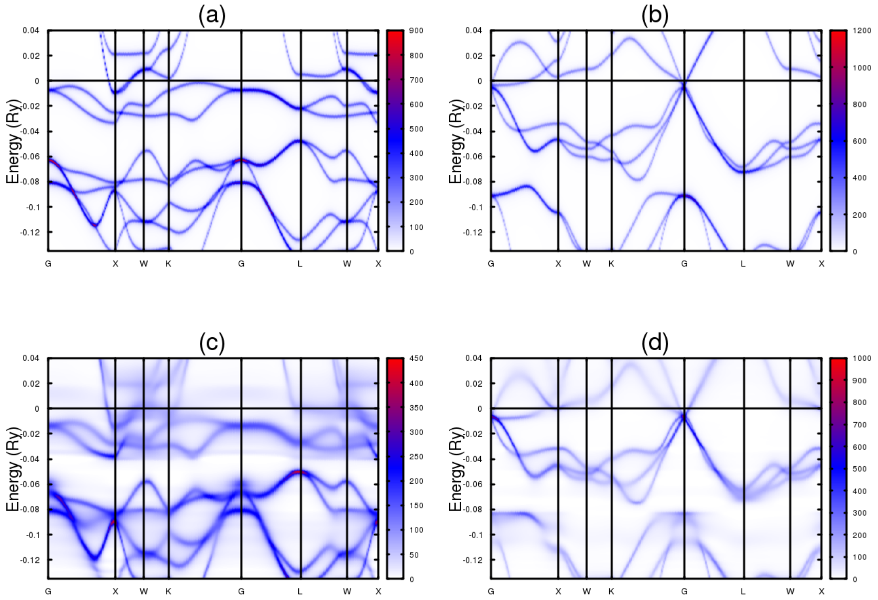

Figure S9: The Bloch spectral function of NiMnFeAl. Up (a) and (b) are order phase, (c) and (d) are 10% Fe-Mn anti-site disorder phase. The left and right are majority and minority spin channels.

References

[1] J.E. Saal, S. Kirklin, M. Aykol, B. Meredig, C. Wolverton, JOM **65** , 1501 (2013).

[2] S. Blugel, H. Akai, R. Zeller, P.H. Dederichs, Phys. Rev.**B** 35, 3271 (1987).

[3] H. Akai, Hyperfine Interact. **68** 1, (1992).

In this work, we carried out a systematic high throughput screening for rare-earth free permanent magnets by incorporating light interstitials (H, B, C, N) into magnetic full Heusler alloys. We successfully identified 32 candidates with an out-of-plane magnetic anisotropy larger than 0.4 MJ/m^3 as well as 10 cases with large in-plane anisotropy. Detailed analysis reveals that the interstitials are very effective in inducing global tetragonal distortions, whereas the local chemical bonding and changes in the crystalline environment result in significant enhancement of MAE. We strongly believe this provides an efficient and generic way of tailoring MAE and hence designing permanent magnets in other types of compounds.

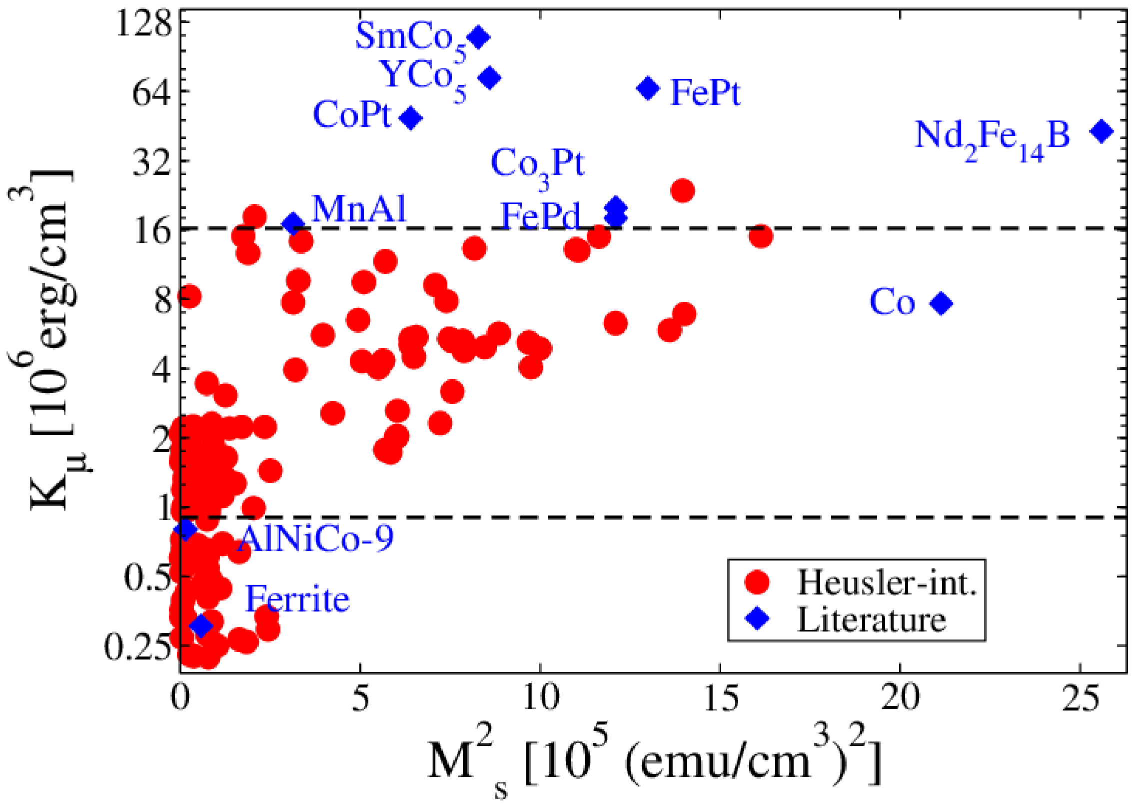

Acta Materialia 186 (2020) 1–8

Contents lists available at ScienceDirect

Acta Materialia

journal homepage: www.elsevier.com/locate/actamat

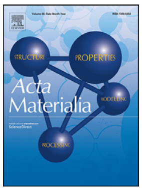

Full length article

Designing rare-earth free permanent magnets in heusler alloys via interstitial doping

Qiang Gao[a], Ingo Opahle[a], Oliver Gutfleisch[a,b], Hongbin Zhang[*,a]

[a] Institut für Materialwissenschaft, Technische Universität Darmstadt, Darmstadt 64287, Germany
[b] Fraunhofer-Research Institution Materials Recycling and Resource Strategies IWKS, Hanau 63457, Germany

ARTICLE INFO

Article History:
Received 6 September 2019
Revised 29 December 2019
Accepted 30 December 2019
Available online 3 January 2020

Keywords:
Permanent magnets
Interstitial
Tetragonal distortion
Magneto-crystalline anisotropy energy

MSC:
00-01
99-00

ABSTRACT

Based on high-throughput density functional theory calculations, we investigated the effects of light interstitial H, B, C, and N atoms on the magnetic properties of cubic Heusler alloys, with the aim to design new rare-earth free permanent magnets. It is observed that the interstitial atoms induce significant tetragonal distortions, leading to 32 candidates with large ($>$ 0.4 MJ/m^3) uniaxial magneto-crystalline anisotropy energies (MAEs) and 10 cases with large in-plane MAEs. Detailed analysis following the perturbation theory and chemical bonding reveals the strong MAE originates from the local crystalline distortions and thus the changes of the chemical bonding around the interstitials. This provides a valuable way to tailor the MAEs to obtain competitive permanent magnets, filling the gap between high performance Sm-Co/Nd-Fe-B and widely used ferrite/AlNiCo materials.

1. Introduction

Permanent magnets are of great technical importance for many key technologies such as electric vehicles, wind turbines, and automatisation and robotics to name only a few [1]. Looking at the intrinsic magnetic properties, such materials demand a large magneto-crystalline anisotropy energy (MAE), a sizable saturation magnetization, and a high Curie temperature. The MAE originates from the spin-orbit coupling (SOC) and sets an upper limit for the microstructure dependent coercivity of permanent magnets. At present, rare-earth magnets based on Sm-Co (MAE: 17.0 MJ/m^3, Magnetization (M_s): 910 kA/m) and Nd-Fe-B (MAE: 5.0 MJ/m^3, M_s: 720 kA/m) are prototypes of high performance permanent magnets, with a substantial cost and performance gap to other classes of commercially available permanent magnets such as AlNiCo (MAE: 0.04 MJ/m^3, M_s: 50 kA/m) and ferrites (MAE: 0.03 MJ/m^3, M_s: 125 kA/m) [2]. Thus, there is a great interest to develop novel permanent magnets so that the full spectra of applications can be achieved, ideally without critical elements such as rare-earth elements [3,4].

An enlightening idea was proposed to achieve giant MAE in tetragonally distorted FeCo alloys [5], where both the tetragonal distortion and fine tuning of the number of electrons by alloying are crucial for the enhanced MAE. Follow-up experimental studies on FeCo alloys deposited on various substrates confirmed the theoretical prediction [6]. Nevertheless, due to the strong tendency for the FeCo alloys to relax, it is difficult to maintain the tetragonal distortion induced by the underlying substrates for thin films thicker than 2 nm [6–8]. Recently, following the prediction based on DFT calculations [9,10], systematic studies have been performed on FeCo+X (X= C and B), where spontaneous tetragonal distortions with c/a=1.04 can be induced by a few atomic percent interstitial doping of C or B atoms occupying the octahedral interstitial sites. The resulting MAE can be as large as 0.5 MJ/m^3 with B concentration up to 4 at%, where the tetragonal strain reaches 5%. For $Fe_{0.38}Co_{0.62}$, a large interstitial concentration of 9.6 at% B was achieved [10]. The effect of light interstitials on the magnetic properties of body-centered cubic (BCC) iron has also been well studied. α-Fe with 12.5 at% content of nitrogen interstitial has been grown by sputtering on the MgO (100) substrates, leading to about 10% tetragonal distortion and significant enhancement of magnetization and MAE [11]. First-principle calculations and experimental results show that Fe with nitrogen interstitial has sizable MAE, favoring perpendicular magnetization [11]. Using the molecular beam epitaxy, boron has been incorporated into bcc Fe as interstitial dopants, which gives rise to tetragonal distortions but the resulting MAE still favors in-plane magnetization due to tendency for B atoms to be agglomerated [12], where the interstitial content of B atoms can be as high as 14 at%.

---

[*] Corresponding author.
E-mail address: hzhang@tmm.tu-darmstadt.de (H. Zhang).

https://doi.org/10.1016/j.actamat.2019.12.049

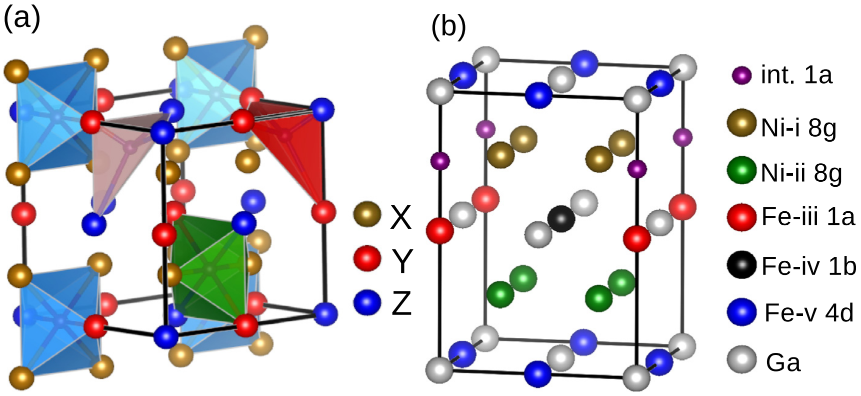

Fig. 1. (a) The possible interstitial sites in the conventional austenite unit cell of full Heusler compounds X_2YZ. The blue and green octahedrons denote the 24f (0.25,0,0) and 24g (0.5,0.25,0.25) interstitial sites, while the red and pink tetrahedrons mark the 16e(0.125,0.875,0.875) and 16e(0.875,0.625,0.875) interstitial sites. (b) The crystal structure (space group No. 99, P4mm) for the tetragonal Heusler compound Ni_2FeGa with interstitials (int.) at the most stable octahedral sites. The corresponding Wyckoff positions for the int., Fe and Ni atoms are as follows, int.: 1a(0,0,0.75+δ), Ni-i: 8g(0.25,0.25,0.75)+δ, Ni-ii: 8g(0.25,0.25,0.25)+δ, Fe-iii: 1a(0,0,0.5+δ), Fe-iv: 1b(0.5,0.5,0.5+δ), and Fe-v: 4d(0.5,0,δ), where δ denotes small displacement from the specified high symmetry locations compatible with the local symmetry. (For interpretation of the references to colour in this figure legend, the reader is referred to the web version of this article.)

Considering only the crystal structure, the austenite phase of Heusler alloys with the conventional cubic cell can be regarded as a 2 × 2 × 2 supercell of the bcc lattice. In this regard, light interstitials such as H, B, C, and N can also be promising to induce significant tetragonal distortions and thus substantial MAE to Heusler alloys, like the FeCo alloys and bcc Fe. It is noted that the Heusler alloys in the tetragonal martensitic phase do show significant MAE. For instance, among 286 Heusler compounds, a systematic high throughput (HTP) screening suggests 19 potential tetragonal systems with large out-of-plane MAE (as large as 0.9 MJ/m^3) [13]. Matsushita et al. found 15 Heusler compounds have tetragonal distortions of which the MAEs range from -12 MJ/m^3 to 5.19 MJ/m^3 [14]. Focus on Ni based full Heusler compounds, Herper *et.al.* [15] found tetragonal Ni_2FeGe has an MAE of 0.95 MJ/m^3, which can be further increased to 1 to 2 MJ/m^3 by non-magnetic doping. Furthermore, imposing strain by proper substrates is helpful to engineer a large MAE out of the cubic Heusler alloys. It is found that the out-of-plane MAE of epitaxial Co_2MnGa (001) films can be remarkably enhanced from 0.11 MJ/m^3 to 0.33 MJ/m^3 by changing the substrate from ErAs/InGaAs/InP to ScErAs/GaAs [16]. Lastly, previous experiments have already demonstrated that interstitials can be incorporated into Heusler alloys, leading to enhanced mechanical stability and magnetocaloric effect [17,18]. For $Ni_{43}Mn_{46}Sn_{11}C_x$, when the interstitial content x is increased from 0 to 8 the martensitic phase transformation temperature is increased from 196 to 249 K, while a remarkable increase of MAE is observed when x is increased from 0 to 2 [17]. Due to large loss of manganese in content of x=8, there is even a distortion of crystal structure from Hg_2CuTi-type to the Cu_2MnAl-type [17]. Similar effect has also been observed in $Ni_{50}Mn_{34.8}In_{14.2}$, $Ni_{43}Mn_{46}Sn_{11}$ and $Ni_{50}Mn_{38}Sb_{12}$ doped with B interstitial [18–20].

In this work, focusing on developing rare-earth free permanent magnets, we have performed high-throughput first-principles calculations to investigate the effects of light interstitials (*e.g.*, H, B, C, and N) on cubic Heusler alloys. After identifying the most favorable site preference of the interstitial atoms, the MAE of compounds with negative formation energy was evaluated to select the most promising candidates. Apart from thermodynamically stable criteria, the disorder effect should also be considered, which is however beyond the scope of the present paper and saved for future study. We observed that the induced MAE can be as large as 2.4 MJ/m^3, and there are 32 systems with a sizable out-of-plane MAE ($>$ 0.4 MJ/m^3). Detailed analysis based on the Bain path and the atom-resolved MAE reveal that not only the global tetragonal distortion but also the associated local chemical bonding are crucial for the interstitial induced magnetic anisotropy.

2. Computational details

Starting from 128 full Heusler alloys with space group $Fm\bar{3}m$ including at least one of the magnetic atoms Cr, Mn, Fe, Co, and Ni from the Inorganic Crystal Structure Database (ICSD) [21] (cf. Table A.1 in Appendix Appendix A), we performed density functional theory (DFT) calculations firstly to identify the energetically most favored interstitial sites for H, B, C, and N atoms. There are four types of interstitial sites based on the symmetries, as shown in Fig. 1(a). The DFT calculations are managed with our in-house developed high-throughput environment (HTE) [22,23], using both the Vienna ab initio Simulation Package (VASP) [24,25] and full-potential local-orbital (FPLO) [26,27] codes. The structure optimization is performed in a two step manner. Firstly, ultrasoft pseudopotentials (US-PP) [28] are used in combination with the PW91 [29] exchange correlation functional, where the cutoff energy for the plane wave basis is set to 250 eV and and a k-mesh density of 30$Å^{-1}$. Secondly, the structure is relaxed using the projector augmented plane wave (PAW) method with the exchange-correlation functional under the generalized gradient approximation (GGA) parameterized by Perdew, Burke, and Ernzerhof (PBE) [30] with increasing plane wave expansion as 350 eV and *k*-mesh density as 40 $Å^{-1}$ to achieve good convergence. After obtaining the energy lowest configuration, the MAEs of candidates with negative formation energies are calculated by using FPLO with a *k*-mesh density of 120 $Å^{-1}$ to guarantee fine convergence. For the MAE calculations of Ni_2FeGa with C interstitial, the resulting *k*–mesh is set as 24 × 24 × 17. The bonding analysis is done in terms of the crystal orbital Hamilton population (COHP) evaluated using the LOBSTER code [31].

3. Results and discussions

As shown in Fig. 1(a), the systems we considered correspond to doping 6.25 at% interstitial atoms (I) into the full Heusler alloys (X_2YZ), leading to a general chemical formula $X_2YZI_{1/4}$. This is in accordance with the typical doping concentrations experimentally accomplishable, *e.g.*, 12.5 at% content of N in Fe and 9.6 at% of B in $Fe_{0.38}Co_{0.62}$. [10,11] Like for the Fe-Co alloys, we find light interstitials can indeed cause stable tetragonal distortion to cubic full Heusler alloys, which is defined by the c/a ratio between the c-axis and in-plane lattice constants. As shown in Table 1, with N interstitials, Fe_2NiAl has a tetragonal distortion as large as c/a=1.57. Such a strong tetragonal distortion prevails in the other Heuslers with the other types of interstitial atoms, which breaks the cubic symmetry

Table 1
The basic information of the most promising candidates of Heusler compounds with interstitials, where “site” marks the energetically preferred interstitial site, ΔH indicate the formation energy in unit of eV/atom, c/a ratio of resulting lattice constants along c-axis and in-plane, MAE in MJ/m^3 and meV/f.u. (in parenthesis), total magnetic moment M_{tot} in the unit of μ_B/f.u., and the magnetization M/V in the unit of μ_B/Å^3. It should be noticed the general chemical formula for Heusler compound with interstitial is $X_2YZI_{1/4}$, where I is the interstitial.

Parent	int.	site	ΔH	c/a	MAE	M_{tot}	M/V
Fe_2CoGa	B	24f	−0.0616	1.45	1.4949 (0.4998)	5.56	0.1120
	C	24f	−0.0486	1.48	1.3017 (0.4072)	5.37	0.1092
	N	24f	−0.1088	1.50	1.3180 (0.4295)	5.36	0.1089
	H	24f	−0.0922	1.48	2.3677 (0.6863)	5.95	0.1227
Ni_2FeGa	C	24f	−0.1207	1.40	0.9636 (0.2961)	2.93	0.0595
	N	24f	−0.1620	1.40	1.4292 (0.4386)	2.97	0.0602
	H	24f	−0.1916	1.39	0.5582 (0.1668)	3.13	0.0654
Fe_2CoGe	H	24f	−0.0627	1.51	0.6291 (0.2080)	5.48	0.1142
	N	24f	−0.0576	1.56	0.4047 (0.1368)	5.01	0.1025
Fe_2NiAl	H	24f	−0.2545	1.53	0.4947 (0.1298)	4.56	0.0955
	N	24f	−0.2842	1.57	0.5270 (0.1368)	4.40	0.0902
Fe_2NiGa	H	24f	−0.1915	1.55	0.5670 (0.1298)	4.67	0.0977
	B	24f	−0.1219	1.51	0.7853 (0.1758)	4.42	0.0893
	C	24f	−0.1208	1.53	0.9217 (0.1863)	4.31	0.0874
	N	24f	−0.1620	1.53	1.3295 (0.2429)	4.45	0.0939
Co_2MnGa	C	24f	−0.1289	1.13	0.5267 (0.6303)	4.52	0.0920
	N	24f	−0.1836	1.12	0.4755 (0.1576)	4.76	0.0922
Co_2MnGe	C	24f	−0.0788	1.25	0.5388 (0.1226)	4.06	0.0831
	N	24f	−0.1226	1.29	0.5476 (0.1325)	4.13	0.0841
Co_2MnSi	C	24f	−0.2571	1.21	0.5384 (0.1464)	4.16	0.0898
Rh_2MnAl	C	24f	−0.5088	1.10	0.9501 (0.3336)	4.25	0.0742
	N	24f	−0.5457	1.06	1.1675 (0.4487)	4.49	0.0784
Rh_2NiSn	H	24f	−0.2288	1.26	0.8236 (0.3063)	0.99	0.0166
Mn_2VGa	C	24f	−0.1533	1.20	1.5038 (0.4874)	2.26	0.0435
	B	24f	−0.1474	1.23	1.8263 (0.5987)	2.48	0.0472
	N	24f	−0.2377	1.21	1.2674 (0.4087)	2.34	0.0451
Co_2FeAl	N	24g	−0.2770	1.08	0.4881 (0.3009)	5.01	0.1038
Au_2MnAl	H	16e	−0.1835	0.92	0.7732 (0.6489)	3.82	0.0582
	N	24g	−0.1975	1.27	−0.4091 (−0.2412)	3.66	0.0476
	C	24g	−0.2770	1.21	−0.5271 (−0.4923)	3.82	0.0574
Ni_2MnIn	C	24f	−0.0057	1.21	−1.0288 (−0.3513)	3.96	0.0685
Ni_2MnGa	H	24f	−0.2519	1.27	−1.3278 (−0.4898)	4.20	0.0852
	B	24f	−0.2204	1.28	−0.5822 (−0.1850)	4.02	0.0788
	C	24f	−0.1780	1.29	−0.9573 (−0.3031)	3.91	0.0771
Fe_3Ge	H	24f	−0.0563	1.42	1.5018 (0.4655)	6.44	0.1319
	B	24f	−0.0254	1.16	0.5868 (0.1812)	5.54	0.1211
Fe_3Ga	B	24f	−0.0710	1.21	0.6896 (0.2142)	6.16	0.1229
	N	24f	−0.1101	1.19	0.5184 (0.1610)	5.92	0.1022
Ni_2MnSn	B	24g	−0.0959	1.06	−0.6747 (−0.2064)	3.75	0.0645
	C	24g	−0.0480	1.17	−0.4261 (−0.1421)	3.70	0.0653
	N	24g	−0.0892	1.17	−0.4756 (−0.1613)	3.74	0.0697
Rh_2MnSn	C	24f	−0.2679	1.26	−0.8846 (−0.3529)	3.66	0.0572

and hence leads to possible significant MAE. From the theoretical point of view, the MAE is defined as the total energy difference between the magnetization parallel to [100] (in-plane) and [001] (out-of-plane) directions as

$$\mathrm{MAE} = E^{[100]} - E^{[001]} \tag{1}$$

where E^{α} is the total energy when magnetization direction is parallel to α. When the MAE value is positive (negative), the spontaneous magnetization will lie in the out-of-plane (in-plane) direction. Nevertheless, not all the interstitials are thermodynamically stable, as indicated by the formation energy. The candidates with an MAE more than 0.4 MJ/m^3 and a negative formation energy are listed in Table 1.

We notice all the parent Heusler compounds listed in Table 1 are ferromagnetic apart from Mn_2VGa and Rh_2MnAl. In our high throughput calculations, for convenience, all Heusler compounds are assumed to be ferromagnetic (FM). Previous studies [32,33] have shown Rh_2MnAl is an antiferromagnet where the Mn atoms are antiferromagnetic coupling between nearest neighbors in the (111) plane, which is still in the same antiferromagnetic phase after incorporating C or N interstitials. As to Mn_2VGa, experimental research [34] has shown it is a half-metallic ferrimagnet with antiferromagnetic coupling between Mn and V with a total net saturation magnetization per formula unit as 1.88 μ_B at 5 K. After inducing interstitial (C, B or N), Mn_2VGa is still ferrimagnettic with antiferromagnetic coupling between Mn and V, although initial spin configuration is ferromagnetic. Mn_2VGa have large MAE values as 1.82 MJ/m^3, 1.50 MJ/m^3 and 1.26 MJ/m^3 with B, C and N interstitial, respectively. However, due to the ferrimagnettic phase, the resulting magnetization densities for Mn_2VGa with B, C and N interstitial are as weak as about 0.04-0.05 μ_B/Å^3. Among all listed compounds in Table 1, Rh_2NiSn is weak ferromagnetic as experimental study [35] suggests it has a magnetic moment 0.6 μ_B per formula unit. Our calculations demonstrate that H interstitials can induce a tetragonal distortion of c/a=1.26 and a sizable MAE value as 0.82 MJ/m^3, whereas the magnetization is only about 0.02 μ_B/Å^3.

As shown in Table 1, we found 32 compounds with a large out-of-plane MAE ($>$ 0.4 MJ/m^3) as well as 10 compounds with a large in-plane MAE (absolute value larger than 0.4 MJ/m^3). In general, the

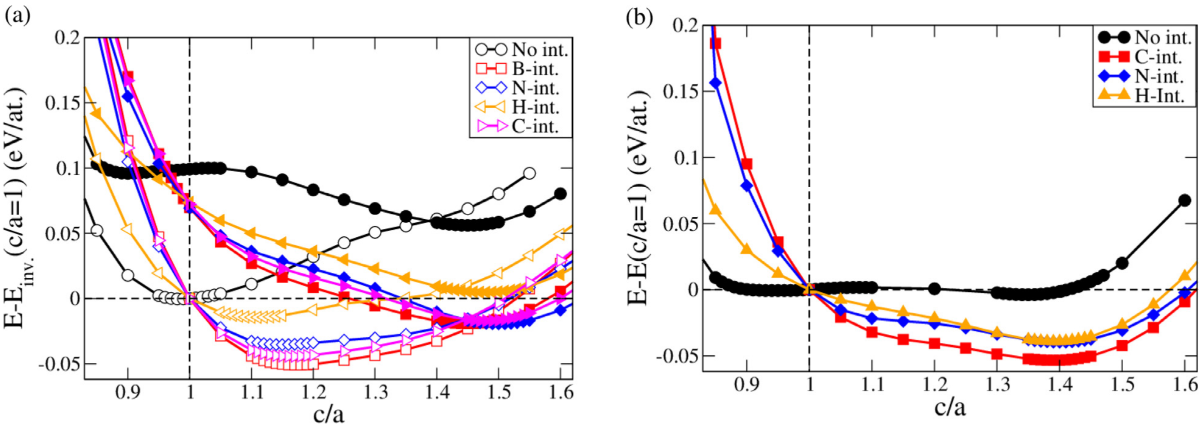

Fig. 2. Total energy as a function of tetragonal distortion ratio (c/a) for Fe_2CoGa with and without interstitials. The reference energy is the energy of the compound in cubic inverse Heusler structure for Fe_2CoGa with each interstitial as well as the parent compound. The opened and filled symbols represent the results of Fe_2CoGa in inverse and full Heusler structures, respectively. (b) The total energy as a function of tetragonal distortion ratio for Ni_2FeGa in full Heusler structure with and without interstitials. Here the reference energy is the energy of the compound in cubic full Heusler structure.

interstitial atoms prefer to be located at the octahedral centers (including both the 24f and 24g sites) except for the H interstitials in Au_2MnAl which is stable at the tetrahedral center. For the cases of octahedral center, the interstitials mostly prefers 24f sites ($\frac{1}{4}$,0,0) where there are the same atoms in the plane perpendicular to the c-axis. On the other hand, for Co_2FeAl with N, Au_2MnAl with N and C, Ni_2MnSn with B, C and N, interstitials prefer 24g sites ($\frac{1}{2}$,$\frac{1}{4}$,$\frac{1}{4}$). We note that Fe_3Ge with H interstitial has the largest magnetization density as 0.13 μ_B /Å^3 as well as quite large MAE value (1.50 MJ/m^3), indicating it is a promising permanent magnet. Furthermore, comparing with the magnetization and MAE of experimentally realized permanent magnets [1,36–40] Heusler alloys with interstitials can fill the gap between the low performance magnets (such as AlNiCo and ferrite) and high performance magnets (such as Sm-Co and Nd-Fe-B) in terms of MAE and magnetization, which can spread a wide spectrum of applications.

Interestingly, Au_2MnAl with H is the only candidate where the interstitials prefer the tetrahedral center (16e site). However, for cases of Au_2MnAl with N and and C, interstitial prefers to be located in the octahedral centers with in-plane MAE. Such special interstitial behaviors can be easily understood based on the chemical bonding. Intuitively, due to the large atomic spheres of Au atoms, there is more space between the tetrahedron edge bound than the other Heusler compound. For instance, in Au_2MnAl with H, the bond length of H-Au pair in tetrahedral center (1.83 Å) is comparable with that in octahedral center (1.93 Å). On the other hand, the bond length of Cu-H pair for Cu_2MnAl with H in tetrahedral center is just 1.62 Å, of which the value is obviously smaller than the H-Au pair for H interstitial in the tetrahedral center of Au_2MnAl (1.83 Å). This suggests Au atom can really provide more space for interstitials in the tetrahedral site. It should be noticed that Cu-H pair in octahedral center also has a bit larger bond length (1.70 Å) than that in tetrahedral center. However, in the tetrahedral center case, the bond length is too small to provide enough space for the interstitials. Thus, the H interstitials prefer the octahedral centers in Cu_2MnAl. On the other hand, for Au_2MnAl with C and N, it is observed that the interstitial atoms still prefer the octahedral center because of the larger atomic radii of C and N atoms compared to that of H. Therefore, in order to get the interstitials incorporated at the tetrahedral center, two conditions should be satisfied: (a) The interstitial atoms should be small; (b) There should be large atoms in the parent compound, providing more space. Different site preference of the H and C/N interstitials induces significant changes on the MAE of Au_2MnAl, *e.g.*, H-interstitial case favors out-of-plane magnetization while C/N interstitial cases lead to in-plane magnetization.

According to Table. 1, Fe_2CoGa with interstitials is a promising candidate for permanent magnets. However, in the ICSD database [21], Fe_2CoGa (ICSD ID: 102385 and 197615) and Fe_2CoGe (ICSD ID: 52954) are in the full Heusler structure, while early Mössbauer measurements have shown Fe_2CoGa and Fe_2CoGe are energetically favored in the inverse Heusler structure [41,42]. Previous theoretical study [43] found that full Heusler Fe_2CoGa have a martensitic phase transition with a c/a ratio as 1.4, which is also confirmed by our calculation (cf. Fig. 2(a)). According to our Bain-path calculations, the inverse Heusler structure is still more energetically favored for Fe_2CoGa, even after considering H, B, C, and N interstitials. Nevertheless, after introducing interstitials, for the full Heusler structure, the c/a ratio is near to 1.4; whereas for the inverse Heusler structure, the c/a ratio of Fe_2CoGa with interstitials is just from 1.1-1.2 due to there is no metastable phase (Fig. 2(a)). The MAE values of the inverse Fe_2CoGa with B, C, N, and H interstitial are 0.1026 MJ/m^3, 0.2148 MJ/m^3, 0.3798 MJ/m^3, and 0.1925 MJ/m^3, respectively. Such lower MAE values are partially due to that interstitials induce much weaker tetragonal distortion to Fe_2CoGa for inverse Heusler structure ($1.1 \le c/a \le 1.2$) than that for full Heusler structure ($1.45 \le c/a \le 1.5$).

More interestingly, C, N, and H interstitials induce significant MAEs to Ni_2FeGa. Experimental studies suggest that Ni_2FeGa can be grown by melt-spinning technique [44] or glass-purify method [45], transforming from high chemical ordering $L2_1$ structure (full Heusler) to martensitic structure at 142 K with a high Curie temperature of 430 K [44]. Further experiments showed polycrystalline alloys $Ni_{53+x}Fe_{20-x}Ga_{27}$ have smaller but comparable entropy changes as classical magnetocaloric Heusler alloy systems Ni-Mn-Ga and Ni-Mn-Sn [46]. DFT calculations suggest that Ni_2FeGa has a tetragonal (corresponding to the martensitic phase) structure of c/a=1.35 [15,47] with an MAE as 0.318 MJ/m^3 [15]. We also found that Ni_2FeGa is stable in the tetragonal structure with a c/a ratio as 1.35 (Fig. 2(b)) and a comparable MAE as 0.2334 MJ/m^3 (0.0698 meV per chemical formula cell). However, the energy difference between tetragonal and cubic structures is as small as 2.80 meV/atom. As proposed by Barman, the martensite phase transition temperature is proportional to the energy difference between cubic and martensite phases [48], as manifested by the experimental martensitic transition at 142 K [44]. After inducing interstitial C, H, or N, Ni_2FeGa is stable in the tetragonal

Table 2
Perturbative analysis of the MAE for $Ni_2FeGaI_{1/4}$ (I = H, N, and C) and tetragonal Ni_2FeGa. The orbital moments μ_L (μ_B) and their variations $\Delta\mu_L$ between the magnetization directions of [001] and [100] are listed for $Ni_2FeGaI_{1/4}$ (I = H, N, and C) and tetragonally distorted Ni_2FeGa with corresponding c/a ratio. The magneto-crystalline anisotropy energy (MAE, meV) from symmetry-distinct atoms is obtained based on the Bruno's formula (Eq. (2)), with the resulting sum ($\sum$) in comparison with the MAE obtained from explicit DFT calculations in parenthesis.

	c/a int.	atom	$\mu_L^{[001]}$ (μ_B)	$\mu_L^{[100]}$ (μ_B)	$\Delta\mu_L$ (μ_B)	MAE (meV)
with interstitial		Ni-i	0.024	0.019	0.005	0.097
		Ni-ii	0.020	0.022	−0.002	−0.039
	1.39	Fe-iii	0.068	0.043	0.025	0.309
	H	Fe-iv	0.063	0.040	0.023	0.284
		Fe-v	0.066	0.046	0.020	0.247
		$\sum$	–	–	–	0.330 (0.167)
		Ni-i	0.025	0.012	0.013	0.250
		Ni-ii	0.020	0.024	−0.004	−0.078
	1.40	Fe-iii	0.068	0.013	0.055	0.681
	N	Fe-iv	0.067	0.053	0.014	0.173
		Fe-v	0.072	0.049	0.023	0.285
		$\sum$	–	–	–	0.528 (0.439)
		Ni-i	0.013	0.011	0.002	0.039
		Ni-ii	0.022	0.024	−0.002	−0.039
	1.40	Fe-iii	0.058	0.017	0.041	0.508
	C	Fe-iv	0.067	0.048	0.019	0.235
		Fe-v	0.073	0.051	0.021	0.260
		$\sum$	–	–	–	0.316 (0.296)
w/o interstitial	1.35	Ni	0.022	0.024	−0.002	−0.039
	-	Fe	0.065	0.044	0.021	0.260
		$\sum$	–	–	–	0.180 (0.070)
	1.40	Ni	0.021	0.023	−0.002	−0.039
	-	Fe	0.061	0.041	0.020	0.248
		$\sum$	-	-	-	0.170 (0.066)

phase with $c/a \approx 1.40$. Correspondingly, the MAEs have been enhanced to 1.43 MJ/m^3, 0.94 MJ/m^3, and 0.56 MJ/m^3 for Heusler Ni_2FeGa with N, C, and H interstitials, respectively. Obviously, C and N interstitials cause more significant enhancement on the MAE than the H interstitials, though the resulting c/a ratios are comparable. Therefore, we suspect that both the tetragonal distortion and the chemical bonding environment will influence the MAE values for Heusler with interstitial, which will be discussed in detail below.

Turning now to the origin of the induced MAE by interstitials, from the theoretical perspective, beside the shape anisotropy due to the magnetic dipole-dipole interaction, the magneto-crystalline anisotropy can be attributed to the spin-orbit coupling (SOC), which is the dominant contribution to MAE and hence coercivity for PMs. Based on the perturbation theory, Bruno [49] pointed out that the MAE can be formulated as

$$\mathrm{MAE} = -\sum_i \frac{\xi_i}{4\mu_B}\Delta\mu_i, \tag{2}$$

where ξ_i denotes the atomic SOC constant and $\Delta\mu_i$ is the orbital moment difference between the magnetization directions parallel to [001] and [100] for the i-th atom. We note that such a model is best applicable for strong magnets where the majority spin channel is almost fully occupied, whereas there is a more general formula considering the spin-flip and quadruple terms [50]. Taking Ni_2FeGa as an example, Table 2 shows the atom-resolved orbital moments and the resulting contributions to the MAE using Bruno's formula, where the atomic SOC constants for Ni and Fe are 630 cm^{-1} (corresponding to 78.1100 meV) and 400 cm^{-1} (corresponding to 49.5937 meV) taken from Ref. [51]. The resulting MAE for Ni_2FeGa with C, N, and H interstitials based on the Eq. (2) are 0.316 meV/f.u., 0.528 meV/f.u. and 0.330 meV/f.u., respectively. Correspondingly, the MAEs based on Eq. (1) are 0.296 meV/f.u., 0.439 meV/f.u. and 0.167 meV/f.u., respectively. The relative MAE differences of Bruno's model to that of Eq. (1) are 17.17%, 23.83% and 79.61%. Nevertheless, the tendency is correctly reproduced and we believe the atomic-resolved contributions evaluated based on Eq. (2) are still valuable to elucidate the origin of MAE. It is noteworthy that the tetragonal distortion ratios for Ni_2FeGa with H, C and N interstitial are 1.39, 1.40 and 1.40, respectively (cf. Table 1). To make a direct comparison to the pristine Ni_2FeGa, we evaluated the MAE and orbital moments for Ni_2FeGa without interstitials but with imposed c/a=1.40, resulting in an MAE of 0.066 meV and 0.170 meV per chemical formula by using Eq. (1) and Bruno's model Eq. (2), respectively. Again, the MAEs obtained from the Bruno's model can be well compared with that from Eq. (1) for Ni_2FeGa with C and N interstitial, but for H interstitial case it is roughly compared. It is noted that the Bruno's model should be applied with caution for multicomponent materials with heavy elements, where substantial atomic SOC will induce strong spin-flip contributions [52–54]. For instance, it is observed that the orbital moment difference $\Delta\mu$ for the Au atoms in $Au_2MnAlI_{1/4}$ (I = H, C and N) is in the magnitude of 0.01 μ_B, which is comparable to that of the Mn atoms. Furthermore, the MAE values based on the Bruno's formula are 0.813, 4.37, and 3.09 meV/f.u. for $Au_2MnAlI_{1/4}$ (I = H, C and N), respectively, which are significantly deviated from the values obtained via self-consistent calculation, *i.e.*, -0.252, -0.220 and -0.178 meV/f.u. Nevertheless, as there is no heavy element in $Ni_2FeGaI_{1/4}$ (I = C, N and H), we believe that the Bruno's model is valuable to elucidate the fact that the main influence of interstitials on MAE is local, *i.e.*, originated from the magnetic atoms surrounding the interstitials.

The remarkable variation of the orbital moments and the resulting significant enhancement of MAEs can be attributed to the magnetic atoms surrounding the interstitial atoms. It is noted that C and N interstitials can give rise a significant MAE to Ni_2FeGa, while the effect of H interstitial is rather weaker. Following Table 2, it is clear that without interstitials (c/a=1.40), Fe atoms have the leading contribution to the MAE of 0.26 meV per atom, while the contribution from Ni (about -0.039 meV per atom) is an order of magnitude lower with opposite sign. The change in c/a from 1.35 to 1.40 has minor influence on the MAE and orbit moment. After considering interstitial N (H), the contribution for Ni-i atoms within the same plane is enhanced to 0.250 meV (0.097 meV) per atom. As to C interstitial atoms, the MAE of Ni-i atoms is slightly (Fig. 1(b)) increased to 0.039 meV per atom. That is, all types of the interstitial atoms lead to a sign change of the contribution to MAE for Ni-i. On the other hand, the orbital moments and thus the resulting MAE contribution are very comparable for the Ni-ii atoms with and without interstitials, because the Ni-ii atoms are far away from the interstitials. Furthermore, for the H interstitial case, both the MAE and orbital moments of all Fe (including iii, iv and v) atoms change only slightly comparing to those in the pristine compound with imposed c/a=1.40, whereas the N and C interstitials lead to significant enhancement of contribution for Fe-iii atoms to MAE. For instance, the MAE contributions of Fe-iii atoms below the interstitials are increased to 0.681 meV and 0.508 meV per atom with N and C interstitials, more than two times larger than that (0.260 meV) in the parent compound. Meanwhile the contributions from Fe-iv and Fe-v atoms are slightly reduced. Therefore, the interstitial atoms have very strong influence on the MAE of the local surrounding atoms, while the global tetragonal distortion has relatively marginal effects.

The effects of interstitials on MAEs and orbital magnetizations can be further understood based on the chemical bonding pairs between the interstitials and surrounding magnetic atoms. For instance, the distance between the interstitial atoms (at the octahedral center) H, C, and N and the Ni-i atoms in the same *z*-plane (Fig. 1 (b)) have comparable bond lengths of 1.85 Å, 1.88 Å, and 1.88 Å, respectively. However, the integrated COHP of the H-(Ni-i) bond is just -0.63 eV, which is much weaker than that of the C-(Ni-i) (-2.12 eV) and N-(Ni-i) (-1.96 eV) bonds. Meanwhile, the pairs between atoms Fe-iii (below the interstitials, Fig. 1 (b)) and the interstitial atoms H, C, and N have the bond lengths of 1.65 Å, 1.83 Å, and 1.83 Å, respectively, with the corresponding bond integrated COHP being -1.24 eV (H-(Fe-iii)), -2.88 eV (C-(Fe-iii)) and -2.38 eV (N-(Fe-iii)). Obviously, the bond strengths between C interstitials and the surrounding magnetic atoms (Fe-iii and Ni-i) are the strongest. This explains the significant change of orbital moments of Ni_2FeGa with C interstitial comparing to Ni_2FeGa at the same tetragonal distortion ratio without interstitial. Therefore, the H interstitial just causes tetragonal distortion to Ni_2FeGa without bonding to the neighboring atoms as indicated by relatively smaller values of the integrated COHP, while both C and N interstitials not only induce tetragonal distortion but also change the local chemical environment by forming strong bonds. Moreover, for all interstitials, bond pairs with Ni-i and Fe-iii atoms have similar bond lengths, but the strength of the former is weaker than the latter. Such bonding behavior explains the effect of interstitials on the magnetization and Fe-iii atoms have more significant contributions to the variation of the MAE than the Ni-i atoms.

4. Conclusion

Based on high-throughput DFT calculations, we investigated the effects of (H, B, C, and N) interstitials on the magnetic properties of cubic full Heusler compounds. We identified 32 compounds with substantial uniaxial MAEs. Detailed analysis reveals that in addition to the breaking of the cubic symmetry, the changes in the local crystalline environment can induce significant contribution to the MAE, which can be attributed to the chemical bonding between the interstitial and surrounding magnetic atoms. This could provide an efficient way to design permanent magnets, which shall be explored further both experimentally and theoretically.

Declaration of Competing Interest

The authors declare that they have no known competing financial interests or personal relationships that could have appeared to influence the work reported in this paper.

Acknowledgments

We acknowledge support from DFG CRC/TRR 270. Qiang Gao thanks the financial support from the China Scholarship Council. The authors gratefully acknowledge computational time on the Lichtenberg High Performance Supercomputer.

Appendix A

Table A.1
All the considered Heusler compounds (Com.) together with the ICSD ID number.

Com.	ID	Com.	ID	Com.	ID	Com.	ID
Au_2MnAl	57504	Co_2CrAl	57600	Co_2FeAl	57607	Co_2HfAl	110,809
Co_2MnAl	606611	Co_2NbAl	57620	Co_2TaAl	606,667	Co_2TiAl	606,680
Co_2VAl	57,643	Co_2ZrAl	57648	Co_2CrGa	102318	Co_2CrIn	416,260
Co_2FeGa	102392	Co_2FeGe	247268	Co_2FeIn	102,392	Co_2FeSi	622985
Co_2HfGa	102,433	Co_2MnGa	623116	Co_2NbGa	623126	Co_2TaGa	102451
Co_2TiGa	102453	Co_2VGa	623,228	Co_2LiGe	53,673	Co_2MnGe	52,971
Co_2TiGe	169,469	Co_2ZnGe	52994	Co_2HfSn	102,483	Co_2MnSb	53,002
Co_2MnSi	106,484	Co_2MnSn	102,332	Co_2NbSn	102,554	Co_2ScSn	102,646
Co_2TiSi	53,080	Co_2VSi	53,086	Co_2TiSn	102,583	Co_2VSn	102684
Co_2ZrSn	102687	Cu_2CrAl	57653	Cu_2MnAl	607012	Cu_2CoSn	103057
Cu_2FeSn	151,205	Cu_2MnIn	102996	Cu_2MnSb	53,312	Cu_2MnSn	103,057
Cu_2NiSn	103,069	Fe_2CrAl	184446	Fe_2MnAl	57,806	Fe_2MoAl	57,807
Fe_2NiAl	57,808	Fe_2TiAl	57,827	Fe_2VAl	57,832	Fe_2CoGa	103473
Fe_2CoGe	52,954	Fe_2CrGa	102,755	Fe_2NiGa	103460	Fe_2TiGa	103469
Fe_2VGa	103,473	Fe_2MnSi	632,569	Fe_2VSi	53555	Fe_2TiSn	103641
Fe_2VSn	103,644	Mn_2VAl	57,994	Mn_2RhGa	247,951	Mn_2VGa	103813
Mn_2RuGe	247,950	Mn_2RuSn	247,949	Mn_2WSn	104,980	Ni_2CrAl	57,662
Ni_2HfAl	57,901	Ni_2MnAl	57,976	Ni_2NbAl	58,016	Ni_2ScAl	58,050
Ni_2TaAl	58,055	Ni_2TiAl	58,063	Ni_2VAl	58,071	Ni_2ZrAl	58081
Ni_2CuSb	53,320	Ni_2CuSn	103,068	Ni_2HfGa	103,734	Ni_2MnGa	103803
Ni_2NbGa	103,839	Ni_2ScGa	103,874	Ni_2TaGa	103,881	Ni_2TiGa	103886
Ni_2VGa	103,892	Ni_2ZrGa	103,902	Ni_2LiGe	53,673	Ni_2MnGe	192566
Ni_2ZnGe	53,865	Ni_2HfIn	54,595	Ni_2HfSn	104250	Ni_2MgIn	51982
Ni_2MnIn	639,954	Ni_2ScIn	59,446	Ni_2TiIn	59451	Ni_2ZrIn	59460
Ni_2LiSi	44,819	Ni_2LiSn	25,325	Ni_2MgSb	104841	Ni_2MgSn	104,842
Ni_2TiSb	76,700	Ni_2ZrSb	76,703	Ni_2ScSn	105,339	Ni_2TiSn	105,369
Ni_2VSn	105,376	Ni_2ZrSn	105,383	Pd_2MnAl	57,981	Pd_2MnAs	107955
Ni_2NbSn	105,181	Pd_2MnGe	53,705	Rh_2NiSn	105,327	Pd_2MnIn	51,990
Pd_2MnSb	643,312	Pd_2MnSn	104,945	Rh_2MnAl	57,986	Rh_2MnGe	53,706
Rh_2MnPb	104936	Rh_2MnSn	104,964	Ru_2FeSi	53,525	Ru_2FeSn	103,615
Fe_3Al	57,793	Fe_3Ga	108,436	Fe_3Ge	53,462	Fe_3Si	53545
Mn_3Si	76,227	Ni_3Al	58,038	Ni_3Sb	76,693	Ni_3Sn	105354

References

[1] O. Gutfleisch, M.A. Willard, E. Brück, C.H. Chen, S.G. Sankar, J.P. Liu, Magnetic materials and devices for the 21st century: stronger, lighter, and more energy efficient, Adv. Mater. 23 (7) (2011) 821–842, doi: 10.1002/adma.201002180. https://onlinelibrary.wiley.com/doi/abs/10.1002/adma.201002180

[2] J.M.D. Coey, Permanent magnets: plugging the gap, Scr. Mater. 67 (6) (2012) 524–529, doi: 10.1016/j.scriptamat.2012.04.036.http://www.sciencedirect.com/science/article/pii/S1359646212002990

[3] S. Sugimoto, Current status and recent topics of rare-earth permanent magnets, J. Phys. D: Appl. Phys. 44 (6) (2011) 064001, doi: 10.1088/0022-3727/44/6/064001.

[4] K.P. Skokov, O. Gutfleisch, Heavy rare earth free, free rare earth and rare earth free magnets - vision and reality, Scr. Mater. 154 (2018) 289–294, doi: 10.1016/j.scriptamat.2018.01.032.http://www.sciencedirect.com/science/article/pii/S1359646218300599

[5] T. Burkert, L. Nordström, O. Eriksson, O. Heinonen, Giant magnetic anisotropy in tetragonal FeCo alloys, Phys. Rev. Lett. 93 (2) (2004) 027203, doi: 10.1103/PhysRevLett.93.027203.https://link.aps.org/doi/10.1103/PhysRevLett.93.027203

[6] G. Andersson, T. Burkert, P. Warnicke, M. Björck, B. Sanyal, C. Chacon, et al., Perpendicular magnetocrystalline anisotropy in tetragonally distorted Fe-Co alloys, Phys. Rev. Lett. 96 (3) (2006) 037205, doi: 10.1103/PhysRevLett.96.037205.https://link.aps.org/doi/10.1103/PhysRevLett.96.037205

[7] F. Yildiz, M. Przybylski, X.-D. Ma, J. Kirschner, Strong perpendicular anisotropy in Fe1-xCox alloy films epitaxially grown on mismatching Pd (001), Ir (001), and Rh (001) substrates, Phys. Rev. B 80 (6) (2009) 064415, doi: 10.1103/PhysRevB.80.064415.https://link.aps.org/doi/10.1103/PhysRevB.80.064415

[8] F. Luo, X.L. Fu, A. Winkelmann, M. Przybylski, Tuning the perpendicular magnetic anisotropy in tetragonally distorted FexCo1-x alloy films on Rh (001) by varying the alloy composition, Appl. Phys. Lett. 91 (26) (2007) 262512, doi: 10.1063/1.2821370.https://aip.scitation.org/doi/abs/10.1063/1.2821370

[9] L. Reichel, L. Schultz, S. Fähler, Lattice relaxation studies in strained epitaxial Fe-Co-C films, J. Appl. Phys. 117 (17) (2015) 17C712, doi: 10.1063/1.4908031.https://aip.scitation.org/doi/10.1063/1.4908031

[10] L. Reichel, L. Schultz, D. Pohl, S. Oswald, S. Fähler, M. Werwiński, et al., From soft to hard magnetic Fe-Co-B by spontaneous strain: a combined first principles and thin film study, J. Phys.: Condens. Matter 27 (47) (2015) 476002, doi: 10.1088/0953-8984/27/47/476002.

[11] H. Zhang, I. Dirba, T. Helbig, L. Alff, O. Gutfleisch, Engineering perpendicular magnetic anisotropy in Fe via interstitial nitrogenation: N choose K, APL Mater. 4 (11) (2016) 116104, doi: 10.1063/1.4967285.https://aip.scitation.org/doi/abs/10.1063/1.4967285

[12] D. Gölden, H. Zhang, I. Radulov, I. Dirba, P. Komissinskiy, E. Hildebrandt, et al., Evolution of anisotropy in bcc Fe distorted by interstitial boron, Phys. Rev. B 97 (1) (2018) 014411, doi: 10.1103/PhysRevB.97.014411.https://link.aps.org/doi/10.1103/PhysRevB.97.014411

[13] S.V. Faleev, Y. Ferrante, J. Jeong, M.G. Samant, B. Jones, S.S.P. Parkin, Heusler compounds with perpendicular magnetic anisotropy and large tunneling magnetoresistance, Phys. Rev. Mater. 1 (2) (2017) 024402, doi: 10.1103/PhysRevMaterials.1.024402.https://link.aps.org/doi/10.1103/PhysRevMaterials.1.024402

[14] Y.-I. Matsushita, G. Madjarova, J.K. Dewhurst, S. Shallcross, C. Felser, S. Sharma, E.K.U. Gross, Large magnetocrystalline anisotropy in tetragonally distorted Heuslers: a systematic study, J. Phys. D: Appl. Phys. 50 (9) (2017) 095002, doi: 10.1088/1361-6463/aa5441.

[15] H.C. Herper, Ni-based Heusler compounds: how to tune the magnetocrystalline anisotropy, Phys. Rev. B 98 (1) (2018) 014411, doi: 10.1103/PhysRevB.98.014411. https://link.aps.org/doi/10.1103/PhysRevB.98.014411

[16] M.J. Pechan, C. Yu, D. Carr, C.J. Palmstrøm, Remarkable strain-induced magnetic anisotropy in epitaxial Co2MnGa (001) films, J. Magn. Magn. Mater. 286 (2005) 340–345, doi: 10.1016/j.jmmm.2004.09.090.http://www.sciencedirect.com/science/article/pii/S0304885304009850

[17] Y. Zhang, J. Liu, Q. Zheng, J. Zhang, W. Xia, J. Du, A. Yan, Large magnetic entropy change and enhanced mechanical properties of Ni-Mn-Sn-C alloys, Scr. Mater. 75 (2014) 26–29, doi: 10.1016/j.scriptamat.2013.11.009.http://www.sciencedirect.com/science/article/pii/S1359646213005666

[18] I. Dubenko, T. Samanta, A. Quetz, A. Kazakov, I. Rodionov, D. Mettus, V. Prudnikov, S. Stadler, P. Adams, J. Prestigiacomo, A. Granovsky, A. Zhukov, N. Ali, The comparison of direct and indirect methods for determining the magnetocaloric parameters in the Heusler alloy Ni50Mn34.8In14.2B, Appl. Phys. Lett. 100 (19) (2012) 192402, doi: 10.1063/1.4714539.https://aip.scitation.org/doi/abs/10.1063/1.4714539

[19] H.C. Xuan, D.H. Wang, C.L. Zhang, Z.D. Han, B.X. Gu, Y.W. Du, Boron's effect on martensitic transformation and magnetocaloric effect in Ni43Mn46Sn11Bx alloys, Appl. Phys. Lett. 92 (10) (2008) 102503, doi: 10.1063/1.2895645.https://aip.scitation.org/doi/abs/10.1063/1.2895645

[20] N.V. Nong, L.T. Tai, N.T. Huy, N.T. Trung, C.R.H. Bahl, R. Venkatesh, et al., Structural, magnetic and magnetocaloric properties of Heusler alloys Ni50Mn38Sb12 with boron addition, Mater. Sci. Eng. B 176 (16) (2011) 1322–1325, doi: 10.1016/j.mseb.2011.07.013. http://www.sciencedirect.com/science/article/pii/S0921510711003345

[21] [link]. http://www2.fiz-karlsruhe.de/icsd_home.html.

[22] I. Opahle, G.K.H. Madsen, R. Drautz, High throughput density functional investigations of the stability, electronic structure and thermoelectric properties of binary silicides, Phys. Chem. Chem. Phys. 14 (47) (2012) 16197–16202, doi: 10.1039/C2CP41826F.https://pubs.rsc.org/en/content/articlelanding/2012/cp/c2cp41826f

[23] I. Opahle, A. Parma, E.J. McEniry, R. Drautz, G.K.H. Madsen, High-throughput study of the structural stability and thermoelectric properties of transition metal silicides, New J. Phys. 15 (10) (2013) 105010, doi: 10.1088/1367-2630/15/10/105010.

[24] G. Kresse, J. Furthmüller, Efficient iterative schemes for ab initio total-energy calculations using a plane-wave basis set, Phys. Rev. B 54 (16) (1996) 11169–11186, doi: 10.1103/PhysRevB.54.11169.https://link.aps.org/doi/10.1103/PhysRevB.54.11169

[25] G. Kresse, D. Joubert, From ultrasoft pseudopotentials to the projector augmented-wave method, Phys. Rev. B 59 (3) (1999) 1758–1775, doi: 10.1103/PhysRevB.59.1758.https://link.aps.org/doi/10.1103/PhysRevB.59.1758

[26] K. Koepernik, H. Eschrig, Full-potential nonorthogonal local-orbital minimum-basis band-structure scheme, Phys. Rev. B 59 (3) (1999) 1743–1757, doi: 10.1103/PhysRevB.59.1743.https://link.aps.org/doi/10.1103/PhysRevB.59.1743

[27] I. Opahle, K. Koepernik, H. Eschrig, Full-potential band-structure calculation of iron pyrite, Phys. Rev. B 60 (20) (1999) 14035–14041, doi: 10.1103/PhysRevB.60.14035.https://link.aps.org/doi/10.1103/PhysRevB.60.14035

[28] D. Vanderbilt, Soft self-consistent pseudopotentials in a generalized eigenvalue formalism, Phys. Rev. B 41 (11) (1990) 7892–7895, doi: 10.1103/PhysRevB.41.7892.https://link.aps.org/doi/10.1103/PhysRevB.41.7892

[29] J.P. Perdew, J.A. Chevary, S.H. Vosko, K.A. Jackson, M.R. Pederson, D.J. Singh, et al., Atoms, molecules, solids, and surfaces: applications of the generalized gradient approximation for exchange and correlation, Phys. Rev. B 46 (11) (1992) 6671–6687, doi: 10.1103/PhysRevB.46.6671.https://link.aps.org/doi/10.1103/PhysRevB.46.6671

[30] J.P. Perdew, K. Burke, M. Ernzerhof, Generalized gradient approximation made simple, Phys. Rev. Lett. 77 (18) (1996) 3865–3868, doi: 10.1103/PhysRevLett.77.3865.https://link.aps.org/doi/10.1103/PhysRevLett.77.3865

[31] V.L. Deringer, A.L. Tchougréeff, R. Dronskowski, Crystal orbital hamilton population (COHP) analysis as projected from plane-wave basis sets, J. Phys. Chem. A 115 (21) (2011) 5461–5466, doi: 10.1021/jp202489s.https://doi.org/10.1021/jp202489s

[32] H. Masumoto, K. Watanabe, New compounds of the Clb, Cl Types of RhMnSb, IrMnSn and IrMnAl, New L21 (Heusler) Type of Ir2mnal and Rh2mnal alloys, and magnetic properties, J. Phys. Soc. Jpn. 32 (1) (1972), doi: 10.1143/JPSJ.32.281. https://www.jstage.jst.go.jp/article/jpsj1946/32/1/32_1_281/_article/-char/ja/

[33] J. Balluff, K. Diekmann, G. Reiss, M. Meinert, High-throughput screening for antiferromagnetic Heusler compounds using density functional theory, Phys. Rev. Mater. 1 (3) (2017) 034404, doi: 10.1103/PhysRevMaterials.1.034404.https://link.aps.org/doi/10.1103/PhysRevMaterials.1.034404

[34] K.R. Kumar, N.H. Kumar, G. Markandeyulu, J.A. Chelvane, V. Neu, P.D. Babu, Structural, magnetic and transport properties of half-metallic ferrimagnet Mn2vga, J. Magn. Magn. Mater. 320 (21) (2008) 2737–2740, doi: 10.1016/j.jmmm.2008.06.003. http://www.sciencedirect.com/science/article/pii/S0304885308006926

[35] J.C. Suits, Structural instability in new magnetic Heusler compounds, Solid State Commun. 18 (3) (1976) 423–425, doi: 10.1016/0038-1098(76)90040-5.http://www.sciencedirect.com/science/article/pii/0038109876900405

[36] A. Sakuma, First principle calculation of the magnetocrystalline anisotropy energy of Fept and copt ordered alloys, J. Phys. Soc. Jpn. 63 (8) (1994) 3053–3058, doi: 10.1143/jpsj.63.3053.https://www.jstage.jst.go.jp/article/jpsj/63/8/63_8_3053/_article/-char/ja/

[37] Y. Kota, A. Sakuma, Relationship between magnetocrystalline anisotropy and orbital magnetic moment in l10-type ordered and disordered alloys, J. Phys. Soc. Jpn. 81 (8) (2012) 084705, doi: 10.1143/JPSJ.81.084705.https://journals.jps.jp/doi/10.1143/JPSJ.81.084705

[38] Y. Yamada, T. Suzuki, H. Kanazawa, J.C. Österman, The origin of the large perpendicular magnetic anisotropy in Co3Pt alloy thin films, J. Appl. Phys. 85 (8) (1999) 5094–5096, doi: 10.1063/1.370101.https://aip.scitation.org/doi/abs/10.1063/1.370101

[39] H.R. Kirchmayr, Permanent magnets and hard magnetic materials, J. Phys. D: Appl. Phys. 29 (11) (1996) 2763–2778, doi: 10.1088/0022-3727/29/11/007.

[40] J. Cui, M. Kramer, L. Zhou, F. Liu, A. Gabay, G. Hadjipanayis, B. Balasubramanian, D. Sellmyer, Current progress and future challenges in rare-earth-free permanent magnets, Acta Mater. 158 (2018) 118–137, doi: 10.1016/j.actamat.2018.07.049. http://www.sciencedirect.com/science/article/pii/S1359645418305858

[41] N.K. Jaggi, K.R.P.M. Rao, A.K. Grover, L.C. Gupta, R. Vijayaraghavan, D.L. Khoi, Mssbauer and NMR study of site preference and local environment effects in co2fega & fe2coga, Hyperfine Interact. 4 (1) (1978) 402–406, doi: 10.1007/BF01021860.https://doi.org/10.1007/BF01021860

[42] T. Gasi, V. Ksenofontov, J. Kiss, S. Chadov, A.K. Nayak, M. Nicklas, J. Winterlik, M. Schwall, P. Klaer, P. Adler, C. Felser, Iron-based Heusler compounds fe$_2$*YZ* comparison with theoretical predictions of the crystal structure and magnetic properties, Phys. Rev. B 87 (6) (2013) 064411, doi: 10.1103/PhysRevB.87.064411.https://link.aps.org/doi/10.1103/PhysRevB.87.064411

[43] A. Dannenberg, M. Siewert, M.E. Gruner, M. Wuttig, P. Entel, Competing structural ordering tendencies in Heusler-type alloys with high Curie temperatures: Fe2CoGa1-xZnx studied by first-principles calculations, Phys. Rev. B 82 (21) (2010) 214421, doi: 10.1103/PhysRevB.82.214421.https://link.aps.org/doi/10.1103/PhysRevB.82.214421

[44] Z.H. Liu, M. Zhang, Y.T. Cui, Y.Q. Zhou, W.H. Wang, G.H. Wu, X.X. Zhang, G. Xiao, Martensitic transformation and shape memory effect in ferromagnetic Heusler alloy ni2fega, Appl. Phys. Lett. 82 (3) (2003) 424–426, doi: 10.1063/1.1534612. https://aip.scitation.org/doi/abs/10.1063/1.1534612

[45] J.F. Qian, H.G. Zhang, J.L. Chen, W.H. Wang, G.H. Wu, Undercooling growth and magnetic characterization of ferromagnetic shape memory alloy Ni2FeGa single crystals, J. Cryst. Growth 388 (2014) 107–111, doi: 10.1016/j.jcrysgro.2013.11.016.http://www.sciencedirect.com/science/article/pii/S0022024813007689

[46] V. Recarte, J.I. Pérez-Landazábal, C. Gómez-Polo, E. Cesari, J. Dutkiewicz, Magnetocaloric effect in Ni-Fe-Ga shape memory alloys, Appl. Phys. Lett. 88 (13) (2006) 132503, doi: 10.1063/1.2189665.https://aip.scitation.org/doi/10.1063/1.2189665
[47] Y. Qawasmeh, B. Hamad, Investigation of the structural, electronic, and magnetic properties of Ni-based Heusler alloys from first principles, J. Appl. Phys. 111 (3) (2012) 033905, doi: 10.1063/1.3681286.https://aip.scitation.org/doi/10.1063/1.3681286
[48] S.R. Barman, A. Chakrabarti, S. Singh, S. Banik, S. Bhardwaj, P.L. Paulose, et al., Theoretical prediction and experimental study of a ferromagnetic shape memory alloy: Ga_2MnNi, Phys. Rev. B 78 (13) (2008) 134406, doi: 10.1103/PhysRevB.78.134406.https://link.aps.org/doi/10.1103/PhysRevB.78.134406
[49] P. Bruno, Tight-binding approach to the orbital magnetic moment and magnetocrystalline anisotropy of transition-metal monolayers, Phys. Rev. B 39 (1) (1989) 865–868, doi: 10.1103/PhysRevB.39.865.https://link.aps.org/doi/10.1103/PhysRevB.39.865
[50] Y. Liu, Z. Xu, P.D. Johnson, G. van der Laan, Spin-orbit coupling, exchange interaction, and hybridization in the photoexcitation of the Ni 3P core level, Phys. Rev. B 52 (12) (1995) R8593–R8596, doi: 10.1103/PhysRevB.52.R8593.https://link.aps.org/doi/10.1103/PhysRevB.52.R8593
[51] D. Dai, H. Xiang, M.H. Whangbo, Effects of spin-orbit coupling on magnetic properties of discrete and extended magnetic systems, J. Comput. Chem. 29 (13) (2008) 2187–2209, doi: 10.1002/jcc.21011.https://www.onlinelibrary.wiley.com/doi/abs/10.1002/jcc.21011
[52] Y. Kota, A. Sakuma, Relationship between magnetocrystalline anisotropy and orbital magnetic moment in L10-type ordered and disordered alloys, J. Phys. Soc. Jpn. 81 (8) (2012) 084705, doi: 10.1143/JPSJ.81.084705.https://journals.jps.jp/doi/abs/10.1143/JPSJ.81.084705
[53] C. Andersson, B. Sanyal, O. Eriksson, L. Nordström, O. Karis, D. Arvanitis, et al., Influence of ligand states on the relationship between orbital moment and magnetocrystalline anisotropy, Phys. Rev. Lett. 99 (17) (2007) 177207, doi: 10.1103/PhysRevLett.99.177207.https://link.aps.org/doi/10.1103/PhysRevLett.99.177207
[54] P. Ravindran, A. Kjekshus, H. Fjellvåg, P. James, L. Nordström, B. Johansson, et al., Large magnetocrystalline anisotropy in bilayer transition metal phases from first-principles full-potential calculations, Phys. Rev. B 63 (14) (2001) 144409, doi: 10.1103/PhysRevB.63.144409.https://link.aps.org/doi/10.1103/PhysRevB.63.144409

4.3 Paper III

In this work, we carried out a systematic high throughput screening for i-MXenes, focusing on the magnetic properties. It is discovered that the spin configurations, hence the magnetic anisotropy, can be tuned by strain. We found that five i-MXenes have observable (>0.5 meV/f.u.) out-of-plane magnetic anisotropy energies, and the four ferromagnetic candidates have significant high Curie temperature based on the 2D Ising model. We found i-MXene can realize large Seebeck effect, antiferromagnetic topological insulator and spin-gapless semiconductors.

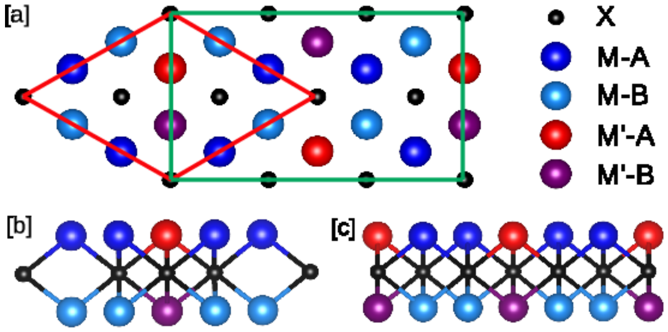

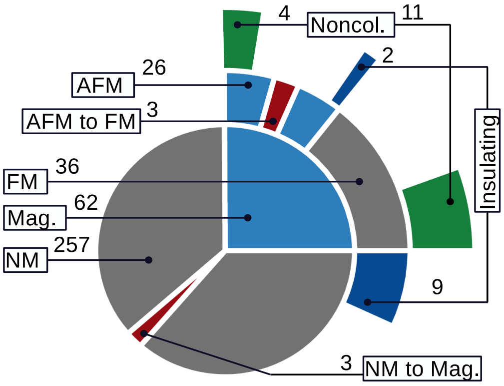

Nanoscale

ROYAL SOCIETY OF CHEMISTRY

PAPER

View Article Online
View Journal | View Issue

Cite this: *Nanoscale*, 2020, **12**, 5995

Magnetic i-MXenes: a new class of multifunctional two-dimensional materials†

Qiang Gao and Hongbin Zhang*

Received 1st December 2019,
Accepted 5th February 2020

DOI: 10.1039/c9nr10181k

rsc.li/nanoscale

Based on density functional theory calculations, we investigated two-dimensional in-plane ordered MXenes (i-MXenes), focusing particularly on their magnetic properties. It has been observed that robust two-dimensional magnetism can be achieved by alloying nonmagnetic MXenes with magnetic transition metal atoms. Moreover, both the magnetic ground states and the magnetocrystalline anisotropy energy of i-MXenes can be effectively manipulated by strain, indicating a strong piezomagnetic effect. Further studies on the transport properties reveal that i-MXenes provide an interesting platform to realize large thermoelectric response, antiferromagnetic topological insulators, and spin-gapless semiconductors. Thus, i-MXenes are a new class of multifunctional two-dimensional magnetic materials which are promising for future spintronic applications.

1. Introduction

The MAX compounds with a general chemical formula of $M_{n+1}AX_n$ (M: early transition metal; A: main group element; X: C or N; n: integer up to 6) have drawn intensive attention recently, due to their potential applications as structural, electrical, and tribological materials.[1] The corresponding two-dimensional (2D) nanosheets $M_{n+1}X_n$, named MXenes, can be obtained by etching the A elements away, *e.g.*, Ti_3C_2 from Ti_3AlC_2.[2] This defines a new class of 2D materials beyond graphene,[3] with a number of materials reported showing multifunctionality, covering energy, spintronic, nano-electronic, and topological applications.[4,5] In recent years, many MXenes have been experimentally synthesized and applied especially as energy materials.[6–17] For instance, theoretical calculations predicted that Ti_3C_2 is a high performance anode material for lithium ion batteries,[18] which was confirmed later by experiments.[19] Although most MXenes are metallic due to the partially occupied d-shells of the transition metal atoms, functionalization can be applied to open up a finite band gap thus further tailoring their properties. For instance, passivated MXenes Mo_2MC_2 (M = Ti, Zr and Hf) with the O_2 group are found to be robust quantum spin Hall insulators with band gaps from 0.1 eV to 0.2 eV.[20] In particular, the magnetic properties of MXenes deserve further investigation, driven by the discovery of 2D magnetic monolayers, such as CrI_3 and $Cr_2Ge_2Te_6$.[21–23] Gao *et al.*[24] predicted that Ti_2C and Ti_2N are nearly half-metals, which can be tuned into spin-gapless semiconductors (SGSs) under biaxial strain. Theoretical calculations also demonstrated that Mn_2N with the functional groups O, OH and F can be half-metals with high Curie temperatures.[25] Based on a theoretical study, He *et al.*[26] found that the functionalized MXene Mn_2CF_2 is a promising half-metal with a high Curie temperature of 520 K, a wide half-metallic gap of 0.9 eV and a sizable magnetic anisotropy of 24 μeV. Although the MXene V_2C is nonmagnetic, inducing vacancy, $(V_{2/3}\square_{1/3})_2CF_2$ ($\square$ is vacancy) is a ferromagnetic semiconductor.[27] By introducing an asymmetrically functionalized group, MXenes will form the so-called Janus structure with a chemical formula of M_2XTT' (T and T′ denote different chemical groups). A theoretical study[28] found that Cr_2CFCl, Cr_2CClBr, Cr_2CHCl, Cr_2CHF, and Cr_2CFOH behave as bipolar antiferromagnetic semiconductors with the opposite spin character in the valence band maximum (CBM) and the conduction band minimum (VBM), providing a new strategy to generate a 2D spin-polarized current for spintronic applications. Such bipolar antiferromagnetic semiconductor behaviour is also predicted in the asymmetrically functionalized double MXene (Cr_2TiC_2FCl).[29] However, high-throughput density functional theory (DFT) calculations reveal that it is difficult to obtain MAX compounds with Fe, Co, and Ni,[30,31] making it challenging to realize magnetic MXenes.

Recently, in-plane ordered MAX (i-MAX) compounds with a formula of $(M_{2/3}M_{1/3})_2AX$ have been synthesized by substituting M in M_2AX compounds with a 1/3 foreign transition metal or a rare earth element M′.[32,33] Based on theoretical studies on i-MAX compounds $(Mo_{2/3}M_{1/3})_2AC$ (M′ = Sc, Y and A = Al, Ga, In, Si, Ge, In), it was found that the stable conditions for the

---

Institute of Material Science, TU Darmstadt, Otto-Berndt-Strasse 3, Darmstadt, Germany. E-mail: hzhang@tmm.tu-darmstadt.de; Fax: +4961511623135; Tel: +4961511623135

† Electronic supplementary information (ESI) available. See DOI: 10.1039/C9NR10181K

formation of i-MAX compounds are: (1) a significant difference between the atomic radii of the dopant metal M′ and the parent M and (2) small A atoms.[34] For the synthesized Cr-based i-MAX compounds, DFT calculations suggest that $(Cr_{2/3}Zr_{1/3})_2AlC$ is stable in an anti-ferromagnetic spin configuration,[35] while $(Cr_{2/3}M'_{1/3})_2AlC$ (M′ = Sc and Y) are probably stable in a mixed state due to a small energy difference between the anti-ferromagnetic and ferromagnetic phases.[36] This suggests that various magnetic states are possible in i-MAX compounds, and thus they are interesting for the formation of the corresponding i-MXenes in the monolayer limit. On the other hand, i-MXenes can also be obtained from i-MAX compounds by etching away the A-element atoms, such as the ordered i-MXenes $W_{4/3}C$ and $Nb_{4/3}C$.[37,38]

In this work, we performed systematic density functional theory calculations to investigate the magnetic and electronic properties of i-MXenes with a general chemical formula $(M_{2/3}M'_{1/3})_2X$, focusing particularly on the cases where M′ is magnetic. It is observed that robust magnetism can be induced, and there exists significant magneto-structural coupling, leading to a tunable magnetic ground state and magnetic anisotropy by strain. Moreover, our calculations suggest that the i-MXenes possess fascinating transport properties, such as a large Seebeck effect, and can be used in antiferromagnetic topological insulators and spin-gapless semiconductors.

2. Computational methods

To maintain reasonable computational effort, we considered 11 known nonmagnetic MXenes as the parent compounds, namely, Sc_2C, V_2C, Mo_2C, Nb_2C, Ta_2C, Ti_2C, Zr_2C, Hf_2C, Ti_2N, Zr_2N, and Hf_2N.[39] With a general chemical formula $(M_{2/3}M'_{1/3})_2X$, the i-MXene can be obtained by substituting one third dopant M′ into M atom in pure MXene with a chemical formula M_2X. Further, the dopant atom M′ is chosen to be one of the transition metal except Tc, leading to 319 compounds. As shown in Fig. 1, the symmetry of the hexagonal MXenes will be lowered after substitution of the dopants, resulting in a rectangular structure. In our calculations, both hexagonal and rectangular structures are considered in order to understand the effect of strain. To determine the magnetic ground state, we consider the non-magnetic (NM), ferromagnetic (FM), interlayer antiferromagnetic (AFM), and intralayer AFM configurations of the magnetic M′ sublattice (Fig. S2 in the ESI†).

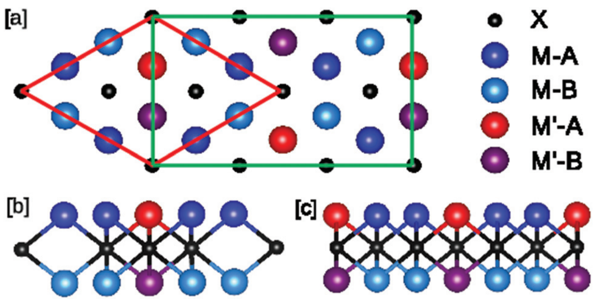

Fig. 1 [a] Top view of the i-MXene $(M_{2/3}M'_{1/3})_2X$ in both hexagonal lattice (red) and rectangular lattice (green). Side views of the i-MXene in hexagonal [b] and rectangular [c] lattices. "-A" and "-B" denote the atoms above or below the central layer of X (X = C or N) atoms in the i-MXene. The original pure MXene crystallizes in a hexagonal lattice. After inducing 1/3 foreign transition metal dopant, the hexagonal symmetry is broken and tilted to the rectangular lattice.

Our DFT calculations are performed in an automated way in the in-house developed high-throughput environment,[40–43] which is interfaced to the Vienna *ab initio* Simulation Package (VASP)[44,45] and the full-potential local-orbital minimum-basis code (FPLO).[46,47] The exchange–correlation functional in the generalized gradient approximation (GGA) is applied, as parameterized by Perdew, Burke, and Ernzerhof (PBE).[48] To guarantee good convergence, the plane-wave energy cutoff and k-mesh density are set at 500 eV and 60 $Å^{-1}$, respectively. The calculations to obtain optimized structures and various magnetic configurations are carried out using the VASP, while the electronic structure and physical properties are determined using the FPLO and WIEN2k[49] codes, as detailed in our previous work.[40,41,50]

It is noticed that only the GGA functional has been applied to pristine MXenes in the literature because the Coulomb interaction is screened significantly in such metallic systems, whereas the hybrid functional gives similar results as those by the GGA functional for MXenes such as Ti_2X and V_2X (X = C and N) as reported in ref. 24. We suspect that the same argument is also valid for most i-MXenes considered in this work which also show metallic behavior. Moreover, our calculations (not shown) reveal that the exchange parameters and hence the resulting Curie temperature have strong dependence on the value of the effective U parameter for the Fe-d states, as observed in ref. 21, 22 and 51–53.

3. Results and discussion

As summarized in Fig. 2, among the 319 i-MXenes exhibiting a rectangular geometry, 257 compounds are non-magnetic, and the remaining 62 compounds are magnetic (with the total magnetic moments greater than $0.2\mu_B$/f.u. in the ferromagnetic spin configuration). Among the magnetic candidates, 40 (26) are in the ferromagnetic (antiferromagnetic) ground states. Furthermore, for compounds in the imposed hexagonal geometry, the magnetic M′ sublattice forms a triangular lattice, which is frustrated and thus can result in an in-plane noncollinear magnetic structure. We found that there are 15 i-MXenes with AFM intralayer exchange coupling between the moments on the M′ sites (*cf.* Table S1 in the ESI†), indicating possible 2D noncollinear magnetic states. Such compounds will be saved for detailed investigation in the future and in the current work we focus only on the collinear magnetic configurations.

Interestingly, comparing the magnetic ground states of i-MXenes in the rectangular and hexagonal geometries, there are 6 compounds whose magnetic configurations can be

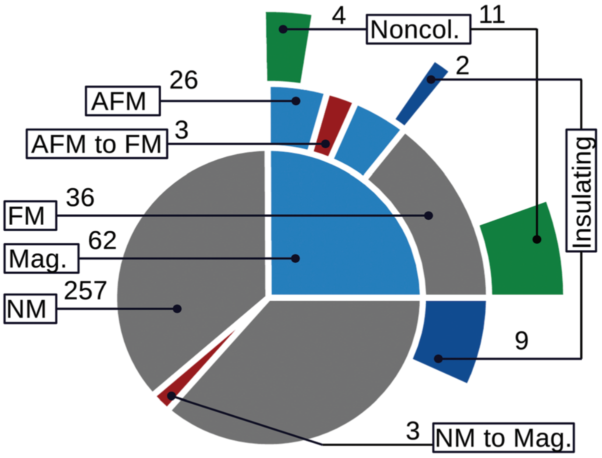

Fig. 2 Classification of the magnetic ground states for the 319 i-MXene, where "NM to FM" and "AFM to FM" mark the compounds whose ground state changes by imposing hexagonal geometry.

changed (Fig. 2), *e.g.*, 3 NM compounds become FM, and 3 AFM compounds change to FM. For instance, $(Zr_{2/3}Ti_{1/3})_2N$ changes from NM (in the rectangular lattice) to FM (in the hexagonal lattice) with a total magnetic moment of $0.95\mu_B$/f.u. The same NM → FM transition occurs for $(Ti_{2/3}Ru_{1/3})_2C$ and $(Zr_{2/3}Cu_{1/3})_2C$, with magnetic moments of 0.29 and $0.30\mu_B$/f.u., respectively. The underlying mechanism can be understood based on the density of states (DOS) of the Zr-5d orbitals as shown in Fig. S4 in the ESI.† Based on the Stoner model, the criterion for a stable ferromagnet is

$$UN(E_F) > 1 \tag{1}$$

where U is the exchange integral and $N(E_F)$ is the DOS at the Fermi level in the paramagnetic state. For the rectangular lattice, the Fermi level is located around a peak of DOS. In the imposed hexagonal structure, the DOS at the Fermi level is significantly enhanced from 5.2 states per eV per u.c. to 6.0 states per eV per u.c. (Fig. S4 in the ESI†), resulting in the instability of the ferromagnetic state. The same behavior is also observed for $(Ti_{2/3}Ru_{1/3})_2C$ and $(Zr_{2/3}Ru_{1/3})_2C$ (*cf.* Fig. S4 in the ESI†).

For compounds with the AFM → FM transition, such as $(Hf_{2/3}Fe_{1/3})_2C$ and $(Ti_{2/3}V_{1/3})_2C$, the magnetic moments of the Fe(V) atoms change from 1.09 $(0.58)\mu_B$ in the rectangular lattice to as large as 1.79 $(0.64)\mu_B$ in the hexagonal lattice. For $(Hf_{2/3}Fe_{1/3})_2C$, the magnetic moments of Fe atoms are enhanced by 64%, which can be attributed to the enhanced exchange splitting (*cf.* Fig. S5 in the ESI†). It also turns out to be a gapless semiconductor, which will be discussed in detail later. On the other hand, the band structures for $(Ti_{2/3}V_{1/3})_2C$ are shown in Fig. S6 in the ESI† in both rectangular (Rect.) and hexagonal (Hex.) lattices along with the anomalous Hall conductivity (AHC) of $(Ti_{2/3}V_{1/3})_2C$ in the hexagonal lattice. In the rectangular lattice, $(Ti_{2/3}V_{1/3})_2C$ is AFM with zero AHC. Obviously, for the FM state in the hexagonal lattice there exists a finite AHC of -160 S cm^{-1} at the Fermi level. In this view, strain can be applied to tune the topological transport properties, leading to the piezospintronic effect as discussed in the case of bulk materials.[54,55]

It is noted that the lattice deformation from the rectangular to the hexagonal lattice is of marginal magnitude. For instance, the strain along the *a* and *b* directions for $(Ti_{2/3}Fe_{1/3})_2C$ are just about 0.14% and 0.18%, where the energy difference between rectangular and hexagonal lattices is as small as 1.2 meV per atom. Thus, it is easy to tailor i-MXenes from a low symmetry rectangular lattice to the hexagonal lattice with higher symmetry. On the other hand, it has been previously reported that the piezomagnetic effect can be realized in pure MXenes M_2C (M = Hf, Nb, Sc, Ta, Ti, V, and Zr) by applying biaxial strain.[56] In this regard, we suspect that the piezomagnetic effect is dramatically enhanced in i-MXenes as manifested by the six aforementioned cases. As the hexagonal lattice with high symmetry is more interesting and easy to obtain, we will focus on the physical properties of such systems in the remaining part of this work.

For two-dimensional magnets, according to the Mermin–Wagner theorem, there is no long range ordering if there is continuous symmetry for the order parameters.[57] In this regard, to stabilize 2D magnets at finite temperature, magnetocrystalline anisotropy energy (MAE) is essential, which breaks the rotational symmetry of Heisenberg moments.[53] The MAEs for magnetic i-MXenes are evaluated using the force theorem:[58]

$$\mathrm{MAE} = \sum_{i \in \mathrm{occ.}} \left(\varepsilon_i^{[100]} - \varepsilon_i^{[001]}\right) \tag{2}$$

where $\varepsilon_i^{[001]}$ and $\varepsilon_i^{[100]}$ denote the energy eigenvalues of the *i*-th band for magnetization along the [001] and [100] directions, respectively.

Table 1 lists 5 i-MXenes with an out-of-plane MAE larger than 0.5 meV per f.u. among all magnetic i-MXenes (*cf.* Table S2 in the ESI† for MAE of all the magnetic cases). It is noticed that $(Hf_{2/3}Fe_{1/3})_2C$ has the largest MAE of 1.39 meV per f.u., favoring the out-of-plane magnetization direction. In addition, the MAEs of $(Zr_{2/3}Fe_{1/3})_2C$ and $(Ti_{2/3}Fe_{1/3})_2C$ are 0.74 meV per f.u. and 0.03 meV per f.u., respectively. Such a trend of increasing MAE with X varying from Ti, Zr and Hf can be attributed to the variation of the strength of the atomic spin–orbit coupling (SOC) as 11.2 meV (Ti), 42.1 meV (Zr) and 126.5 meV (Hf).[59,60] Furthermore, the enhanced MAE of $(Zr_{2/3}Fe_{1/3})_2C$ and $(Hf_{2/3}Fe_{1/3})_2C$ originates from the trigonal crystal fields which lead to strongly coupled SOC bands around the Fermi energy, as manifested by the orbital projected band structures (Fig. S8 in the ESI†). As shown in the orbital projected band structures (Fig. S8 in the ESI†), for $(Hf_{2/3}Fe_{1/3})_2C$, the Fe-3d_{xy} and Fe-3$d_{x^2-y^2}$ bands are split by 73 meV along the K–Γ section, while for $(Zr_{2/3}Fe_{1/3})_2C$, the Fe-3d_{xy} and Fe-3$d_{x^2-y^2}$ bands are split by 40 meV along the M–K section. As the d_{xy} and $d_{x^2-y^2}$ orbitals are strongly coupled by SOC, such a special electronic structure leads to high MAEs. Such a mechanism is in good agreement with the giant MAE realized in artificial Fe atoms adsorbed on III–V nitride thin films with local trigonal symmetry.[61]

Table 1 The basic information about the magnetic i-MXene candidates in the hexagonal lattice with an out-of-plane MAE larger than 0.5 meV per f.u., including the MAE with the unit of meV per f.u., the magnetic moment (M_{at}) per magnetic atom with the unit of μ_B, magnetic order, the exchange coupling parameters, the main magnetic atom and the Curie temperature (T_C)

Compound	MAE (meV per f.u.)	M_{at} (μ_B per at.)	Magnetic order	Magnetic atom	J_{inter} (meV)	J_{intra} (meV)	T_C (K)
$(Ta_{2/3}Fe_{1/3})_2C$	0.86	1.82	AFM	Fe	−10.05	0.56	—
$(Zr_{2/3}Fe_{1/3})_2C$	0.74	1.71	FM	Fe	10.16	−2.24	267.54
$(Hf_{2/3}Fe_{1/3})_2C$	1.39	1.79	FM	Fe	33.94	0.70	893.67
$(Hf_{2/3}Cr_{1/3})_2N$	0.76	1.01	FM	Cr	13.06	0.20	343.90
$(Ti_{2/3}Hf_{1/3})_2N$	0.71	0.30	FM	Ti	7.22	0.97	190.11

To obtain the Curie temperature, we took $(Hf_{2/3}Fe_{1/3})_2C$ as an example and evaluated the exchange parameters between magnetic Fe atoms by mapping the DFT total energies to the Heisenberg model:

$$H = -\frac{1}{2}\sum_{i \neq j} J_{ij}\boldsymbol{S}_i \cdot \boldsymbol{S}_j \tag{3}$$

where J_{ij} is the exchange parameter for the local moments at the i and j sites, and $\boldsymbol{S}_{i/j}$ marks the on-site spin operator. Considering three magnetic configurations, *i.e.*, FM, AFM-0, and AFM-β (*cf.* Fig. S2† for spin configurations AFM-β and AFM-0), the energy differences can be formulated in terms of the interlayer (J_{inter}) and intralayer (J_{intra}) exchange parameters (*cf.* Fig. S3 in the ESI† for J_{intra} and J_{inter}):

$$E_{FM} - E_{AFM\text{-}0} = -J_{inter}S^2, (4) \tag{4}$$

$$E_{FM} - E_{AFM\text{-}\beta} = -8J_{intra}S^2. \tag{5}$$

Here we use the square of the local spin moment length to represent the square of the spin operator. The resulting exchange coupling parameters for $(Hf_{2/3}Fe_{1/3})_2C$ are: J_{inter} = 36.75 meV and J_{intra} = 0.70 meV. Similarly, we obtained the exchange coupling parameters for other ferromagnetic compounds such as $(Hf_{2/3}Cr_{1/3})_2N$, $(Ta_{2/3}Fe_{1/3})_2C$, $(Ti_{2/3}Hf_{1/3})_2N$, and $(Zr_{2/3}Fe_{1/3})_2C$ (Table 1). Obviously, the value of interlayer exchange coupling is much larger than that of the intralayer coupling for all the compounds listed above. Due to the significantly large magnetic anisotropy, we can use the 2D Ising model to estimate the Curie temperature[51,62]

$$T_C = \frac{2J_{inter}}{k_B \ln(1+\sqrt{2})}. \tag{6}$$

with the results listed in Table 1. Surprisingly, the Curie temperatures of $(Hf_{2/3}Fe_{1/3})_2C$ and $(Hf_{2/3}Cr_{1/3})_2N$ are even above room temperature. It is noted that for the recently synthesized 2D magnet CrI_3 with a Curie temperature of 45 K, the MAE is about 1.71 meV per f.u.[21,22,52,53] Obviously, the out-of-plane MAEs of $(Hf_{2/3}Fe_{1/3})_2C$ and $(Hf_{2/3}Cr_{1/3})_2N$ are almost the same as that of CrI_3. Futhermore, for CrI_3 the interlayer and intralayer exchange parameters are 11.64 meV and 2.37 meV.[63] So, the exchange parameters for $(Hf_{2/3}Fe_{1/3})_2C$ and $(Hf_{2/3}Cr_{1/3})_2N$ are larger than that of CrI_3. In this view, we suspect that i-MXenes $(Hf_{2/3}Fe_{1/3})_2C$ and $(Hf_{2/3}Cr_{1/3})_2N$ are promising 2D magnets with high Curie temperatures.

4. Electronic properties

4.1. Thermoelectric properties of semiconductors

Previously, it has been reported that 2D semiconductors have very large thermoelectric power.[64,65] For example, SnSe monolayers are regarded as promising thermoelectric materials, *e.g.*, the Seebeck coefficient is increased from 160 μV K^{-1} to 300 μV K^{-1} when the temperature is increased from 300 K to 700 K.[64] Although most i-MXenes tend to be metallic, there are nine nonmagnetic semiconductors, *i.e.*, $(Sc_{2/3}X_{1/3})_2C$ (X = Au, Cu, Ir, Ni, Zn, Cd, and Hg), $(Hf_{2/3}Ir_{1/3})_2C$ and $(Ti_{2/3}Au_{1/3})_2C$. Among them, $(Sc_{2/3}Cd_{1/3})_2C$ and $(Sc_{2/3}Hg_{1/3})_2C$ are large gap semiconductors (with the finite band gap larger than 0.4 eV and less than 1.0 eV), which can be good thermoelectric materials. The band structures of these two semiconductors in the hexagonal lattice are displayed in Fig. 3 together with the Seebeck coefficients as a function of chemical potential. The band gaps of $(Sc_{2/3}Cd_{1/3})_2C$ and $(Sc_{2/3}Hg_{1/3})_2C$ are as large as 0.41 and 0.79 eV, respectively. Furthermore, the valence band maximum (VBM) and conduction band minimum (CBM) are flat around

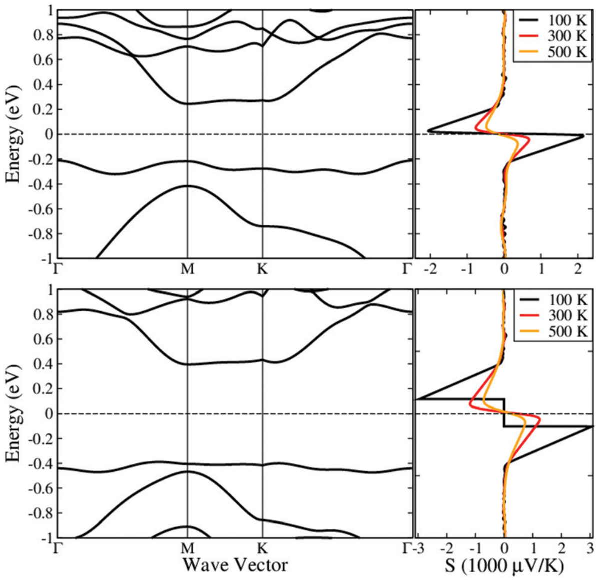

Fig. 3 Band structures and Seebeck coefficients for $(Sc_{2/3}Cd_{1/3})_2C$ [a] and $(Sc_{2/3}Hg_{1/3})_2C$ [b]. The horizontal dashed lines denote the Fermi level.

the Fermi level. Such a behavior implies that both compounds have the potential to realize a large Seebeck effect. To confirm this, the Seebeck coefficients have been evaluated for these two compounds, as shown in Fig. 3. The peaks of Seebeck coefficients around the Fermi level for $(Sc_{2/3}Cd_{1/3})_2C$ ($(Sc_{2/3}Hg_{1/3})_2C$) are remarkably as high as 2100 (3000) μV K^{-1} at 100 K, 820 (1200) μV K^{-1} at 300 K, and 520 (700) μV K^{-1} at 500 K. The enhanced Seebeck coefficients can be attributed to the large derivative of the DOS with respect to the energy and hence the flat bands above and below the Fermi energy (*cf.* Fig. S7 in the ESI†). It is noted that the densities of states for these two systems are very comparable for the hexagonal and rectangular lattices, leading to negligible changes in the Seebeck coefficients (*cf.* Fig. S7 in the ESI†). Therefore, we suspect that $(Sc_{2/3}Cd_{1/3})_2C$ and $(Sc_{2/3}Hg_{1/3})_2C$ are good candidates as 2D thermoelectric materials.

4.2. Topological properties

As discussed above, most i-MXenes are metallic due to the partially filled d-shells of the transition metal atoms. However, motivated by the reported nontrivial topological state in some functionalized MXenes,[20] we also studied the topological nature of the i-MXene $(Ta_{2/3}Fe_{1/3})_2C$ with a tiny band gap of 1.34 meV. Surprisingly, $(Ta_{2/3}Fe_{1/3})_2C$ with a collinear AFM ground state hosts a nontrivial state, as shown in the bulk and surface electronic structures in Fig. 4. Without considering spin–orbit coupling (SOC), the VBM and CBM almost cross each other at the Fermi energy. According to the fat band analysis (Fig. S9 in the ESI†), these two bands are mainly contributed by the Fe-3d$_{yz}$ and Fe-3d$_{zx}$ orbital character, which is strongly coupled by SOC. Upon switching on SOC, a remarkable direct gap of 75.0 meV is opened, leading to band inversion and thus the occurrence of the topological nontrivial state. This is clearly confirmed by our explicit calculation of the edge states of the corresponding 1D ribbons with a width of 70 units, as shown in Fig. 4(b). Furthermore, the nontrivial edge state is protected by a combination of the time reversal (T) and space inversion (P) symmetries (TP), as demonstrated for CuMnAs in ref. 66.

4.3. Spin-gapless semiconductors

It has been reported that the MXene Ti_2C can become a spin-gapless semiconductor (SGS) under 2% strain.[24] We found two SGS candidates among i-MXenes in the hexagonal geometry, *e.g.*, $(Hf_{2/3}Fe_{1/3})_2C$ and $(Zr_{2/3}Fe_{1/3})_2C$ with total magnetic moments of 1.79 and $0.74\mu_B$/f.u., respectively. These two SGSs are not within the classification of four types of SGSs defined in our previous work,[50] because the VBM and CBM have both spin characters, as shown in Fig. 5. For such SGSs at the Fermi level, in the spin up channel the CBM and VBM touch each other directly between K–Γ (in the A region), while in the spin down channel there is only a small gap for the CBM and VBM between K–M (in region B). That is the VBM and CBM of the spin up and spin down channels can be roughly seen at the same energy level. When SOC is switched on, the touching bands open a local band gap, suggesting a topologically non-

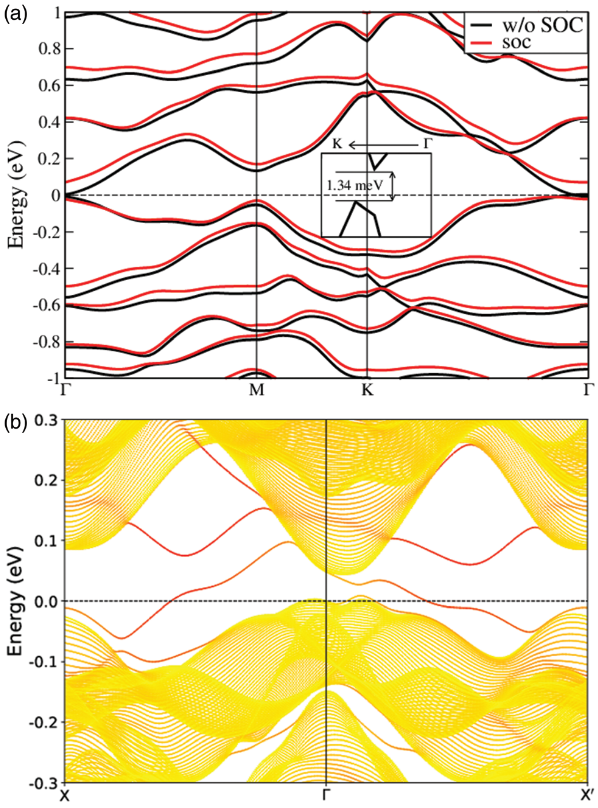

Fig. 4 Band structures [a] and edge states [b] for the AFM topological insulator $(Ta_{2/3}Fe_{1/3})_2C$. When SOC is turned off, the band structures of the spin up channel overlap with those of the spin down channel. So only the band structure in one spin channel is shown. In both [a] and [b], the dashed line denotes the Fermi level.

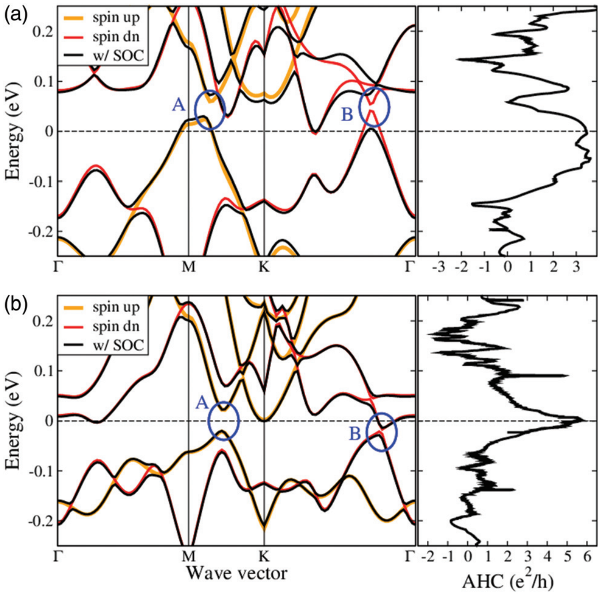

Fig. 5 The band structures (left) and anomalous Hall conductivity (right) of $(Hf_{2/3}Fe_{1/3})_2C$ [a] and $(Zr_{2/3}Fe_{1/3})_2C$ [b]. The horizontal dashed lines denote the Fermi energies.

trivial state. This can be manifested by explicit evaluation of the anomalous Hall conductivity. For instance, it is observed that the anomalous Hall conductivity is finite around the Fermi energy, which is almost quantized to 3 and $5e^2/h$ with tiny band gaps of 3.8 meV and 0.3 meV for $(Hf_{2/3}Fe_{1/3})_2C$ and $(Zr_{2/3}Fe_{1/3})_2C$, respectively. That is, such i-MXenes are Chern insulators with nontrivial Chern numbers of 3 and 5, though the band gaps are small.

5. Conclusions

In conclusion, we systematically studied the magnetic and electronic properties of i-MXene compounds, which provide an interesting platform for multifunctional applications. The magnetic ground states for i-MXenes are investigated for both rectangular and hexagonal lattices, where slight strain can be applied to tune the magnetic ground state. Due to the underlying crystal fields, the magnetocrystalline anisotropy of i-MXenes can be significantly enhanced, *i.e.*, there are 5 systems with the magnetic crystalline anisotropy energy larger than 0.5 meV per f.u. Furthermore, investigation on the electronic properties reveals that i-MXenes can host fascinating transport properties. Semi-classical transport calculations demonstrate that i-MXenes $(Sc_{2/3}Cd_{1/3})_2C$ and $(Sc_{2/3}Hg_{1/3})_2C$ have significantly large Seebeck coefficients with a magnitude of 1000 $\mu V\ K^{-1}$. Based on edge state calculations, $(Ta_{2/3}Fe_{1/3})_2C$ can be classified as an antiferromagnetic topological insulator. We observe that $(Hf_{2/3}Fe_{1/3})_2C$ and $(Zr_{2/3}Fe_{1/3})_2C$ are spin-gapless semiconductors with enhanced anomalous Hall conductivity. Thus our calculations suggest that i-MXenes are a new class of 2D materials which are promising for future applications, calling for further experimental exploration.

Conflicts of interest

There are no conflicts to declare.

Acknowledgements

We acknowledge support from DFG CRC/TRR 270, and also the LOEWE project FLAME funded by the Ministry of Higher Education, Research, and the Arts (HMWK) of the Hessen state. Qiang Gao acknowledges the financial support from the China Scholarship Council. The authors gratefully acknowledge the computational time on the Lichtenberg High Performance Supercomputer.

References

1 Z. M. Sun, *Int. Mater. Rev.*, 2011, **56**, 143–166.
2 M. Naguib, M. Kurtoglu, V. Presser, J. Lu, J. Niu, M. Heon, L. Hultman, Y. Gogotsi and M. W. Barsoum, *Adv. Mater.*, 2011, **23**, 4248–4253.
3 M. Naguib, V. N. Mochalin, M. W. Barsoum and Y. Gogotsi, *Adv. Mater.*, 2014, **26**, 992–1005.
4 B. Anasori, M. R. Lukatskaya and Y. Gogotsi, *Nat. Rev. Mater.*, 2017, **2**, 16098.
5 Y. Gogotsi and B. Anasori, *ACS Nano*, 2019, **13**, 8491–8494.
6 A. Miranda, J. Halim, M. W. Barsoum and A. Lorke, *Appl. Phys. Lett.*, 2016, **108**, 033102.
7 C. J. Zhang, B. Anasori, A. Seralâ-Ascaso, S.-H. Park, N. McEvoy, A. Shmeliov, G. S. Duesberg, J. N. Coleman, Y. Gogotsi and V. Nicolosi, *Adv. Mater.*, 2017, **29**, 1702678.
8 D. Er, J. Li, M. Naguib, Y. Gogotsi and V. B. Shenoy, *ACS Appl. Mater. Interfaces*, 2014, **6**, 11173–11179.
9 X. Liang, Y. Rangom, C. Y. Kwok, Q. Pang and L. F. Nazar, *Adv. Mater.*, 2017, **29**, 1603040.
10 M. Alhabeb, K. Maleski, B. Anasori, P. Lelyukh, L. Clark, S. Sin and Y. Gogotsi, *Chem. Mater.*, 2017, **29**, 7633–7644.
11 X. Jiang, S. Liu, W. Liang, S. Luo, Z. He, Y. Ge, H. Wang, R. Cao, F. Zhang, Q. Wen, J. Li, Q. Bao, D. Fan and H. Zhang, *Laser Photonics Rev.*, 2018, **12**, 1700229.
12 J. Halim, S. Kota, M. R. Lukatskaya, M. Naguib, M.-Q. Zhao, E. J. Moon, J. Pitock, J. Nanda, S. J. May, Y. Gogotsi and M. W. Barsoum, *Adv. Funct. Mater.*, 2016, **26**, 3118–3127.
13 Z. W. Seh, K. D. Fredrickson, B. Anasori, J. Kibsgaard, A. L. Strickler, M. R. Lukatskaya, Y. Gogotsi, T. F. Jaramillo and A. Vojvodic, *ACS Energy Lett.*, 2016, **1**, 589–594.
14 L. Ding, Y. Wei, Y. Wang, H. Chen, J. Caro and H. Wang, *Angew. Chem., Int. Ed.*, 2017, **56**, 1825–1829.
15 X. Liang, A. Garsuch and L. F. Nazar, *Angew. Chem., Int. Ed.*, 2015, **54**, 3907–3911.
16 K. Rasool, M. Helal, A. Ali, C. E. Ren, Y. Gogotsi and K. A. Mahmoud, *ACS Nano*, 2016, **10**, 3674–3684.
17 Z. Ling, C. E. Ren, M.-Q. Zhao, J. Yang, J. M. Giammarco, J. Qiu, M. W. Barsoum and Y. Gogotsi, *Proc. Natl. Acad. Sci. U. S. A.*, 2014, **111**, 16676–16681.
18 C. J. Takacs, Y. Sun, G. C. Welch, L. A. Perez, X. Liu, W. Wen, G. C. Bazan and A. J. Heeger, *J. Am. Chem. Soc.*, 2012, **134**, 16597–16606.
19 M. R. Lukatskaya, O. Mashtalir, C. E. Ren, Y. Dall'Agnese, P. Rozier, P. L. Taberna, M. Naguib, P. Simon, M. W. Barsoum and Y. Gogotsi, *Science*, 2013, **341**, 1502–1505.
20 C. Si, K.-H. Jin, J. Zhou, Z. Sun and F. Liu, *Nano Lett.*, 2016, **16**, 6584–6591.
21 B. Huang, G. Clark, D. R. Klein, D. MacNeill, E. Navarro-Moratalla, K. L. Seyler, N. Wilson, M. A. McGuire, D. H. Cobden, D. Xiao, W. Yao, P. Jarillo-Herrero and X. Xu, *Nat. Nanotechnol.*, 2018, **13**, 544.
22 B. Huang, G. Clark, E. Navarro-Moratalla, D. R. Klein, R. Cheng, K. L. Seyler, D. Zhong, E. Schmidgall, M. A. McGuire, D. H. Cobden, W. Yao, D. Xiao, P. Jarillo-Herrero and X. Xu, *Nature*, 2017, **546**, 270–273.
23 C. Gong, L. Li, Z. Li, H. Ji, A. Stern, Y. Xia, T. Cao, W. Bao, C. Wang, Y. Wang, Z. Q. Qiu, R. J. Cava, S. G. Louie, J. Xia and X. Zhang, *Nature*, 2017, **546**, 265–269.

24 G. Gao, G. Ding, J. Li, K. Yao, M. Wu and M. Qian, *Nanoscale*, 2016, **8**, 8986–8994.
25 H. Kumar, N. C. Frey, L. Dong, B. Anasori, Y. Gogotsi and V. B. Shenoy, *ACS Nano*, 2017, **11**, 7648–7655.
26 J. He, P. Lyu and P. Nachtigall, *J. Mater. Chem. C*, 2016, **4**, 11143–11149.
27 S. Li, J. He, P. Nachtigall, L. Grajciar and F. Brivio, *Phys. Chem. Chem. Phys.*, 2019, **21**, 25802–25808.
28 J. He, P. Lyu, L. Z. Sun, M. García and P. Nachtigall, *J. Mater. Chem. C*, 2016, **4**, 6500–6509.
29 J. He, G. Ding, C. Zhong, S. Li, D. Li and G. Zhang, *Nanoscale*, 2018, **11**, 356–364.
30 D. Ohmer, G. Qiang, I. Opahle, H. K. Singh and H. Zhang, *Phys. Rev. Mater.*, 2019, **3**, 053803.
31 D. Ohmer, I. Opahle, H. K. Singh and H. Zhang, *J. Phys.: Condens. Matter*, 2019, **31**, 405902.
32 M. Dahlqvist, J. Lu, R. Meshkian, Q. Tao, L. Hultman and J. Rosen, *Sci. Adv.*, 2017, **3**, e1700642.
33 Q. Tao, J. Lu, M. Dahlqvist, A. Mockute, S. Calder, A. Petruhins, R. Meshkian, O. Rivin, D. Potashnikov, E. N. Caspi, H. Shaked, A. Hoser, C. Opagiste, R.-M. Galera, R. Salikhov, U. Wiedwald, C. Ritter, A. R. Wildes, B. Johansson, L. Hultman, M. Farle, M. W. Barsoum and J. Rosen, *Chem. Mater.*, 2019, **31**, 2476–2485.
34 M. Dahlqvist, A. Petruhins, J. Lu, L. Hultman and J. Rosen, *ACS Nano*, 2018, **12**, 7761–7770.
35 L. Chen, M. Dahlqvist, T. Lapauw, B. Tunca, F. Wang, J. Lu, R. Meshkian, K. Lambrinou, B. Blanpain, J. Vleugels and J. Rosen, *Inorg. Chem.*, 2018, **57**, 6237–6244.
36 J. Lu, A. Thore, R. Meshkian, Q. Tao, L. Hultman and J. Rosen, *Cryst. Growth Des.*, 2017, **17**, 5704–5711.
37 R. Meshkian, M. Dahlqvist, J. Lu, B. Wickman, J. Halim, J. Thörnberg, Q. Tao, S. Li, S. Intikhab, J. Snyder, M. W. Barsoum, M. Yildizhan, J. Palisaitis, L. Hultman, P. O. Å. Persson and J. Rosen, *Adv. Mater.*, 2018, **30**, 1706409.
38 C. Zhan, W. Sun, Y. Xie, D.-e. Jiang and P. R. C. Kent, *ACS Appl. Mater. Interfaces*, 2019, **11**, 24885–24905.
39 M. Khazaei, A. Ranjbar, K. Esfarjani, D. Bogdanovski, R. Dronskowski and S. Yunoki, *Phys. Chem. Chem. Phys.*, 2018, **20**, 8579–8592.
40 Z. Zhang, R.-W. Zhang, X. Li, K. Koepernik, Y. Yao and H. Zhang, *J. Phys. Chem. Lett.*, 2018, **9**, 6224–6231.
41 X. Li, Z. Zhang, Y. Yao and H. Zhang, *2D Mater.*, 2018, **5**, 045023.
42 I. Opahle, A. Parma, E. J. McEniry, R. Drautz and G. K. H. Madsen, *New J. Phys.*, 2013, **15**, 105010.
43 I. Opahle, G. K. H. Madsen and R. Drautz, *Phys. Chem. Chem. Phys.*, 2012, **14**, 16197–16202.
44 G. Kresse and D. Joubert, *Phys. Rev. B: Condens. Matter Mater. Phys.*, 1999, **59**, 1758–1775.
45 G. Kresse and J. Furthmüller, *Phys. Rev. B: Condens. Matter Mater. Phys.*, 1996, **54**, 11169–11186.
46 K. Koepernik and H. Eschrig, *Phys. Rev. B: Condens. Matter Mater. Phys.*, 1999, **59**, 1743–1757.
47 I. Opahle, K. Koepernik and H. Eschrig, *Phys. Rev. B: Condens. Matter Mater. Phys.*, 1999, **60**, 14035–14041.
48 J. P. Perdew, K. Burke and M. Ernzerhof, *Phys. Rev. Lett.*, 1996, **77**, 3865–3868.
49 *(PDF) WIEN2k: An Augmented Plane Wave plus Local Orbitals Program for Calculating Crystal Properties*, https://www.researchgate.net/publication/237132866WIEN2kAnAugmentedPlaneWaveplusLocalOrbitalsProgramforCalculatingCrystalProperties.
50 Q. Gao, I. Opahle and H. Zhang, *Phys. Rev. Mater.*, 2019, **3**, 024410.
51 M. Gibertini, M. Koperski, A. F. Morpurgo and K. S. Novoselov, *Nat. Nanotechnol.*, 2019, **14**, 408–419.
52 M. A. McGuire, H. Dixit, V. R. Cooper and B. C. Sales, *Chem. Mater.*, 2015, **27**, 612–620.
53 S. Haastrup, M. Strange, M. Pandey, T. Deilmann, P. S. Schmidt, N. F. Hinsche, M. N. Gjerding, D. Torelli, P. M. Larsen, A. C. Riis-Jensen, J. Gath, K. W. Jacobsen, J. J. Mortensen, T. Olsen and K. S. Thygesen, *2D Mater.*, 2018, **5**, 042002.
54 D. Boldrin, I. Samathrakis, J. Zemen, A. Mihai, B. Zou, F. Johnson, B. D. Esser, D. W. McComb, P. K. Petrov, H. Zhang and L. F. Cohen, *Phys. Rev. Mater.*, 2019, **3**, 094409.
55 I. Samathrakis and H. Zhang, arXiv:1905.11798 [cond-mat], 2019.
56 S. Zhao, W. Kang and J. Xue, *Appl. Phys. Lett.*, 2014, **104**, 133106.
57 N. D. Mermin and H. Wagner, *Phys. Rev. Lett.*, 1966, **17**, 1133–1136.
58 X. Wang, D.-s. Wang, R. Wu and A. J. Freeman, *J. Magn. Magn. Mater.*, 1996, **159**, 337–341.
59 D. Dai, H. Xiang and M.-H. Whangbo, *J. Comput. Chem.*, 2008, **29**, 2187–2209.
60 W. C. Martin, *J. Res. Natl. Bur. Stand., Sect. A*, 1971, **75**, 109–111.
61 J.-X. Yu and J. Zang, *Sci. Adv.*, 2018, **4**, eaar7814.
62 L. Onsager, *Phys. Rev.*, 1944, **65**, 117–149.
63 O. Besbes, S. Nikolaev, N. Meskini and I. Solovyev, *Phys. Rev. B: Condens. Matter Mater. Phys.*, 2019, **99**, 104432.
64 L.-D. Zhao, G. Tan, S. Hao, J. He, Y. Pei, H. Chi, H. Wang, S. Gong, H. Xu, V. P. Dravid, C. Uher, G. J. Snyder, C. Wolverton and M. G. Kanatzidis, *Science*, 2016, **351**, 141–144.
65 A. Shafique and Y.-H. Shin, *Sci. Rep.*, 2017, **7**, 506.
66 L. Šmejkal, J. Železný, J. Sinova and T. Jungwirth, *Phys. Rev. Lett.*, 2017, **118**, 106402.

Supplementary to Magnetic i-MXene: a new class of multifunctional two-dimensional materials

Qiang Gao and Hongbin Zhang

S1 Spin configuration

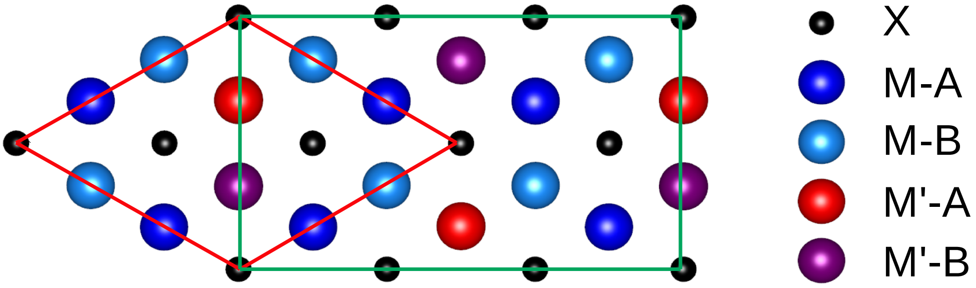

Figure S1: Crystal structure for i-MXene $(M_{2/3}M'_{1/3})_2X$ in hexagonal (red) and rectangular (green) lattices. The "A" and "B" symbols denote the corresponding atoms lie above and below the center layer X (X = C and N) atoms. In the following structures, the atom labels have the same meaning as this figure.

S2 Noncolinear spin configurations

In the hexagonal lattice, the doped transition metal M′ of intralayer forms a triangular lattice in the 2×2×1 super cell as showing in Fig. S3, implying the noncolinear antiferromagnetic state may be stable. Table S1 lists the noncolinear antiferromagnetic candidates.

Table S1: The noncolinaer antiferromagnetic candidates

spin	Candidate
AFM-β	$(Sc_{2/3}Mo_{1/3})_2C$ $(Nb_{2/3}Mn_{1/3})_2C$ $(Zr_{2/3}Mn_{1/3})_2C$ $(Sc_{2/3}Nb_{1/3})_2C$
AFM-α	$(Ta_{2/3}Mn_{1/3})_2C$ $(Mo_{2/3}Fe_{1/3})_2C$ $(Zr_{2/3}Ni_{1/3})_2C$ $(Zr_{2/3}Fe_{1/3})_2C$ $(Hf_{2/3}Mn_{1/3})_2C$ $(Zr_{2/3}Co_{1/3})_2N$ $(Ti_{2/3}Fe_{1/3})_2N$ $(Zr_{2/3}Mn_{1/3})_2N$ $(Zr_{2/3}Fe_{1/3})_2N$ $(V_{2/3}Mn_{1/3})_2C$ $(Hf_{2/3}Cr_{1/3})_2N$

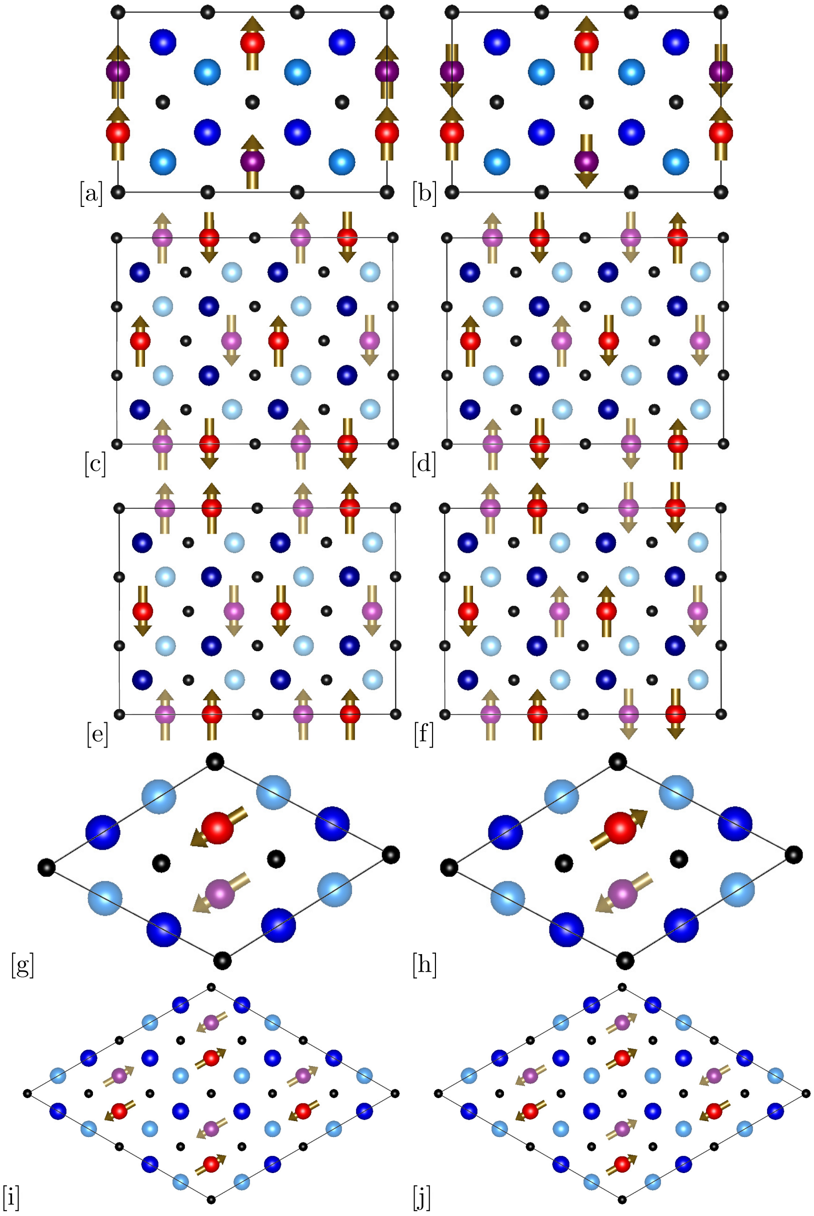

Figure S2: Spin configurations for i-MXene in rectangular lattice: [a] ferromagnetic (FM) and [b] interlayer antiferromagnetic (AFM-0) spin state. For comparison with hexagonal i-MXene in noncolinear spin configuration, we also calculate rectangular i-MXene in similar spin configurations. [c] AFM-1 and [d] AFM-2 are the interlayer antiferromagnetic coupling spin configurations, while [e] AFM-3 and [f] AFM-4 are the interlayer ferromagnetic coupling spin configurations. Noncolinear antiferromagnetic spin configurations for the interlayer coupling of antiferromagnetic (AFM-α) [i] and ferromagnetic (AFM-β) [j] cases.

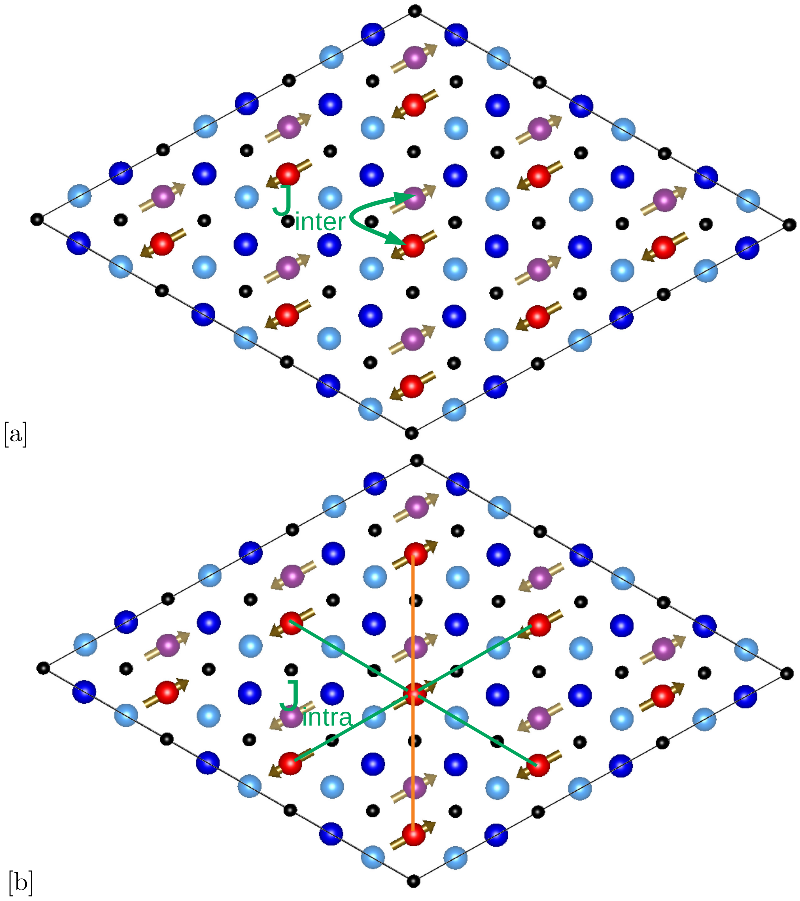

Figure S3: The schematic diagrams of exchange coupling parameters [a] J_{inter} and [b] J_{intra} for i-MXene $(Hf_{2/3}Fe_{1/3})_2C$. [a] AFM-0: The exchange coupling of Fe atoms of above and below layers is set as antiferromagnetic, while the intralayer coupling for Fe is set as ferromagnetic. [b] AFM-β: The intralayer coupling of Fe atoms is set as noncolinear antiferromagnetic while the interlayer coupling of Fe atoms are ferromagnetic. It should be noticed there are in total 6 nearest neighbor Fe atoms for each Fe, of which four are antiferromagnetic and two are ferromagnetic to the center of Fe atom of the hexagonal Fe atoms.

S3 DOS for some i-MXene.

In order to discuss i-MXene with spin configuration transition from NM to FM, we have shown the density of states (DOS) for $(Zr_{2/3}Ti_{1/3})_2N$, $(Ti_{2/3}Ru_{1/3})_2C$ and $(Zr_{2/3}Ru_{1/3})_2C$ in Fig. S4. We also show the Fe atomic DOS in $(Hf_{2/3}Fe_{1/3})_2C$ with the hexagonal and rectangular lattice in order to understand the spin configuration transition from AFM to FM.

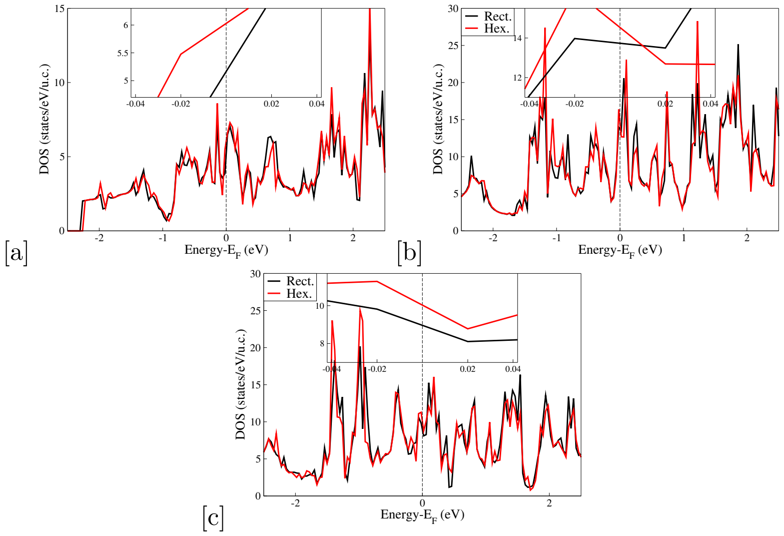

Figure S4: Density of states comparison between rectangular (Rect.) and hexagonal (Hex.) lattices for [a] $(Zr_{2/3}Ti_{1/3})_2N$, [b] $(Ti_{2/3}Ru_{1/3})_2C$ and [c] $(Zr_{2/3}Ru_{1/3})_2C$ in non-magnetic spin configuration.

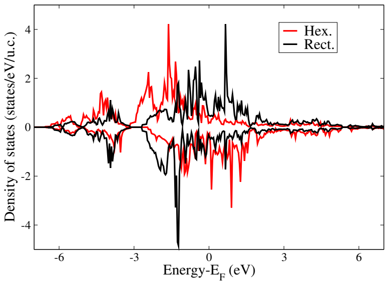

Figure S5: Fe atomic DOS in $(Hf_{2/3}Fe_{1/3})_2C$ withe the hexagonal and rectangular lattice.

S4 Band structures and AHC for $(\mathrm{Ti}_{2/3}\mathrm{V}_{1/3})_2\mathrm{C}$.

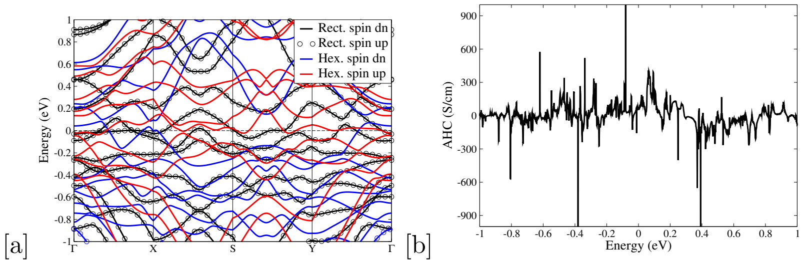

Figure S6: [a] Band structures for $(\mathrm{Ti}_{2/3}\mathrm{V}_{1/3})_2\mathrm{C}$ in rectangular (Rect.) and hexagonal (Hex.) lattices. In rectangular lattice, the band structures of spin up and spin down (dn) are overlapping. For the hexagonal lattice, here we use the $k-$path of rectangular lattice for comparison. [b] Anomalous hall conductivity for $(\mathrm{Ti}_{2/3}\mathrm{V}_{1/3})_2\mathrm{C}$ in the hexagonal lattice.

S5 DOS and Seebeck coefficients for $(\mathrm{Sc}_{2/3}\mathrm{Cd}_{1/3})_2\mathrm{C}$ and $(\mathrm{Sc}_{2/3}\mathrm{Hg}_{1/3})_2\mathrm{C}$.

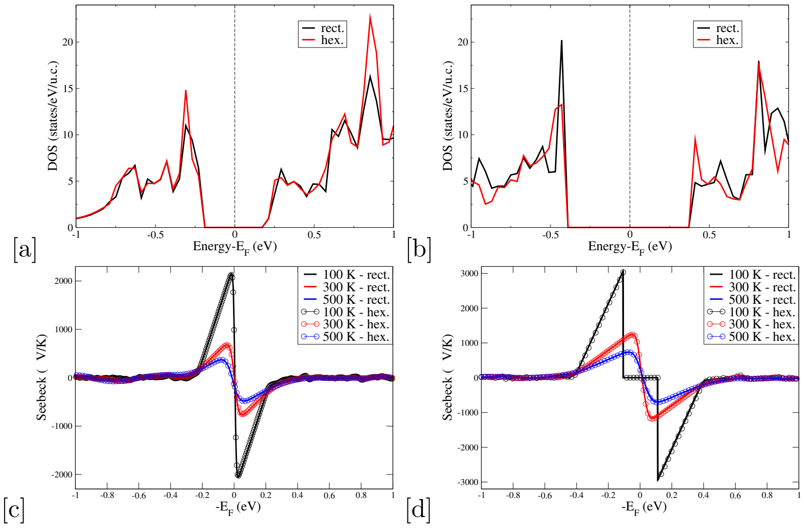

Figure S7: DOS for $(\mathrm{Sc}_{2/3}\mathrm{Cd}_{1/3})_2\mathrm{C}$ [a] and $(\mathrm{Sc}_{2/3}\mathrm{Hg}_{1/3})_2\mathrm{C}$ [b]. Seebeck coefficient as a function of chemical potential for $(\mathrm{Sc}_{2/3}\mathrm{Cd}_{1/3})_2\mathrm{C}$ [a] and $(\mathrm{Sc}_{2/3}\mathrm{Hg}_{1/3})_2\mathrm{C}$ [b]. The ”rect.” and ”hex.” denote the results in rectangular and hexagonal lattices.

S6 Projected band structures

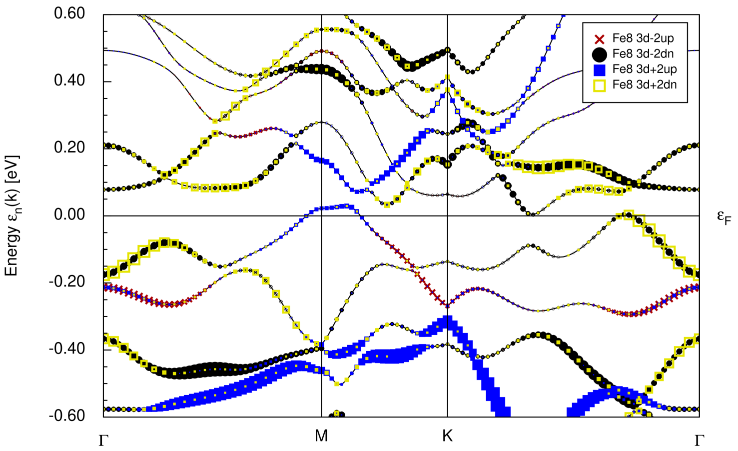

[a]

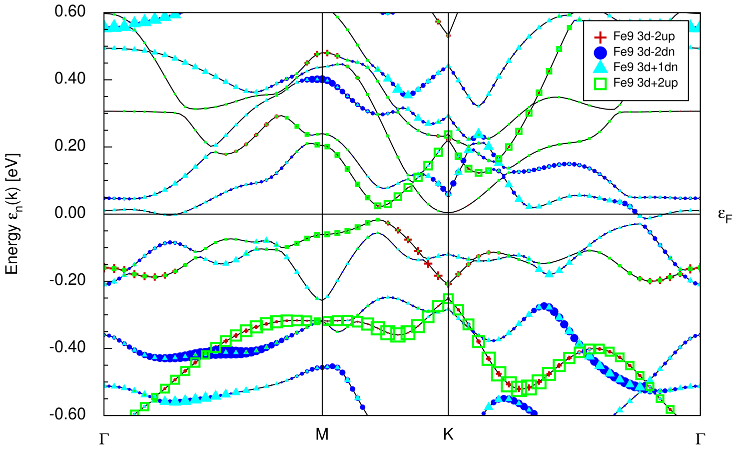

[b]

Figure S8: Orbital projected band structures for $(Hf_{2/3}Fe_{1/3})_2C$ (a) and $(Zr_{2/3}Fe_{1/3})_2C$. The Fe 3d-2 and Fe 3d+2 symbols denote the Fe $3d_{xy}$ and Fe-$3d_{x^2-y^2}$ orbitals, respectively.

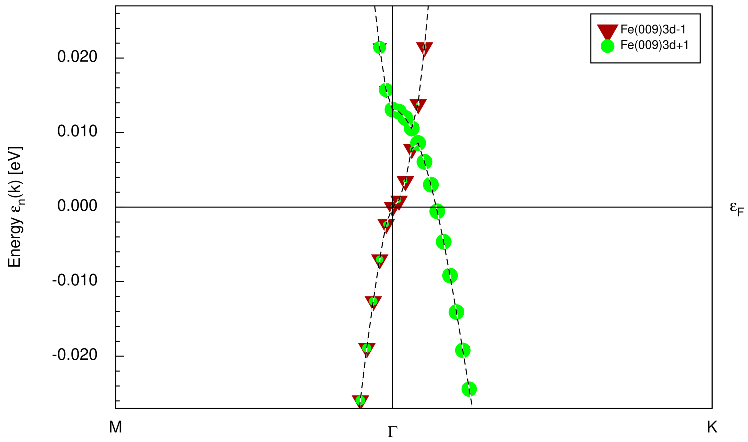

[a]

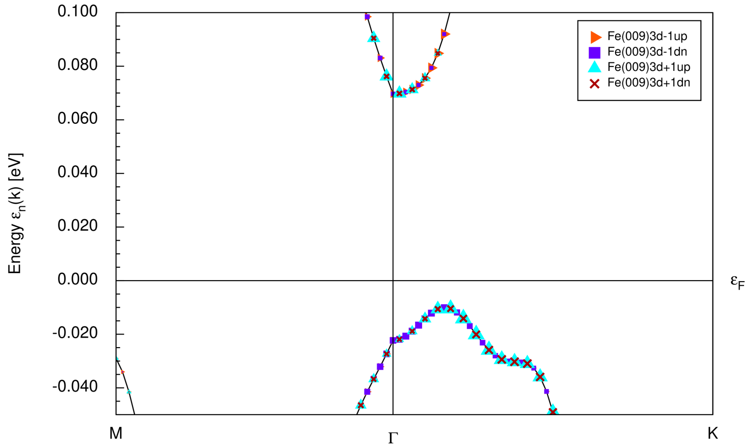

[b]

Figure S9: Orbital projected band structures for Fe atoms in $(Ta_{2/3}Fe_{1/3})_2C$ without and with SOC. The Fe 3d+1 and Fe 3d-1 symbols denote the Fe 3d$_{zx}$ and Fe 3d$_{yz}$ orbitals, respectively.

S7 MAE

Table S2: MAE values for i-MXene in hexagonal and rectangular lattices in unit of meV/f.u. $\Delta E = E_{hex.} - E_{rect.}$

Com.	hex	rect.	ΔE	Comp.	hex	rect.	ΔE
$(Hf_{2/3}Cr_{1/3})_2C$	0.092	0.0431	0.0489	$(Hf_{2/3}Fe_{1/3})_2C$	1.3854	1.4141	-0.0287
$(Hf_{2/3}Hg_{1/3})_2C$	-0.0001	-0.7499	0.7498	$(Hf_{2/3}Mn_{1/3})_2C$	-0.0567	-0.0979	0.0412
$(Mo_{2/3}Cr_{1/3})_2C$	0.0561	-0.0114	0.0675	$(Mo_{2/3}Fe_{1/3})_2C$	-0.0558	-0.0018	-0.054
$(Mo_{2/3}Mn_{1/3})_2C$	0.0109	-0.0319	0.0428	$(Nb_{2/3}Co_{1/3})_2C$	0.0158	-0.041	0.0568
$(Nb_{2/3}Fe_{1/3})_2C$	0.0286	0.0253	0.0033	$(Nb_{2/3}Mn_{1/3})_2C$	0.201	0.1018	0.0992
$(Nb_{2/3}Sc_{1/3})_2C$	0.0001	0.0	0.0001	$(Sc_{2/3}Cr_{1/3})_2C$	0.0775	0.0005	0.077
$(Sc_{2/3}Mn_{1/3})_2C$	0.0357	0.0159	0.0198	$(Sc_{2/3}Mo_{1/3})_2C$	0.0042	0.0	0.0042
$(Sc_{2/3}Nb_{1/3})_2C$	-0.0001	-0.0007	0.0006	$(Sc_{2/3}Ta_{1/3})_2C$	0.001	0.0665	-0.0655
$(Sc_{2/3}V_{1/3})_2C$	-0.009	0.0024	-0.0114	$(Ta_{2/3}Co_{1/3})_2C$	0.3184	0.2116	0.1068
$(Ta_{2/3}Fe_{1/3})_2C$	0.8628	0.3584	0.5044	$(Ta_{2/3}Mn_{1/3})_2C$	-0.0442	0.0868	-0.131
$(Ta_{2/3}Nb_{1/3})_2C$	0.0	-0.0001	0.0001	$(Ti_{2/3}Cr_{1/3})_2C$	0.0015	-0.0015	0.003
$(Ti_{2/3}Mo_{1/3})_2C$	0.0339	0.0253	0.0086	$(Ti_{2/3}Nb_{1/3})_2C$	0.0193	0.0254	-0.0061
$(Ti_{2/3}Pd_{1/3})_2C$	-0.0211	-0.0051	-0.016	$(Ti_{2/3}Sc_{1/3})_2C$	-0.0005	0.0023	-0.0028
$(Ti_{2/3}Ta_{1/3})_2C$	0.0565	-0.0093	0.0658	$(Ti_{2/3}V_{1/3})_2C$	0.0216	0.0195	0.0021
$(Ti_{2/3}Y_{1/3})_2C$	0.038	0.0083	0.0297	$(V_{2/3}Co_{1/3})_2C$	-0.0124	-0.0467	0.0343
$(V_{2/3}Fe_{1/3})_2C$	0.0535	0.0667	-0.0132	$(V_{2/3}Mn_{1/3})_2C$	0.0993	0.1013	-0.002
$(V_{2/3}Rh_{1/3})_2C$	-0.0505	-0.0708	0.0203	$(V_{2/3}Sc_{1/3})_2C$	-0.0128	0.0016	-0.0144
$(V_{2/3}Ti_{1/3})_2C$	0.0057	0.0059	-0.0002	$(Zr_{2/3}Cr_{1/3})_2C$	0.0056	0.0349	-0.0293
$(Zr_{2/3}Fe_{1/3})_2C$	0.7446	0.8125	-0.0679	$(Zr_{2/3}Hf_{1/3})_2C$	-0.6085	-0.0467	-0.5618
$(Zr_{2/3}Mn_{1/3})_2C$	0.0688	0.132	-0.0632	$(Zr_{2/3}Ni_{1/3})_2C$	0.0587	0.0348	0.0239
$(Hf_{2/3}Co_{1/3})_2N$	0.1272	0.1094	0.0178	$(Hf_{2/3}Cr_{1/3})_2N$	0.7536	0.6041	0.1495
$(Hf_{2/3}Fe_{1/3})_2N$	0.3874	-0.5089	0.8963	$(Hf_{2/3}Mn_{1/3})_2N$	-0.4437	-0.5283	0.0846
$(Hf_{2/3}Sc_{1/3})_2N$	-0.6875	-1.0708	0.3833	$(Hf_{2/3}Zr_{1/3})_2N$	0.054	0.0934	-0.0394
$(Ti_{2/3}Fe_{1/3})_2N$	-0.1369	-0.1276	-0.0093	$(Ti_{2/3}Hf_{1/3})_2N$	0.7144	0.4739	0.2405
$(Ti_{2/3}Mn_{1/3})_2N$	0.0735	0.0024	0.0711	$(Ti_{2/3}Nb_{1/3})_2N$	-0.0157	0.0496	-0.0653
$(Ti_{2/3}Sc_{1/3})_2N$	0.0026	0.002	0.0006	$(Ti_{2/3}V_{1/3})_2N$	0.0029	0.0049	-0.002
$(Ti_{2/3}Y_{1/3})_2N$	-0.021	0.0029	-0.0239	$(Zr_{2/3}Co_{1/3})_2N$	-0.0404	-0.0613	0.0209
$(Zr_{2/3}Fe_{1/3})_2N$	-0.0638	-0.0768	0.013	$(Zr_{2/3}Hf_{1/3})_2N$	0.0558	-0.1121	0.1679
$(Zr_{2/3}Mn_{1/3})_2N$	0.056	0.0532	0.0028	$(Zr_{2/3}Sc_{1/3})_2N$	0.0	0.0454	-0.0454
$(Zr_{2/3}V_{1/3})_2N$	0.0252	0.0145	0.0107	$(Ti_{2/3}Ti_{1/3})_2C$	0.0063	0.0	0.0063
$(Ti_{2/3}Ti_{1/3})_2N$	-0.0223	0.0	-0.0223				

S8 Energy comparison for Hexagonal and rectangular lattice

Table S3: The energy comparison for i-MXene in NM and FM spin configurations within hexagonal and rectangular lattice. E_{NM} and E_{FM} denote the energy of NM and FM spin configurations in unit of eV/atom. M_{tot} is the total magnetic moment in unit of $\mu_B/f.u.$

	Rect.			Hex.		
commpound	E_{NM}	E_{FM}	M_{tot}	E_{NM}	E_{FM}	M_{tot}
$(Hf_{2/3}Cr_{1/3})_2C$	0.0034	0.0	0.4118	0.0034	0.0	0.4293
$(Hf_{2/3}Hg_{1/3})_2C$	0.0022	0.0	0.2573	0.0005	0.0	0.344
$(Mo_{2/3}Cr_{1/3})_2C$	0.0085	0.0	0.8835	0.0109	0.0	0.842
$(Mo_{2/3}Fe_{1/3})_2C$	0.0452	0.0	1.182	0.044	0.0	1.173
$(Mo_{2/3}Mn_{1/3})_2C$	0.0588	0.0	1.2948	0.0594	0.0	1.318
$(Nb_{2/3}Co_{1/3})_2C$	0.0039	0.0	0.4637	0.0039	0.0	0.4497
$(Nb_{2/3}Fe_{1/3})_2C$	0.0283	0.0	1.0397	0.0288	0.0	1.0473
$(Ta_{2/3}Co_{1/3})_2C$	0.0053	0.0	0.4113	0.0058	0.0	0.453
$(Ta_{2/3}Mn_{1/3})_2C$	0.0283	0.0	0.7803	0.0283	0.0	0.7713
$(Ti_{2/3}Nb_{1/3})_2C$	0.0125	0.0	0.7057	0.0134	0.0	0.7147
$(Ti_{2/3}Pd_{1/3})_2C$	0.0041	0.0	0.3772	0.0049	0.0	0.382
$(Ti_{2/3}Sc_{1/3})_2C$	0.0093	0.0	0.8355	0.0113	0.0	0.836
$(Ti_{2/3}Ta_{1/3})_2C$	0.0112	0.0	0.725	0.0134	0.0	0.718
$(Ti_{2/3}Ti_{1/3})_2C$	0.0278	0.0	0.8935	0.0414	0.0	0.9207
$(V_{2/3}Co_{1/3})_2C$	0.0064	0.0	0.638	0.0073	0.0	0.6497
$(V_{2/3}Fe_{1/3})_2C$	0.0331	0.0	1.0948	0.0335	0.0	1.1273
$(V_{2/3}Mn_{1/3})_2C$	0.0277	0.0	0.697	0.0275	0.0	0.705
$(V_{2/3}Rh_{1/3})_2C$	0.0009	0.0	0.3035	0.0005	0.0	0.3033
$(Zr_{2/3}Cr_{1/3})_2C$	0.0034	0.0	0.3828	0.0034	0.0	0.425
$(Zr_{2/3}Fe_{1/3})_2C$	0.011	0.0	0.8817	0.0129	0.0	0.9173
$(Zr_{2/3}Ni_{1/3})_2C$	0.0033	0.0	0.3608	0.0032	0.0	0.336
$(Hf_{2/3}Co_{1/3})_2N$	0.0051	0.0	0.3463	0.0059	0.0	0.3637
$(Hf_{2/3}Cr_{1/3})_2N$	0.0012	0.0	0.2668	0.0016	0.0	0.3557
$(Hf_{2/3}Mn_{1/3})_2N$	0.035	0.0	0.7438	0.036	0.0	0.6857
$(Hf_{2/3}Zr_{1/3})_2N$	0.0025	0.0	0.5643	0.0031	0.0	0.5553
$(Ti_{2/3}Fe_{1/3})_2N$	0.0385	0.0	1.1135	0.0382	0.0	1.1017
$(Ti_{2/3}Hf_{1/3})_2N$	0.0035	0.0	0.5707	0.0043	0.0	0.5777
$(Ti_{2/3}Mn_{1/3})_2N$	0.0416	0.0	0.804	0.0413	0.0	0.8093
$(Ti_{2/3}Sc_{1/3})_2N$	0.0121	0.0	0.5993	0.0121	0.0	0.5753
$(Ti_{2/3}Ti_{1/3})_2N$	0.0003	0.0	0.5787	0.0144	0.0	0.575
$(Ti_{2/3}Y_{1/3})_2N$	0.002	0.0	0.3975	0.0016	0.0	0.3777
$(Zr_{2/3}Co_{1/3})_2N$	0.0094	0.0	0.4592	0.0101	0.0	0.469
$(Zr_{2/3}Fe_{1/3})_2N$	0.0341	0.0	1.235	0.0379	0.0	1.266
$(Zr_{2/3}Hf_{1/3})_2N$	0.0053	0.0	0.5257	0.0058	0.0	0.53
$(Zr_{2/3}Mn_{1/3})_2N$	0.0324	0.0	1.0635	0.034	0.0	1.07
$(Zr_{2/3}Y_{1/3})_2N$	0.0035	0.0	0.4002	0.0039	0.0	0.4207

Table S3: The energy comparison for i-MXene in NM and FM spin configurations within hexagonal and rectangular lattice. E_{NM} and E_{FM} denote the energy of NM and FM spin configurations in unit of eV/atom. M_{tot} is the total magnetic moment in unit of $\mu_B/f.u.$. (continued)

	Rect.			Hex.		
commpound	NM	FM	M_{tot}	NM	FM	M_{tot}
$(Nb_{2/3}Mn_{1/3})_2C$	0.0299	0.0	0.7793	0.0295	0.0	0.799
$(Nb_{2/3}Sc_{1/3})_2C$	0.0017	0.0	0.4298	0.0024	0.0	0.412
$(Sc_{2/3}Cr_{1/3})_2C$	0.0095	0.0	1.101	0.0066	0.0	1.1063
$(Sc_{2/3}Mn_{1/3})_2C$	0.0013	0.0	0.6163	0.0011	0.0	0.6443
$(Sc_{2/3}Mo_{1/3})_2C$	0.0008	0.0	0.8827	0.0048	0.0	0.731
$(Sc_{2/3}Nb_{1/3})_2C$	0.0028	0.0	0.4998	0.005	0.0	0.5507
$(Sc_{2/3}Ta_{1/3})_2C$	0.002	0.0	0.4267	0.0028	0.0	0.4363
$(Sc_{2/3}V_{1/3})_2C$	0.0	0.0	0.9322	0.0049	0.0	0.4447
$(Ta_{2/3}Fe_{1/3})_2C$	0.0237	0.0	1.0207	0.0249	0.0	1.0117
$(Ta_{2/3}Sc_{1/3})_2C$	0.0008	0.0	0.5032	0.0015	0.0	0.341
$(Ti_{2/3}Cr_{1/3})_2C$	0.001	0.0	0.2468	0.001	0.0	0.2323
$(Ti_{2/3}Mo_{1/3})_2C$	0.0019	0.0	0.2175	0.0022	0.0	0.2063
$(Ti_{2/3}Y_{1/3})_2C$	0.0039	0.0	0.7477	0.0002	0.0	0.2853
$(V_{2/3}Sc_{1/3})_2C$	0.0015	0.0	0.4797	0.0002	0.0	0.541
$(V_{2/3}Ti_{1/3})_2C$	0.0063	0.0	0.519	0.0019	0.0	0.4413
$(Zr_{2/3}Hf_{1/3})_2C$	0.0001	0.0	0.2242	0.0013	0.0	0.5593
$(Zr_{2/3}Mn_{1/3})_2C$	0.0026	0.0	0.7227	0.0041	0.0	0.714
$(Zr_{2/3}Y_{1/3})_2C$	0.0025	0.0	0.3045	0.002	0.0	0.666
$(Hf_{2/3}Fe_{1/3})_2N$	0.0321	0.0	1.0337	0.032	0.0	1.0477
$(Hf_{2/3}Sc_{1/3})_2N$	0.0065	0.0	0.4035	0.0009	0.0	0.6017
$(Ti_{2/3}Nb_{1/3})_2N$	0.0005	0.0	0.2492	0.0057	0.0	0.5223
$(Ti_{2/3}V_{1/3})_2N$	0.0011	0.0	0.2352	0.0	0.0	0.298
$(Zr_{2/3}Sc_{1/3})_2N$	0.0112	0.0	0.6917	0.0088	0.0	0.699
$(Hf_{2/3}Fe_{1/3})_2C$	0.0019	0.0	0.9	0.016	0.0	0.8797
$(Hf_{2/3}Mn_{1/3})_2C$	0.0068	0.0	0.525	0.0008	0.0	0.5257
$(Ti_{2/3}V_{1/3})_2C$	0.0053	0.0	0.722	0.0069	0.0	0.701

Table S4: The energy comparison for i-MXene with NM to FM spin configuration transition when the lattice is changed from hexagonal and rectangular.

commpound	NM	FM	AFM-0	AFM-β	AFM-α
$(Ti_{2/3}Ru_{1/3})_2C$	0.0007	0.0	0.0007	0.0007	0.0007
$(Zr_{2/3}Cu_{1/3})_2C$	0.0012	0.0	0.0012	0.0008	0.0012
$(Zr_{2/3}Ti_{1/3})_2N$	0.0015	0.0	0.0014	0.0016	0.0011

Table S5: Energy (in unit of eV/atom) compassion for i-MXene within various spin configurations in both rectangular (Rect.) and hexagonal (Hex.) lattice.

Compound	Structure	NM	FM	AFM-0	AFM-3 /AFM-β	AFM-2 /AFM-α	AFM-4	AFM-1
AFM→ FM								
$(Hf_{2/3}Fe_{1/3})_2C$	Rect.	0.016	0.0107	0.0	0.0018	0.0045	0.015	0.015
	Hex.	0.0105	0.0	0.0039	0.0021	0.0091	-	-
$(Hf_{2/3}Mn_{1/3})_2C$	Rect.	0.0084	0.0084	0.0050	0.0079	0.0	0.0147	0.0215
	Hex.	0.0119	0.0055	0.0089	0.0	0.0046	-	-
$(Ti_{2/3}V_{1/3})_2C$	Rect.	0.0069	0.0022	0.0	0.0055	0.0038	0.0062	0.0009
	Hex.	0.0042	0.0	0.002	0.0052	0.002	-	-
AFM→ AFM								
$(Nb_{2/3}Mn_{1/3})_2C$	Rect.	0.0408	0.0109	0.0076	0.0043	0.0	0.0069	0.0121
	Hex.	0.0361	0.0066	0.0031	0.0027	0.0	-	-
$(Nb_{2/3}Sc_{1/3})_2C$	Rect.	0.005	0.0033	0.0	0.0048	0.0043	0.0047	0.0043
	Hex.	0.0055	0.0031	0.0	0.0049	0.0054	-	-
$(Sc_{2/3}Cr_{1/3})_2C$	Rect.	0.0182	0.0087	0.0	0.0036	0.0156	0.0172	0.017
	Hex.	0.0184	0.0118	0.0	0.0176	0.0039	-	-
$(Sc_{2/3}Mn_{1/3})_2C$	Rect.	0.0079	0.0066	0.0016	0.0044	0.0011	0.0051	0.0
	Hex.	0.0089	0.0078	0.0	0.0039	0.0037	-	-
$(Sc_{2/3}Mo_{1/3})_2C$	Rect.	0.0023	0.0015	0.0	0.0031	0.0027	0.003	0.0029
	Hex.	0.0077	0.0029	0.0009	0.0027	0.0	-	-
$(Sc_{2/3}Nb_{1/3})_2C$	Rect	0.0126	0.0098	0.0073	0.0011	0.0061	0.0016	0.0
	Hex.	0.0147	0.0097	0.0084	0.0019	0.0	-	-
$(Sc_{2/3}Ta_{1/3})_2C$	Rect.	0.0054	0.0034	0.0	0.0014	0.004	0.0027	0.0025
	Hex.	0.0065	0.0037	0.0	0.0019	0.0025	-	-
$(Sc_{2/3}V_{1/3})_2C$	Rect.	0.0072	0.0072	0.0	0.0021	0.0031	0.024	0.0015
	Hex.	0.0061	0.0012	0.0	0.0008	0.0005	-	-
$(Ta_{2/3}Fe_{1/3})_2C$	Rect.	0.0278	0.0041	0.0	0.0147	0.0058	0.0099	0.022
	Hex.	0.0286	0.0037	0.0	0.0103	0.0152	-	-
$(Ta_{2/3}Sc_{1/3})_2C$	Rect.	0.0014	0.0006	0.0	0.0009	0.0009	0.0009	0.0009
	Hex.	0.0024	0.0009	0.0	0.0013	0.0013	-	-
$(Ti_{2/3}Cr_{1/3})_2C$	Rect.	0.0028	0.0018	0.0	0.0028	0.0024	0.0028	0.0021
	Hex.	0.0029	0.0019	0.0	0.0029	0.0028	-	-
$(Ti_{2/3}Mo_{1/3})_2C$	Rect.	0.0022	0.0003	0.0	0.0021	0.002	0.0021	0.0018
	Hex.	0.0029	0.0007	0.0	0.0025	0.0025	-	-
$(Ti_{2/3}Y_{1/3})_2C$	Rect.	0.0053	0.0014	0.0	0.0011	0.0013	0.0021	0.0027
	Hex.	0.0011	0.0009	0.0	0.0007	0.0009	-	-
$(V_{2/3}Sc_{1/3})_2C$	Rect.	0.0051	0.0036	0.0	0.0034	0.0033	0.0036	0.0033
	Hex.	0.0045	0.0043	0.0	0.0044	0.0041	-	-
$(V_{2/3}Ti_{1/3})_2C$	Rect.	0.0092	0.0029	0.0	0.0024	0.0026	0.0028	0.0027
	Hex.	0.0032	0.0013	0.0	0.0031	0.0026	-	-
$(Zr_{2/3}Hf_{1/3})_2C$	Rect.	0.0037	0.0036	0.0	0.0022	0.0016	0.0015	0.0008
	Hex.	0.0064	0.0051	0.0	0.0032	0.0036	-	-
$(Zr_{2/3}Mn_{1/3})_2C$	Rect.	0.0132	0.0106	0.0087	0.0016	0.0032	0.002	0.0
	Hex.	0.0126	0.0085	0.0075	0.0003	0.0	-	-
$(Zr_{2/3}Y_{1/3})_2C$	Rect.	0.0044	0.0019	0.0	0.0005	0.002	0.002	0.0009
	Hex.	0.0039	0.0019	0.0	0.0012	0.0008	-	-
$(Hf_{2/3}Fe_{1/3})_2N$	Rect.	0.0411	0.009	0.0088	0.0241	0.0139	0.0109	0.0
	Hex.	0.0413	0.0093	0.0085	0.0	0.0233	-	-
$(Hf_{2/3}Sc_{1/3})_2N$	Rect.	0.0104	0.0039	0.0007	0.0036	0.0006	0.0035	0.0
	Hex.	0.0041	0.0032	0.0	0.0031	0.0031	-	-
$(Ti_{2/3}Nb_{1/3})_2N$	Rect.	0.0025	0.002	0.0	0.0027	0.0024	0.0023	0.0024
	Hex.	0.0079	0.0022	0.0	0.0019	0.002	-	-
$(Ti_{2/3}V_{1/3})_2N$	Rect.	0.0027	0.0016	0.0	0.0025	0.0028	0.0026	0.0027
	Hex.	0.0029	0.0029	0.0	0.0029	0.0026	-	-
$(Zr_{2/3}Sc_{1/3})_2N$	Rect.	0.0179	0.0067	0.0	0.0124	0.0087	0.011	0.0073
	Hex.	0.0164	0.0076	0.0	0.0111	0.012	-	-

Table S5: Energy (in unit of eV/atom) compassion for i-MXene within various spin configurations in both rectangular (Rect.) and hexagonal (Hex.) lattice. (continued)

Compound	Structure	NM	FM	AFM-0	AFM-3 /AFM-β	AFM-2 /AFM-α	AFM-4	AFM-1
FM→ FM								
$(Zr_{2/3}Co_{1/3})_2N$	Rect.	0.0105	0.0011	0.0098	0.0099	0.0012	0.0	0.0012
	Hex.	0.0113	0.0012	0.0113	0.0	0.0105	-	-
$(Zr_{2/3}Mn_{1/3})_2N$	Rect.	0.0438	0.0114	0.0268	0.0	0.0151	0.0106	0.0162
	Hex.	0.0342	0.0002	0.0161	0.0	0.0041	-	-
$(Zr_{2/3}Y_{1/3})_2N$	Rect.	0.0041	0.0006	0.0146	0.0024	0.0024	0.0	0.0033
	Hex.	0.0039	0.0	0.0031	0.0026	0.0022	-	-
$(Zr_{2/3}Fe_{1/3})_2N$	Rect.	0.0451	0.011	0.0201	0.0264	0.0154	0.0	0.0177
	Hex.	0.0473	0.0094	0.0205	0.0	0.0278	-	-
$(Zr_{2/3}Hf_{1/3})_2N$	Rect.	0.0053	0.0	0.0119	0.0023	0.0031	0.0037	0.0014
	Hex.	0.0058	0.0	0.0052	0.004	0.0021	-	-
$(Hf_{2/3}Cr_{1/3})_2C$	Rect.	0.0034	0.0	0.0025	0.0036	0.0019	0.0017	0.0004
	Hex.	0.0034	0.0	0.0023	0.002	0.0034	-	-
$(Hf_{2/3}Hg_{1/3})_2C$	Rect.	0.0022	0.0	0.0007	0.0021	0.0012	0.0021	0.0012
	Hex.	0.0005	0.0	0.0002	0.0005	0.0005	-	-
$(Mo_{2/3}Cr_{1/3})_2C$	Rect.	0.0089	0.0004	0.0065	0.0	0.0017	0.0031	0.0021
	Hex.	0.0109	0.0	0.0068	0.0046	0.0006	-	-
$(Mo_{2/3}Fe_{1/3})_2C$	Rect.	0.0452	0.0	0.0021	0.0163	0.0087	0.0003	0.0083
	Hex.	0.0442	0.0002	0.0027	0.0	0.0158	-	-
$(Mo_{2/3}Mn_{1/3})_2C$	Rect.	0.0588	0.0	0.0077	0.021	0.0016	0.0021	0.0152
	Hex.	0.0594	0.0	0.008	0.0023	0.0214	-	-
$(Nb_{2/3}Co_{1/3})_2C$	Rect.	0.0039	0.0	0.0039	0.0037	0.0017	0.001	0.0017
	Hex.	0.0039	0.0	0.0039	0.0009	0.0036	-	-
$(Nb_{2/3}Fe_{1/3})_2C$	Rect.	0.0283	0.0	0.0024	0.012	0.0038	0.0059	0.0174
	Hex.	0.0288	0.0	0.0021	0.0061	0.0123	-	-
$(Ta_{2/3}Co_{1/3})_2C$	Rect.	0.0053	0.0	0.0053	0.0052	0.0031	0.0001	0.0016
	Hex.	0.0058	0.0	0.0058	0.0003	0.0059	-	-
$(Ta_{2/3}Mn_{1/3})_2C$	Rect.	0.0362	0.0079	0.0084	0.0053	0.0	0.0113	0.0146
	Hex.	0.0304	0.0021	0.0026	0.0	0.0055	-	-
$(Ti_{2/3}Nb_{1/3})_2C$	Rect.	0.0125	0.0	0.0012	0.0076	0.0051	0.0076	0.0038
	Hex.	0.0134	0.0	0.0017	0.0083	0.0083	-	-
$(Ti_{2/3}Pd_{1/3})_2C$	Rect.	0.0041	0.0	0.0041	0.0041	0.0013	0.0012	0.0013
	Hex.	0.0049	0.0	0.0049	0.0014	0.0049	-	-
$(Ti_{2/3}Sc_{1/3})_2C$	Rect.	0.0093	0.0	0.0007	0.0093	0.0093	0.0093	0.0093
	Hex.	0.0113	0.0	0.0016	0.0104	0.0104	-	-
$(Ti_{2/3}Ta_{1/3})_2C$	Rect.	0.0112	0.0	0.0003	0.0059	0.0055	0.0061	0.004
	Hex.	0.0134	0.0	0.0018	0.0071	0.0077	-	-
$(Ti_{2/3}Ti_{1/3})_2C$	Rect.	0.0278	0.0	0.0116	0.011	0.013	0.0087	0.0091
	Hex.	0.0414	0.0	0.014	0.028	0.0263	-	-
$(V_{2/3}Co_{1/3})_2C$	Rect.	0.0064	0.0	0.0052	0.0064	0.003	0.0024	0.003
	Hex.	0.0073	0.0	0.0063	0.0027	0.0073	-	-
$(V_{2/3}Fe_{1/3})_2C$	Rect.	0.0331	0.0	0.0039	0.0136	0.007	0.0088	0.0168
	Hex.	0.0335	0.0	0.0042	0.0092	0.014	-	-
$(V_{2/3}Mn_{1/3})_2C$	Rect.	0.0314	0.0037	0.0073	0.0	0.0006	0.005	0.0042
	Hex.	0.031	0.0035	0.0068	0.0	0.0047	-	-
$(V_{2/3}Rh_{1/3})_2C$	Rect.	0.0009	0.0	0.0009	0.0009	0.0009	0.0009	0.0009
	Hex.	0.0005	0.0	0.0005	0.0005	0.0005	-	-
$(Zr_{2/3}Cr_{1/3})_2C$	Rect.	0.0043	0.0	0.0028	0.0039	0.0033	0.0023	0.0009
	Hex.	0.0034	0.0	0.0018	0.0014	0.003	-	-
$(Zr_{2/3}Fe_{1/3})_2C$	Rect.	0.0159	0.0049	0.0081	0.0035	0.0003	0.0	0.0074
	Hex.	0.0168	0.0039	0.0072	0.0	0.0041	-	-
$(Zr_{2/3}Ni_{1/3})_2C$	Rect.	0.0037	0.0004	0.0037	0.0035	0.0014	0.0	0.0014
	Hex.	0.0041	0.0009	0.0041	0.0	0.0042	-	-
$(Hf_{2/3}Co_{1/3})_2N$	Rect.	0.0051	0.0	0.0033	0.0052	0.0005	0.0013	0.0005
	Hex.	0.0059	0.0	0.0059	0.001	0.0058	-	-
$(Hf_{2/3}Cr_{1/3})_2N$	Rect.	0.0078	0.0066	0.0078	0.0	0.0035	0.0074	0.0017
	Hex.	0.008	0.0064	0.0078	0.0	0.0072	-	-
$(Hf_{2/3}Mn_{1/3})_2N$	Rect.	0.0382	0.0032	0.0291	0.0091	0.0	0.0064	0.0073
	Hex.	0.036	0.0	0.0271	0.0032	0.0055	-	-
$(Hf_{2/3}Zr_{1/3})_2N$	Rect.	0.0025	0.0	0.0035	0.0029	0.0041	0.0027	0.0015
	Hex.	0.0031	0.0	0.0068	0.0031	0.0031	-	-
$(Ti_{2/3}Fe_{1/3})_2N$	Rect.	0.0408	0.0023	0.0152	0.0219	0.011	0.0	0.0135
	Hex.	0.0405	0.0023	0.0153	0.0	0.0219	-	-
$(Ti_{2/3}Hf_{1/3})_2N$	Rect.	0.0035	0.0	0.0017	0.0016	0.0016	0.0018	0.0016
	Hex.	0.0043	0.0	0.0026	0.0028	0.0023	-	-
$(Ti_{2/3}Mn_{1/3})_2N$	Rect.	0.0416	0.0	0.0239	0.0087	0.0005	0.0103	0.007
	Hex.	0.0413	0.0	0.0242	0.0101	0.008	-	-
$(Ti_{2/3}Sc_{1/3})_2N$	Rect.	0.0121	0.0	0.0004	0.0091	0.0085	0.0085	0.0085
	Hex.	0.0121	0.0	0.0091	0.0085	0.0092	-	-
$(Ti_{2/3}Ti_{1/3})_2N$	Rect.	0.0003	0.0	0.0003	0.006	0.0098	0.006	0.006
	Hex.	0.0144	0.0	0.0032	0.01	0.0083	-	-
$(Ti_{2/3}Y_{1/3})_2N$	Rect.	0.002	0.0	0.0013	0.0012	0.0016	0.0015	0.0015
	Hex.	0.0016	0.0	0.0012	0.0014	0.0012	-	-

Table S6: The atomic magnetic moments for transition mental atoms M and M$'$ in i-MXene $(M_{2/3}M'_{1/3})_2X$ within both rectangular and hexagonal lattices. Rect. and Hex. represent the rectangular and hexagonal lattice, respectively. M_M, $M_{M'}$ and M_{tot} are the magnetic moment for M (in unit of μ_B) atom, M$'$ atom (in unit of μ_B) and total magnetic moment (in unit of μ_B/f.u.).

$(M_{2/3}M'_{1/3})_2X$	Rect.			Hex.		
	M_M	$M_{M'}$	M_{tot}	M_M	$M_{M'}$	M_{tot}
NM→FM						
$(\mathrm{Ti}_{2/3}\mathrm{Ru}_{1/3})_2\mathrm{C}$	0	0	0	0.166	0.104	0.290
$(\mathrm{Zr}_{2/3}\mathrm{Ti}_{1/3})_2\mathrm{N}$	0	0	0	0.470	0.54	0.950
$(\mathrm{Zr}_{2/3}\mathrm{Cu}_{1/3})_2\mathrm{C}$	0	0	0	0.225	0.0	0.30
FM→FM						
$(\mathrm{Hf}_{2/3}\mathrm{Cr}_{1/3})_2\mathrm{C}$	-0.014	0.664	0.412	-0.005	0.69	0.429
$(\mathrm{Hf}_{2/3}\mathrm{Hg}_{1/3})_2\mathrm{C}$	0.185	0.021	0.257	0.258	0.031	0.344
$(\mathrm{Mo}_{2/3}\mathrm{Cr}_{1/3})_2\mathrm{C}$	0.039	1.305	0.884	0.009	1.282	0.842
$(\mathrm{Mo}_{2/3}\mathrm{Fe}_{1/3})_2\mathrm{C}$	-0.052	1.921	1.182	-0.046	1.905	1.173
$(\mathrm{Mo}_{2/3}\mathrm{Mn}_{1/3})_2\mathrm{C}$	-0.111	2.235	1.295	-0.101	2.247	1.318
$(\mathrm{Nb}_{2/3}\mathrm{Co}_{1/3})_2\mathrm{C}$	0.019	0.646	0.464	0.017	0.632	0.45
$(\mathrm{Nb}_{2/3}\mathrm{Fe}_{1/3})_2\mathrm{C}$	-0.121	1.791	1.04	-0.099	1.794	1.047
$(\mathrm{Ta}_{2/3}\mathrm{Co}_{1/3})_2\mathrm{C}$	-0.02	0.643	0.411	0.0	0.678	0.453
$(\mathrm{Ta}_{2/3}\mathrm{Mn}_{1/3})_2\mathrm{C}$	-0.199	1.593	0.78	-0.2	1.581	0.771
$(\mathrm{Ti}_{2/3}\mathrm{Nb}_{1/3})_2\mathrm{C}$	0.383	0.339	0.706	0.39	0.345	0.715
$(\mathrm{Ti}_{2/3}\mathrm{Pd}_{1/3})_2\mathrm{C}$	0.281	0.037	0.377	0.287	0.037	0.382
$(\mathrm{Ti}_{2/3}\mathrm{Sc}_{1/3})_2\mathrm{C}$	0.525	0.299	0.836	0.534	0.3	0.836
$(\mathrm{Ti}_{2/3}\mathrm{Ta}_{1/3})_2\mathrm{C}$	0.359	0.405	0.725	0.354	0.392	0.718
$(\mathrm{Ti}_{2/3}\mathrm{Ti}_{1/3})_2\mathrm{C}$	0.475	0.475	0.893	0.489	0.489	0.921
$(\mathrm{V}_{2/3}\mathrm{Co}_{1/3})_2\mathrm{C}$	0.118	0.742	0.638	0.129	0.746	0.65
$(\mathrm{V}_{2/3}\mathrm{Fe}_{1/3})_2\mathrm{C}$	-0.091	1.804	1.095	-0.059	1.814	1.127
$(\mathrm{V}_{2/3}\mathrm{Mn}_{1/3})_2\mathrm{C}$	-0.261	1.575	0.697	-0.253	1.575	0.705
$(\mathrm{V}_{2/3}\mathrm{Rh}_{1/3})_2\mathrm{C}$	0.217	0.051	0.303	0.13	0.031	0.303
$(\mathrm{Zr}_{2/3}\mathrm{Cr}_{1/3})_2\mathrm{C}$	-0.033	0.665	0.383	-0.026	0.729	0.425
$(\mathrm{Zr}_{2/3}\mathrm{Fe}_{1/3})_2\mathrm{C}$	-0.075	1.502	0.882	-0.047	1.515	0.917
$(\mathrm{Zr}_{2/3}\mathrm{Ni}_{1/3})_2\mathrm{C}$	0.224	0.106	0.361	0.204	0.098	0.336
$(\mathrm{Hf}_{2/3}\mathrm{Co}_{1/3})_2\mathrm{N}$	0.107	0.322	0.346	0.086	0.398	0.364
$(\mathrm{Hf}_{2/3}\mathrm{Cr}_{1/3})_2\mathrm{N}$	0.091	-0.582	-0.267	-0.117	0.763	0.356
$(\mathrm{Hf}_{2/3}\mathrm{Mn}_{1/3})_2\mathrm{N}$	-0.371	1.84	0.744	-0.391	1.791	0.686
$(\mathrm{Hf}_{2/3}\mathrm{Zr}_{1/3})_2\mathrm{N}$	0.302	0.242	0.564	0.3	0.244	0.555
$(\mathrm{Ti}_{2/3}\mathrm{Fe}_{1/3})_2\mathrm{N}$	-0.162	1.937	1.113	-0.166	1.932	1.102
$(\mathrm{Ti}_{2/3}\mathrm{Hf}_{1/3})_2\mathrm{N}$	0.316	0.248	0.571	0.318	0.249	0.578
$(\mathrm{Ti}_{2/3}\mathrm{Mn}_{1/3})_2\mathrm{N}$	-0.352	1.862	0.804	-0.355	1.869	0.809
$(\mathrm{Ti}_{2/3}\mathrm{Sc}_{1/3})_2\mathrm{N}$	0.359	0.228	0.599	0.335	0.221	0.575
$(\mathrm{Ti}_{2/3}\mathrm{Ti}_{1/3})_2\mathrm{N}$	0.306	0.52	0.579	0.301	0.301	0.575
$(\mathrm{Ti}_{2/3}\mathrm{Y}_{1/3})_2\mathrm{N}$	0.237	0.142	0.397	0.219	0.135	0.378
$(\mathrm{Zr}_{2/3}\mathrm{Co}_{1/3})_2\mathrm{N}$	0.034	-0.737	-0.459	0.029	-0.753	-0.469
$(\mathrm{Zr}_{2/3}\mathrm{Fe}_{1/3})_2\mathrm{N}$	-0.063	1.959	1.235	-0.042	1.977	1.266
$(\mathrm{Zr}_{2/3}\mathrm{Hf}_{1/3})_2\mathrm{N}$	0.254	0.295	0.526	0.251	0.296	0.53
$(\mathrm{Zr}_{2/3}\mathrm{Mn}_{1/3})_2\mathrm{N}$	-0.088	1.782	1.064	-0.105	1.808	1.07
$(\mathrm{Zr}_{2/3}\mathrm{Y}_{1/3})_2\mathrm{N}$	0.226	0.169	0.4	0.225	0.176	0.421

Table S7: The atomic magnetic moments for transition mental atoms M and M′ in i-MXene $(M_{2/3}M'_{1/3})_2X$ within both rectangular and hexagonal lattices. Rect. and Hex. represent the rectangular and hexagonal lattice, respectively. The magnetic moment is in unit of μ_B/atom. ↑ and ↓ denote the up and down layer transition atom, respectively.

$(M_{2/3}M'_{1/3})_2X$	Rect.				Hex.			
	$M_{M\uparrow}$	$M_{M\downarrow}$	$M_{M'\uparrow}$	$M_{M'\downarrow}$	$M_{M\uparrow}$	$M_{M\downarrow}$	$M_{M'\uparrow}$	$M_{M'\downarrow}$
AFM→AFM								
$(Nb_{2/3}Mn_{1/3})_2C$	0.183	-0.183	1.555	-1.555	0.061	-0.061	1.807	-1.807
$(Nb_{2/3}Sc_{1/3})_2C$	0.251	-0.251	0.17	-0.17	0.263	-0.263	0.195	-0.195
$(Sc_{2/3}Cr_{1/3})_2C$	0.239	-0.239	1.241	-1.241	0.077	-0.077	1.409	-1.409
$(Sc_{2/3}Mn_{1/3})_2C$	0.145	-0.145	0.673	-0.673	0.028	-0.028	1.326	-1.326
$(Sc_{2/3}Mo_{1/3})_2C$	0.347	-0.347	0.624	-0.624	0.104	-0.104	0.449	-0.449
$(Sc_{2/3}Nb_{1/3})_2C$	0.205	-0.205	0.388	-0.388	0.185	-0.185	0.343	-0.343
$(Sc_{2/3}Ta_{1/3})_2C$	0.157	-0.157	0.357	-0.357	0.172	-0.172	0.349	-0.349
$(Sc_{2/3}V_{1/3})_2C$	0.298	-0.298	0.865	-0.865	0.148	-0.148	0.5	-0.5
$(Ta_{2/3}Fe_{1/3})_2C$	0.154	-0.154	1.816	-1.816	0.079	-0.079	1.723	-1.723
$(Ta_{2/3}Sc_{1/3})_2C$	0.297	-0.297	0.179	-0.179	0.269	-0.269	0.173	-0.173
$(Ti_{2/3}Cr_{1/3})_2C$	0.103	-0.103	0.166	-0.166	0.175	-0.175	0.438	-0.438
$(Ti_{2/3}Mo_{1/3})_2C$	0.132	-0.132	0.054	-0.054	0.181	-0.181	0.083	-0.083
$(Ti_{2/3}Y_{1/3})_2C$	0.46	-0.46	0.28	-0.28	0.202	-0.202	0.125	-0.125
$(V_{2/3}Sc_{1/3})_2C$	0.327	-0.327	0.119	-0.119	0.319	-0.319	0.126	-0.126
$(V_{2/3}Ti_{1/3})_2C$	0.282	-0.282	0.24	-0.24	0.335	-0.335	0.173	-0.173
$(Zr_{2/3}Hf_{1/3})_2C$	0.104	-0.104	0.134	-0.134	0.246	-0.246	0.289	-0.289
$(Zr_{2/3}Mn_{1/3})_2C$	0.016	-0.016	1.167	-1.167	0.117	-0.117	1.052	-1.052
$(Zr_{2/3}Y_{1/3})_2C$	0.183	-0.183	0.118	-0.118	0.221	-0.221	0.155	-0.155
$(Hf_{2/3}Fe_{1/3})_2N$	0.206	-0.206	1.936	-1.936	0.232	-0.232	1.934	-1.934
$(Hf_{2/3}Sc_{1/3})_2N$	0.236	-0.236	0.142	-0.142	0.319	-0.319	0.199	-0.199
$(Ti_{2/3}Nb_{1/3})_2N$	0.115	-0.115	0.156	-0.156	0.152	-0.152	0.246	-0.246
$(Ti_{2/3}V_{1/3})_2N$	0.129	-0.129	0.108	-0.108	0.167	-0.167	0.299	-0.299
$(Zr_{2/3}Sc_{1/3})_2N$	0.377	-0.377	0.3	-0.3	0.487	-0.487	0.357	-0.357
AFM→FM								
$(M_{2/3}M'_{1/3})_2X$	Rect.				Hex.			
	$M_{M\uparrow}$	$M_{M\downarrow}$	$M_{M'\uparrow}$	$M_{M'\downarrow}$	M_M	$M_{M'}$	M_{tot}	
$(Hf_{2/3}Fe_{1/3})_2C$	0.087	-0.087	1.04	-1.04	-0.137	1.623	0.899	
$(Hf_{2/3}Mn_{1/3})_2C$	0.128	-0.128	0.919	-0.919	-0.125	1.089	0.559	
$(Ti_{2/3}V_{1/3})_2C$	0.367	-0.367	0.698	-0.698	0.314	0.454	0.721	

5 Conclusion

In this thesis, we have done systematic high-throughput computational screening for multi-functional magnetic materials from bulk to 2D forms, focusing on the properties driven by SOC.

Firstly, we have done HTP screening for spin-gapless semiconductors (SGS) in quaternary Heusler alloys, based on the empirical valence electron number rule. Among about 19,000 possible compounds, we identify 70 newly stable SGS candidates based on formation energy together with mechanical and dynamical stabilities, where 17 cases have a distance to the convex hull less than 0.10 eV/atom. Based on the chemical bonding analysis, we found a new crystal splitting scheme of the $\mathrm{D_{4h}}$-*like picture* to explain the magnetization of SGS Heusler compounds with two magnetic atoms, which is beyond the conventional competing mechanism between the t_{2g} and e_g splitting and exchange interaction. All four types of SGSs can be realized based on the spin characters of the touching bands around Fermi level, where various transport properties are observed. We found type-II SGSs are especially interesting for spintronic applications: a) The spin polarization of the longitudinal conductivity can be manipulated by the chemical potential. b) The anomalous Hall conductivity (AHC) changes its sign across the Fermi level, leading to a significant large anomalous Nernst effect. Additionally, we have also found that spin-orbit coupling will have a remarkably strong effect on the electronic structures of SGSs with heavy elements, where the transport properties can be tuned by the magnetization direction. We conclude that SGSs are promising candidates for future spintronic applications.

Secondly, we have done HTP calculations for the light interstitial (H, B, C and N) effect on the magnetic properties of full Heusler compounds, aiming at designing rare earth free permanent magnets. The light interstitial breaks the cubic symmetry and hence induces a stable tetragonal distortion to the Heusler alloy based on Bain path calculations, leading to a substantial uniaxial magneto-crystalline anisotropy energy (MAE). In total, we found 32 compounds with a sizable out-of plane MAE as well as 10 cases with a sizable in-plane MAE, filling in the application spectral gap between high and low performance permanent magnets. Chemical bonding analysis reveals that the chemical environment around the light interstitial will enhance the MAE further.

Thirdly, we have done a systematic HTP screening for 2D in-plane ordered MXene (i-MXene), providing a new playground for 2D magnets. It has been found the magnetic spin configurations can be manipulated by imposed strain from rectangular to hexagonal lattices. Due to the underlying trigonal crystal fields, the MAE of i-MXene will be significantly enhanced, resulting in five cases with an out-of plane larger than 0.5 meV/f.u. Electronic structure calculations reveal that i-MXenes can host fascinating transport properties, *i.e.* i-MXene $(\mathrm{Sc_{2/3}Cd_{1/3}})_2\mathrm{C}$ and $(\mathrm{Sc_{2/3}Hg_{1/3}})_2\mathrm{C}$ have significantly large Seebeck coefficients with the magnitude of 1000 μV/K, $(\mathrm{Ta_{2/3}Fe_{1/3}})_2\mathrm{C}$ is an anti-ferromagnetic topological insulator based on edge state calculations, and $(\mathrm{Hf_{2/3}Fe_{1/3}})_2\mathrm{C}$ and $(\mathrm{Zr_{2/3}Fe_{1/3}})_2\mathrm{C}$ are both spin gapless semiconductors with enhanced anomalous hall conductivity. Such results demonstrate that i-MXenes can be used in multifunctional applications.

In summary, we have established and applied HTP methods to perform HTP design of magnetic materials. It paves the way for further investigations, particularly magnets as green energy solutions.

References

[1] W. D. Callister and D. G. Rethwisch, Materials science and engineering, vol. 5. John wiley & sons NY, 2011.

[2] J. M. D. Coey, "Magnetism and Magnetic Materials," Mar. 2010.

[3] O. Gutfleisch, M. A. Willard, E. Brück, C. H. Chen, S. G. Sankar, and J. P. Liu, "Magnetic Materials and Devices for the 21st Century: Stronger, Lighter, and More Energy Efficient," Advanced Materials, vol. 23, no. 7, pp. 821–842, 2011.

[4] J. Kübler, Theory of itinerant electron magnetism, vol. 106. Oxford University Press, 2017.

[5] I. Žutić, J. Fabian, and S. D. Sarma, "Spintronics: Fundamentals and applications," Reviews of modern physics, vol. 76, no. 2, p. 323, 2004.

[6] K. S. Novoselov, A. K. Geim, S. V. Morozov, D. Jiang, Y. Zhang, S. V. Dubonos, I. V. Grigorieva, and A. A. Firsov, "Electric field effect in atomically thin carbon films," Science, vol. 306, no. 5696, pp. 666–669, 2004.

[7] H. Eschrig, M. Richter, and I. Opahle, "Chapter 12 - relativistic solid state calculations," in Theoretical and Computational Chemistry (P. Schwerdtfeger, ed.), vol. 14 of Relativistic Electronic Structure Theory, pp. 723–776, Elsevier, Jan. 2004.

[8] N. D. Mermin and H. Wagner, "Absence of ferromagnetism or antiferromagnetism in one- or two-dimensional isotropic heisenberg models," Physical Review Letters, vol. 17, pp. 1133–1136, Nov. 1966.

[9] L. Onsager, "Crystal statistics. i . a two-dimensional model with an order–disorder transition," Physical Review, vol. 65, pp. 117–149, Feb. 1944.

[10] J. M. D. Coey, "Permanent magnets: Plugging the gap," Scripta Materialia, vol. 67, pp. 524–529, Sept. 2012.

[11] E. Callen and H. B. Callen, "Magnetostriction, Forced Magnetostriction, and Anomalous Thermal Expansion in Ferromagnets," Physical Review, vol. 139, pp. A455–A471, July 1965.

[12] M. Richter, "Band structure theory of magnetism in 3d–4f compounds," Journal of Physics D: Applied Physics, vol. 31, pp. 1017–1048, May 1998.

[13] P. Bruno, "Tight-binding approach to the orbital magnetic moment and magnetocrystalline anisotropy of transition-metal monolayers," Physical Review B, vol. 39, pp. 865–868, Jan. 1989.

[14] G. v. d. Laan, "Microscopic origin of magnetocrystalline anisotropy in transition metal thin films," Journal of Physics: Condensed Matter, vol. 10, pp. 3239–3253, Apr. 1998.

[15] A. Ermolenko, "Exchange interactions and magnetocrystalline anisotropy of rare earth–cobalt compounds with $CaCu_5$-type structure," IEEE Transactions on Magnetics, vol. 15, pp. 1765–1770, Nov. 1979.

[16] J. Schweizer and F. Tasset, "Polarised neutron study of the RCo_5 intermetallic compounds. I. The cobalt magnetisation in YCo_5," Journal of Physics F: Metal Physics, vol. 10, no. 12, p. 2799, 1980.

[17] M. Kuz'min and A. Tishin, "Chapter Three Theory of Crystal-Field Effects in 3d-4f Intermetallic Compounds," in Handbook of Magnetic Materials, vol. 17, pp. 149–233, Elsevier, 2007.

[18] K. Haule, C.-H. Yee, and K. Kim, "Dynamical mean-field theory within the full-potential methods: Electronic structure of $CeIrIn_5$, $CeCoIn_5$, and $CeRhIn_5$," Physical Review B, vol. 81, p. 195107, May 2010.

[19] A. Hausoel, M. Karolak, E. Şaşoğlu, A. Lichtenstein, K. Held, A. Katanin, A. Toschi, and G. Sangiovanni, "Local magnetic moments in iron and nickel at ambient and Earth′s core conditions," Nature Communications, vol. 8, pp. 1–9, July 2017.

[20] B. Chakrabarti, M. E. Pezzoli, G. Sordi, K. Haule, and G. Kotliar, "α-β transition in cerium: Magnetic form factor and dynamic magnetic susceptibility in dynamical mean-field theory," Physical Review B, vol. 89, p. 125113, Mar. 2014.

[21] J. Cui, M. Kramer, L. Zhou, F. Liu, A. Gabay, G. Hadjipanayis, B. Balasubramanian, and D. Sellmyer, "Current progress and future challenges in rare-earth-free permanent magnets," Acta Materialia, vol. 158, pp. 118–137, Oct. 2018.

[22] R. Skomski and J. M. D. Coey, "Magnetic anisotropy–How much is enough for a permanent magnet?," Scripta Materialia, vol. 112, pp. 3–8, Feb. 2016.

[23] J. M. D. Coey, "Hard Magnetic Materials: A Perspective," IEEE Transactions on Magnetics, vol. 47, pp. 4671–4681, Dec. 2011.

[24] J. M. D. Coey, "New permanent magnets; manganese compounds," Journal of Physics: Condensed Matter, vol. 26, p. 064211, Jan. 2014.

[25] T. Ohtani, N. Kato, S. Kojima, K. Kojima, Y. Sakamoto, I. Konno, M. Tsukahara, and T. Kubo, "Magnetic properties of Mn-Al-C permanent magnet alloys," IEEE Transactions on Magnetics, vol. 13, pp. 1328–1330, Sept. 1977.

[26] Tu Chen and W. Stutius, "The phase transformation and physical properties of the MnBi and $Mn_{1.08}Bi$ compounds," IEEE Transactions on Magnetics, vol. 10, pp. 581–586, Sept. 1974.

[27] J. B. Yang, W. B. Yelon, W. J. James, Q. Cai, M. Kornecki, S. Roy, N. Ali, and P. l'Heritier, "Crystal structure, magnetic properties and electronic structure of the MnBi intermetallic compound," Journal of Physics: Condensed Matter, vol. 14, pp. 6509–6519, June 2002.

[28] X. Xu, Y.-K. Hong, J. Park, W. Lee, A. M. Lane, and J. Cui, "Magnetic self-assembly for the synthesis of magnetically exchange coupled MnBi/Fe–Co composites," Journal of Solid State Chemistry, vol. 231, pp. 108–113, Nov. 2015.

[29] T. R. Gao, L. Fang, S. Fackler, S. Maruyama, X. H. Zhang, L. L. Wang, T. Rana, P. Manchanda, A. Kashyap, K. Janicka, A. L. Wysocki, A. T. N'Diaye, E. Arenholz, J. A. Borchers, B. J. Kirby, B. B. Maranville, K. W. Sun, M. J. Kramer, V. P. Antropov, D. D. Johnson, R. Skomski, J. Cui, and I. Takeuchi, "Large energy product enhancement in perpendicularly coupled MnBi/CoFe magnetic bilayers," Physical Review B, vol. 94, p. 060411, Aug. 2016.

[30] A. Mubarok, N. Bordeaux, E. Poirier, F. E. Pinkerton, J. Gattacceca, P. Rochette, R. Reisener, L. H. Lewis, and J. I. Goldstein, "Microstructural and Magnetic Characterization of the NWA 6259 Iron Meteorite," Meteoritics and Planetary Science Supplement, vol. 76, p. 5125, Sept. 2013.

[31] M. Gong and S. Ren, "Phase Transformation-Driven Surface Reconstruction of FeNi Nanostructures," Chemistry of Materials, vol. 27, pp. 7795–7800, Nov. 2015.

[32] S. Goto, H. Kura, E. Watanabe, Y. Hayashi, H. Yanagihara, Y. Shimada, M. Mizuguchi, K. Takanashi, and E. Kita, "Synthesis of single-phase $L1_0$ -FeNi magnet powder by nitrogen insertion and topotactic extraction," Scientific Reports, vol. 7, pp. 1–7, Oct. 2017.

[33] T. Burkert, L. Nordström, O. Eriksson, and O. Heinonen, "Giant Magnetic Anisotropy in Tetragonal FeCo Alloys," Physical Review Letters, vol. 93, p. 027203, July 2004.

[34] M. Gong, A. Kirkeminde, M. Wuttig, and S. Ren, "Phase Transformation-Induced Tetragonal FeCo Nanostructures," Nano Letters, vol. 14, pp. 6493–6498, Nov. 2014.

[35] W. Y. Zhang, X. Z. Li, S. Valloppilly, R. Skomski, J. E. Shield, and D. J. Sellmyer, "Magnetism of rapidly quenched rhombohedral $Zr_{2}Co_{11}$-based nanocomposites," Journal of Physics D: Applied Physics, vol. 46, p. 135004, Mar. 2013.

[36] X. Zhao, M. Nguyen, W. Zhang, C. Wang, M. Kramer, D. Sellmyer, X. Li, F. Zhang, L. Ke, V. Antropov, and K. Ho, "Exploring the Structural Complexity of Intermetallic Compounds by an Adaptive Genetic Algorithm," Physical Review Letters, vol. 112, p. 045502, Jan. 2014.

[37] X. Lu, K. Cheng, S. Liu, K. Li, F. Zheng, and Y. Du, "Experimental investigation of phase equilibria in the Co–Hf system," Journal of Alloys and Compounds, vol. 627, pp. 251–260, Apr. 2015.

[38] X. Z. Li, Y. L. Jin, M. Y. Wang, J. E. Shield, R. Skomski, and D. J. Sellmyer, "Electron diffraction study of cobalt-rich Hf-Co," Intermetallics, vol. 75, pp. 54–61, Aug. 2016.

[39] B. Balamurugan, B. Das, W. Y. Zhang, R. Skomski, and D. J. Sellmyer, "Hf–Co and Zr–Co alloys for rare-earth-free permanent magnets," Journal of Physics: Condensed Matter, vol. 26, p. 064204, Jan. 2014.

[40] P. Kumar, A. Kashyap, B. Balamurugan, J. E. Shield, D. J. Sellmyer, and R. Skomski, "Permanent magnetism of intermetallic compounds between light and heavy transition-metal elements," Journal of Physics: Condensed Matter, vol. 26, p. 064209, Jan. 2014.

[41] F. Luo, X. L. Fu, A. Winkelmann, and M. Przybylski, "Tuning the perpendicular magnetic anisotropy in tetragonally distorted Fe_xCo_{1-x} alloy films on Rh (001) by varying the alloy composition," Applied Physics Letters, vol. 91, p. 262512, Dec. 2007.

[42] F. Yildiz, M. Przybylski, X.-D. Ma, and J. Kirschner, "Strong perpendicular anisotropy in $Fe_{1-x}Co_x$ alloy films epitaxially grown on mismatching Pd(001), Ir(001), and Rh(001) substrates," Physical Review B, vol. 80, p. 064415, Aug. 2009.

[43] G. Andersson, T. Burkert, P. Warnicke, M. Björck, B. Sanyal, C. Chacon, C. Zlotea, L. Nordström, P. Nordblad, and O. Eriksson, "Perpendicular Magnetocrystalline Anisotropy in Tetragonally Distorted Fe-Co Alloys," Physical Review Letters, vol. 96, p. 037205, Jan. 2006.

[44] L. Reichel, L. Schultz, D. Pohl, S. Oswald, S. Fähler, M. Werwiński, A. Edström, E. K. Delczeg-Czirjak, and J. Rusz, "From soft to hard magnetic Fe–Co–B by spontaneous strain: a combined first principles and thin film study," Journal of Physics: Condensed Matter, vol. 27, p. 476002, Nov. 2015.

[45] L. Reichel, L. Schultz, and S. Fähler, "Lattice relaxation studies in strained epitaxial Fe-Co-C films," Journal of Applied Physics, vol. 117, p. 17C712, Feb. 2015.

[46] N. V. Nong, L. T. Tai, N. T. Huy, N. T. Trung, C. R. H. Bahl, R. Venkatesh, F. W. Poulsen, and N. Pryds, "Structural, magnetic and magnetocaloric properties of Heusler alloys $Ni_{50}Mn_{38}Sb_{12}$ with boron addition," Materials Science and Engineering: B, vol. 176, pp. 1322–1325, Sept. 2011.

[47] I. Dubenko, T. Samanta, A. Quetz, A. Kazakov, I. Rodionov, D. Mettus, V. Prudnikov, S. Stadler, P. Adams, J. Prestigiacomo, A. Granovsky, A. Zhukov, and N. Ali, "The comparison of direct and indirect methods for determining the magnetocaloric parameters in the Heusler alloy $Ni_{50}Mn_{34.8}In_{14.2}B$," Applied Physics Letters, vol. 100, p. 192402, May 2012.

[48] H. C. Xuan, D. H. Wang, C. L. Zhang, Z. D. Han, B. X. Gu, and Y. W. Du, "Boron's effect on martensitic transformation and magnetocaloric effect in ni43mn46sn11bx alloys," Applied Physics Letters, vol. 92, p. 102503, Mar. 2008.

[49] Y. Zhang, J. Liu, Q. Zheng, J. Zhang, W. Xia, J. Du, and A. Yan, "Large magnetic entropy change and enhanced mechanical properties of Ni–Mn–Sn–C alloys," Scripta Materialia, vol. 75, pp. 26–29, Mar. 2014.

[50] Q. Gao, I. Opahle, O. Gutfleisch, and H. Zhang, "Designing rare-earth free permanent magnets in heusler alloys via interstitial doping," Acta Materialia, vol. 186, pp. 355–362, Mar. 2020.

[51] P. Grünberg, R. Schreiber, Y. Pang, M. B. Brodsky, and H. Sowers, "Layered Magnetic Structures: Evidence for Antiferromagnetic Coupling of Fe Layers across Cr Interlayers," Physical Review Letters, vol. 57, pp. 2442–2445, Nov. 1986.

[52] M. N. Baibich, J. M. Broto, A. Fert, F. N. Van Dau, F. Petroff, P. Etienne, G. Creuzet, A. Friederich, and J. Chazelas, "Giant Magnetoresistance of (001)Fe/(001)Cr Magnetic Superlattices," Physical Review Letters, vol. 61, pp. 2472–2475, Nov. 1988.

[53] G. Binasch, P. Grünberg, F. Saurenbach, and W. Zinn, "Enhanced magnetoresistance in layered magnetic structures with antiferromagnetic interlayer exchange," Physical Review B, vol. 39, pp. 4828–4830, Mar. 1989.

[54] P. M. Levy, S. Zhang, and A. Fert, "Electrical conductivity of magnetic multilayered structures," Physical Review Letters, vol. 65, pp. 1643–1646, Sept. 1990.

[55] R. E. Camley and J. Barnaś, "Theory of giant magnetoresistance effects in magnetic layered structures with antiferromagnetic coupling," Physical Review Letters, vol. 63, pp. 664–667, Aug. 1989.

[56] S. S. P. Parkin, N. More, and K. P. Roche, "Oscillations in exchange coupling and magnetoresistance in metallic superlattice structures: Co/Ru, Co/Cr, and Fe/Cr," Physical Review Letters, vol. 64, pp. 2304–2307, May 1990.

[57] C. Dupas, P. Beauvillain, C. Chappert, J. P. Renard, F. Trigui, P. Veillet, E. Vélu, and D. Renard, "Very large magnetoresistance effects induced by antiparallel magnetization in two ultrathin cobalt films," Journal of Applied Physics, vol. 67, pp. 5680–5682, May 1990.

[58] S. Ikeda, J. Hayakawa, Y. Ashizawa, Y. M. Lee, K. Miura, H. Hasegawa, M. Tsunoda, F. Matsukura, and H. Ohno, "Tunnel magnetoresistance of 604% at 300k by suppression of Ta diffusion in CoFeB/MgO/CoFeB pseudo-spin-valves annealed at high temperature," Applied Physics Letters, vol. 93, p. 082508, Aug. 2008.

[59] J. C. Slonczewski, "Current-driven excitation of magnetic multilayers," Journal of Magnetism and Magnetic Materials, vol. 159, pp. L1–L7, June 1996.

[60] L. Berger, "Emission of spin waves by a magnetic multilayer traversed by a current," Physical Review B, vol. 54, pp. 9353–9358, Oct. 1996.

[61] A. Dussaux, B. Georges, J. Grollier, V. Cros, A. Khvalkovskiy, A. Fukushima, M. Konoto, H. Kubota, K. Yakushiji, S. Yuasa, et al., “Large microwave generation from current-driven magnetic vortex oscillators in magnetic tunnel junctions,” Nature communications, vol. 1, no. 1, pp. 1–6, 2010.

[62] J. Grollier, P. Boulenc, V. Cros, A. Hamzić, A. Vaurès, A. Fert, and G. Faini, “Switching a spin valve back and forth by current-induced domain wall motion,” Applied Physics Letters, vol. 83, pp. 509–511, July 2003.

[63] M. Hosomi, H. Yamagishi, T. Yamamoto, K. Bessho, Y. Higo, K. Yamane, H. Yamada, M. Shoji, H. Hachino, C. Fukumoto, et al., “A novel nonvolatile memory with spin torque transfer magnetization switching: Spin-ram,” in IEEE InternationalElectron Devices Meeting, 2005. IEDM Technical Digest., pp. 459–462, IEEE, 2005.

[64] A. Fert and F. N. Van Dau, “Spintronics, from giant magnetoresistance to magnetic skyrmions and topological insulators,” Comptes Rendus Physique, vol. 20, pp. 817–831, Nov. 2019.

[65] E. Sagasta, Y. Omori, S. Vélez, R. Llopis, C. Tollan, A. Chuvilin, L. E. Hueso, M. Gradhand, Y. Otani, and F. Casanova, “Unveiling the mechanisms of the spin Hall effect in Ta,” Physical Review B, vol. 98, p. 060410, Aug. 2018.

[66] X. Tao, Q. Liu, B. Miao, R. Yu, Z. Feng, L. Sun, B. You, J. Du, K. Chen, S. Zhang, L. Zhang, Z. Yuan, D. Wu, and H. Ding, “Self-consistent determination of spin Hall angle and spin diffusion length in Pt and Pd: The role of the interface spin loss,” Science Advances, vol. 4, p. eaat1670, June 2018.

[67] W. Zhang, M. B. Jungfleisch, W. Jiang, J. E. Pearson, A. Hoffmann, F. Freimuth, and Y. Mokrousov, “Spin Hall Effects in Metallic Antiferromagnets,” Physical Review Letters, vol. 113, p. 196602, Nov. 2014.

[68] M. Gamino, E. F. Silva, O. Alves Santos, J. B. S. Mendes, R. L. Rodríguez-Suárez, F. L. A. Machado, A. Azevedo, and S. M. Rezende, “The role of metallic nanoparticles in the enhancement of the spin Hall magnetoresistance in YIG/Pt thin films,” Journal of Magnetism and Magnetic Materials, vol. 466, pp. 267–272, Nov. 2018.

[69] Y. Sun, Y. Zhang, C. Felser, and B. Yan, “Strong Intrinsic Spin Hall Effect in the TaAs Family of Weyl Semimetals,” Physical Review Letters, vol. 117, p. 146403, Sept. 2016.

[70] H. Zhang, C.-X. Liu, X.-L. Qi, X. Dai, Z. Fang, and S.-C. Zhang, “Topological insulators in Bi_2Se_3, Bi_2Te_3 and Sb_2Te_3 with a single Dirac cone on the surface,” Nature Physics, vol. 5, pp. 438–442, June 2009.

[71] Y. K. Kato, R. C. Myers, A. C. Gossard, and D. D. Awschalom, “Observation of the Spin Hall Effect in Semiconductors,” Science, vol. 306, pp. 1910–1913, Dec. 2004.

[72] C. Heyn, M. Klingbeil, C. Strelow, A. Stemmann, S. Mendach, and W. Hansen, “Single-dot Spectroscopy of GaAs Quantum Dots Fabricated by Filling of Self-assembled Nanoholes,” Nanoscale Research Letters, vol. 5, pp. 1633–1636, Oct. 2010.

[73] D. C. Ralph and R. A. Buhrman, “Kondo-assisted and resonant tunneling via a single charge trap: A realization of the Anderson model out of equilibrium,” Physical Review Letters, vol. 72, pp. 3401–3404, May 1994.

[74] L. Landau and E. Lifshitz, “3 - on the theory of the dispersion of magnetic permeability in ferromagnetic bodiesreprinted from physikalische zeitschrift der sowjetunion 8, part 2, 153, 1935.,” in Perspectives in Theoretical Physics (L. P. Pitaevski, ed.), pp. 51–65, Amsterdam: Pergamon, Jan. 1992.

[75] A. Manchon, J. Železný, I. Miron, T. Jungwirth, J. Sinova, A. Thiaville, K. Garello, and P. Gambardella, “Current-induced spin-orbit torques in ferromagnetic and antiferromagnetic systems,” Reviews of Modern Physics, vol. 91, p. 035004, Sept. 2019.

[76] V. M. Edelstein, “Spin polarization of conduction electrons induced by electric current in two-dimensional asymmetric electron systems,” Solid State Communications, vol. 73, pp. 233–235, Jan. 1990.

[77] K. Garello, I. M. Miron, C. O. Avci, F. Freimuth, Y. Mokrousov, S. Blügel, S. Auffret, O. Boulle, G. Gaudin, and P. Gambardella, “Symmetry and magnitude of spin–orbit torques in ferromagnetic heterostructures,” Nature Nanotechnology, vol. 8, pp. 587–593, Aug. 2013.

[78] L. Liu, C.-F. Pai, Y. Li, H. W. Tseng, D. C. Ralph, and R. A. Buhrman, “Spin-Torque Switching with the Giant Spin Hall Effect of Tantalum,” Science, vol. 336, pp. 555–558, May 2012.

[79] L. Liu, O. J. Lee, T. J. Gudmundsen, D. C. Ralph, and R. A. Buhrman, “Current-Induced Switching of Perpendicularly Magnetized Magnetic Layers Using Spin Torque from the Spin Hall Effect,” Physical Review Letters, vol. 109, p. 096602, Aug. 2012.

[80] S. Karube, K. Kondou, and Y. Otani, "Experimental observation of spin-to-charge current conversion at non-magnetic metal/Bi_2O_3 interfaces," Applied Physics Express, vol. 9, p. 033001, Jan. 2016.

[81] E. Lesne, Y. Fu, S. Oyarzun, J. C. Rojas-Sánchez, D. C. Vaz, H. Naganuma, G. Sicoli, J.-P. Attané, M. Jamet, E. Jacquet, J.-M. George, A. Barthélémy, H. Jaffrès, A. Fert, M. Bibes, and L. Vila, "Highly efficient and tunable spin-to-charge conversion through Rashba coupling at oxide interfaces," Nature Materials, vol. 15, pp. 1261–1266, Dec. 2016.

[82] J. C. R. Sánchez, L. Vila, G. Desfonds, S. Gambarelli, J. P. Attané, J. M. D. Teresa, C. Magén, and A. Fert, "Spin-to-charge conversion using Rashba coupling at the interface between non-magnetic materials," Nature Communications, vol. 4, pp. 1–7, Dec. 2013.

[83] K. Ando, S. Takahashi, J. Ieda, H. Kurebayashi, T. Trypiniotis, C. H. W. Barnes, S. Maekawa, and E. Saitoh, "Electrically tunable spin injector free from the impedance mismatch problem," Nature Materials, vol. 10, pp. 655–659, Sept. 2011.

[84] O. Mosendz, J. E. Pearson, F. Y. Fradin, G. E. W. Bauer, S. D. Bader, and A. Hoffmann, "Quantifying Spin Hall Angles from Spin Pumping: Experiments and Theory," Physical Review Letters, vol. 104, p. 046601, Jan. 2010.

[85] A. Brataas, G. Zaránd, Y. Tserkovnyak, and G. E. W. Bauer, "Magnetoelectronic Spin Echo," Physical Review Letters, vol. 91, p. 166601, Oct. 2003.

[86] D. Wei, M. Obstbaum, M. Ribow, C. H. Back, and G. Woltersdorf, "Spin Hall voltages from a.c. and d.c. spin currents," Nature Communications, vol. 5, pp. 1–6, Apr. 2014.

[87] J. Železný, H. Gao, K. Výborný, J. Zemen, J. Mašek, A. Manchon, J. Wunderlich, J. Sinova, and T. Jungwirth, "Relativistic Néel-Order Fields Induced by Electrical Current in Antiferromagnets," Physical Review Letters, vol. 113, p. 157201, Oct. 2014.

[88] V. Baltz, A. Manchon, M. Tsoi, T. Moriyama, T. Ono, and Y. Tserkovnyak, "Antiferromagnetic spintronics," Reviews of Modern Physics, vol. 90, p. 015005, Feb. 2018.

[89] V. Tshitoyan, C. Ciccarelli, A. P. Mihai, M. Ali, A. C. Irvine, T. A. Moore, T. Jungwirth, and A. J. Ferguson, "Electrical manipulation of ferromagnetic NiFe by antiferromagnetic IrMn," Physical Review B, vol. 92, p. 214406, Dec. 2015.

[90] Y. Ou, S. Shi, D. C. Ralph, and R. A. Buhrman, "Strong spin Hall effect in the antiferromagnet PtMn," Physical Review B, vol. 93, p. 220405, June 2016.

[91] Y.-W. Oh, S.-h. C. Baek, Y. Kim, H. Y. Lee, K.-D. Lee, C.-G. Yang, E.-S. Park, K.-S. Lee, K.-W. Kim, G. Go, et al., "Field-free switching of perpendicular magnetization through spin–orbit torque in antiferromagnet/ferromagnet/oxide structures," Nature nanotechnology, vol. 11, no. 10, pp. 878–884, 2016.

[92] L. Frangou, S. Oyarzun, S. Auffret, L. Vila, S. Gambarelli, and V. Baltz, "Enhanced spin pumping efficiency in antiferromagnetic irmn thin films around the magnetic phase transition," Physical review letters, vol. 116, no. 7, p. 077203, 2016.

[93] S. Fukami, C. Zhang, S. DuttaGupta, A. Kurenkov, and H. Ohno, "Magnetization switching by spin–orbit torque in an antiferromagnet–ferromagnet bilayer system," Nature materials, vol. 15, no. 5, pp. 535–541, 2016.

[94] W. Zhang, W. Han, S.-H. Yang, Y. Sun, Y. Zhang, B. Yan, and S. S. Parkin, "Giant facet-dependent spin-orbit torque and spin hall conductivity in the triangular antiferromagnet irmn3," Science Advances, vol. 2, no. 9, p. e1600759, 2016.

[95] T. Moriya, "Anisotropic superexchange interaction and weak ferromagnetism," Physical Review, vol. 120, pp. 91–98, Oct. 1960.

[96] I. Dzyaloshinsky, "A thermodynamic theory of "weak" ferromagnetism of antiferromagnetics," Journal of Physics and Chemistry of Solids, vol. 4, pp. 241–255, Jan. 1958.

[97] G. Finocchio, F. Büttner, R. Tomasello, M. Carpentieri, and M. Kläui, "Magnetic skyrmions: from fundamental to applications," Journal of Physics D: Applied Physics, vol. 49, p. 423001, Sept. 2016.

[98] A. Fert, N. Reyren, and V. Cros, "Magnetic skyrmions: advances in physics and potential applications," Nature Reviews Materials, vol. 2, pp. 1–15, June 2017.

[99] I. Žutić, J. Fabian, and S. Das Sarma, "Spintronics: Fundamentals and applications," Reviews of Modern Physics, vol. 76, pp. 323–410, Apr. 2004.

[100] T. Dietl and H. Ohno, “Dilute ferromagnetic semiconductors: Physics and spintronic structures,” Reviews of Modern Physics, vol. 86, pp. 187–251, Mar. 2014.

[101] X. L. Wang, “Proposal for a New Class of Materials: Spin Gapless Semiconductors,” Physical Review Letters, vol. 100, p. 156404, Apr. 2008.

[102] S. Ouardi, G. H. Fecher, C. Felser, and J. Kübler, “Realization of Spin Gapless Semiconductors: The Heusler Compound Mn_2CoAl,” Physical Review Letters, vol. 110, p. 100401, Mar. 2013.

[103] Q. Gao, H.-H. Xie, L. Li, G. Lei, J.-B. Deng, and X.-R. Hu, “First-principle study on some new spin-gapless semiconductors: The Zr-based quaternary Heusler alloys,” Superlattices and Microstructures, vol. 85, pp. 536–542, Sept. 2015.

[104] X. Wang, Z. Cheng, J. Wang, X.-L. Wang, and G. Liu, “Recent advances in the Heusler based spin-gapless semiconductors,” Journal of Materials Chemistry C, vol. 4, no. 30, pp. 7176–7192, 2016.

[105] K. Özdoğan, E. Şaşıoğlu, and I. Galanakis, “Slater-Pauling behavior in LiMgPdSn-type multifunctional quaternary Heusler materials: Half-metallicity, spin-gapless and magnetic semiconductors,” Journal of Applied Physics, vol. 113, p. 193903, May 2013.

[106] Q. Gao, I. Opahle, and H. Zhang, “High-throughput screening for spin-gapless semiconductors in quaternary Heusler compounds,” Physical Review Materials, vol. 3, p. 024410, Feb. 2019.

[107] H. H. Kim, B. Yang, S. Li, S. Jiang, C. Jin, Z. Tao, G. Nichols, F. Sfigakis, S. Zhong, C. Li, S. Tian, D. G. Cory, G.-X. Miao, J. Shan, K. F. Mak, H. Lei, K. Sun, L. Zhao, and A. W. Tsen, “Evolution of interlayer and intralayer magnetism in three atomically thin chromium trihalides,” Proceedings of the National Academy of Sciences, vol. 116, pp. 11131–11136, June 2019.

[108] C. Gong, L. Li, Z. Li, H. Ji, A. Stern, Y. Xia, T. Cao, W. Bao, C. Wang, Y. Wang, Z. Q. Qiu, R. J. Cava, S. G. Louie, J. Xia, and X. Zhang, “Discovery of intrinsic ferromagnetism in two-dimensional van der Waals crystals,” Nature, vol. 546, pp. 265–269, June 2017.

[109] O. Besbes, S. Nikolaev, N. Meskini, and I. Solovyev, “Microscopic origin of ferromagnetism in the trihalides $CrCl_3$ and CrI_3,” Physical Review B, vol. 99, p. 104432, Mar. 2019.

[110] A. R. Wildes, K. C. Rule, R. I. Bewley, M. Enderle, and T. J. Hicks, “The magnon dynamics and spin exchange parameters of FePS3,” Journal of Physics: Condensed Matter, vol. 24, p. 416004, Sept. 2012.

[111] K. Kim, S. Y. Lim, J.-U. Lee, S. Lee, T. Y. Kim, K. Park, G. S. Jeon, C.-H. Park, J.-G. Park, and H. Cheong, “Suppression of magnetic ordering in XXZ-type antiferromagnetic monolayer $NiPS_3$,” Nature Communications, vol. 10, pp. 1–9, Jan. 2019.

[112] A. K. Geim, “Graphene: Status and Prospects,” Science, vol. 324, pp. 1530–1534, June 2009.

[113] K. S. Novoselov, A. K. Geim, S. V. Morozov, D. Jiang, M. I. Katsnelson, I. V. Grigorieva, S. V. Dubonos, and A. A. Firsov, “Two-dimensional gas of massless Dirac fermions in graphene,” Nature, vol. 438, pp. 197–200, Nov. 2005.

[114] K. S. Novoselov, D. Jiang, F. Schedin, T. J. Booth, V. V. Khotkevich, S. V. Morozov, and A. K. Geim, “Two-dimensional atomic crystals,” Proceedings of the National Academy of Sciences, vol. 102, pp. 10451–10453, July 2005.

[115] “The Nobel Prize in Physics 2010.”

[116] C. Gong, E. M. Kim, Y. Wang, G. Lee, and X. Zhang, “Multiferroicity in atomic van der Waals heterostructures,” Nature Communications, vol. 10, pp. 1–6, June 2019.

[117] Y. Liu, Y. Huang, and X. Duan, “Van der Waals integration before and beyond two-dimensional materials,” Nature, vol. 567, pp. 323–333, Mar. 2019.

[118] C. Gong and X. Zhang, “Two-dimensional magnetic crystals and emergent heterostructure devices,” Science, vol. 363, Feb. 2019.

[119] B. Huang, G. Clark, E. Navarro-Moratalla, D. R. Klein, R. Cheng, K. L. Seyler, D. Zhong, E. Schmidgall, M. A. McGuire, D. H. Cobden, W. Yao, D. Xiao, P. Jarillo-Herrero, and X. Xu, “Layer-dependent ferromagnetism in a van der Waals crystal down to the monolayer limit,” Nature, vol. 546, pp. 270–273, June 2017.

[120] J. Yi, H. Zhuang, Q. Zou, Z. Wu, G. Cao, S. Tang, S. A. Calder, P. R. C. o. Kent, D. Mandrus, and Z. O. Gai, "Competing antiferromagnetism in a quasi-2d itinerant ferromagnet: Fe_3GeTe_2," 2D Materials, vol. 4, Nov. 2016.

[121] H. L. Zhuang, P. R. C. Kent, and R. G. Hennig, "Strong anisotropy and magnetostriction in the two-dimensional Stoner ferromagnet Fe_3GeTe_2," Physical Review B, vol. 93, p. 134407, Apr. 2016.

[122] W. Ding, J. Zhu, Z. Wang, Y. Gao, D. Xiao, Y. Gu, Z. Zhang, and W. Zhu, "Prediction of intrinsic two-dimensional ferroelectrics in In_2Se_3 and other III_2 -VI_3 van der Waals materials," Nature Communications, vol. 8, pp. 1–8, Apr. 2017.

[123] M. D. Girardeau and M. Popovic-Boziv, "Magnetic ordering in a generalized Heisenberg model with biquadratic exchange. I. Hamiltonian and two-spin eigenstates," Journal of Physics C: Solid State Physics, vol. 10, pp. 2471–2478, July 1977.

[124] P. A. Joy and S. Vasudevan, "Magnetism in the layered transition-metal thiophosphates MPS_3 (M=Mn, Fe, and Ni)," Physical Review B, vol. 46, pp. 5425–5433, Sept. 1992.

[125] J.-G. Park, "Opportunities and challenges of 2d magnetic van der Waals materials: magnetic graphene?," Journal of Physics: Condensed Matter, vol. 28, p. 301001, June 2016.

[126] J. M. Kosterlitz and D. J. Thouless, "Ordering, metastability and phase transitions in two-dimensional systems," Journal of Physics C: Solid State Physics, vol. 6, pp. 1181–1203, Apr. 1973.

[127] Y. Liu and C. Petrovic, "Three-dimensional magnetic critical behavior in CrI_3," Physical Review B, vol. 97, p. 014420, Jan. 2018.

[128] B. Huang, G. Clark, D. R. Klein, D. MacNeill, E. Navarro-Moratalla, K. L. Seyler, N. Wilson, M. A. McGuire, D. H. Cobden, D. Xiao, W. Yao, P. Jarillo-Herrero, and X. Xu, "Electrical control of 2D magnetism in bilayer CrI_3," Nature Nanotechnology, vol. 13, pp. 544–548, July 2018.

[129] P. Jiang, C. Wang, D. Chen, Z. Zhong, Z. Yuan, Z.-Y. Lu, and W. Ji, "Stacking tunable interlayer magnetism in bilayer CrI_3," Physical Review B, vol. 99, p. 144401, Apr. 2019.

[130] N. Sivadas, S. Okamoto, X. Xu, C. J. Fennie, and D. Xiao, "Stacking-Dependent Magnetism in Bilayer CrI_3," Nano Letters, vol. 18, pp. 7658–7664, Dec. 2018.

[131] S. Jiang, J. Shan, and K. F. Mak, "Electric-field switching of two-dimensional van der Waals magnets," Nature Materials, vol. 17, pp. 406–410, May 2018.

[132] S. Jiang, L. Li, Z. Wang, K. F. Mak, and J. Shan, "Controlling magnetism in 2D CrI_3 by electrostatic doping," Nature Nanotechnology, vol. 13, pp. 549–553, July 2018.

[133] Y. Deng, Y. Yu, Y. Song, J. Zhang, N. Z. Wang, Z. Sun, Y. Yi, Y. Z. Wu, S. Wu, J. Zhu, J. Wang, X. H. Chen, and Y. Zhang, "Gate-tunable room-temperature ferromagnetism in two-dimensional Fe_3GeTe_2," Nature, vol. 563, pp. 94–99, Nov. 2018.

[134] B. L. Chittari, Y. Park, D. Lee, M. Han, A. H. MacDonald, E. Hwang, and J. Jung, "Electronic and magnetic properties of single-layer MPX_3 metal phosphorous trichalcogenides," Physical Review B, vol. 94, p. 184428, Nov. 2016.

[135] Y. Wang, J. Ying, Z. Zhou, J. Sun, T. Wen, Y. Zhou, N. Li, Q. Zhang, F. Han, Y. Xiao, P. Chow, W. Yang, V. V. Struzhkin, Y. Zhao, and H.-k. Mao, "Emergent superconductivity in an iron-based honeycomb lattice initiated by pressure-driven spin-crossover," Nature Communications, vol. 9, pp. 1–7, May 2018.

[136] Z. Wu, J. Yu, and S. Yuan, "Strain-tunable magnetic and electronic properties of monolayer CrI_3," Physical Chemistry Chemical Physics, vol. 21, pp. 7750–7755, Apr. 2019.

[137] S. Pak, J. Lee, Y.-W. Lee, A.-R. Jang, S. Ahn, K. Y. Ma, Y. Cho, J. Hong, S. Lee, H. Y. Jeong, H. Im, H. S. Shin, S. M. Morris, S. Cha, J. I. Sohn, and J. M. Kim, "Strain-Mediated Interlayer Coupling Effects on the Excitonic Behaviors in an Epitaxially Grown MoS_2/WS_2 van der Waals Heterobilayer," Nano Letters, vol. 17, pp. 5634–5640, Sept. 2017.

[138] W. Sun, W. Wang, D. Chen, Z. Cheng, and Y. Wang, "Valence mediated tunable magnetism and electronic properties by ferroelectric polarization switching in 2D FeI_2/In_2Se_3 van der Waals heterostructures," Nanoscale, vol. 11, no. 20, pp. 9931–9936, 2019.

[139] M. Naguib, M. Kurtoglu, V. Presser, J. Lu, J. Niu, M. Heon, L. Hultman, Y. Gogotsi, and M. W. Barsoum, "Two-Dimensional Nanocrystals Produced by Exfoliation of Ti_3AlC_2," Advanced Materials, vol. 23, no. 37, pp. 4248–4253, 2011.

[140] M. Khazaei, A. Ranjbar, K. Esfarjani, D. Bogdanovski, R. Dronskowski, and S. Yunoki, "Insights into exfoliation possibility of MAX phases to MXenes," Physical Chemistry Chemical Physics, vol. 20, no. 13, pp. 8579–8592, 2018.

[141] G. Gao, G. Ding, J. Li, K. Yao, M. Wu, and M. Qian, "Monolayer MXenes: promising half-metals and spin gapless semiconductors," Nanoscale, vol. 8, no. 16, pp. 8986–8994, 2016.

[142] H. Kumar, N. C. Frey, L. Dong, B. Anasori, Y. Gogotsi, and V. B. Shenoy, "Tunable Magnetism and Transport Properties in Nitride MXenes," ACS Nano, vol. 11, pp. 7648–7655, Aug. 2017.

[143] D. Ohmer, G. Qiang, I. Opahle, H. K. Singh, and H. Zhang, "High-throughput design of 211–M_2AX compounds," Physical Review Materials, vol. 3, p. 053803, May 2019.

[144] D. Ohmer, I. Opahle, H. K. Singh, and H. Zhang, "Stability predictions of magnetic M_2AX compounds," Journal of Physics: Condensed Matter, vol. 31, p. 405902, July 2019.

[145] Q. Tao, J. Lu, M. Dahlqvist, A. Mockute, S. Calder, A. Petruhins, R. Meshkian, O. Rivin, D. Potashnikov, E. N. Caspi, H. Shaked, A. Hoser, C. Opagiste, R.-M. Galera, R. Salikhov, U. Wiedwald, C. Ritter, A. R. Wildes, B. Johansson, L. Hultman, M. Farle, M. W. Barsoum, and J. Rosen, "Atomically layered and ordered rare-earth i-MAX phases: A new class of magnetic quaternary compounds," Chemistry of Materials, vol. 31, pp. 2476–2485, Apr. 2019.

[146] M. Dahlqvist, J. Lu, R. Meshkian, Q. Tao, L. Hultman, and J. Rosen, "Prediction and synthesis of a family of atomic laminate phases with Kagomé-like and in-plane chemical ordering," Science Advances, vol. 3, p. e1700642, July 2017.

[147] Q. Gao and H. Zhang, "Magnetic i-MXene: a new class of multifunctional two-dimensional materials," Nanoscale, 2020.

[148] P. Hohenberg and W. Kohn, "Inhomogeneous Electron Gas," Physical Review, vol. 136, pp. B864–B871, Nov. 1964.

[149] W. Kohn and L. J. Sham, "Self-Consistent Equations Including Exchange and Correlation Effects," Physical Review, vol. 140, pp. A1133–A1138, Nov. 1965.

[150] "The Nobel Prize in Chemistry 1998."

[151] R. Jones, "Density functional theory: Its origins, rise to prominence, and future," Reviews of Modern Physics, vol. 87, pp. 897–923, Aug. 2015.

[152] M. Born and R. Oppenheimer, "Zur Quantentheorie der Molekeln," Annalen der Physik, vol. 389, no. 20, pp. 457–484, 1927.

[153] L. H. Thomas, "The calculation of atomic fields," Mathematical Proceedings of the Cambridge Philosophical Society, vol. 23, pp. 542–548, Jan. 1927.

[154] D. R. Hartree, "The Wave Mechanics of an Atom with a Non-Coulomb Central Field. Part II. Some Results and Discussion," Mathematical Proceedings of the Cambridge Philosophical Society, vol. 24, pp. 111–132, Jan. 1928.

[155] J. C. Slater, "The Self Consistent Field and the Structure of Atoms," Physical Review, vol. 32, pp. 339–348, Sept. 1928.

[156] J. P. Perdew and Y. Wang, "Accurate and simple analytic representation of the electron-gas correlation energy," Physical Review B, vol. 45, pp. 13244–13249, June 1992.

[157] G. B. Bachelet, D. M. Ceperley, and M. G. B. Chiocchetti, "Novel pseudo-Hamiltonian for quantum Monte Carlo simulations," Physical Review Letters, vol. 62, pp. 2088–2091, May 1989.

[158] S. H. Vosko, L. Wilk, and M. Nusair, "Accurate spin-dependent electron liquid correlation energies for local spin density calculations: a critical analysis," Canadian Journal of Physics, vol. 58, pp. 1200–1211, Aug. 1980.

[159] L. A. Cole and J. P. Perdew, "Calculated electron affinities of the elements," Physical Review A, vol. 25, pp. 1265–1271, Mar. 1982.

[160] J. P. Perdew and A. Zunger, "Self-interaction correction to density-functional approximations for many-electron systems," Physical Review B, vol. 23, pp. 5048–5079, May 1981.

[161] M. Slamet and V. Sahni, "The gradient expansion approximation for exchange: A physical prespective," International Journal of Quantum Chemistry, vol. 44, no. S26, pp. 333–345, 1992.

[162] J. P. Perdew, K. Burke, and M. Ernzerhof, “Generalized Gradient Approximation Made Simple,” Physical Review Letters, vol. 77, pp. 3865–3868, Oct. 1996.

[163] A. D. Becke, “Density-functional exchange-energy approximation with correct asymptotic behavior,” Physical Review A, vol. 38, pp. 3098–3100, Sept. 1988.

[164] P. A. M. Dirac and R. H. Fowler, “The quantum theory of the electron,” Proceedings of the Royal Society of London. Series A, Containing Papers of a Mathematical and Physical Character, vol. 117, pp. 610–624, Feb. 1928.

[165] F. J. Dyson and D. Derbes, Advanced quantum mechanics. World Scientific, 2011.

[166] J. Kübler, Theory of itinerant electron magnetism, vol. 106. Oxford University Press, 2017.

[167] G. Dresselhaus, “Spin-Orbit Coupling Effects in Zinc Blende Structures,” Physical Review, vol. 100, pp. 580–586, Oct. 1955.

[168] E. Rashba, “Symmetry of Energy Bands in Crystals of Wurtzite Type .1. Symmetry of Bands Disregarding Spin-Orbit Interaction,” Soviet Physics-Solid State, vol. 1, no. 3, pp. 368–380, 1959. WOS:A1959WT32000010.

[169] I. Opahle, A. Parma, E. J. McEniry, R. Drautz, and G. K. H. Madsen, “High-throughput study of the structural stability and thermoelectric properties of transition metal silicides,” New Journal of Physics, vol. 15, p. 105010, Oct. 2013.

[170] I. Opahle, G. K. H. Madsen, and R. Drautz, “High throughput density functional investigations of the stability, electronic structure and thermoelectric properties of binary silicides,” Physical Chemistry Chemical Physics, vol. 14, no. 47, pp. 16197–16202, 2012.

[171] G. Kresse and J. Furthmüller, “Efficient iterative schemes for ab initio total-energy calculations using a plane-wave basis set,” Physical Review B, vol. 54, pp. 11169–11186, Oct. 1996.

[172] G. Kresse and D. Joubert, “From ultrasoft pseudopotentials to the projector augmented-wave method,” Physical Review B, vol. 59, pp. 1758–1775, Jan. 1999.

[173] J. P. Perdew, P. Ziesche, and H. Eschrig, Electronic structure of solids’ 91. Akademie Verlag, Berlin, 1991.

[174] K. Koepernik and H. Eschrig, “Full-potential nonorthogonal local-orbital minimum-basis band-structure scheme,” Physical Review B, vol. 59, pp. 1743–1757, Jan. 1999.

[175] I. Opahle, K. Koepernik, and H. Eschrig, “Full-potential band-structure calculation of iron pyrite,” Physical Review B, vol. 60, pp. 14035–14041, Nov. 1999.

[176] X. Wang, D.-s. Wang, R. Wu, and A. J. Freeman, “Validity of the force theorem for magnetocrystalline anisotropy,” Journal of Magnetism and Magnetic Materials, vol. 159, pp. 337–341, July 1996.

[177] P. Blaha, K. Schwarz, G. K. Madsen, D. Kvasnicka, and J. Luitz, “Wien2k,” An augmented plane wave+ local orbitals program for calculating crystal properties, 2001.

[178] G. K. H. Madsen and D. J. Singh, “BoltzTraP. A code for calculating band-structure dependent quantities,” Computer Physics Communications, vol. 175, pp. 67–71, July 2006.

[179] “Materials Genome Initiative | WWW.MGI.GOV.” `https://www.mgi.gov/`.

[180] A. Jain, G. Hautier, C. J. Moore, S. Ping Ong, C. C. Fischer, T. Mueller, K. A. Persson, and G. Ceder, “A high-throughput infrastructure for density functional theory calculations,” Computational Materials Science, vol. 50, pp. 2295–2310, June 2011.

[181] S. Curtarolo, W. Setyawan, G. L. W. Hart, M. Jahnatek, R. V. Chepulskii, R. H. Taylor, S. Wang, J. Xue, K. Yang, O. Levy, M. J. Mehl, H. T. Stokes, D. O. Demchenko, and D. Morgan, “AFLOW: An automatic framework for high-throughput materials discovery,” Computational Materials Science, vol. 58, pp. 218–226, June 2012.

[182] J. E. Saal, S. Kirklin, M. Aykol, B. Meredig, and C. Wolverton, “Materials design and discovery with high–throughput density functional theory: The open quantum materials database (oqmd),” JOM, vol. 65, pp. 1501–1509, Nov. 2013.

[183] G. Pizzi, A. Cepellotti, R. Sabatini, N. Marzari, and B. Kozinsky, “Aiida: automated interactive infrastructure and database for computational science,” Computational Materials Science, vol. 111, pp. 218–230, Jan. 2016.

[184] S. Haastrup, M. Strange, M. Pandey, T. Deilmann, P. S. Schmidt, N. F. Hinsche, M. N. Gjerding, D. Torelli, P. M. Larsen, A. C. Riis-Jensen, J. Gath, K. W. Jacobsen, J. J. Mortensen, T. Olsen, and K. S. Thygesen, "The computational 2d materials database: high-throughput modeling and discovery of atomically thin crystals," 2D Materials, vol. 5, p. 042002, Sept. 2018.

[185] "High-throughput prediction of the ground-state collinear magnetic order of inorganic materials using density functional theory," vol. 5.

[186] A. Togo and I. Tanaka, "First principles phonon calculations in materials science," Scripta Materialia, vol. 108, pp. 1–5, Nov. 2015.

[187] J. D. Anderson and J. Wendt, Computational fluid dynamics, vol. 206. Springer, 1995.

[188] J. M. Ziman, Principles of the Theory of Solids. Cambridge university press, 1972.

[189] D. J. Tritton, Physical fluid dynamics. Springer Science & Business Media, 2012.

[190] F. Bloch, "Über die Quantenmechanik der Elektronen in Kristallgittern," Zeitschrift für Physik, vol. 52, pp. 555–600, July 1929.

[191] M. Born and V. Fock, "Beweis des adiabatensatzes," Zeitschrift für Physik, vol. 51, pp. 165–180, Mar. 1928.

[192] M. V. Berry, "Quantal phase factors accompanying adiabatic changes," Proceedings of the Royal Society of London. A. Mathematical and Physical Sciences, vol. 392, pp. 45–57, Mar. 1984.

[193] J. von Neuman and E. Wigner, "Uber merkwürdige diskrete Eigenwerte. Uber das Verhalten von Eigenwerten bei adiabatischen Prozessen," Physikalische Zeitschrift, vol. 30, pp. 467–470, 1929.

[194] S.-Q. Shen, Topological insulators, vol. 174. Springer, 2012.

[195] Y. Yao, L. Kleinman, A. H. MacDonald, J. Sinova, T. Jungwirth, D.-s. Wang, E. Wang, and Q. Niu, "First Principles Calculation of Anomalous Hall Conductivity in Ferromagnetic bcc Fe," Physical Review Letters, vol. 92, p. 037204, Jan. 2004.

[196] D. Ködderitzsch, K. Chadova, and H. Ebert, "Linear response Kubo-Bastin formalism with application to the anomalous and spin Hall effects: A first-principles approach," Physical Review B, vol. 92, p. 184415, Nov. 2015.

Curriculum Vitae

Personal

- Qiang Gao
- Born on September 11, 1988
- From Shenyang, Liaoning Province, China

Education background

- 10.2016–04.2020

  Theorie magnetischer Materialien, Fachbereich Material–und Geowissenschaften, Technische Universität Darmstadt, Darmstadt, Germany

  Supervisor: Prof. Hongbin Zhang. Subject: Material Science. Thesis title: High-throughput screening research for multifunctional magnetic materials

  Doctoral student

- 09.2013–06.2016

  School of Physical Science and Technology, Lanzhou University, Lanzhou, China

  Supervisor: Prof. Xianru Hu and Prof. Jianbo Deng. Subject: Theoretical Physics. Thesis title: First Principle Study on Some Spintronic Materials

  Master of Science

- 09.2009–06.2013

  School of Physical Science and Technology, Sichuan University, Chengdu, China

  Subject: Nuclear Physics

  Bachelor of Science